UNIVERSIDAD NACIONAL DE COLOMBIA
SEDE BOGOTÁ

Experimental research of the nuclear quasicontinuum and exploration of methods for the study of the nuclear continuum

Wilmar Rodríguez Herrera

Universidad Nacional de Colombia
Facultad de Ciencias
Departamento de Física
Bogotá, Colombia
2019

Experimental research of the nuclear quasicontinuum and exploration of methods for the study of the nuclear continuum

Wilmar Rodríguez Herrera

Doctoral thesis submitted in partial fulfillment of the requirements for the degree of:
PhD in physics

Supervisor:
Professor, Fernando Cristancho Mejía

Research area:
Nuclear structure
Research group:
Grupo de Física Nuclear de la Universidad Nacional

Universidad Nacional de Colombia
Facultad de Ciencias
Departamento de Física
Bogotá, Colombia
2019

Dedicated

to my parents

Whose unconditional support has allowed me to reach this point.

Abstract

Level lifetime and sidefeeding time measurements were performed on the excited states of the normally deformed bands of ^{83}Y using the Doppler-Shift Attenuation Method (DSAM). The high spin states of ^{83}Y were populated using the fusion-evaporation reaction ^{58}Ni(^{32}S,α3p)^{83}Y at 135 MeV. 22 level lifetime and sidefeeding times were determined in most of the cases by comparing the lineshapes gated with transitions above and below the state under study. Quadrupole moments determined from lifetime measurements are in the range $1.1 - 3.1$ eb, which are similar to the ones found for some of the neighboring nuclei. ^{83}Y excited states were studied with paired Cranked Nilsson Strutinsky-Bogoliubov (CNSB) calculations. Unpaired Cranked Nilsson Strutinsky (CNS) calculations were used to specify configurations and study the band crossings. The measured $|Q_t|$ values show an agreement with CNSB calculations. Cranked shell model analysis evinced that the smallest quadrupole moment appears at the sharpest band crossing of the bands studied and CNSB calculations show an increase of the deformation thereinafter. The measured sidefeeding times were compared with predictions made by the simulations carried out with the GAMMAPACE code. The results were in agreement with the experimental values by assuming reduced transition probabilities of the collective transitions in the continuum region, lying in the range $40 - 80$ W.u.

The combination of the Hk technique with the EOS (Energy Ordered Spectra) was studied as a possible new experimental technique to be used in future research of the nuclear continuum region. The experimental detector array PARIS was tested by Monte Carlo simulation for the application of the Hk technique. The results show that the simulated geometry for the PARIS array has a combined triggering effieciency at high energies which is very low for the implementation of the Hk technique, in spite that the design of the PARIS detectors was intended for the detection of high energy γ-rays. Adequate geometries and detector features of the experimental array for the application of the Hk-EOS technique are proposed.

Keywords: Gamma-ray Spectroscopy, DSA measurements, Lifetime and sidefeeding times, Nuclear continuum, Fusion-evaporation Reactions, Nuclear Structure.

Resumen

Mediciones de tiempos de vida y tiempos de alimentación lateral fueron realizadas en los estados excitados de las bandas normalmente deformadas de ^{83}Y haciendo uso del método de atenuación por efecto Doppler (DSAM). Los estados de alto espín de ^{83}Y fueron poblados usando la reacción de fusión-evaporación ^{58}Ni(^{32}S,α3p)^{83}Y a 135 MeV. 22 tiempos de vida y tiempos de alimentación lateral fueron determinados, en la mayoría de los casos, por comparación de las formas de línea producidas de los espectros en coincidencia con transiciones arriba y abajo del estado de interés. Los momentos quadrupolares que fueron determinados de las medidas de tiempos de vida están en el rango $1.1 - 3.1$ eb, similares a los encontrados para algunos núcleos vecinos. Los estados excitados del ^{83}Y fueron estudiados por medio de cálculos que incluyen el efecto de emparejamiento (CNSB). Cálculos sin incluir el efecto de emparejamiento fueron utilizados para especificar las configuraciones y estudiar los cruces de banda. Análisis hechos por medio del modelo de capas en rotación evidenciaron que el momento cuadrupolar más bajo aparece en el cruce de banda más agudo de las bandas estudiadas y los cálculos CNSB muestran un aumento de la deformación desde ese punto. Los tiempos de alimentación lateral medidos se compararon con predicciones hechas con simulaciones llevadas a cabo con el código GAMMAPACE. Los resultados encontrados concuerdan con los valores experimentales cuando se asumen probabilidades de transición colectivas en la región del continuo que se encuentran en el rango de $40 - 80$ W.u.

La combinación de la técnica Hk con los EOS (Espectros Energéticamente Ordenados) fue estudiada como una posible técnica experimental nueva para ser usada en futuras investigaciones de la región del continuo nuclear. El arreglo experimental de detectores PARIS fue estudiado para la aplicación de la técnica Hk. Los resultados de la simulación muestran que la geometría simulada para el arreglo PARIS tiene una eficiencia de disparo combinado que es muy baja para la implementación de la técnica Hk, a pesar de que el diseño de los detectores de PARIS fue planeado para la detección de rayos γ de alta energía. Geometrías adecuadas y características de los detectores del arreglo experimental para la aplicación de la técnica Hk son propuestas.

Palabras clave: Espectroscopía de rayos Gamma, Continuo nuclear, Reacciones de fusión-evaporación, Estructura Nuclear

Contents

1. Introduction

The interaction between two nucleons (protons or neutrons) mediated by the strong nuclear force, has not a complete theoretical explanation yet. Furthermore, for most of the nuclei the number of nucleons is not low enough to try to solve the system by use of ab-initio calculations and it is also not large enough, so that statistical models can be applied only for some nuclei. These are some of the reasons why many models have been proposed to explain the nuclear properties. Currently, the models continue being tested in order to improve them or to identify their limits. To succeed in this goal nuclei in several mass regions, must be experimentally characterized because predictions of the models depends on the nuclear region.

Most of the experimental techniques to study the nuclei are based on the analysis of the radiation that is emitted by them. The detection of γ-rays is one of the most utilized technique. By studying the γ-rays emitted from discrete and continuum states it is possible to study the nuclear properties of the discrete excited states and of the states in the continuum.

During the last decades most of the experimental studies of the nuclei have been intended to understand the behavior of the nuclei in the discrete region. On the other hand only few techniques as the Oslo method [1] have been developed to study the continuum region. Although currently there is a lack of experimental techniques able to distinguish the radiation emitted from the continuum states, it has been shown by numerical simulations [2] that the EOS (Energy Ordered Spectra) technique could be used to study the nuclear properties of the continuum states. To reconstruct the spin and energy point originating an EOS the Hk technique can be applied. However before an experiment can be proposed it is necessary to evaluate the influence of the experimental array on the application of the Hk technique to study the continuum and this is one of the aspects studied in this work.

A possibility to study the nuclear properties in the quasicontinuum region is by making use of the measurement of the so called “sidefeeding” states, which are those states whose transitions are feeding the discrete states. By means of numerical simulations in which the continuum properties are introduced, the experimental values can be compared with the simulated sidefeeding times. The output of these comparisons will be the possible nuclear configurations of the quasicontinuum states. The process of measuring the sidefeeding times involves the measurement of lifetimes as well.

The lifetime measurements of collective excited states provide the most powerful tool to determine their quadrupole moments and to study rotational properties of the nucleus.

In particular the lifetimes of most of the states currently known for ^{83}Y had not yet been measured, which did not allow a complete study of the nuclear shape evolution of this nucleus, before this work. Moreover, the methodology used in previous works [3–6] involves the simultaneous measurement of sidefeeding and level lifetimes, i.e., using the same lineshape, possibly introducing not valid correlations between both of them. In the present work that problem is avoided by obtaining lineshapes using Gates From Above (GFA) and Gates From Below (GFB) the transition of interest where possible. The results presented here aim to complement current information on nuclear structure of normally deformed bands of ^{83}Y by means of lifetime measurements. The later will provide more precise determination of quadrupole moments providing better and new data to test the theoretical models.

In Chapter 2 the general physics concepts implied in the development of this thesis will be presented. The current research status and the motivation to perform the studies carried out are explained in Chapter 3. The experimental details implied both in the lifetimes measurements and in the implementation of the Hk-EOS technique are described in Chapter 4. The data analysis carried out to determine the lifetime and sidefeeding time measurements of the ^{83}Y excited states are detailed in Chapter 5. The methodology to study the continuum by means of the Hk-EOS technique is described in Chapter 6 and finally the analysis of the results obtained will be presented in Chapter 7.

2. Nuclear structure concepts

2.1. Chart of nuclides and the region under study

There are 254 stable nuclei, and more than 3000 radioactive isotopes have been produced in the laboratory, so far. A common way to visualize all those nuclei is to sort them in the so called "chart of nuclides", shown in Figure **2-1**, The Y-axis indicates the number of protons and the X-axis indicates the number of neutrons.

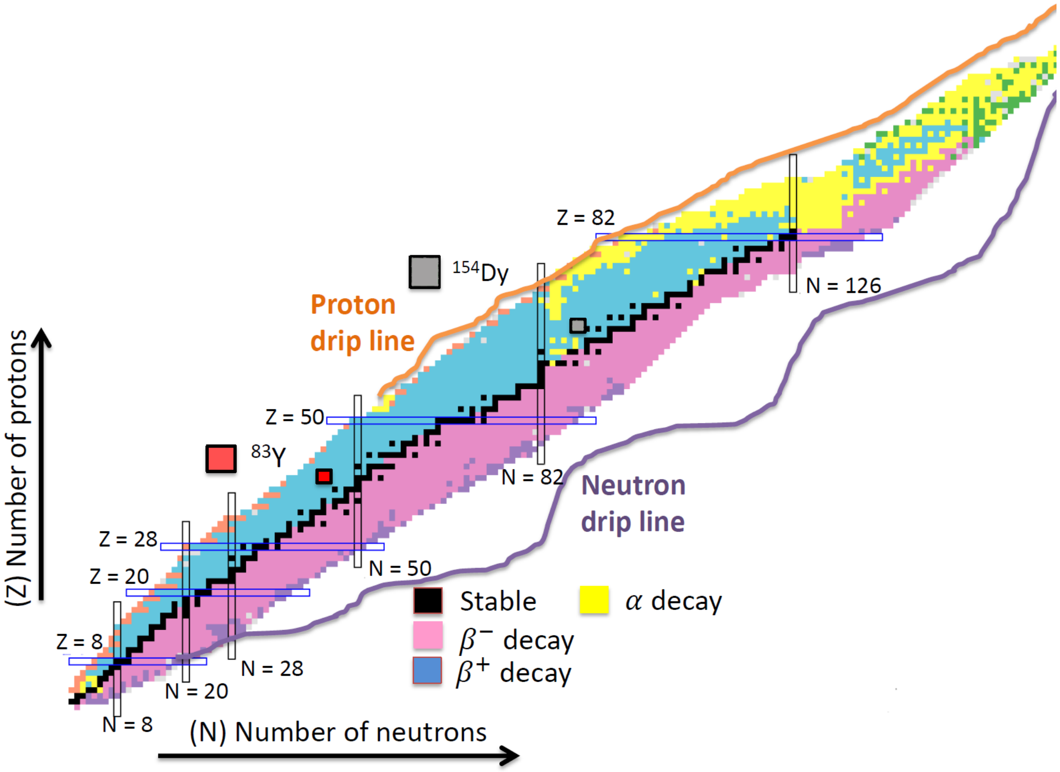

Figure 2-1.: Chart of nuclides. The magic numbers for protons and neutrons and some of the decay modes are shown as well as the proton and neutron drip lines. The nuclei of interest in this thesis are also marked with the squares red and green. Modified from the original at [7].

Figure **2-1** also shows some decay modes for radioactive nuclei which are α, β^+ or β^- decays. The neutron and proton drip lines indicate the limits in the number of protons or neutrons for which those nuclei could generate bound states.

Depending on the region of the chart of nuclides that we want to study, many types of reactions can be carried out (Coul-ex, Deep-inelastic, fusion-evaporation, etc.). The nuclei related with this thesis (^{83}Y and ^{154}Dy) are located in Figure **2-1**. To populate excited states of those nuclei belonging to the continuum region a fusion-evaporation reaction can be used.

2.2. The spin-energy plane

In nuclear physics the total angular momentum of the nucleus is referred as the nuclear spin. A useful representation of the excited states of the nucleus is achieved in the spin-energy plane, as the one shown in Figure **2-2** where the compound nucleus produced in a fusion-evaporation reaction is shown in the highest part of the figure. Fusion-evaporation reactions produce nuclei at high spin states. In these kind of reactions the so called “compound nucleus” is generated at a high excitation energy that makes the nucleus emit nucleons and γ-rays. Afterwards it is converted in other nuclei, among them, the nucleus of interest. The nucleus of interest is produced with an spin-energy entry distribution (labeled as entry states in Figure **2-2**) from which the nucleus will decay by emitting γ-rays until it reaches its ground state. For a given nuclear spin the nucleus has a energy low limit. This limit is called “yrast” line, which indicates the maximum value of spin allowed for a given energy.

The higher the excitation energy of the nucleus above the yrast line the smaller energy space between the excited states are. Additionally the energy width of the excited states increases with excitation energy and a continuum region is generated. Three different regions can be distinguished in Figure **2-2**, the discrete, the quasicontinuum and the continuum regions. In general, nuclei, can be characterized by two type of quantities:

- structural: deformation parameter β, moment of inertia $\mathcal{J}(\beta)$, quadrupole moment $Q(\beta)$ [8–10].
- statistical: density of states ρ, gamma strength Γ [8, 9].

The structural quantities are properties of the discrete region whereas the quasicontinuum and continuum regions are characterized by both structural and statistical properties. Structural quantities have been related with thermodynamical quantities which can be used to describe the nucleus in the continuum and the quasicontinuum region [11–13].

The nuclear properties in each region can be studied both by studying the radiation emitted in such regions and by studying the effects of those γ-rays on the population of the discrete states. The later requires the understanding of the discrete transitions which will be described in the next section.

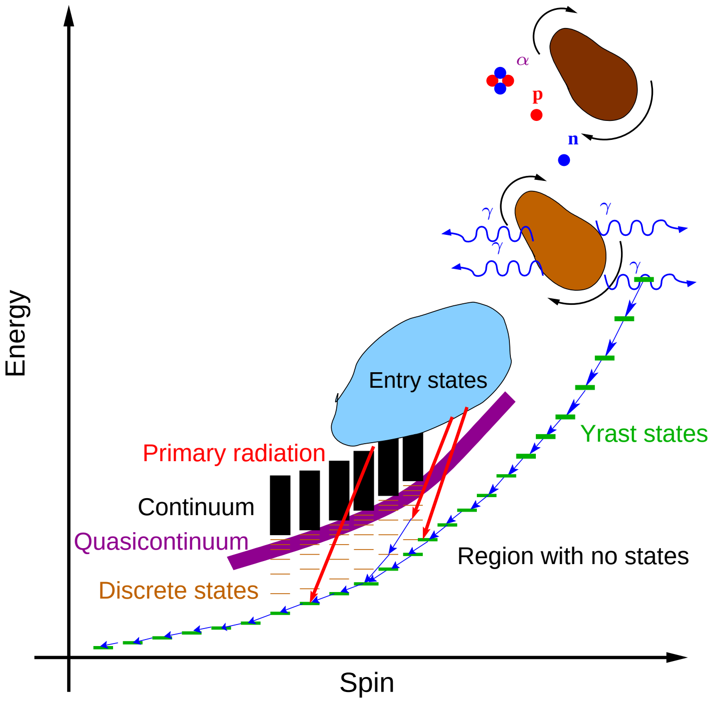

Figure 2-2.: Scheme of the nucleus production and decay in a spin-energy plane.

2.3. Discrete states

Figure **2-3** depicts the intensity of the transitions as they result from a heavy-ion reaction. The thicker the line representing a transition, the larger the corresponding intensity is. In Figure **2-3** it is suggested that the intensity of a γ-ray emitted in a transition, increases when the transition takes place at a lower energy level, due to the sidefeeding. Therefore the intensities are larger for γ-rays emitted at low energy levels.

For every state the level lifetimes τ are inversely proportional to the decay probability. Likewise the side feeding times are related to the decay probability of states belonging to the quasicontinuum region. Measuring level lifetimes and sidefeeding times makes possible to determine structural and statistical properties of the quasicontinuum which was the methodology used in this thesis to study the excited states of the ^{83}Y nucleus.

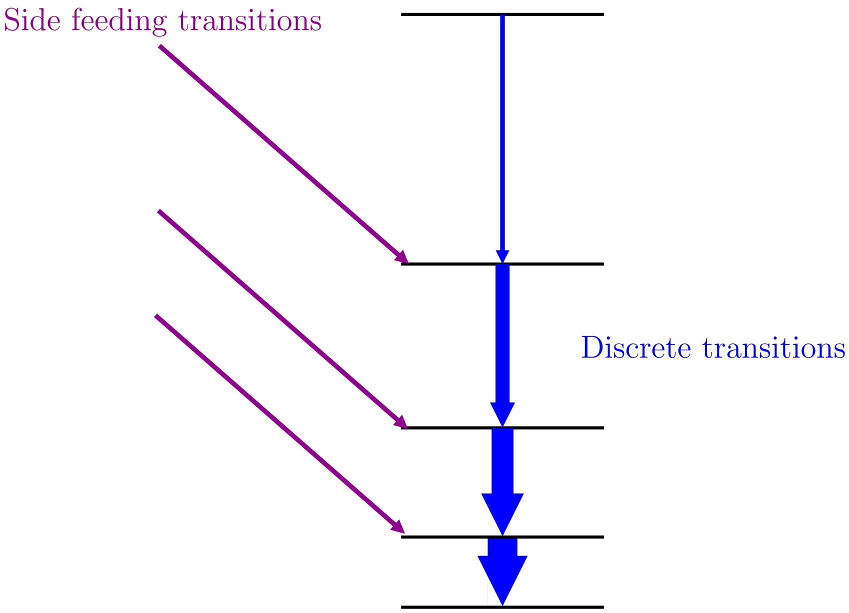

Figure 2-3.: Level scheme showing the discrete transitions and the side feeding of the discrete states. The intensity of the transitions is proportional to the width of the arrow.

2.4. Rotational bands

In a fusion-evaporation reaction, the resulting compound nucleus has a very large angular momentum which is typically some tens of $\hbar$ and a rotational behavior of the nucleus is produced. This behavior has been described theoretically by assuming a rigid rotor model of the nucleus as,

$$\mathbf{H} = \frac{\mathbf{R}^2}{2\mathcal{J}^{(1)}} \longrightarrow E = \frac{I(I+1)}{2\mathcal{J}^{(1)}} \cdot \hbar^2. \tag{2-1}$$

where $\mathbf{R}$ is the angular momentum associated to the collective rotation. $\mathcal{J}^{(1)}$ is the kinetic moment of inertia of the nucleus.

In the model of the rotating nucleus the energy is changed by the discrete changes in the quantum angular momentum. In a rotational band two consecutive excited states have a spin difference of $2\hbar$. The kinetic moment of inertia $\mathcal{J}^{(1)}$ is defined as [14]

$$\frac{\mathcal{J}^{(1)}}{\hbar^2} = \frac{1}{2}\left(\frac{dE}{dI(I+1)}\right)^{-1} = \frac{2I-1}{E_I - E_{I-2}} \tag{2-2}$$

A representation of the level scheme and the corresponding spectrum of an ideal rotational band are shown in Figure **2-4**. An spectrum with a constant energy space between the photopeaks, as the one depicted in Figure **2-4**, indicates a perfect rigid rotor nucleus.

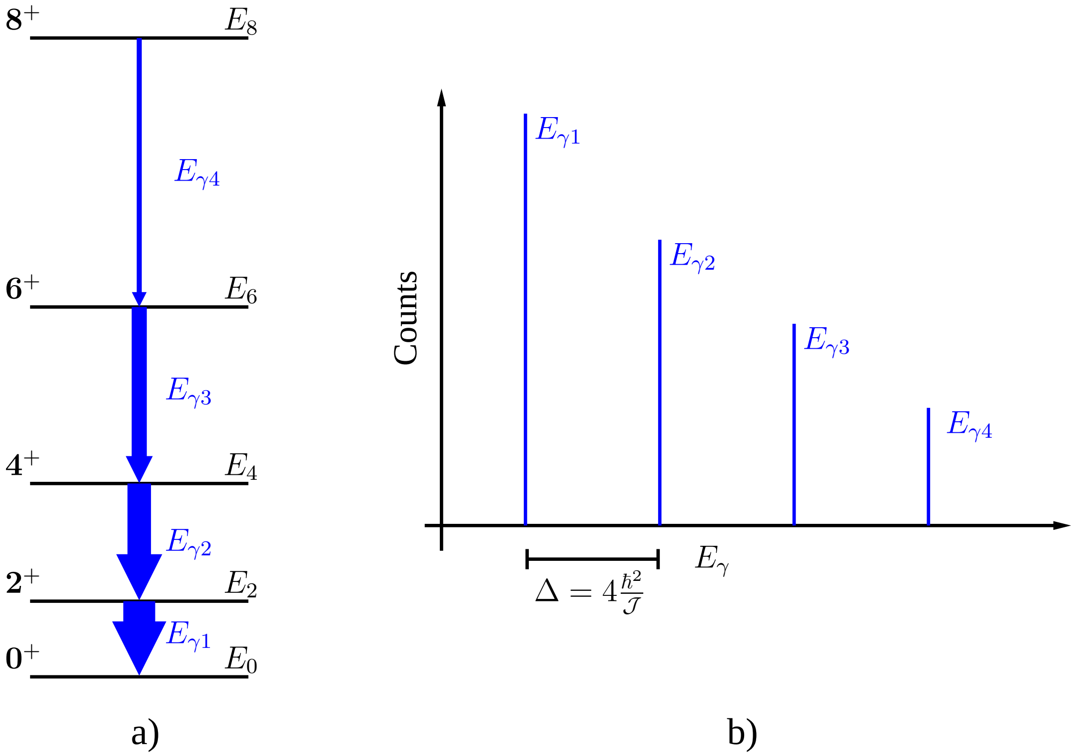

Figure 2-4.: a) Level scheme of a rotational band. b) A perfect spectrum of a rotational band

To examine the variations of the kinetic moment of inertia the dynamic moment of inertia $\mathcal{J}^{(2)}$ is defined as

$$\frac{\mathcal{J}^{(2)}}{\hbar^2} = \left(\frac{d^2E}{dI(I+1)}\right)^{-1}. \tag{2-3}$$

From the definition of the kinetic and dynamical moments of inertia $\mathcal{J}^{(1)}$ and $\mathcal{J}^{(2)}$ a relationship among them can be deduced

$$\mathcal{J}^{(2)}(\omega) = \mathcal{J}^{(1)}(\omega) + \omega\frac{d\mathcal{J}^{(1)}(\omega)}{d\omega} \tag{2-4}$$

When $\mathcal{J}^{(1)}$ is constant it is said that the nucleus undergoes a rigid rotation. From Equation (2-4) it can be inferred that when $\mathcal{J}^{(1)}$ is constant $\mathcal{J}^{(1)} = \mathcal{J}^{(2)}$. To analize the regions for which there is a rigid rotation, $\mathcal{J}^{(1)}$ and $\mathcal{J}^{(2)}$ can be plotted together as it will be done and analized for the ^{83}Y nucleus in Chapter 7.

In analogy to classical mechanics (where the angular momentum is denoted as L instead of I) a rotational frequency ω can be defined as the derivative of the energy E with respect to the angular momentum. Applying such derivative to Equation (2-1) it is obtained that

$$\hbar\omega = \frac{dE}{d[I(I+1)]^{1/2}} = \sqrt{(I^2 - I + 1)}\left(\frac{E_\gamma}{2I-1}\right). \tag{2-5}$$

An approximation of this expression is usually applied for spin values $I \gtrsim 6\hbar$

$$\hbar\omega \simeq \frac{1}{2}E_\gamma \tag{2-6}$$

2.4.1. Odd-even rotating nuclei

Odd-even nuclei can be interpreted as to be composed by the core constituted by the even-even number of protons and neutrons plus one uncoupled nucleon. The core will have a total angular momentum $I = 0$ following the seniority rule which states that identical particles will be coupled by pairs to $I = 0$ [15]. An important quantum mechanical effect is that collective rotations along the symetry axis of the nucleus will not produce any observable change since such a rotation will change the wave function only by a phase factor. An schematic representation of an odd-even nucleus illustrating the most important quantum numbers is shown in Figure **2-5**.

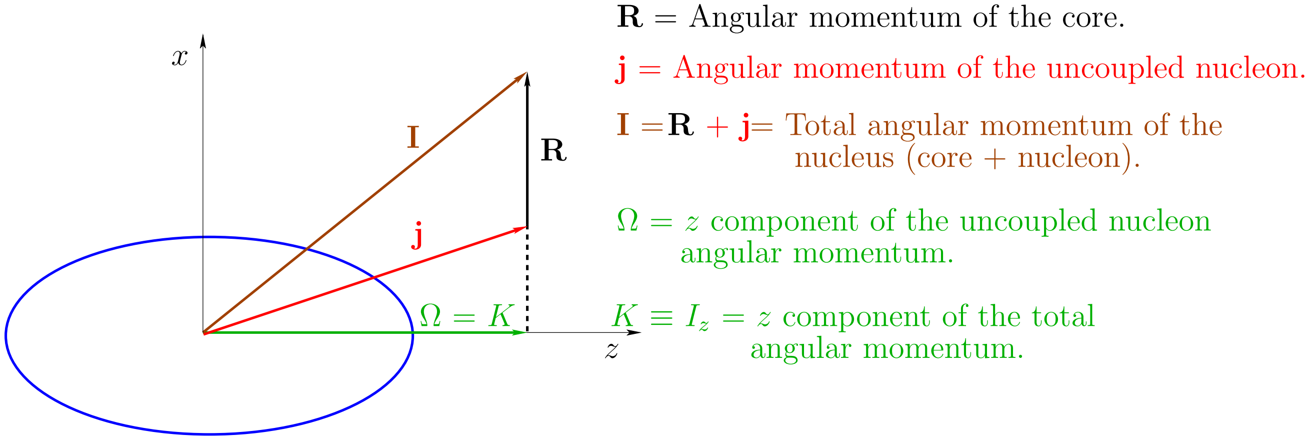

Figure 2-5.: Schematic representation of the quantum numbers describing the rotation of an odd-even nucleus.

2.4.2. Band crossings

A rotational band is a sequence of states which can be interpreted as being originated by a rotating nucleus with a given set of quantum numbers as parity and signature. Same parity and signature can be produced by different configurations in which one or more nucleon pairs can be uncoupled from the core of the nucleus. The rotating nucleus will produce a Coriollis force on the uncoupled nucleons that will tend to align their spin along the rotation axis producing configurations of lower energy. Such an effect will start to become important when increasing the rotational frequency. The initial configuration of a rotational band is the one with less uncoupled nucleons. However by increasing the nuclear spin the uncoupled nucleons configuration become more favoured in energy and band crossings can appear as it is schematically shown in Figure **2-6**.

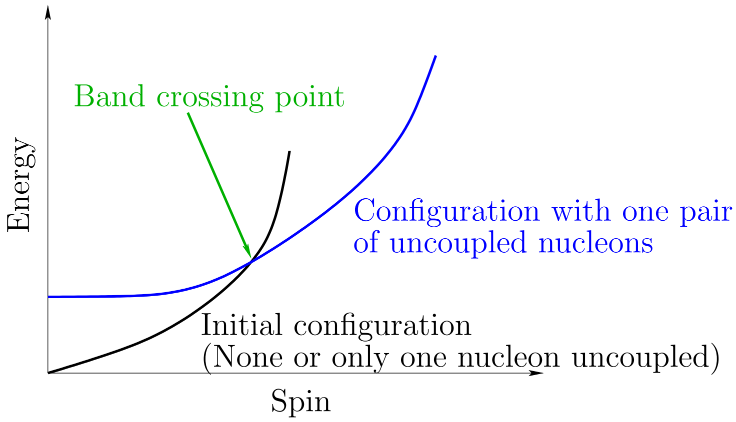

Figure 2-6.: Schematic representation of a band crossing.

The sequence of states that will have the transitions with the largest intensity in an experiment is the one for which the state energy is lowest for each spin value. Thus in Figure **2-6** for spin values lower than the one in which the band crossing occurs, the transitions represented by the black curve will have larger intensity than the transitions represented by the blue curve. After the band crossing the situation will be the opposite. In most of the cases lower intensity configurations are not observed in the experiment and therefore only the lower energy states are visible.

When a band crossing occurs usually the value of the kinetic moment of inertia $\mathcal{J}^{(1)}$ of the observed band will present a sudden change that will be visualized better in a plot of the dynamic moment of inertia $\mathcal{J}^{(2)}$ as it will be shown in Sections 7.5.3 and 7.5.4. Another important change that arises in a band crossing is that the spin (total angular momentum in nuclear physics) of the uncoupled nucleons of the observed band will present a sudden change in its aligment. This is due to the aligment that uncoupled nucleons experience due to Coriollis force, as it was mentioned earlier.

2.5. Deformed nuclear potential

The spherical shell model of the nucleus is not enough to describe many nuclei and deformed nuclear potentials are usually applied. The modified harmonic oscillator potential is the simplest analytical model that can be used to illustrate the nuclear deformation concepts. The pure harmonic oscillator potential is not adecuate to describe the nuclear mean potential. The radial dependence should lie in between the one for the square well and the one of the harmonic oscillator potentials, as it is the case of the Woods-Saxon potential. An aditional term $(\mathbf{I}^2 - \langle \mathbf{I} \rangle)$ with $\mathbf{I}$ the angular momentum is added to the harmonic oscillator potential to get a better description of the nuclear mean potential. From now on only the term which inludes the explicit spatial dependence and thus the deformation will be presented. The spherical harmonic oscillator potential $\mathbf{V_S}$ is given by

$$\mathbf{V_S} = \frac{1}{2} M\omega_0^2 \mathbf{r}^2. \tag{2-7}$$

where ω_0 is the oscillation frequency, M the nuclear mass and $\mathbf{r}$ the radial coordinate operator. Quadrupolar axial deformation can be introduced in the potential by writing it as

$$\mathbf{V_D} = \frac{M}{2}\left[\omega_\perp^2(\mathbf{X}^2 + \mathbf{Y}^2) + \omega_z^2\mathbf{Z}^2\right], \tag{2-8}$$

where the oscillation frequencies $\omega_\perp$ and ω_z are expressed in the case of quadrupolar deformation by

$$\omega_\perp = \omega_0[1 + 2/3\varepsilon_2] \tag{2-9}$$
$$\omega_z = \omega_0[1 - 2/3\varepsilon_2]. \tag{2-10}$$

ε_3 is the quadrupolar elongation parameter that complies

$$\varepsilon_2 = (\omega_\perp - \omega_z)/\omega_0 \quad \text{where} \begin{cases} \varepsilon_2 > 0 & \text{prolate shape} \\ \varepsilon_2 = 0 & \text{spherical shape} \\ \varepsilon_2 < 0 & \text{oblate shape} \end{cases} \tag{2-11}$$

The geometrical surface of the nucleus for an axially symetric nucleus can in general be written as a series of Legendre plynomials $P_\lambda(\cos\theta)$ as

$$R(\theta) = R_\beta \left[1 + \left(\frac{2\lambda+1}{4\pi}\right)^{1/2} \sum_{\lambda=2,3,\ldots} \beta_\lambda(P_\lambda(\cos\theta))\right], \tag{2-12}$$

where quadrupolar shapes are described by the term with $\lambda = 2$. The ε parameter defined in Equation (2-11) is related to the quadrupolar deformation parameter β_2 by

$$\varepsilon_2 = \frac{3}{2}\left(\frac{5}{4\pi}\right)^{1/2} \approx 0.95 \cdot \beta_2 \tag{2-13}$$

In spite of the fact that some nuclei can be described by axially symetric potential shapes there are others for which such a potential shape does not provide a satisfactory description. Aditionally some nuclei that can be described in their ground states with axially symetric shapes, change their shape to become triaxial with the rotation at high spin. For this reason axially asymetric or triaxial shapes are introduced in the harmonic oscillator potential.

This is usually done by introducing oscillation frequencies which satisfy the relationship $\omega_x \neq \omega_y \neq \omega_z$. Thus the triaxial harmonic oscillator potential is written as

$$\mathbf{V_T} = \frac{M}{2}\left[\omega_x^2\mathbf{X}^2 + \omega_y\mathbf{Y}^2 + \omega_z^2\mathbf{Z}^2\right], \tag{2-14}$$

where the frequencies are written in terms of a new parameter γ as

$$\omega_x = \omega_0\left[1 - \frac{2}{3}\varepsilon_2\cos\left(\gamma + \frac{2\pi}{3}\right)\right] \tag{2-15}$$

$$\omega_y = \omega_0\left[1 - \frac{2}{3}\varepsilon_2\cos\left(\gamma - \frac{2\pi}{3}\right)\right] \tag{2-16}$$

$$\omega_z = \omega_0\left[1 - \frac{2}{3}\varepsilon_2\cos\gamma\right]. \tag{2-17}$$

The set of deformation parameters $(\varepsilon_2, \gamma, \varepsilon_4, ..)$ are called the Nilsson deformation parameters [14]. With the description of Equation (2-14) the shape of the nucleus will be prolate for $\gamma = 0°$ and oblate for $\gamma = -60°$ and it will have triaxial shape for intermediate values. The relation between the γ and β_2 parameters is schematically shown in Figure **2-7**.

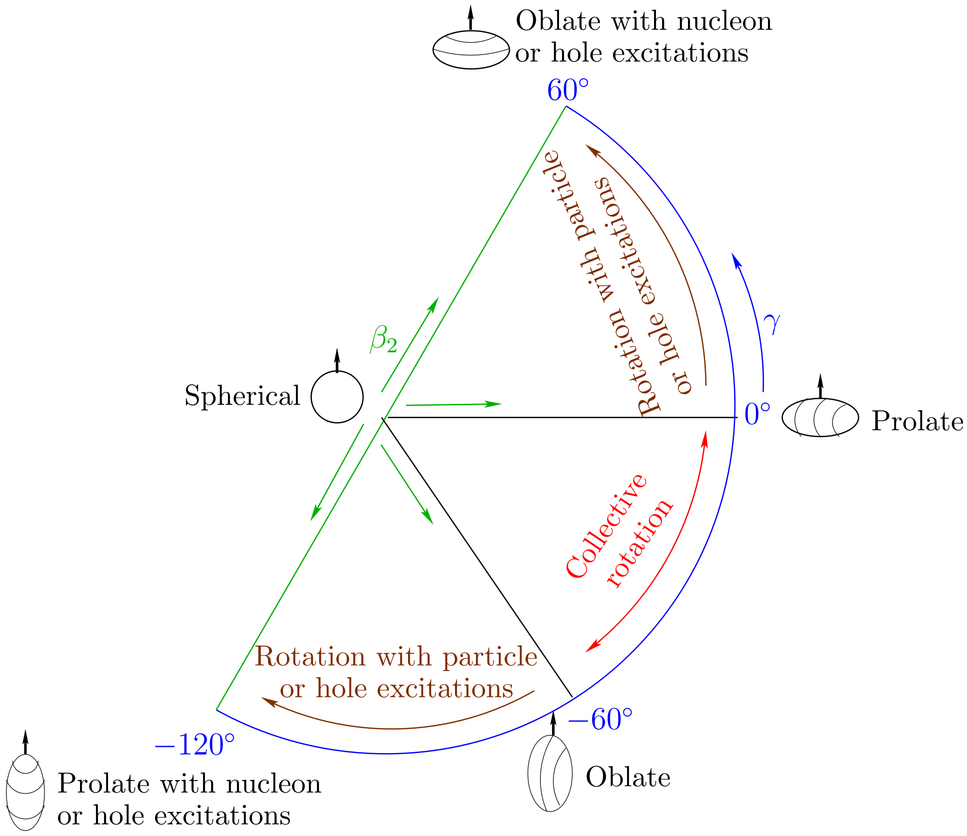

Figure 2-7.: Schematic representation of nuclear shapes and their relation with γ and β_2 values.

The β_2 and γ parameters can be linked to the quadrupole moment (see Section 7.3) since they are both related to the nuclear shape.

2.6. Band termination

Band termination phenomena have been described widely, see for example Ref. [16]. This an effect in which the final configuration of the nucleus does not allow to increase the angular momentum of the nucleus. In such a state the nucleus will be in a non-collective aligned state. Thus the valence particles and holes will be all as aligned to the rotation axis as the Pauli principle allows them to be. In such state the shape should be described either as oblate with $\gamma = 60°$ or prolate with $\gamma = -120°$. However the experimental data do not provide direct evidence to which of this shapes are building the terminating state. The maximum spin that can be built in a nucleus can be estimated by looking at the valence configuration in a Nilsson diagram and then calculating the maximum angular momentum that can be coupled with the valence particles in the valence space.

2.7. Kinetic moment of inertia of ^{83}Y normally deformed bands

The moment of inertia of a spherical nucleus can be calculated as a reference to be compared with experimental values. Clasically the moment of inertia of a rigid sphere of mass M and radius R is given by

$$\mathcal{J}_{sphere} = \frac{2}{5} M R^2, \tag{2-18}$$

The nuclear radius can be approximated as $R = 1.2(A^{1/3})$ fm. For ^{83}Y the Equation (2-18) can be written as

$$\mathcal{J}_{sphere} \approx 0.0138 \cdot A^{5/3} \left.\frac{\hbar^2}{\mathrm{MeV}}\right._{A=83} = 22 \frac{\hbar^2}{\mathrm{MeV}}. \tag{2-19}$$

The moment of inertia for a quadropole-deformed nucleus can be calculated starting from the $\mathcal{J}_{sphere}$ value by using the deformation parameters β_2 and γ

$$\mathcal{J}^{(1)} = \mathcal{J}_{sphere} \left[1 + \sqrt{\frac{5}{4\pi}} \beta_2 \sin(30° + \gamma) \right]. \tag{2-20}$$

From Ref. [17] the quadrupole deformation for the ground state of the ^{83}Y nucleus is $\beta_2 = -0.15$. By using several values of γ in Equation (2-20) the corresponding moment of inertia values can be calculated. The comparison of such values with the experimentally obtained are shown in Figure **2-8**.

In Figure **2-8** positive and negative parity states are drawn by full and dashed lines, respectively. Closed (open) symbols are used for signature $\alpha = 1/2$ ($\alpha = -1/2$). This notation is adopted for all of the figures. The labels of the bands were assigned using parity π and signature α as (π, α) and the equivalences $\alpha = +1/2 \equiv +$ and $\alpha = -1/2 \equiv -$ were used.

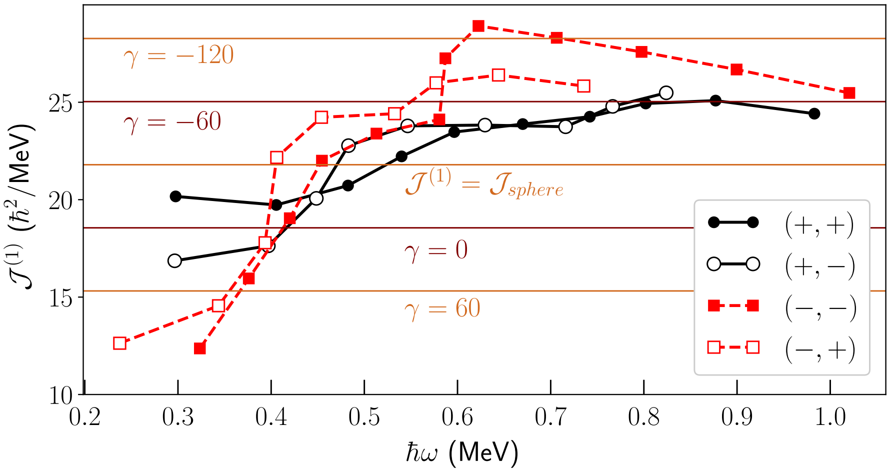

Figure 2-8.: Kinetic moment of inertia $\mathcal{J}^{(1)}$ of the normally deformed bands $(+,+)$, $(+,-)$, $(-,+)$ and $(-,-)$ of the ^{83}Y nucleus. In all figures, positive and negative parity states are drawn by full and dashed lines, respectively. Closed (open) symbols are used for signature $\alpha = 1/2$ ($\alpha = -1/2$).

The gradual increment of $\mathcal{J}^{(1)}$ at low rotational frequencies shown in Figure **2-8** can be explained by the aligment of the quasiparticles (nucleons or holes) as it will be shown in Sections 7.5.3 and 7.5.4. From Figure **2-8** it can be seen that the $\mathcal{J}_{sphere}$ value is below the saturation value $\sim 26\hbar^2/\text{MeV}$, found in Ref. [18] for nuclei with $A \sim 80$ for all of the bands plotted, which is reasonable because an spherical nucleus shape cannot show rotational behaviour. On the other hand the value which best approximates the saturation of the moment of inertia is $\gamma = -60°$ indicating that, under the assumption of $\beta_2 = -0.15$ the nucleus should have high collectivity with an oblate shape.

2.8. Electromagnetic radiation emitted by the nucleus

For radiating systems whose dimensions are much smaller than the wavelenght of the radiation they emit, the long wave approximation can be used. This approximation consists on considering $kr \ll 1$ (with k the wavenumber and r de dimensions of the emiter, see Ref [19]) in the Bessel functions resulting in the expression for the amplitude of the electromagnetic fields produced by radiating systems. The nucleus has a size which is in the order of a few fermis and the radiation it emits has a typical wavelenght in the order of a hundred fermis which justifies the use of the long wave approximation in this case. Within this approximation it can be shown that the amplitude of the radiated electromagnetic field $a_E(\ell)$ produced by the electric multipolar distribution of charges can be written as

$$a_E(\ell) = f(\ell)k^{\ell+2}Q_\ell, \tag{2-21}$$

where $f(\ell)$ is a function of the multipolar order ℓ and Q_ℓ is the electric multipolar moment of order ℓ. The amplitude of the electromagnetic radiation produced by the presence of magnetic multipolar moments, M_ℓ, in the nucleus have a similar expression to Equation (2-21). The charge density of the protons represents the main contribution to Q_ℓ. Nonetheless due to the spin of the neutrons and protons a magnetization density will arise in the nucleus generating a contribution to electric moments. However it can be shown, under the Weisskopfs approximations [10], that the charge density contribution to Q_ℓ is approximately 10^3 larger than the contribution of the spin. Therefore usually the electric moment values are interpreted as being produced by the charge distribution of the protons inside the nucleus.

2.9. Emission probability

The power produced by electromanetic radiation is proportional to the square of the field amplitudes $a_E(\ell)^2$ per time unit. The transition emission probability T is by definition the number of photons emitted per time unit. Thus the power radiated and the transition probability will be proportional and the transition probability can be written as

$$T = \frac{1}{\tau} = C \cdot \frac{a_E(\ell)^2}{k^3}, \tag{2-22}$$

where C is a constant and τ is the lifetime of the state emitting the radiation. The transition probability can be rewritten using the relation of the energy of the γ-ray with the wavenumber $k\hbar c = E_\gamma$ and separating the part which contains the contribution of the quantum numbers of the states as

$$T = \frac{1}{\tau} = g(\ell)E_\gamma^{2\ell+1}B(\ell), \tag{2-23}$$

where $g(\ell)$ is a function of the multipolar order ℓ and $B(\ell)$ is the so called “reduced transition probability” which is the part of the transition probability that contains the influence of the quantum structure of the states implied in the transition.

2.10. Quadrupolar electric transitions $E2$

It has been experimentally proved that rotational decay sequences have quadrupolar electric transitions $E2$, which means multipolar order $\ell = 2$ in Equations (2-21) to (2-23). Thus an expression for the electric quadrupole reduced transition probability will be studied. From Equation (2-23) it can be deduced that

$$B(E2) = \frac{815.6}{E_\gamma^5(\text{MeV})\tau(\text{ps})} \tag{2-24}$$

where the energy E_γ is in MeV, the lifetime τ in picoseconds and $B(E2)$ in $e^2\text{fm}^4$.

Combining Equations (2-21) to (2-23) it can be seen that $B(E2) \propto Q^2$ and asuming a nucleus with axial symmetry the following relation can be deduced

$$|Q_t| = \sqrt{\frac{16\pi}{5}} \frac{\sqrt{B(E2)}}{|\langle I_i, K; 20 | I_i - 2, K\rangle|}, \tag{2-25}$$

where Q_t is the convention used to denote the "transitional quadrupole moment", I_i is the nuclear spin of the initial state and K is the quantum number represented in Figure **2-5**.

2.11. The Weisskopf model

Theoretical values of $B(E2)$ can be obtained applying the Weisskopf model [10] which is built under the approximation that the nucleons can be considered as independent particles moving in an average potential. Matematically the approximation of independent particles is carried out by writing the wave function of the nucleus as a product of wave fuctions of every nucleon. The sources of error of that approximation appear for example when there is a tendency of the nucleons to create clusters of alpha particles and in general when the movements of the nucleons are somehow correlated among them. Despite Weisskopf model is an approximation, for the case of $E2$ transitions it has demonstrated that its predictions for the gamma strengths are very close to experimental values, see Ref. [20]. $B(E2)$ can be calculated within the Weisskopf model [20] to obtain the single particle transition probability

$$B(E2)(1 \text{ W.u.}) = 0.05940 \cdot A^{4/3} \text{ e}^2\text{fm}^4. \tag{2-26}$$

Equation (2-26) defines one Weisskopf unit (1 W.u.) for $E2$ transitions and it provides the value for the case when one single nucleon is involved in the transition. Within this model the values obtained for the transition probabilities using the experimental lifetimes τ and energies E_γ with Equation (2-24) can now be normalized to evaluate how many Weisskopf units the experimentally obtained values represent. The usefulness of applying this model is that asuming its validity the number of nucleons involved in the transition can be calculated by evaluating the expression

$$B(E2)(\text{W.u.}) = \frac{815.6}{[E_\gamma(\text{MeV})]^5\tau(\text{ps}) \cdot 0.0594 \cdot A^{4/3}}. \tag{2-27}$$

2.12. Routhians $E_x^\omega(I)$

The energy of a rotational state in the intrinsic frame of reference is called "Routhian". The term $\hbar\omega I_x$ is the quantum mechanical analogue of the Coriollis and centrifugal forces in classical mechanics. The total Routhian $E_x^\omega(I)$ which represents the energy in the intrinsic rotating frame of reference is given by

$$E_x^\omega(I) = E_x(I) - \hbar\omega I_x(I), \tag{2-28}$$

with $E_x(I)$ the energy of the level with spin I and

$$I_x = \sqrt{I(I+1) - K^2}. \tag{2-29}$$

The expression for I_x (the angular momentum along the rotation axis) can be understood by looking the Figure **2-5**. $E_x^\omega(I)$ contains a contribution from the collective rotation together with intrinsic excitations of the unpaired nucleons. The energy of the quasiparticles e (nucleons or holes) can be extracted from $E_x^\omega(I)$. The procedure implemented to get e for ^{83}Y will be presented in the Section 2.12.1.

Figure **2-9** shows for the ^{83}Y nucleus the energy of excited states E_x, and the angular momentum along the rotation axis I_x, both quantities exhibiting an increase with $\hbar\omega$ showing notable increments in the $(-,+)$ band at $\hbar\omega \approx 0.58$ MeV and also in the $(-,-)$ band at $\hbar\omega \approx 0.40$ MeV. This phenomenon will be estudied in more detail in Chapter 7. Figure **2-9** also shows the total Routhian, E_x^ω which is clearly following a completely different behavior than E_x. The increments in E_x are due mainly to the rotational behavior of the nucleus. On the other hand when looking at the intrinsic frame of reference the energy starts at 0 MeV and decreases with the rotational frequency as a result of the alignment to the rotation axis that quasiparticles experience due to the Coriollis force which tend to push the system to a lower energy configuration.

2.12.1. Quasiparticle routhians $e(\omega)$

The routhians $E_x^\omega(I)$ contain contribution from both the collective rotation and the intrinsic excitation of the quasiparticles. As it was stated in Ref. [21] the so called quasiparticle energies and aligned angular momentum can be calculated starting from $E_x^\omega(I)$ and extracting the reference energy values of the collective rotation. The reference or ground configuration of a nucleus is understood as the rotating core of the nucleus when no nucleons have been unpaired. Such ground configuration can be obtained for even-even nuclei by taking the yrast band before the first band crossing arises. However for even-odd nuclei as ^{83}Y it is necessary to look at the even-even neighboring nuclei as ^{82}Sr which can be interpreted as if it would be the ^{83}Y nucleus after removing the unpaired proton. With $E_g(\omega)$ being the energy of the

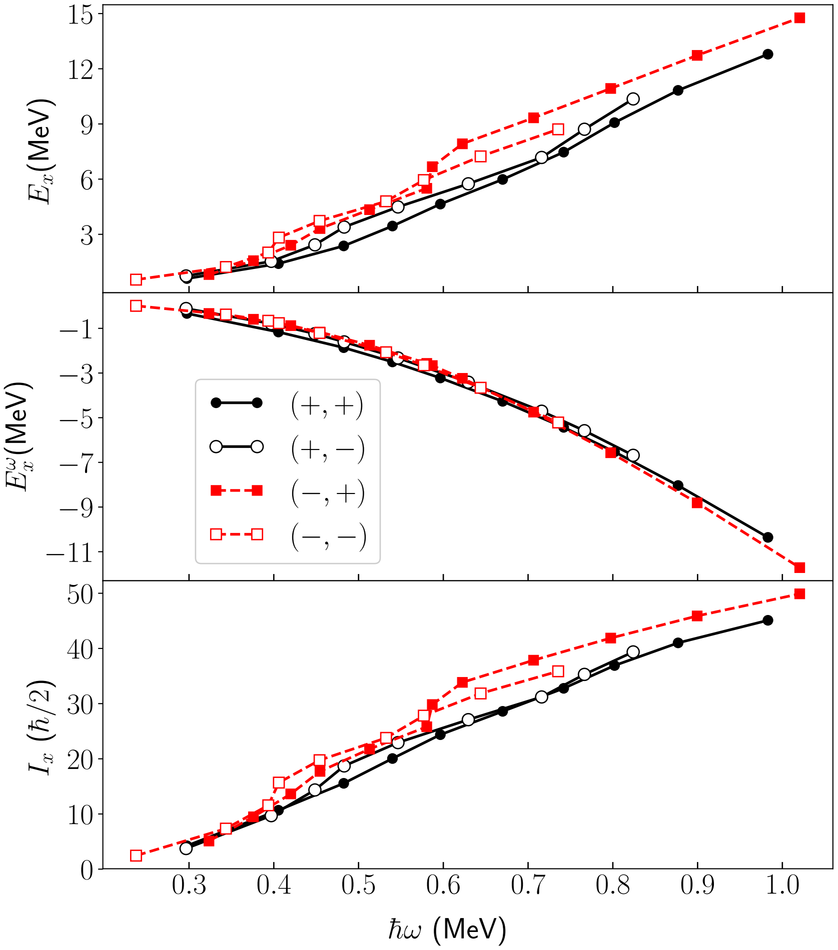

Figure 2-9.: Energies, E_x of the excited states, routhians, $E_x^\omega(I(\omega))$ of the bands and momentum angular, I_x along the rotation axis as function of the rotational frequency.

core of the nucleus in the ground configuration and $e(\omega)$ the energy of the quasiparticles in the intrinsic reference frame of the rotating nucleus, thus the relation

$$e(\omega) = E_x^\omega(I(\omega)) - E_g(\omega), \tag{2-30}$$

holds and similar equation can be written for the aligned angular momentum $i(\omega)$, of the quasiparticles in the intrinsic rotating frame of reference.

$$i(\omega) = I_x(\omega) - I_g^x(\omega), \tag{2-31}$$

where $I_g^x(\omega)$ is the aligned angular momentum of the core in the ground configuration. As band crossings usually occur at low rotational frequencies the typical procedure is to extrapolate the low frequency parts. The parametrization

$$I_g^x(\omega) = (\mathcal{J}_0 + \omega^2 \mathcal{J}_1)\omega + \ell \tag{2-32}$$

is used, where $\mathcal{J}_0$, $\mathcal{J}_1$ and ℓ are constant values which can be obtained from a fit to the experimental data of the kinetic moment of inertia, $\mathcal{J}_{eff}$ of the core of the nucleus for the yrast band before the first band crossing. The relation $\mathcal{J}_{eff} = I_g^x(\omega)/\omega$ which is analogous to the classical relation between the moment of inertia angular momentum and rotational frequency, is used to relate $\mathcal{J}_0$, $\mathcal{J}_1$ and ℓ with $\mathcal{J}_{eff}$.

$$\mathcal{J}_{eff} = I_g^x(\omega)/\omega = \mathcal{J}_0 + \omega^2 \mathcal{J}_1 + \frac{\ell}{\omega}. \tag{2-33}$$

To get the energy of the ground configuration, $E_g(\omega)$ the Equation (2-32) can be integrated

$$E_g(\omega) = -\int I_g^x(\omega) d\omega = -\frac{1}{2}\omega^2 \mathcal{J}_0 - \frac{1}{4}\omega^4 \mathcal{J}_1 - \ell\omega + \frac{1}{8}\hbar^2/\mathcal{J}_0. \tag{2-34}$$

In Section 7.5.2 the quasiparticle energies and alignments for the normally deformed bands of ^{83}Y will be studied.

2.13. The rotating liquid drop model

The similarities of the nuclear system with a liquid drop led to the proposal of the nuclear liquid drop model. To understand the feasibility of the model, firstly note that the molecules in a liquid drop interacts mostly with their neighboring molecules as the nucleons in the nuclei do. This interaction generate also a surface tension in the outer molecules (liquid drop) and nucleons (nucleus) due to the attraction to the inner part of the nucleus that they experience. Finally the evaporation of a molecule in a liquid drop is similar to the evaporations of nucleons, both being phenomena which are manifested with the presence of excitation energy in the whole system. Thus the binding energy of the nucleus can be described in the liquid drop model taking into account the following nuclear properties:

- The binding energy of the nucleus reach a saturation value when increasing the number of nucleons due to the fact that the nuclear force have a short range. This lead to the volumetric term.
- The nucleons at the surface are less bound because they interact with less nucleons than the case where they are located inside instead.
- The Coulomb interaction of the protons inside the nucleus decreases the binding energy.

- Nuclei with $Z \gtrsim 20$ need more neutrons than protons to build a bound system because of the Coulomb interaction which justify the need of inclusion of the asymmetry term.
- Nucleons tend to couple to lower energy configurations by pairs and therefore pairing energy should be considered.

With the considerations mentioned above, the description of the deformed nucleus as exposed in Section 2.5 is included in the liquid drop model to produce the formula for the energy at the spin of the ground state I_{GS} [16],

$$\begin{aligned} E_{ld}(I = I_{GS})(\text{def}) = &- a_v \left[1 + a_a \left(\frac{N-Z}{A}\right)^2\right] A \;+\; \frac{3}{5}\frac{e^2 Z^2}{r_0}\left[B_c(\text{def}) - \frac{5\pi^2}{6}\left(\frac{d}{r_0}\right)^2\right] \\ &+\; a_s \left[1 - a_a \left(\frac{N-Z}{A}\right)^2\right] A^{2/3} B_s(\text{def}) + \Delta. \end{aligned} \tag{2-35}$$

The four general terms of Equation (2-35) can be identified as the volumetric, Coloumb, surface and pairing terms respectively. The asymmetry term is also included as the factor multiplying the constant a_a. In Equation (2-35) A is the number of nucleons, $(\text{def}) \equiv (\varepsilon_2, \gamma, \varepsilon_4, ...)$, $r_0 \approx 1.2A^{1/3}$ fm and d is the diffuseness of the nuclear potential. The terms $B_c(\text{def}) = E_{Coul}(\varepsilon)/E_{Coul}(\varepsilon = 0)$ and $B_s(\text{def}) = E_{Surf}(\varepsilon)/E_{Surf}(\varepsilon = 0)$ correspond to the ratio between deformed and spherical shapes for the Coulomb and surface energy contributions. The parameters in Ref. [22] are used, namely

$$a_v = 15.49 \text{ MeV}, \quad a_s = 17.94 \text{ MeV}, \quad a_a = 1.78 \;\text{ and }\; d = 0.54 \text{ fm}. \tag{2-36}$$

The liquid drop model can be used as an approximation for the description of the rotational behavior of the nucleus with energies given by

$$E_{rld}(\text{def}) = E_{ld}(I = I_{GS})(\text{def}) + \frac{I(I+1)}{2\mathcal{J}_{rig}}. \tag{2-37}$$

As before the variable “def” denotates the deformation parameters. The second term in Equation (2-37) can be calculated for prolate nuclei with deformations $\beta_2 \sim 0.26 - 0.32$ or oblate nuclei with deformations $\beta_2 \sim 0.16$ following the expression in Ref. [23] for the moment of inertia of the rigid rotation,

$$\mathcal{J}_{rig} = \frac{A^{5/3}}{64.6}\left(\frac{\hbar^2}{\text{MeV}}\right). \tag{2-38}$$

In Sections 7.4 and 7.5.1 the rotating liquid drop energy of the normally deformed bands of ^{83}Y will be studied and compared with values of neghboring nuclei.

2.14. CNS and CNSB formalisms

In the Cranked Nilsson Strutinsky (CNS) formalism the modified harmonic oscillator potential h_q^M described in Section 2.5 is used together with the cranking term $\hbar\omega I_x$ described in Section 2.12 to produce the hamiltonian

$$H_{\mathrm{CNS}}(\omega) = \sum_{q=p,n} \left(h_q^M(\mathrm{def}) - \hbar\omega I_x \right), \tag{2-39}$$

where the subindex q runs over the p protons and the n neutrons and (def) denotates the set of Nilsson deformation parameters $(\varepsilon_2, \gamma, \varepsilon_4, ...)$ defined in Section 2.5. The hamiltonian $H_{\mathrm{CNS}}(\omega)$ can be solved with the Strutinsky method in which the energies are obtained with the Hartree-Fock method minimizing the deformation parameters. The resulting energies depend on the rotational frequencies ω. In the CNS formalism the particle number is conserved and the resulting wave functions and energies have specific particle configurations together with deformation parameters. The description of the rotational bands of the nucleus with the CNS calculations have demonstrated to produce values of the deformation parameters that are in agreement with measured quadrupole moments (see for example Refs. [24, 25]). The energies obtained with the CNS calculations usually present a difference with the experimental data that is lower for high spin states [26]. This difference can be explained because in $H_{\mathrm{CNS}}(\omega)$ the pairing energies were neglected. The pairing effect produces smaller contributions at high spin states since in that regime several quasiparticles are aligned. A detailed description of the CNS formalism can be found in Refs. [16, 27, 28].

To include the pairing effect in the hamiltonian the creation and anihilation operators $P_q^\dagger$ and P_q should be introduced together with the particle number operator $\hat{N}_q$ to account for nucleons being aligned. The resulting Cranked Nilsson Strutinsky Bogoliubov (CNSB) hamiltonian is

$$H_{\mathrm{CNSB}}(\omega) = H_{\mathrm{CNS}}(\omega) + \sum_{q=p,n} \Delta_q (P_q^\dagger + P_q) + \lambda_q \hat{N}_q, \tag{2-40}$$

where Δ is the pairing energy and λ the Fermi energy. The Hartree Fock Bogoliubov method [29] is used to solve the $H_{\mathrm{CNSB}}(\omega)$ hamiltonian. In this method the wave functions and energies are obtained by the minimization of the Δ_q and λ_q parameters together with the deformation parameters. The CNSB formalism produce much better energy predictions for low spin states than the the CNS formalism since in that regime several particles are paired [26].

In Section 7.6 CNS and CNSB calculations carried out for the normally deformed bands of ^{83}Y will be discussed and compared with experimental data.

2.15. Transition probabilities in the continuum

The emission probability for γ-rays coming from the excited states of the nucleus in the continuum region can be described by the Fermi's golden rule

$$P_{i\to f} \propto \rho(E_f, I_f)\langle\varphi_i|H|\varphi_f\rangle = \rho(E_f, I_f)\mathit{\Gamma}, \tag{2-41}$$

where ρ is the level density and $\mathit{\Gamma}$ is the gamma strength. These two variables will be discussed in the next subsections.

2.15.1. Level density

The level density is one of the main topics of interest in the nuclear continuum studies. The level density, ρ, for the nucleus can be modeled using the statistical definition of the entropy

$$S(A, E) = k\ln(\rho(A, E)), \tag{2-42}$$

where E is the excitation energy, A is the mass number and k is the Boltzman's constant. From Equation (2-42) the constant temperature approximation for the level density can be obtained,

$$\rho(A, E) = \rho(A, E_0)\exp\left(\frac{E - E_0}{kT}\right) \equiv \rho(A, E_0)\exp\left(\frac{U}{kT}\right), \tag{2-43}$$

where U is the excitation energy of the nucleus above the yrast line, E_0 is the energy of the yrast line at a given spin and T is the nuclear temperature.

There are other models for the level density like the one proposed in Ref. [30]

$$\rho(U) = \frac{1}{\sqrt{48U}}\rho_A(0)\exp(2\sqrt{aU}), \tag{2-44}$$

where a is the level density parameter. Dependencies of the level density parameter with the temperature have been predicted by theoretical calculations [31].

2.15.2. Gamma strengths

The gamma strength functions can be described by the formulation that was presented in Section 2.9. Such formulation leads to a dependence of $\mathit{\Gamma}$ with the energy of the γ-ray, E_γ given by

$$\mathit{\Gamma}(A, X\ell, E_\gamma) = C(A, X\ell)E_\gamma^{2\ell+1}, \tag{2-45}$$

which is equivalent to Equation (2-23) taking into account that $\mathit{\Gamma} = \hbar/\tau$. In Equation (2-45) X indicates the electromagnetic character, ℓ the multipolarity of the transition and A the number of nucleons.

There are also other phenomena not described by Weisskopf model as the case of the Giant Dipole Resonance transitions (GDR) which are one of the main decay modes of the nucleus from the continuum region.

Giant dipole resonance transitions (GDR)

Because of a collective vibration of protons against neutrons with a dipole spatial pattern (see Figure **2-10**), dipole radiation is produced in the nucleus.

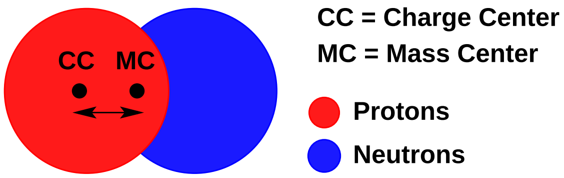

Figure 2-10.: Schematic representation of giant dipole resonance.

For GDR transitions it has been found a gamma strength function which fits the experimental results [32], given by

$$\Gamma_{GDR}(E_\gamma) \propto E_\gamma^4 \frac{\Gamma_G}{[E_\gamma^2 - E_G^2]^2 + [\Gamma E_\gamma]^2}, \tag{2-46}$$

where E_G and Γ are the energy and width of the GDR peak. The parameters Γ_G and E_G can be obtained as a function of the number of nucleons, A, and the quadrupole deformation parameter β [33]. For the case of the ^{154}Dy nucleus the GDR function is shown in Figure **2-11**.

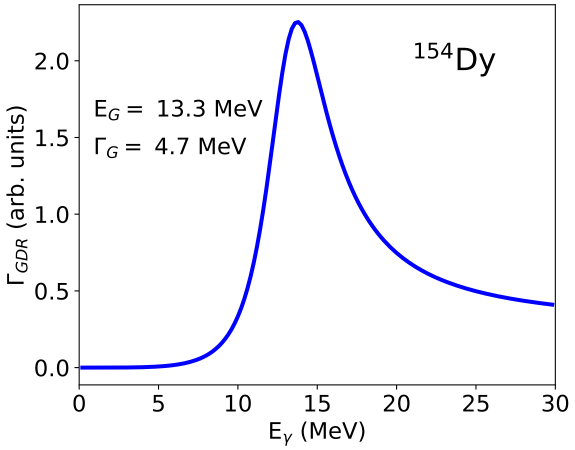

Figure 2-11.: Giant dipole resonance function.

To test the theoretical predictions of the nuclear properties that have been exposed in the previous sections, there are experimental techniques which however are not suffcient yet to be able of determine the behavior of the nucleus in the continuum region. A general description on the results and limitations of such tecniques will be presented in the next chapter.

3. Current research status and motivation

3.1. ^{83}Y normally deformed bands

The study of the nuclear shape evolution through nuclear excited states is a task of current interest in nuclear physics because theoretical models predicting the behaviour and shape of the nucleus are being tested in order to try to reproduce the specific shape evolution of different regions in the chart of nuclides.

Neutron defficient nuclei with $A \sim 80$ lie in the region where both number of neutrons and protons are in the middle between the magic numbers 28 and 50. Discrete excited states of these nuclei show rotational behavior (see for example [18]). Several phenomena like shape evolution, band termination and band crossings and their relation with the behavior of quasiparticle energies and alignment have been studied in nuclei in this region. In particular from ^{83}Y excited states several phenomena remain to be studied.

The lifetime measurements of collective excited states provide the most powerful tool to determine their quadrupole moments when axially deformed models can be applied. Nevertheless some experimental dificulties arise when measuring the lifetimes of high spin states. One of them is the fact that the required intensity for such measurements should be much higher than the one required to build the level scheme. Another experimental difficulty is the wide range, in cases as wide as four orders of magnitude, tipically found for lifetimes of states going from high to low spin sates. The later makes difficult, or in most of the cases not possible, to optimize a single experiment for the measurement of the lifetimes of all of the interesting states. Therefore several experiments are required to perform the study of a single nucleus. For the ^{83}Y case the nuclear structure of the first excited states of the yrast band has been previosuly studied by lifetime measurements using different methods [3–5]. Recoil Distance Doppler Shift Attenuation Method (RDDSAM) in [4] was implemented with the reaction ^{54}Fe(^{32}S,3p)^{83}Y at 105 MeV to measure lifetimes of low spin states. The most complete version of the level scheme of ^{83}Y is reported in Ref. [6] where lifetimes of some excited states were also published. Nonetheless the lifetimes of most of the states currently known for ^{83}Y have not been measured, which did not allow a complete study of the nuclear shape evolution of this nucleus. Moreover, the methodology used in Refs. [3–6] involves the simultaneous measurement of sidefeeding and level lifetimes, i.e., using the same lineshape, possibly introducing not valid correlations between both of them. In the present work that problem is avoided by obtaining lineshapes using Gates From Above (GFA) and Gates From Below (GFB) the transition of interest where possible.

Band termination of the $(-,+)$ band (the notation parity π and signature α $(\pi,\alpha) = (-,+)$ was used) was suggested in Ref. [6]. However no quadrupole moments were available to support the explanation of the band termination phenomenon. The results presented here aim to complement current information on nuclear structure of normally deformed bands of ^{83}Y by means of lifetime measurements using GFA and GFB the transitions of interest. The later will provide more precise determination of quadrupole moments providing better and new data to test the theoretical models.

3.2. Continuum and quasicontinuum studies

3.2.1. The Argonne method and the ^{154}Dy nucleus

The ^{152,154,156}Dy isotopes have been studied in the quasicontinuum region [34] by analyzing their E2 transitions using the methodology exposed in Ref. [35]. The (spin,energy) entry points related with each E2 quasicontinuum spectra were obtained. Instead of a discrete spectrum, the spectra of Figure **3-1** are continuous as it is expected because of rotational damping [36].

From Figure **3-1** it can be seen that the spectrum for ^{154}Dy has two peaks whereas such behaviour is not present in the ^{152,156}Dy isotopes. According to the thermodynamic description of the nucleus [11–13], the two peaks in Figure **3-1** can be described as a phase transition. A theoretical description of the phase transition in a wider region of the spin-energy plane was performed in Ref. [37]. From Figure **3-2** two different regions can be distinguished for which the shape of ^{154}Dy is either oblate or prolate depending on its spin and energy. Nevertheless it is important to characterize experimentally better the theoretically proposed phase transition from Figure **3-2**, in order to test the theory used in Ref. [37].

Those facts encourage the proposal of new methodologies to study the continuum and quasicontinuum nuclear properties. This work proposes a novel method which intends to perform experimental studies which allow to test the theoretical predictions shown in Figure **3-2**. Phase transitions imply changes on the structural and statistical quantities describing the nucleus. Such phase transitions can be studied by measuring the γ-rays coming from each poin in the (E,I) plane of Figure **3-2**. The general theoretical description of the transition probability which leads to the emission of such γ-rays will be exposed in the next section.

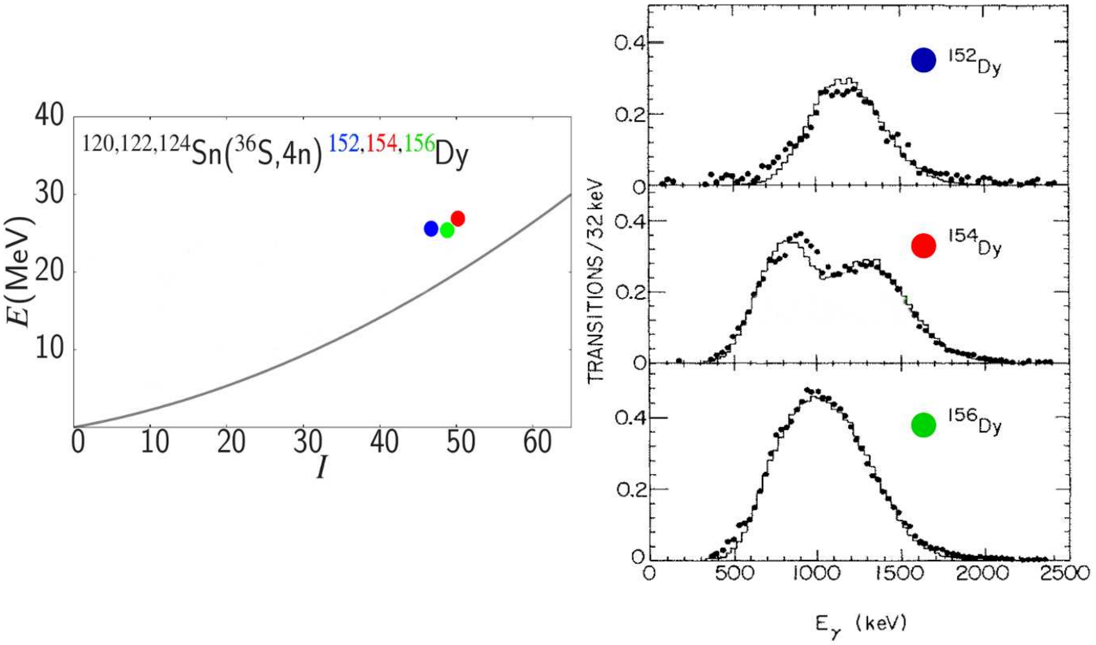

a) b)

Figure 3-1.: a) Average entry points corresponding to the E2 quasicontinuum spectra measured, for the isotopes ^{152,154,156}Dy. b) Quasicontinuum E2 spectra [34].

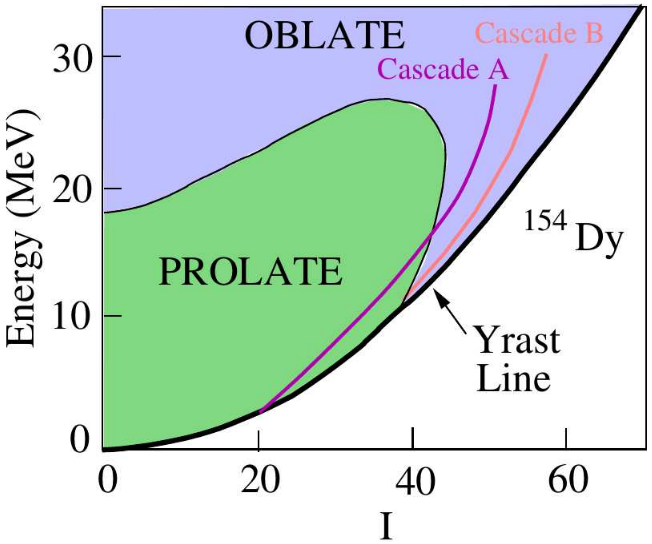

Figure 3-2.: Theoretical phase transition proposed in Ref. [37]. Figure taken from Ref. [38].

3.3. Level densities

From Figure **3-3** (based on Ref. [31]) can be seen that at low temperatures, the shell effects are predominant over the level density parameter but these effects vanish for larger nuclear temperatures. Nonetheless there is a lack of experimental data to confirm or rule out such behavior that should be measured for different nuclei.

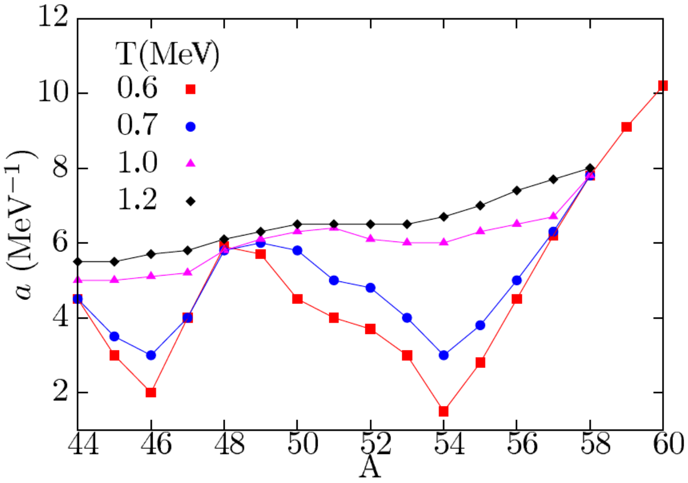

Figure 3-3.: Theoretical calculations for the level density parameter a as a function of the mass number A for different values of the nucleus temperature and for $^{44-58}$Fe isotopes [31]. Figure taken from [38].

In this document it is proposed to test the capabilities of an experimental technique which allows to measure the level density parameter a in Equation (2-44).

4. Experimental details

4.1. Doppler Shift Attenuation measurements

4.1.1. The reaction

High spin states of ^{83}Y were populated through the reaction ^{32}S + ^{58}Ni at 135(1) MeV conducted at Lawrence Berkeley National Laboratory. The 88 inch cyclotron with a K-value (kinetic energy reached by protons from bending strength in non-relativistic approximation) of 140 MeV was used to accelerate the beam. A 415 μg/cm^2 ^{58}Ni target followed by a backing of 10.3 mg/cm^2 of ^{181}Ta were used in an experiment optimized for Doppler Shift Attenuation (DSA) measurements. The reaction used is schematically shown in Figure **A-1**. In such reaction the compound nucleus ^{90}Ru is created and after the emission of one α particle and 3 protons the ^{83}Y nucleus is produced. The target of the reaction used in this experiment was parallel along the side of a stopper of ^{181}Ta as it is shown in Figure **A-1**. The products of the reaction emit γ-rays in flight while they are slowed down inside the ^{181}Ta. The shape of the spectrum produced by the γ-rays emitted in flight will present a Doppler shift that depends on several variables, among them the lifetime of the state.

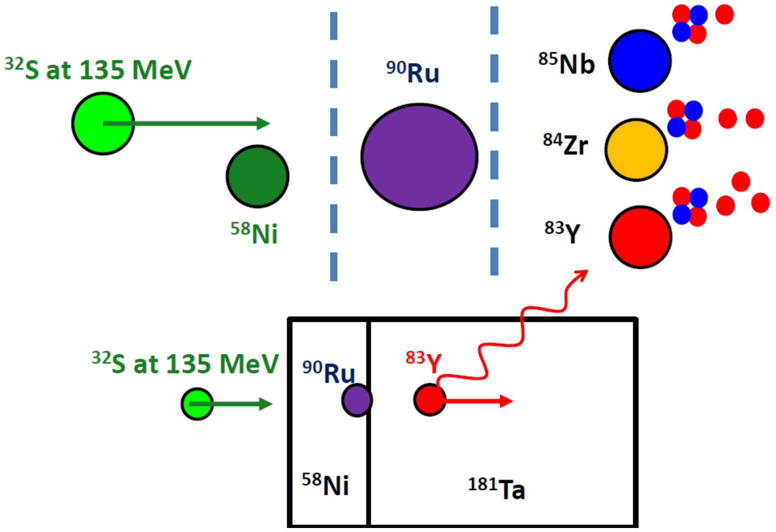

Figure 4-1.: Schematic representation of the nuclear reaction used in the experiment.

The arrays Microball [39] and Gammasphere [40] were used to acquire data of charged particle emissions and γ-rays respectively.

In Appendix A several quantities related to the velocities and the stopping times of the the nuclei of interest are calculated. These results allow us to conclude that

- The attenuation of the velocity of the projectile (^{32}S), the compund nucleus (^{90}Ru), and the ^{83}Y nucleus inside the target (^{58}Ni) is negligible even in the extreme cases when the traveling nucleus crosses the complete thickness of the target (0.47 μm).
- The thickness of the stopper (620 μm) is much greater than the stopping distance of ^{83}Y (13.5 μm) inside the stopper which was calculated with maximum kinetic energy possible for ^{83}Y. It is therefore clear that ^{83}Y is completely stopped inside the stopper.
- The initial velocity of the ^{83}Y nucleus inside the stopper is in the range of (0.027 - 0.046)$\cdot c$ which are values to take into account to perform the Doppler correction.
- The lifetimes that can be measured with the data of the experiment are $\tau \lessapprox \tau_{\text{stopping}} =$ 0.95 ps. For lifetimes greater than the $\tau_{\text{stopping}} = 0.95$ ps, the Doppler effect will not be observed because the nuclei of ^{83}Y will emmit mostly at rest.

4.1.2. The experimental array Microball + Gammasphere

Microball is an array of 95 CsI(Tl) scintillators located in a sphere covering a solid angle of $0.97 \cdot 4\pi$. The detectors are arranged in 9 rings as it is shown in Figure **4-2**.

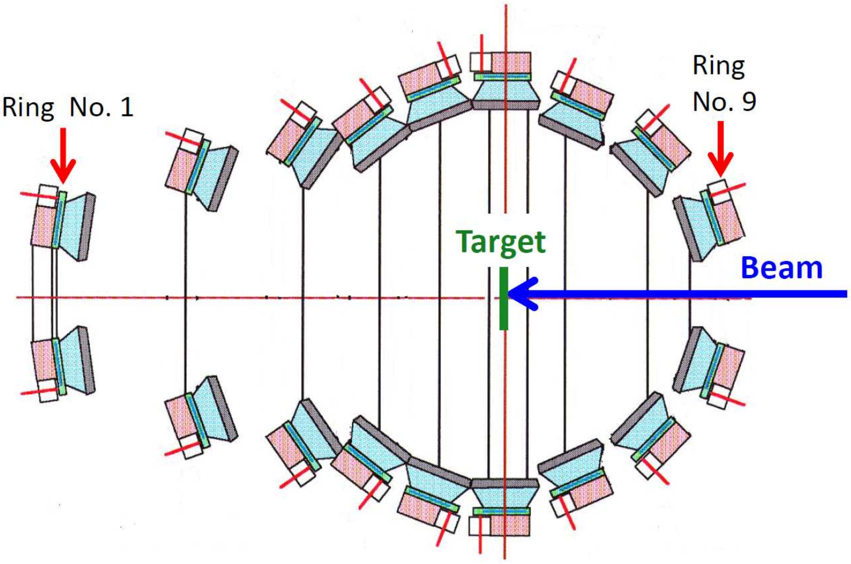

Figure 4-2.: Schematic image of Microball array. Modified from the original at https://pages.wustl.edu/sarantites/microball/images-microball

The MICROBALL array is used to detect the charged particles produced in the reaction. For the experiment analyzed in this work α particles and protons were detected in coincidence with the γ-rays. For the selection of ^{83}Y events, the detection of one α particle and three protons in MICROBALL (see Figure **4-3**) was set as a condition for selecting the γ-rays to analize. With this procedure most of the γ-rays emitted by other nuclei are filtered out. The γ-rays were detected with the GAMMASPHERE array.

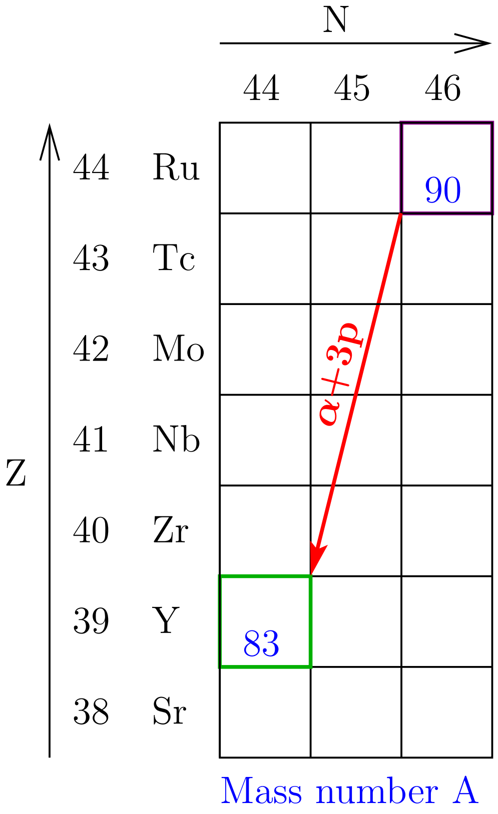

Figure 4-3.: Representation of the ^{90}Ru and ^{83}Y nuclei and their relative distance in protons Z and neutrons N in the chart of nuclei.

Figure **4-4** shows an image of the main components of GAMMASPHERE and also the location of the MICROBALL array.

GAMMASPHERE is an array of up to 110 HPGe detectors, each one surrounded by BGO Compton suppressor detectors which suppress most of the Compton events from the Ge detectors by using the coincidence technique as it is schematically shown in Figure **4-5**. The GAMMASPHERE detectors are arranged in 17 rings, each one located at a different polar angle with its detectors uniformly distributed over the azimuthal angle. With this configuration the detectors are covering a solid angle $\sim 4\pi$. The angular information of the detectors used in the experiment to perform the lifetime measurements is shown in Table **4-1**.

The selected data were sorted out in $\gamma - \gamma$ matrices containing in the y-axis the γ-

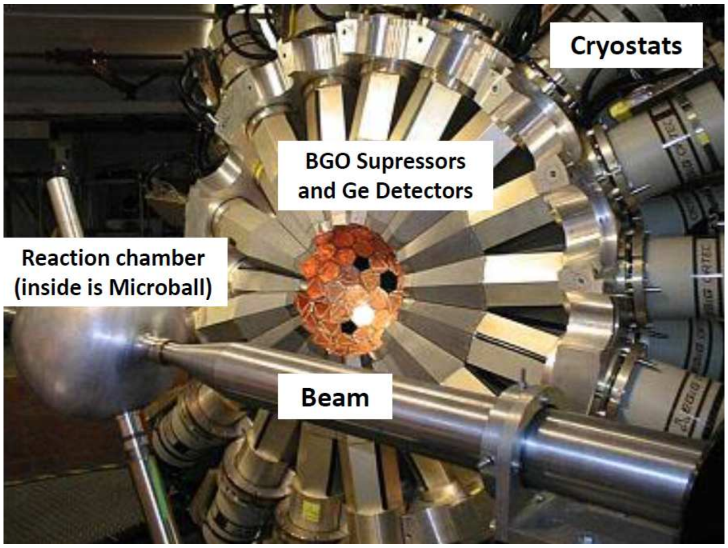

Figure 4-4.: The GAMMASPHERE array. Modified from the original image at http://rnc.lbl.gov/nsd/nuclear_structure/research.htm

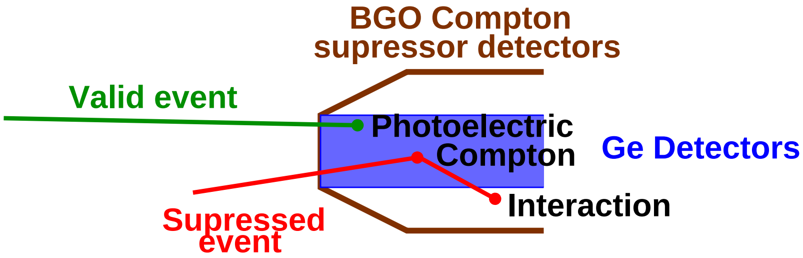

Figure 4-5.: Scheme of the side view of a BGO Compton suppressor detector surrounding a Ge detector.

rays detected at any angle and for the x-axis of the matrices two consecutive pairs of rings were used in combination for the study of the lineshapes detected at different angles. For each pair of rings the weighted average angle $\bar{\theta}$ was used. Therefore lineshapes measured at $\bar{\theta} = 35.0°, 145.5°, 52.8°, 127.2°$ were used in the lifetime analysis. Doppler correction over the y axis was applied with $\beta = v/c$ values ranging from 0.00 to 0.04 in order to perform the gates to study the lineshapes observed at different angles.

Ring angle (θ)	Available detectors	Detectors working	Weighted average angle $\bar{\theta}$	Available detectors	Detectors working
31.7°	5	3	35.0°	10	**7**
37.4°	5	4			
142.6°	5	5	145.5°	10	**10**
148.3°	5	5			
50.1°	10	10	52.8°	15	**15**
58.3°	5	5			
121.7°	5	5	127.0°	15	**15**
129.9°	10	10			

Table 4-1.: Available and working detectors used at different angles.

4.2. Experimental techniques used in nuclear continuum studies

In order to perform experimental studies of the nuclear continuum region the radiation coming from states of that region should be measured. Such radiation could connect two continuum states or a continuum state with a discrete state but in both situations the experimental spectrum will not be discrete which implies that the traditional spectroscopy methods cannot be used. The Oslo group [1] has developed a methodology to isolate the γ radiation coming from an specific excitation energy of the nucleus of interest produced by means of pick-up reactions. See for example Ref. [1] where the reaction ^{163}Dy(^{3}He,α)^{162}Dy was used. In the Oslo method, the energy of the α particle is measured and therefore the excitation energy of the ^{162}Dy can be obtained. Thereby from the time-coincidence between the α particle and the γ-ray detection, the spectra of radiation coming from the continuum region can be obtained. Such methodology has been used to obtain level densities and gamma strength functions [41–48]. Nevertheless that methodology has several limitations. At first the mandatory use of pick-up reactions limits the nuclei that can be studied. Aditionally, only low spin states can be populated with such reactions. This last disadvantage makes that theoretical predictions of nuclear phase transitions as the proposed in Ref. [34] and shown in Figure **3-2** cannot be experimentally checked.

Another experimental technique to study the nuclear continuum makes use of the Energy Ordered Spectra (EOS). This methodology was originally proposed in Ref. [49]. Since then, by means of numerical simulations other works have been developed to try to extract physical information from such spectra, see for example [2]. Several topics related with the use of the EOS for nuclear continuum studies have been studied. One of them is the application of statistical tools as Order and Extreme Statistics applied to fitting functions for the EOS spectra [50–52]. Based on previous works the best fitting function for the EOS produced to date is described in Ref. [53].

The influence of the detection system on the applicability of the fitting functions has been also investigated [38, 54]. In Ref. [38] it was shown for the Gasp array [55] (which will be explained in Sections 6.3 and 6.4) that the Hk-EOS technique is a promising tool to study the nuclear continuum properties. However in that work the numerical simulations could not be run for sufficient number of events which did not allow to confirm and test the complete capabilities of the technique. Currently the numerical simulation codes have evolved and also the computer processing capabilities have improved significantly. These facts encourage the development of new simulations allowing to test the full capabilities of the Hk-EOS technique. Additionally better fitting functions to the EOS spectra have been developed since then [53]. Nowadays other experimental arrays which fit better the requirements of the Hk-EOS technique are also being developed. All these facts encourage performing new improved numerical simulations to test the capabilities of the Hk-EOS technique.

4.3. The PARIS detectors

There is an experimental array which is currently under development. It is called PARIS (Photon Array for studies with Radioactive Ions and Stable Beams) [56]. The geometry for this array is being designed to cover as close as possible a 4π solid angle. Moreover the detectors of PARIS are proposed to be composed of two layers of scintillators of $LaBr_3$(Ce) and NaI(Tl). The aim of the inner layer ($LaBr_3$(Ce)) is to measure the multiplicity and the energy of the low energy γ-rays, $E \lesssim 3$ MeV. The outer layer (NaI(Tl)) is designed to detect high energy γ-rays, up to ~ 10 MeV). Numerical simulations of PARIS can be used to test the capabilities of the Hk-EOS technique. A simulation software of this array is also under development [57].

Currently only a few PARIS clusters are under operation. However the geometry of the array has been already proposed [57]. Nonetheless the Geant4 simulation does not include yet the total geometry and other modules are also under construction. In Section 6.5 the simulation details implemented in this thesis including the geometry simulated starting from the tool in [57] will be exposed.

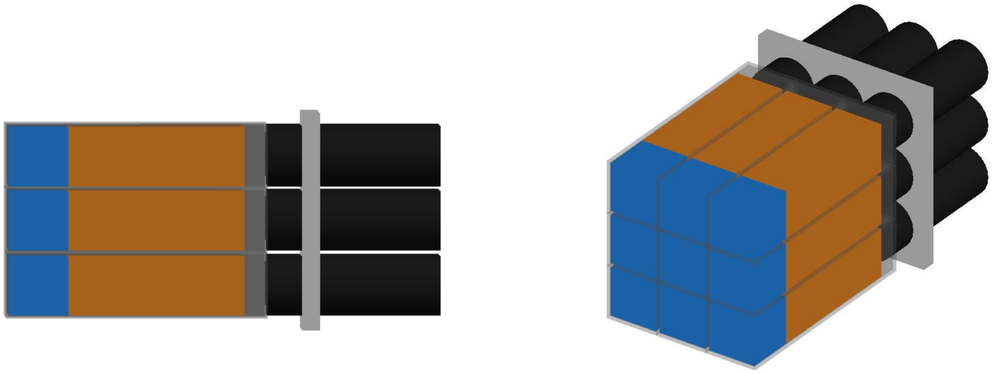

Figure 4-6.: PARIS cluster composed by 9 phoswhich detectors. $\mathrm{LaBr_3(Ce)}$ are shown in blue being a cubic crystal of 2″. The 6″ lenght NaI(Tl) are shown in orange and the photomultipliers tubes are plotted in black.

5. Data analysis DSA experiment

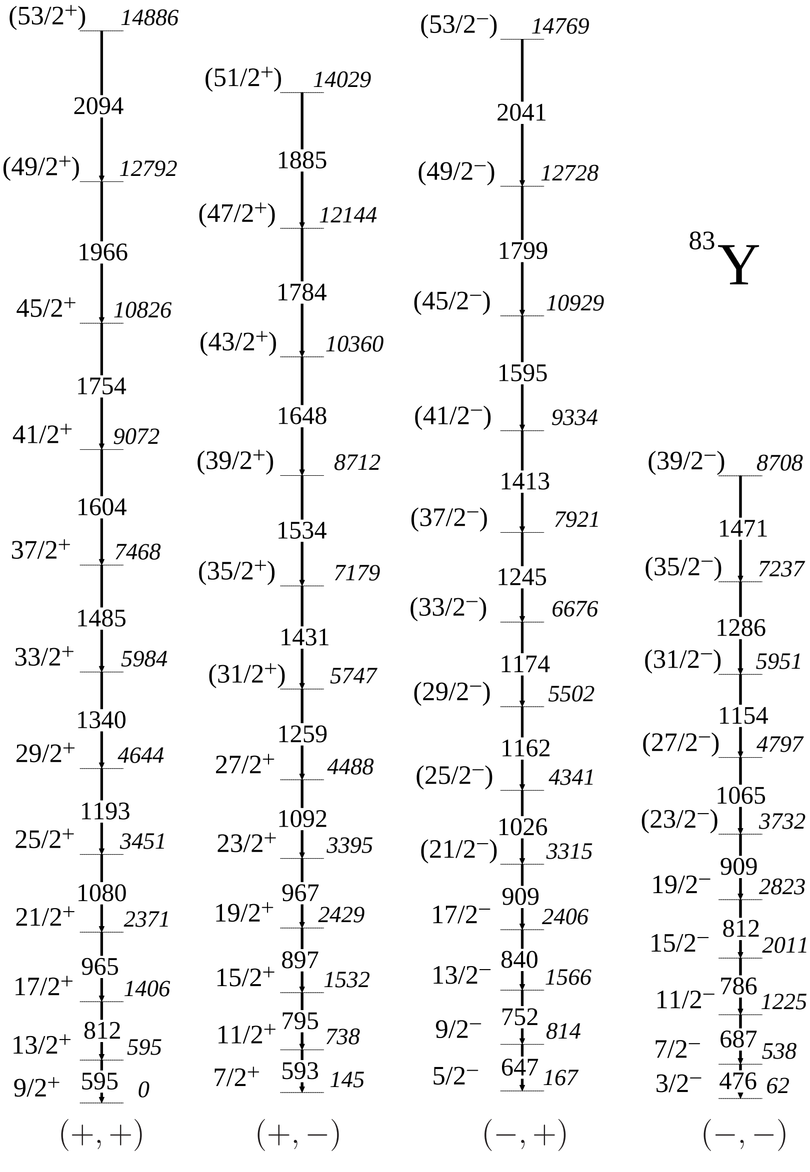

Figure 5-1.: Partial level scheme of ^{83}Y showing normally deformed bands in agreement with the data analyzed in this work and complemented with transitions reported in Ref. [6] at $(39/2)^{-}$ $(47/2)^{+}$, $(51/2)^{+}$ and $(53/2)^{+}$. Spin and parities were extracted from Ref. [6].

Fig. **5-1** shows a partial level scheme of normally deformed bands of ^{83}Y singling out relevant states and transitions for this work, showing transitions in agreement with observed data analyzed here and complemented with transitions reported in [6]. Interband transitions shown in previous publications [6, 58] were not observed in this analysis, probably because of low intensity, making them not relevant for the lifetime measurements presented here. For this reason such transitions were omitted in Fig. **5-1**. The transitions from states at $(39/2^-)$, $(47/2^+)$, $(51/2^+)$ and $(53/2^+)$ were not observed in our data, they are included in Fig. **5-1** for completeness, as spin and parities, they were taken from Ref. [6]. The labels of the bands were assigned using parity π and signature α as (π, α) and the equivalences $\alpha = +1/2 \equiv +$ and $\alpha = -1/2 \equiv -$ were used. This labeling coincides with the one adopted in Ref. [58].

The procedure to carry out the data analysis will be presented in the following sections of this chapter.

5.1. General features of the analysis

5.1.1. Doppler correction illustrated with the $(+,+)$ band case

γ-rays emitted in flight and detected at different angles will present a Doppler shift of their energies given by

$$E_\gamma = E_\gamma^0(1 + \beta \cdot \cos(\theta)), \tag{5-1}$$

where E_γ is the detected energy at the azimuthal angle θ when the velocity of the traveling nucleus, in light velocity units at the instant of emission, is β. E_γ^0 is the energy of the transition in the rest frame.

As it is shown in Appendix A the velocity of the ^{83}Y nuclei traveling through the stopper (^{181}Ta) is in the range of $\beta = 0.027$ - 0.046. Since from the data acquired in this experiment is not possible to perform the Doppler correction for every single event, only one β value can be chosen for the Doppler correction of each excited state. Figures **5-2** and **5-3** show the effect of applying the Doppler correction on the excited states of the $(+,+)$ band that were analized in this work. Different ranges of energy are plotted in Figures **5-2** and **5-3**. In all of these figures Doppler correction with the different β values indicated in each figure were applied. It can be seen how the emissions at low spin and low energy are produced mostly at rest and therefore no Doppler correction is needed to reconstruct the peak in the spectrum. The 812 keV transition in Figure **5-2** does not shows even a small Doppler broadening which does not allow to determine its lifetime from the data acquired in this experiment. On the other hand the 1966 keV transition in Figure **5-3** is most clearly reconstructed when the Doppler correction with $\beta = 0.03$ is applied which is one of the highest β values used.

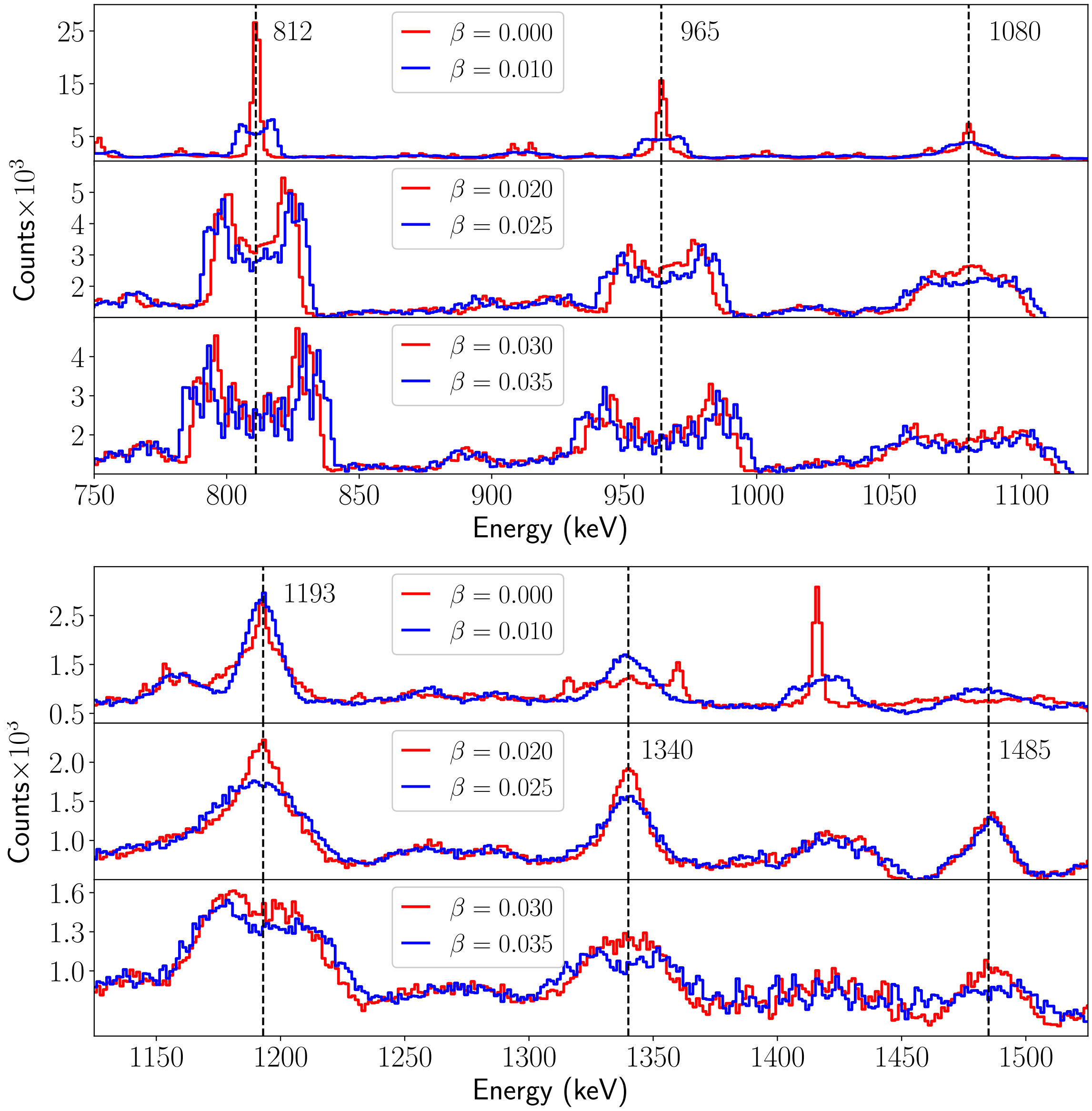

Figure 5-2.: Projection on the y-axis of the $\gamma - \gamma$ coincidence matrices showing the effect of the Doppler correction for the transitions emitted at low spin for the $(+,+)$ band. The energy labels of the transitions are located in the figure whose β value is the one which best reconstructs the peak. For example the labels 1340 and 1485 are located in the middle panel with the Doppler correction with $\beta = 0.02$

5.1.2. Lineshape sensitivity illustrated with the $(+,+)$ band case

Once the Doppler correction has been applied on the y-axis (any detector) of the matrices (see Section 4.1.2 for the definition of the matrices), the gates on these transitions can be performed in order to obtain a spectrum on the x-axis (the selected angle). Figure **5-4**

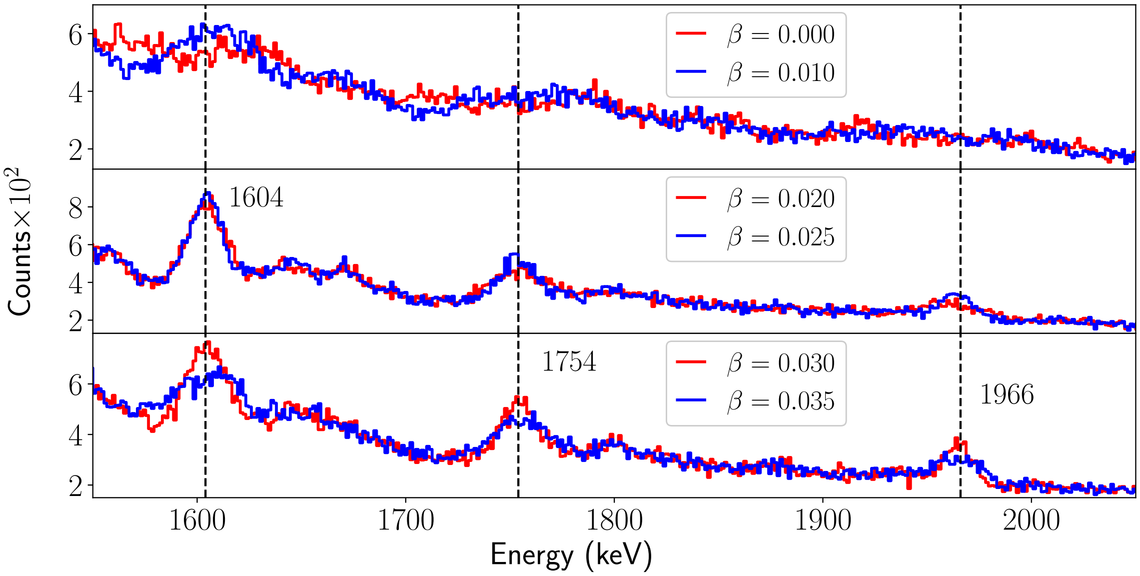

Figure 5-3.: Projection on the y-axis of the $\gamma - \gamma$ coincidence matrices showing the effect of the Doppler correction for the transitions emitted at high spin for the $(+,+)$ band. The energy labels of the transitions are located in the figure whose β value is the one which best reconstructs the peak.

shows the different lineshapes observed by gating from above the transitions plotted. These lineshapes depend on several variables among them the feeding pattern of the transitition involved and also on the lifetime of the state emitting each γ-ray.

In Figure **5-4** it can be seen how the less energetic transitions produce the lineshapes with most of the counts in the "stop peak" (or the transition energy) indicated with the dashed lines in Figure **5-4**. On the other hand the most energetic transitions produce the lineshapes whose distribution of counts is farther away from the transition energy. Therefore it is expected to find lifetime of the excited states having small values at high spin (the most energetic transitions) and that the lifetime values increase when going down to low spins. However several other variables help to determine the lineshape. To extract the lifetime from the lineshapes obtained, the code AhKin [59] whose main features will be presented in the next section, was used.

5.1.3. Lineshape calculation using the code AhKin

The general procedure to produce the theoretical lineshapes with the code AhKin will be exposed in this section. Further details can be found in Ref. [59].

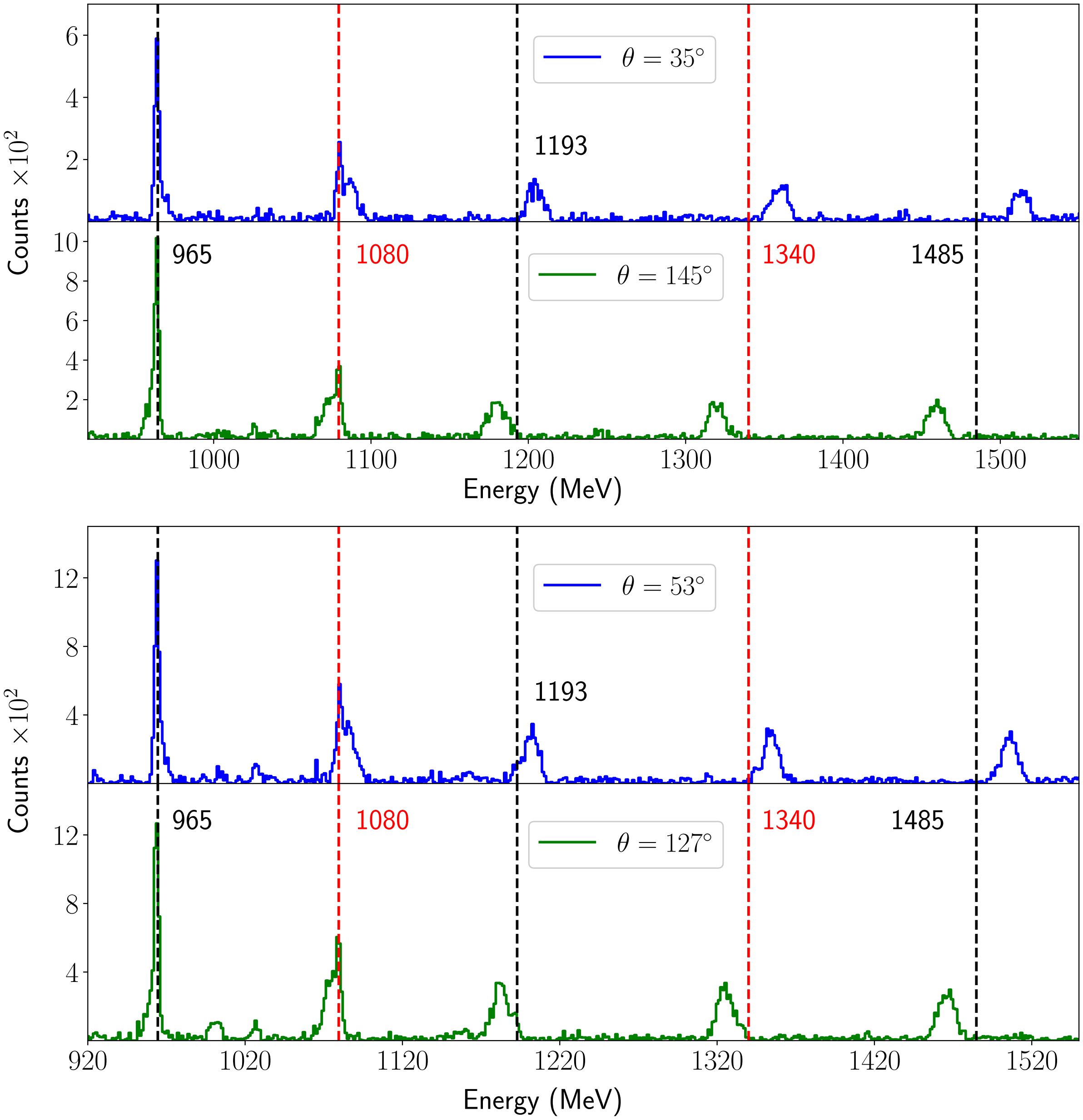

Figure 5-4.: Spectra showing transitions of the yrast band taken with the detectors located at average angles of 35°, 145°, 53° and 127°. The spectra were obtained from the sum of gates at energies 1965, 1754 and 1604 keV. The vertical dashed lines indicate the position of the transition energy at the rest frame of reference.

Stopping power

All the variables determining the lineshape should be considered in order to produce a theoretical lineshape. The energy lost per length unit dE/dx of the ^{83}Y nuclei inside the target and the stopper will influence the resulting lineshape. Figure **5-5** shows dE/dx in the stopper as a function of the energy, calculated using the SRIM code [60].

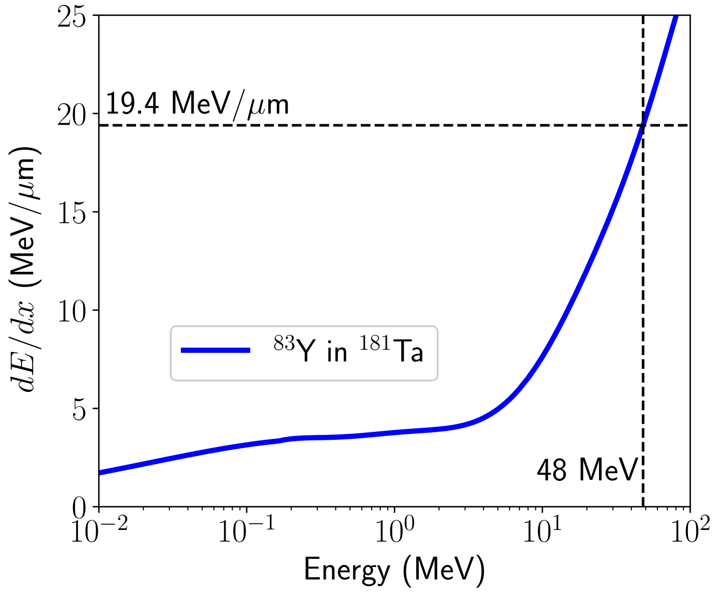

Figure 5-5.: Stopping power of the ^{83}Y in ^{181}Ta calculated using the program SRIM [60]. The stopping power at 48 MeV (the initial energy of the ^{83}Y inside the stopper) is indicated.

Velocity distribution of ^{83}Y in ^{181}Ta

With the stopping power it is possible to calculate the velocity as a function of time of the ^{83}Y nuclei inside the stopper. Figure **5-6** shows the β value as a function of time. It can be seen how the β value becomes very close to zero for times $\gtrsim 1.3$ ps. Therefore after this time the nucleus will emit at rest and no Doppler broadening of these emissions will be observed. Thus 1.3 ps is an upper limit for the lifetimes that can be measured from the data of this experiment.

The velocity distribution of nuclei can be described by a Gaussian distribution which becomes narrower with time [61]. Figure **5-7** shows the velocity distribution for different times between 0.0 and 1.0 ps.

Angular distribution of the detection

As it is shown in Equation (5-1) the Doppler effect depends on the azimuthal angle of the detection, θ. Nonetheless although the detectors are located at specific angles, they have an angular aperture which introduce uncertainty to the measurement. This effect however can be decreased by taking into account the probability distribution of a γ-ray to be detected at a specific angle inside the angular aperture of the detector. Figure **5-8** shows how two different rays γ_1 and γ_2 have different possible traveling distances inside the detector. In a given

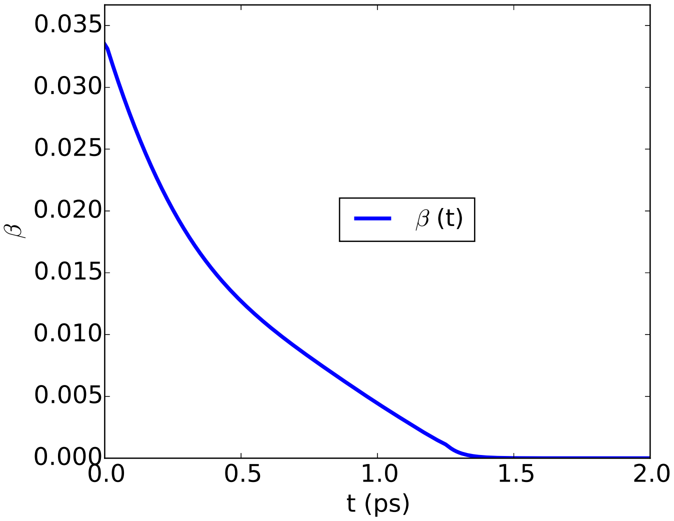

Figure 5-6.: Velocity in c units as a function of the time for the ^{83}Y in ^{181}Ta, calculated by the code AhKin [59].

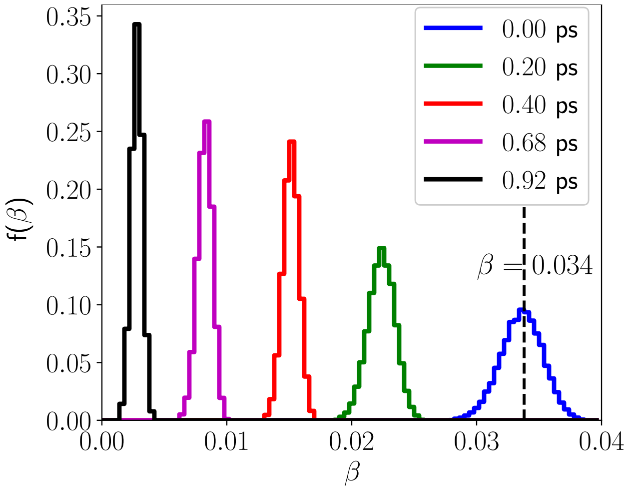

Figure 5-7.: Velocity distribution for different time instants of the ^{83}Y in ^{181}Ta, calculated by the code AhKin [59]. For an initial velocity of $\beta = 0.034$.

direction the photon has the probability to travel larger distances within the detector than in other directions and this effect should be taken into account in the detection probability to reduce the uncetainty of the measurement.

Figure **5-9** shows the probability distribution of the detection of γ-rays for the detectors located at 50.07° and 58.28°, calculated by the code AhKin [59]. The distribution is centered at 53° and has a width determined by the angular aperture of the detectors.

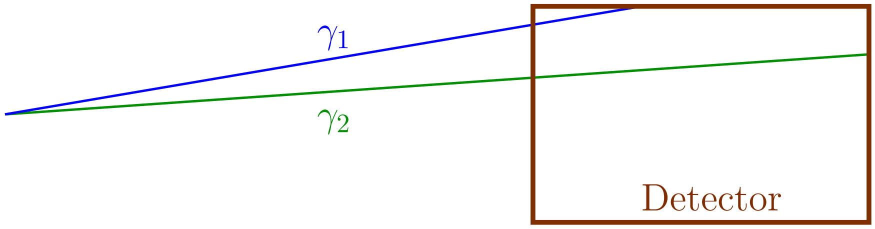

Figure 5-8.: Schematic representation illustrating how the rays, γ_1 and γ_2, have different traveling distances inside the detector.

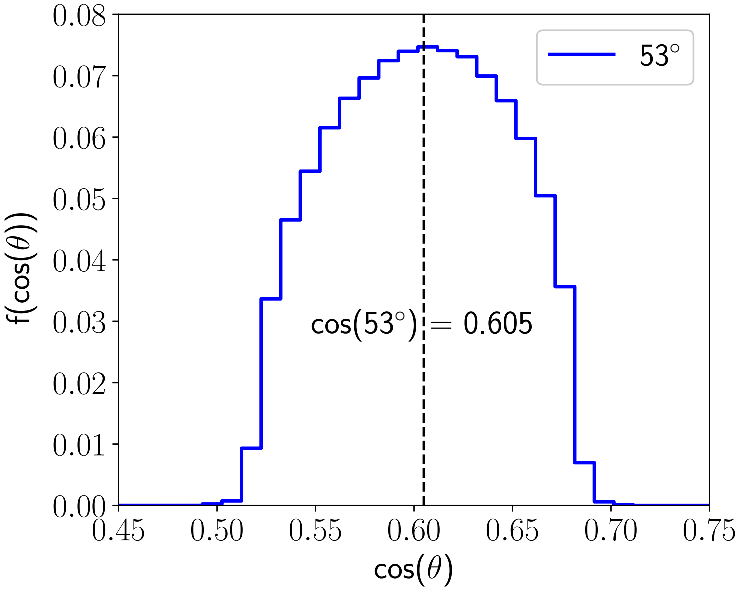

Figure 5-9.: Probability distribution of the direction of the γ-rays hitting the detectors inside the rings at 50.07° and 58.28°, calculated by the code AhKin [59].

Velocity and angular distribution of the detection

The probabilty distribution of detecting γ-rays at the time, t, for a given velocity, β, and detection angle, θ, is illustrated in Figure **5-10** where it can be noted that the distributions are closer to each other than in Figure **5-7** (some distributions overlap with others in Figure **5-10**) where no angular aperture of the detectors was considered.

Lineshape calculation

Besides the variables discussed previously the lineshape of a transition will also depend on the lifetimes and the relative initial population of the states feeding the state of interest. To

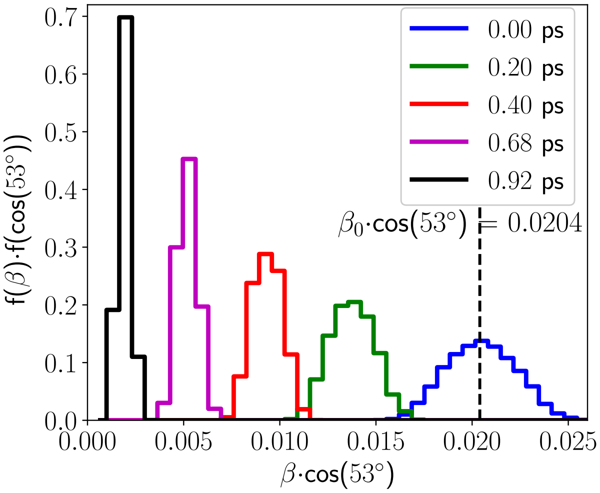

Figure 5-10.: Distribution of $\beta\cos(\theta)$ for different time instants of the ^{83}Y in ^{181}Ta, calculated by the code AhKin [59].

take into account this effect the decay equations (5-2) should be numerically solved.

$$\frac{dN_i}{dt} = \frac{-N_i}{\tau_i} + \sum_j \frac{b_{ij}}{\tau_j}. \tag{5-2}$$

N_i and τ_i are the population and lifetime of the state of interest, N_j and τ_j are the population and lifetime of the states that feed the state of interest and b_{ij} is the branching ratio of the state j to the state i. When using other codes to reproduce the lineshape as the case of the code FITS [61] the population of the states that feed the state of interest is varied together with the lifetime of the state of interest in order to find the lineshape that best fits the experimental data. A difference with the AhKin program is that AhKin needs the population of the states that feed the state of interest as input values. Unlike FITS, AhKin only varies the lifetime of the state of interest until it finds the lineshape that best fit to the experimental results.

χ^2_{red} calculation

The program AhKin generates several theoretical lineshapes and calculates the χ^2_{red} value for each one of these lineshapes as

$$\chi^2_{red}(\tau) = \frac{1}{N}\sum_i^N \frac{(y_i - h_i(\tau))^2}{\sigma_i^2}, \tag{5-3}$$

where N is the number of channels of the spectrum used to compare the experimental and the theoretical lineshapes, y_i is number of counts of the i-th channel, $h_i(\tau)$ is the calculated number of counts for the i-th channel and σ_i is the standard deviation of the probability distribution of y_i. As the number of counts follows the Poisson distribution thus $\sigma_i = \sqrt{y_i}$. Equation (5-3) gives less weight to experimental values with larger uncertainty. The uncertainty is obtained using the criteria of min$[\chi^2_{red}]$ +1 [62] which is illustrated in the Figure **5-11**.

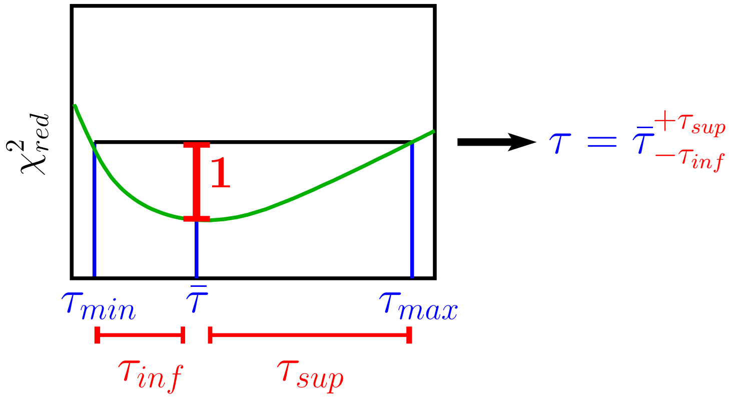

Figure 5-11.: Schematic representation of the obtention of τ and its uncertainty from the χ^2_{red} curve.

5.1.4. Gates From Above (GFA) and Gates From Below (GFB)

Gate is the term used to indicate a temporal coincidence condition. For examaple gating on a transition of energy $E_{\gamma 1}$ means selecting the data that were detected in temporal coincidence with the detection of a γ-ray of energy $E_{\gamma 1}$. In order to obtain the lineshapes to study as the ones shown in Figure **5-4**, gates should be applied on the y-axis of the matrices (see Section 4.1.2) containing the data.

As it was stated before the lineshape depends on the lifetimes and relative population of the states feeding the states of interest. For this reason the determination of the lifetimes in this work was carried out starting from the highest spin state populated down to low spins. Figure **5-12** shows two types of GFA that could be applied to study the same state of interest. By applying a GFA the contribution of the sidefeeding to the lineshape under study will be eliminated allowing the independent determination of the lifetime of the state. Several sidefeeding contributions could be eliminated as well depending on the position of the gate. The latter illustrated in Figures **5-12**(a) and (b). Whichever of the gates shown in Figure **5-12** can be used for the study of the same state of interest. The lifetimes and relative population of all of the states feeding either directly or indirectly the state of interest, should be previously determined. Gates From Below (GFB) can also be applied and for these cases the sidefeeding of the state of interest will contribute to the lineshape. For this reason it is desirable that the lifetime of the state had been previously determined and with the spectrum produced with the GFB, the sidefeeding time can be determined independently from the lifetime of the state. Figure **5-13** shows different GFB that can be applied. Several

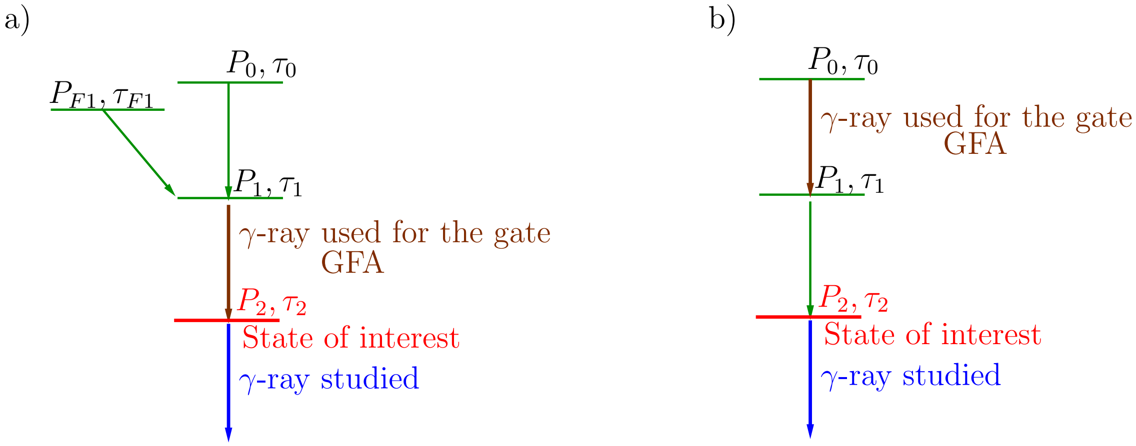

Figure 5-12.: Possible Gates From Above (GFA) that can be used to study the same state. (a) Gate at the previous transition of the cascade to the γ-ray studied. In this case the quantities $P_0\tau_0$, $P_{F1}\tau_{F1}$, $P_1\tau_1$ should be previously determined. (b) Gate at any other transition above the γ-ray studied. In this case the quantities $P_0\tau_0$, $P_1\tau_1$ should be previously determined.

GFB can also be added to increase the number of counts in the lineshape when needed.

5.1.5. Efficiency correction

By using the code AhKin the initial population of the states feeding the state under study is needed as input values. Before obtaining the initial feeding population the efficiency correction should be applied to the spectra measured. The relative detection efficiency is defined by

$$\epsilon_{rel}(E_{\gamma_i}) = \frac{\text{number of } \gamma_i \text{ detected}}{b_{\gamma_i}}, \tag{5-4}$$

where b_{γ_i} is the branching ratio of the γ-ray under study. Figure **5-14** shows the curve obtained for the efficiency of the Gammasphere array.

From Figure **5-14** can be seen that the γ-rays with low energies are more efficiently detected than the γ-rays at high energies. However this is not true for energies lower than $\sim$ 200 keV where is located the maximum of efficiency in Figure **5-14**. If the number of counts of a spectrum is divided by the function in Figure **5-14**, then the spectrum will be corrected by efficiency and the effect to detect some energies more efficiently than other ones, is corrected.

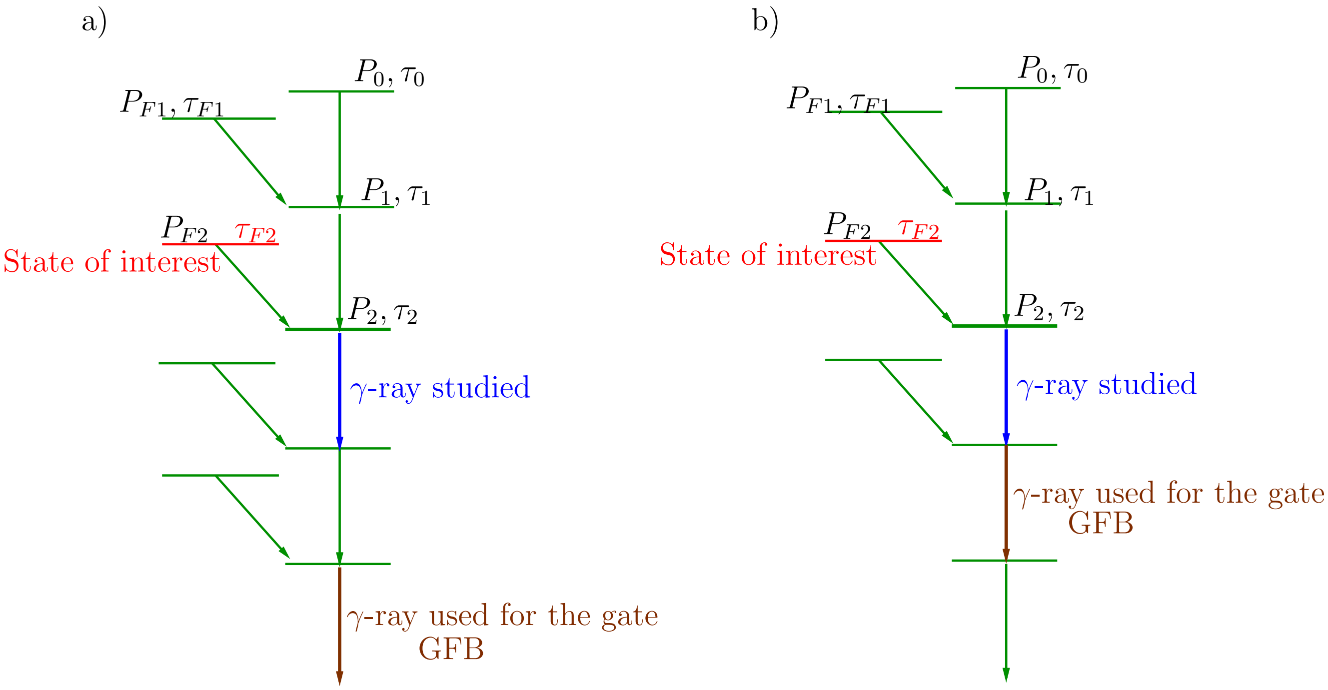

Figure 5-13.: Possible Gates From Below (GFB) that can be used to study the same state. (a) Gate at the next transition of the cascade to the γ-ray studied. (b) Gate at a any other transition below the γ-ray studied. In these two cases the quantities $P_0\tau_0$, $P_{F1}\tau_{F1}$, $P_1\tau_1$, P_{F2} and $P_2\tau_2$ should be previously determined. Sum of several gates of types (a) and (b) can also be used.

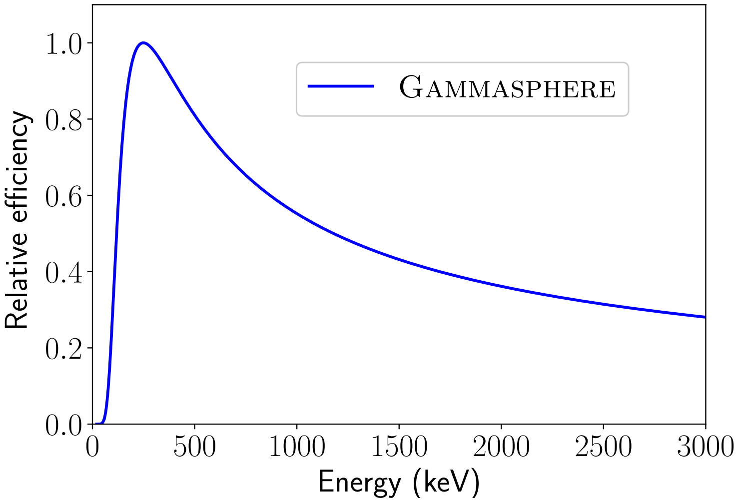

Figure 5-14.: Total relative efficiency of the GAMMASPHERE array [63].

5.1.6. Correlation method

For a few transtions GFA was not used because of the presence of interference with other transitions from the ^{83}Y nucleus or from the ^{82}Sr nucleus that were registered when one charged particle was not detected by MICROBALL. For these cases only the GFB was available to make a comparison with the theoretical curves.

As it was shown in Section 5.1.4 with a GFB the sidefeeding of the state will contribute to the resulting lineshape and since the level lifetime cannot be determined previously with a GFA, therefore the determination of both the level lifetime and the side feeding time have to be conducted using the same lineshape. A variation on both variables and subsequent minimization has to be performed. The general procedure followed in these cases was

1. Fix the value of the sidefeeding time and generate the χ^2_{red} curve as function of the level lifetime. Repeat this procedure for several values of sidefedding times inside the range [0.01-5.00] ps.

2. Extract the minimum value of each one of the χ^2_{red} curves generated in the previous step. Plot the "Minimun values of χ^2_{red}" as function of its respective lifetime, which we call here "τ (ps) with the minimum χ^2_{red}". See for example the curves of in the Figure **5-15** for the 967 keV transition of the $(+,-)$ band.

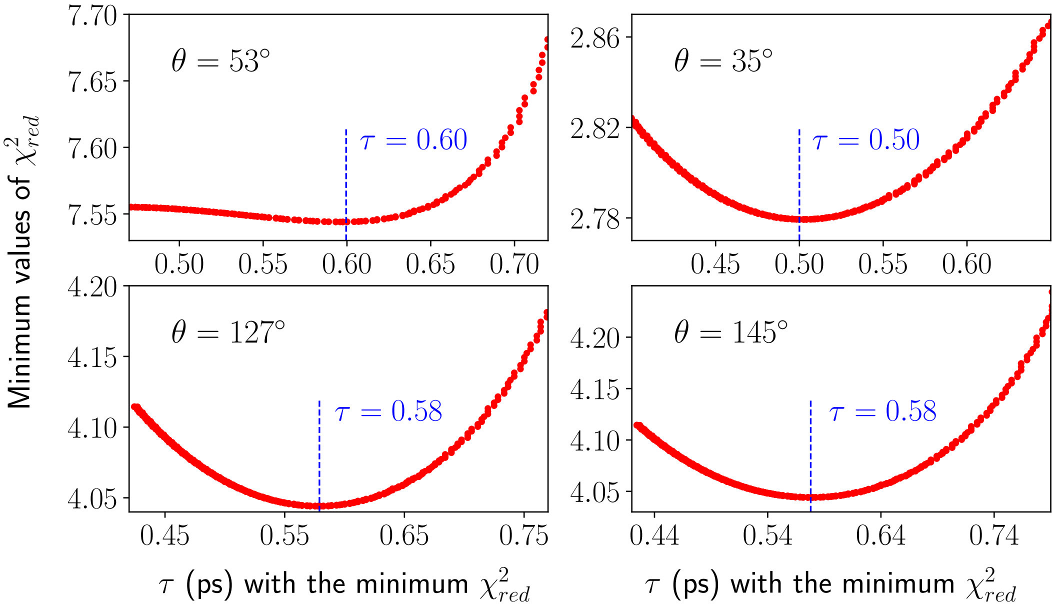

Figure 5-15.: Curves used to determine the level lifetime or the 967 keV transition of the $(+,-)$ band by means of the correlation method.

3. Fix the value of the level lifetime to the minimum value of the curve obtained in previous step (see the values in blue of the Figure **5-15** for the 967 keV transtion). Determine the sidefeeding time by varying the sidefeeding time only and comparing with the spectrum that was produced with a GFB. This latter procedure is similar to the one used in the case when the level lifetime is obtained previously by making a GFA.

4. Check the consistency of the method by fixing the sidefeeding time to the value determined in the previous step and determine again the level lifetime with its uncertainty. The level lifetimes determined in this step should be the same as the values in blue of the Figure **5-15** obtained in the step 2.

For the state of $I_i = 23/2$ emitting the γ-ray of 967 keV the χ^2_{red} curves of the level lifetime and sidefeeding times obtained by applying the correlation method are shown in Figure **5-16**. The τ values in Figure **5-15** are consistent with the values of Figure **5-16**(a) showing the consistency of the correlation method. The calculated lineshapes are shown in Figure **5-17**.

5.1.7. Weighted average of the four angles analyzed

From the lifetimes measured at the four different angles the weighted average τ_{avg} is calculated to get the final value used for the analyses that will be exposed in Chapter 7. If τ_i is the lifetime measured at each of the i angles thus τ_{avg} can be calculated as

$$\tau_{\text{avg}} = \frac{\sum_i w_i \tau_i}{\sum_i w_i}, \quad \text{with} \quad w_i = \sum_i \frac{1}{\Delta_i^2}. \tag{5-5}$$

where the sub-index i runs over the four angles analized and Δ_i is the uncertainty of τ_i. The uncertainty of τ_{avg} will be

$$\Delta_{\text{avg}} = \frac{1}{\sqrt{\sum_i w_i}}. \tag{5-6}$$

The standard deviation σ of the four values τ_i is also included in the total uncertainty Δ_{Total} which was calculated as

$$\Delta_{Total} = \Delta_{\text{avg}} + \sigma \tag{5-7}$$

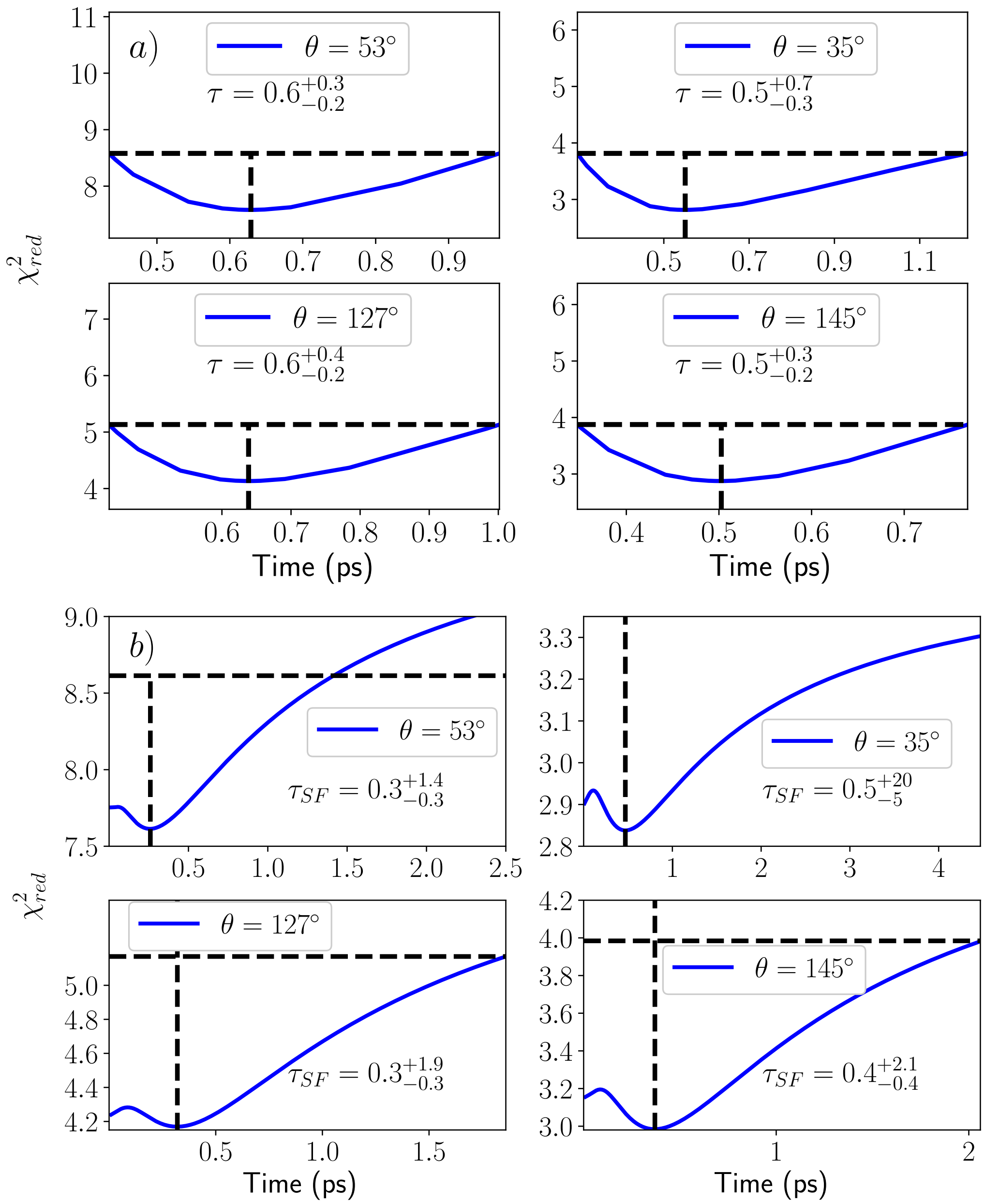

Figure 5-16.: Curves used to determine the level lifetime or the 967 keV transtion of the $(+,-)$ band by means of the correlation method. The four curves in the upper part correspond to the level lifetime τ. The four curves at bottom corresponds to the sidefeeding time τ_{SF}. The horizontal dashed lines indicate the value of min$[\chi^2_{red}]$+1 used to calculate the uncertainty as it was explained in the Figure **5-11**.

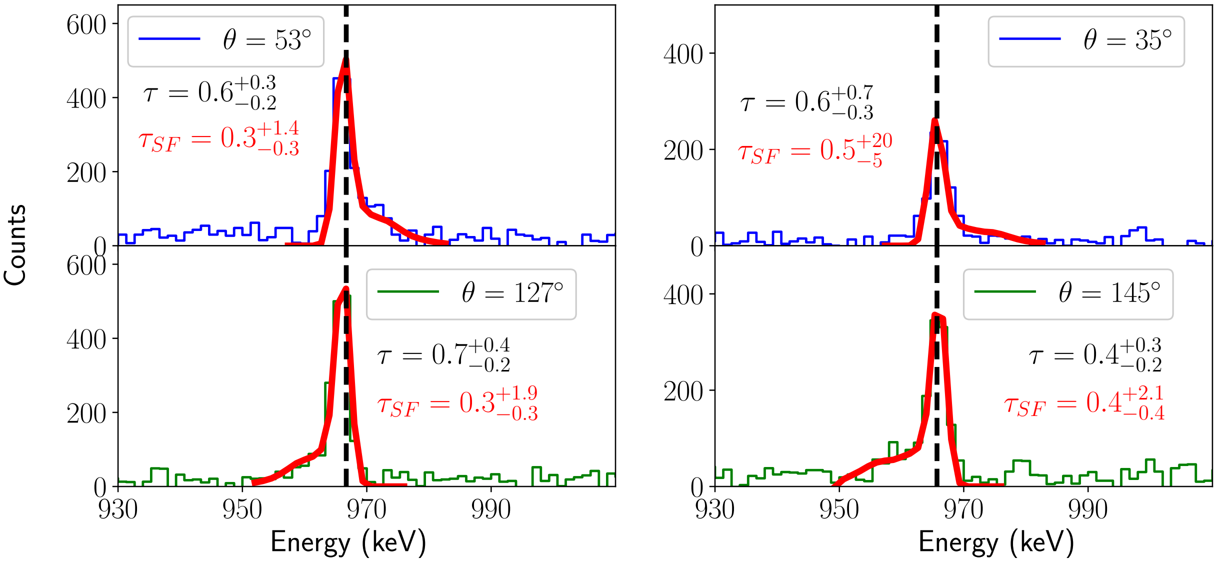

Figure 5-17.: Fits performed by the program AhKin to study the side feeding time of the state at 3397 keV by using the γ-ray of 967 keV detected at different angles.

5.2. $(+,+)$ band

Doppler correction on the transitions of this band was already discussed in Section 5.1.1. Some of the resulting lineshapes of this band were also shown in Section 5.1.2.

5.2.1. Relative intensity of the transitions of the $(+,+)$ band

To determine the relative initial population, the relative intensities of the γ-rays were measured at the angles shown in Table **5-1**. The gate on the 595 keV energy was applied and the number of counts on the lineshape produced at each angle were determined. The values obtained for each transition were normalized to the number of counts of the 965 keV transition. The relative intensities obtained are shown in Table **5-1**. Same procedure was performed by applying the gate on the 811 keV transition and the resulting values are displayed in Table **5-2**.

Relative intensities to I(965 keV)					
Gate at 595 keV					
E_γ (keV)	53°	127°	35°	145°	Average
595	-	-	-	-	-
812	109.8(5)	115.6(5)	110.9(7)	119.4(6)	114(5)
965	100.0(5)	100.0(5)	100.0(6)	100.0(5)	100
1080	75.6(3)	66.9(3)	76.5(5)	63.1(4)	76.0(4)
1193	56.8(3)	62.5(2)	60.0(5)	63.1(4)	61(3)
1340	40.7(2)	40.5(2)	46.3(4)	44.7(3)	43(3)
1485	32.2(2)	35.2(2)	33.6(3)	32.2(3)	33(1)
1604	18.0(1)	17.9(1)	18.1(2)	18.1(2)	18.0(1)
1754	13.3(1)	13.4(1)	16.8(2)	12.0(1)	14(2)
1966	6.2(1)	6.1(1)	8.3(1)	7.3(1)	7(1)

Table 5-1.: Relative intensities of the transitions of the yrast band by gating at 595 keV. The red numbers correspond to the cases where the measured value is affected by the interference shown in Figure **6-1**. Intensities of 595 keV is not reported since this energy was used for the gate.

By comparing the values of Tables **5-1** and **5-2** with each other it can be seen that the values of the intensities obtained applying different gates are the same, as it is expected. No Doppler broadening was observed for the lineshapes corresponding to the transitions of 811

Relative intensities to I(964 keV)					
Gate at 812 keV					
E_γ (keV)	53°	127°	35°	145°	Average
595*	117.9(7)	118.8(6)	116.3(9)	121.1(8)	118(2)
812	-	-	-	-	-
964	100.0(6)	100.0(6)	100.0(8)	100.0(7)	100.0(3)
1080	77.8(5)	70.1(4)	78.8(7)	64.7(5)	78.3(6)
1193	55.8(4)	59.8(4)	54.4(5)	60.2(5)	58(3)
1340	46.9(3)	46.1(3)	43.7(5)	45.5(3)	46(1)
1485	37.6(2)	37.8(2)	42.2(4)	40.3(2)	39(2)
1604	22.8(2)	24.5(2)	19.8(3)	20.3(2)	22(2)
1754	17.2(2)	15.0(2)	14.6(2)	13.3(2)	15(2)
1966	10.0(1)	8.2(1)	7.3(2)	5.0(1)	8(2)

Table 5-2.: Relative intensities of the transitions of the yrast band by gating at 811 keV.
* These values represent the intensity of 811 keV instead of the 595 keV one. This is due to the gate applied which makes that the sidefeeding to the 595 keV transition will not be included in the spectrum analyzed. The red numbers correspond to the cases where the measured value is affected by the interference shown in Figure **6-1**

Relative intensities to I(964 keV)					
Total projection					
E_γ (keV)	53°	127°	35°	145°	Average
595	169.3(1)	169.7(2)	161.4(2)	168.7(1)	167(4)
811	120.3(1)	125.5(2)	119.3(1)	126.0(1)	123(3)
964	100.0(1)	100.0(2)	100.0(1)	100.0(1)	100.0(1)

Table 5-3.: Relative intensities of the transitions of the yrast band by gating at 812 keV.

and 595 keV and therefore their lifetimes cannot be determined. However for completeness purposes the intensity of these transitions was determined as well. For these two transitions being the most intense among all the detected transtions, the toal spectrum without applying any gate was used to determine the relative intensity to the transition of 965 keV. The resulting values are shown in Table **5-3**.

For the 1080 keV γ-ray interference from a peak at 1062 keV did not allow the correct determination of the intensity from the spectra at 127° and 145° as it can be seen in Figure **5-18**. For this case the intensity was calculated using only the other two spectra at 53° and 35°.

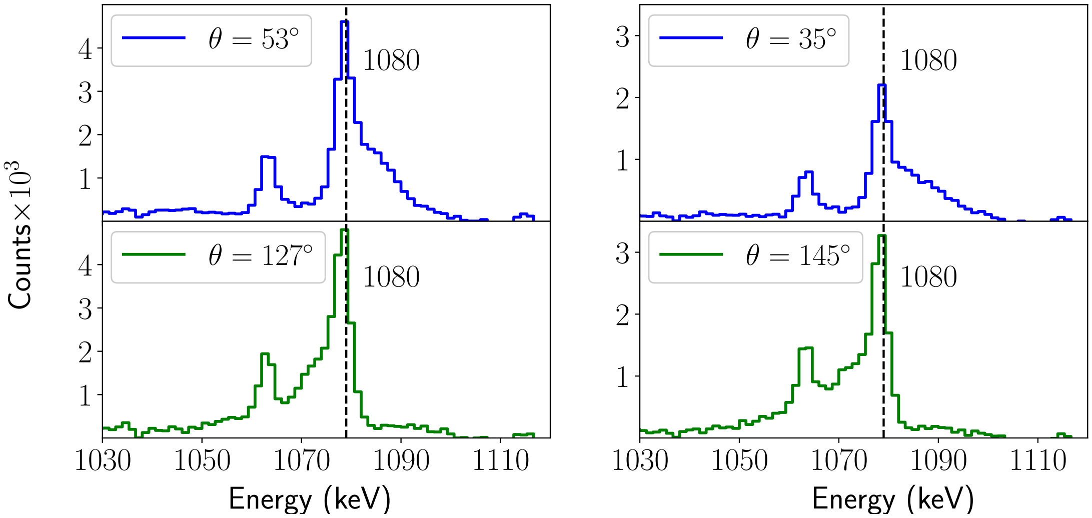

Figure 5-18.: Transition at 1080 keV from the spectrum gated at 595 keV.

The averaged relative intensities and the corresponding level scheme of the $(+,+)$ are shown in Figure **5-19**.

5.2.2. Lineshapes and lifetimes

The complete set of lineshapes and the lifetimes obtained for each of the transitions analized in this Thesis is presented in the Appendix B. In this section some remarks on the lineshapes found will be presented.

The determination of the level lifetimes τ and sidefeeding times τ_{SF} were carried out by comparison of the experimental lineshapes with the calculated ones produced by the AhKin code [59] using the methodology exposed in Section 5.1.3.

Examples of the lineshapes obtained are shown in Figure **5-20** which also shows the fits performed on the lineshapes of the γ-ray detected at the four angles analyzed. It also shows the corresponding χ^2_{red} curves indicating the limits used to determine the uncertainty. From the minimum values of χ^2_{red} in Figure **5-20** which vary from ∼3 to ∼11 it could be say, at first glance, that the theoretical lineshape it is not good. However by looking at the fits it can be seen that the number of counts in the region where the theoretical lineshape predicts values of zero represent the channels with the largest difference when compared with the experimental spectrum. This difference between the calculated and the experimental lineshapes for several channels increases the value of χ^2_{red} to become greater than 1. There are different reasons that

$(+,+)$ band	
Relative intensities to $I(965$ keV$)$	
E_γ (keV)	Average of the four angles
595	167(4)
811	119(4)
965	100(1)
1080	77.4(4)
1193	60(3)
1340	44(2)
1485	36(2)
1604	20(1)
1754	14(2)
1966	7(2)

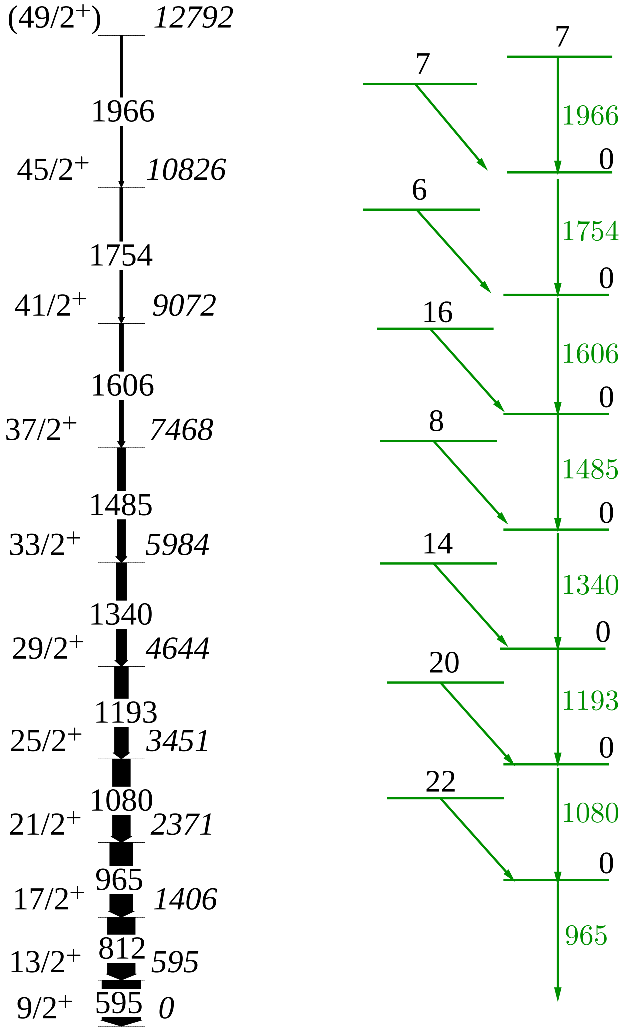

Figure 5-19.: Relative intensities of the transitions of the $(+,+)$ band and the correspondig deduced level scheme (spin and parities were taken from Ref. [6]). The width of the black arrows is proportional to the intensity of the transition. The level scheme at right shows the initial relative population deduced from the measured intensities.

explains these differences between the experimental and calculated lineshapes. The random coincidences represent one of the main sources of differences and in general not having a perfect detection system that always get the timing and energy information of the protons, α-particles and not Compton suppressed and scattered γ-rays are the explanations for those differences.

By performing GFA and GFB, sidefeeding times can also be extracted. Figure **5-21** shows the comparison of the lineshapes obtained for the γ-ray of 1340 keV emitted by the

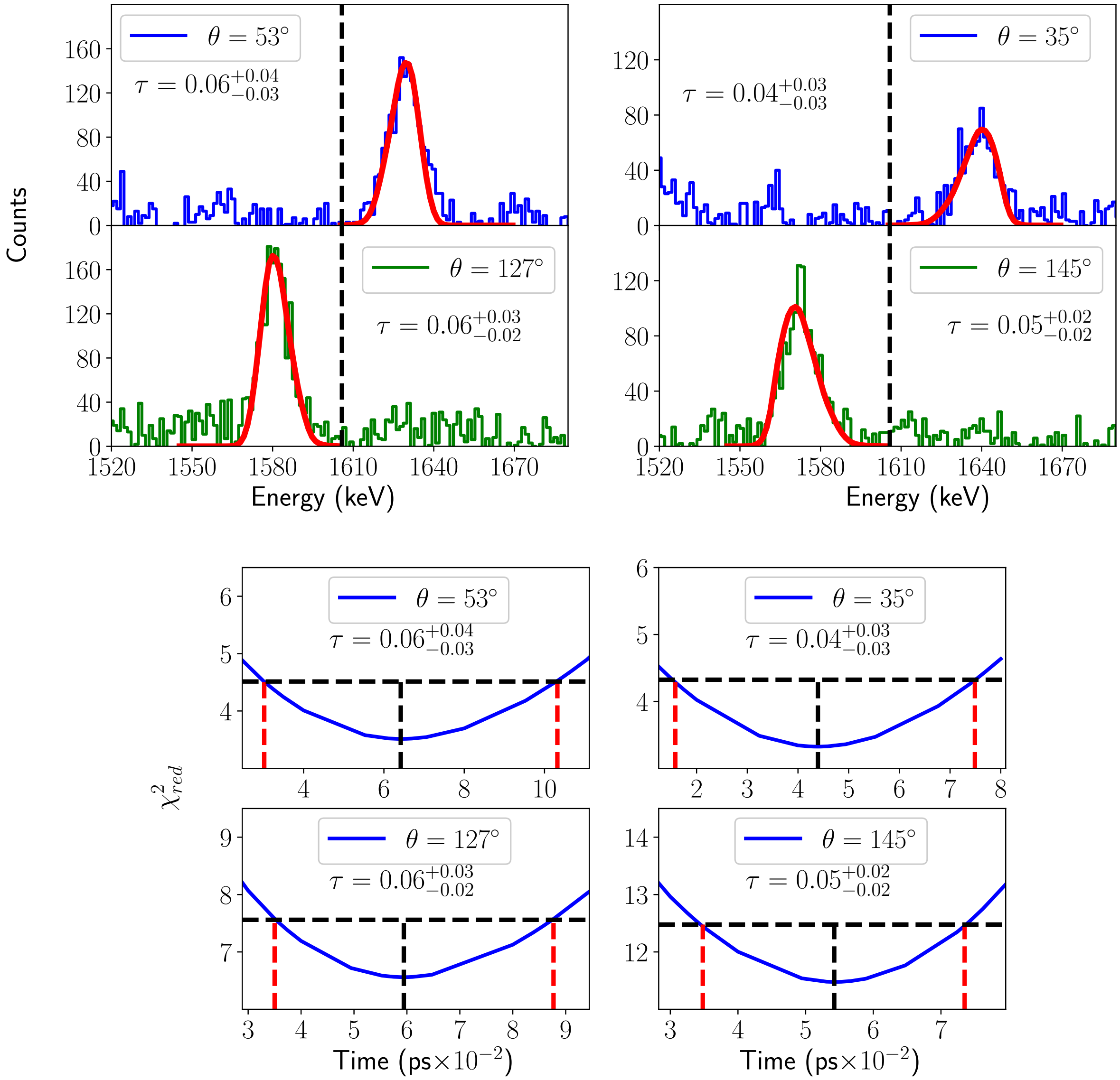

Figure 5-20.: Experimental and calculated lineshapes of the 1606 keV γ-ray when applying a gate from above at the 1754 keV γ-ray, together with their respective χ^2_{red} curve showing the intervals of uncertainty.

state of $I_i = 33/2$. The gates used to produce the lineshapes are displayed in Figure **5-21** as well. It can be seen how the relative number of counts in the "stop peak" increases in the GFB spectrum compared with the GFA lineshape. This effect suggest that the sidefeeding time will be larger than the level lifetime.

Fig. **5-22**(b) shows the lineshapes of the 1080 keV transition when gating from above and from below. This is another example in which it can be seen that the relative number of counts in the "stop peak" increases in the GFB lineshape compared with the GFA lineshape,

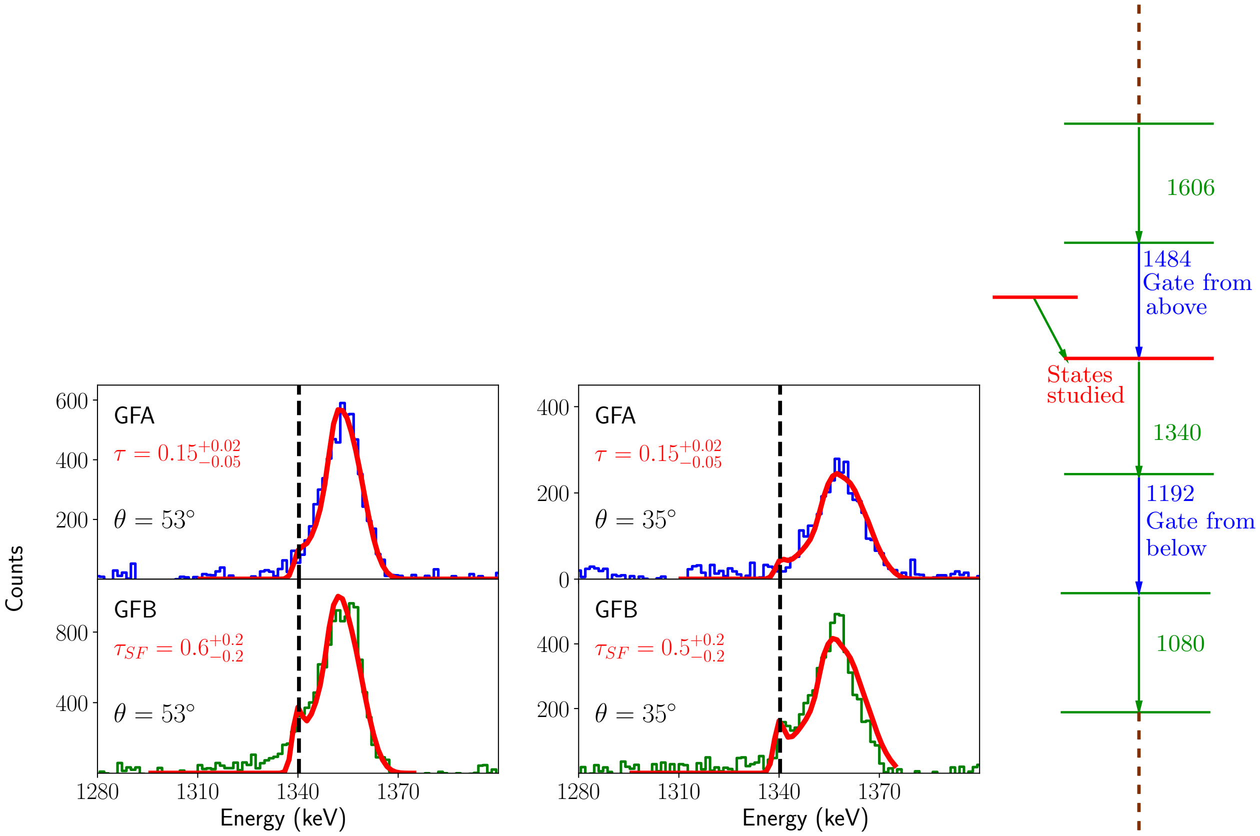

Figure 5-21.: Lineshape of 1340 keV compared when making GFA at 1481 keV and GFB at 1192 keV.

indicating a larger value of τ_{SF} compared with τ. In general the measured values follow the inequality $\tau_{SF} \gtrsim \tau$ as can be seen in Figure **5-22**(a) for the $(+,+)$ band.

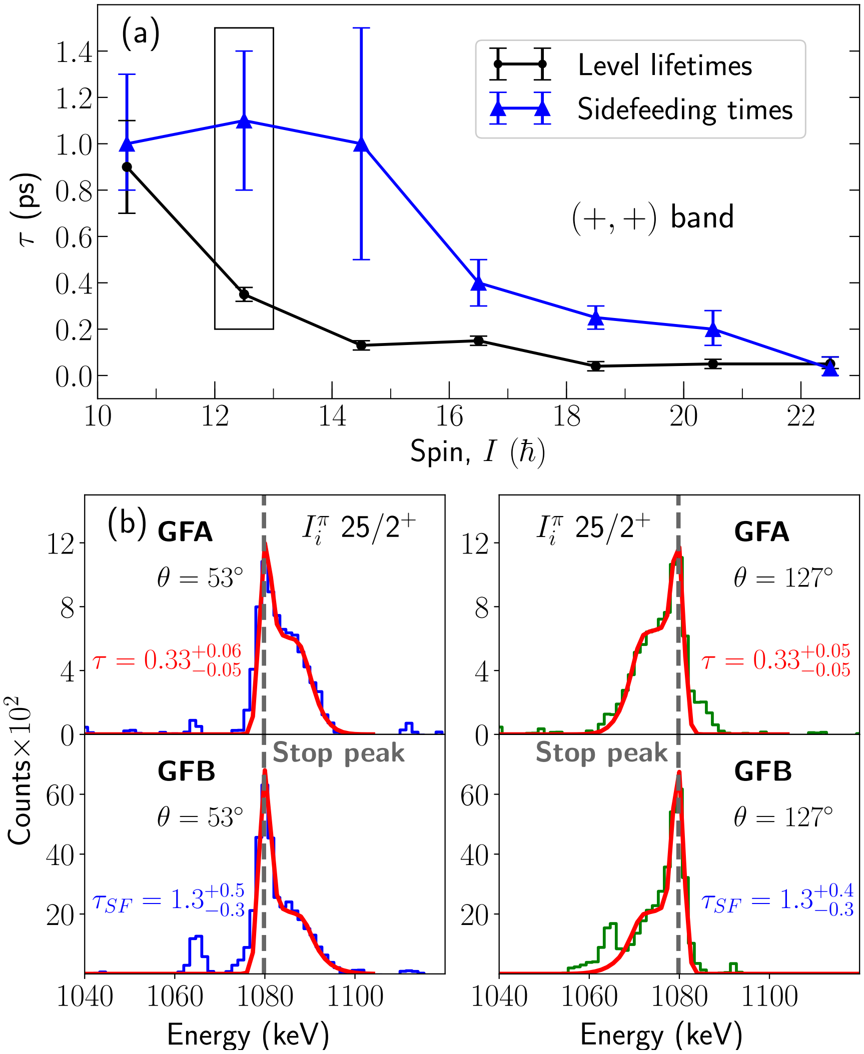

Figure 5-22.: (a) level lifetime and sidefeeding times for the (+, +) band. It can be seen that in general $\tau_{SF} \gtrsim \tau$. The rectangle encloses the state at $25/2^+$ emitting the γ-ray of 1080 keV. (b) lineshape of 1080 keV compared when making GFA at 1340 keV and GFB at 595 keV.

5.3. $(+,-)$ band

5.3.1. Doppler corection

The effect of applying the Doppler correction on the transitions of the $(+,-)$ band is shown in Figure **5-23**. Similar to the behavior of the $(+,+)$ band, the higher the energy of the γ-rays the larger the value of β for an appropiate Doppler correction is.

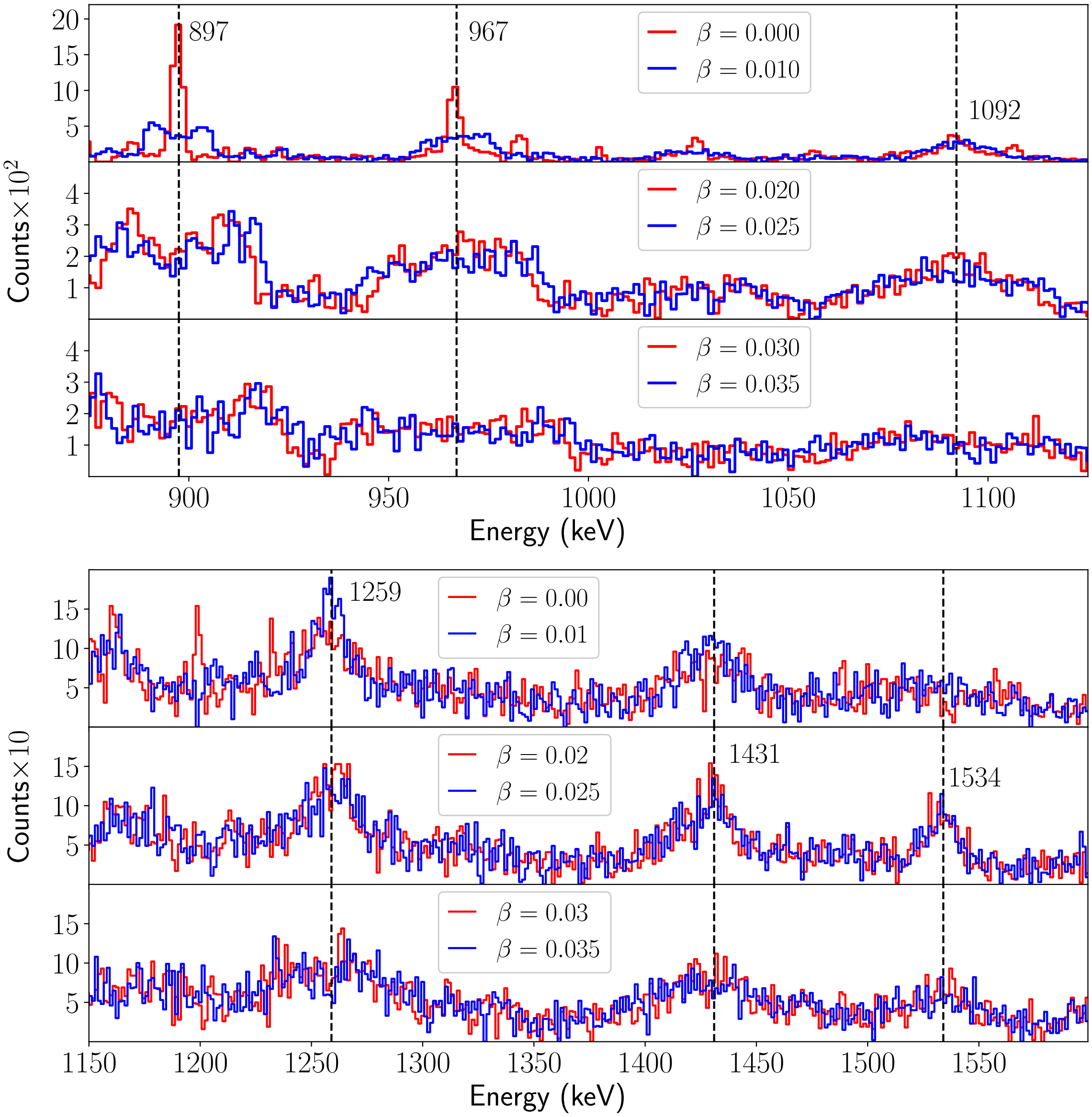

Figure 5-23.: Projection on the y-axis of the matrices showing the effect of the Doppler correction for the transitions of the $(+,-)$ band. The energy labels of the transitions are located in the figure whose β value is the one which best reconstructs the peak.

5.3.2. Lineshape sensitivity

Fig. **5-24** shows the lineshapes measured for some of the transitions in the $(+,-)$ band when gating from below at $E_\gamma = 897$ keV, the $15/2^+ \to 11/2^+$ transition energy. The sensitivity of the lineshape of different transitions produced by states having different feeding population and lifetimes can be visualized. The higher the energy of the transition the farther the lineshape distribution is, indicating shorter lifetimes for high energy transitions than those of lower energy.

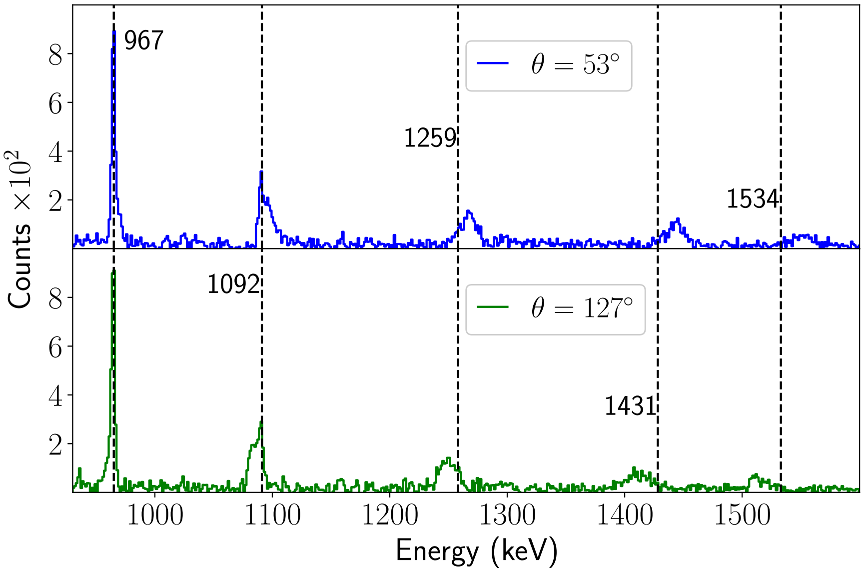

Figure 5-24.: Spectra showing transitions of the $(+,-)$ band detected at $\bar{\theta} = 52.8°, 127.2°$. The spectra were obtained by a GFB on the transition of 898 keV.

5.3.3. Relative intensity of the transitions of the $(+,-)$ band

To determine the relative initial feeding population of the states of the $(+,-)$ band, the gate at 897 keV was used and the intensities of the transtions were normalized to the intensity of the 897 keV γ-ray. The values obtained are shown in Table **5-4**.

The averaged intensity values, the level scheme and the corresponding initial feeding population are shown in Figure **5-25**.

5.3.4. Lineshapes and lifetimes

Figure **5-26**(b) shows the comparison of the lineshpaes of the γ-ray of 1260 keV when applying GFA and GFB. It can be seen how the relative number of counts in the "stop peak" increases for the lineshapes produced with the GFB compared with the ones produced with

Relative intensities to I(897 keV)					
Gate at 897 keV					
E_γ (keV)	53°	127°	35°	145°	Average
795	100.0(7)	100.0(7)	110.9(8)	119.4(8)	100.0(3)
897	-	-	-	-	-
967	89(2)	92(2)	93(2)	95(2)	92(3)
1092	72(1)	63(1)	80(2)	71(2)	72(7)
1259	57(1)	63(1)	66(2)	62(1)	62(4)
1431	61(1)	62(1)	59(1)	56(1)	59(2)
1534	34(1)	36(1)	38(1)	44(1)	38(4)
1648	30(1)	33(1)	45(1)	32(1)	35(7)

Table 5-4.: Relative intensities of the transitions of the $(+,-)$ band by gating at 897 keV.

GFA. The resulting level lifetimes and sidefeeding times of the $(+,-)$ band are shown in Figure **5-26** (a), where it can be seen that the inequality $\tau_{SF} \gtrsim \tau$ holds. The Figure **5-26**(a) also shows that the level lifetimes increase when decreasing the spin. This is the same trend that was observed in the $(+,+)$ band.

(+, −) band	
Relative intensities to I(897 keV)	
E_γ (keV)	Average of the four angles
795	100.0(3)
897	Gate
967	92(3)
1092	72(7)
1260	62(4)
1431	59(2)
1534	38(4)
1648	35(7)

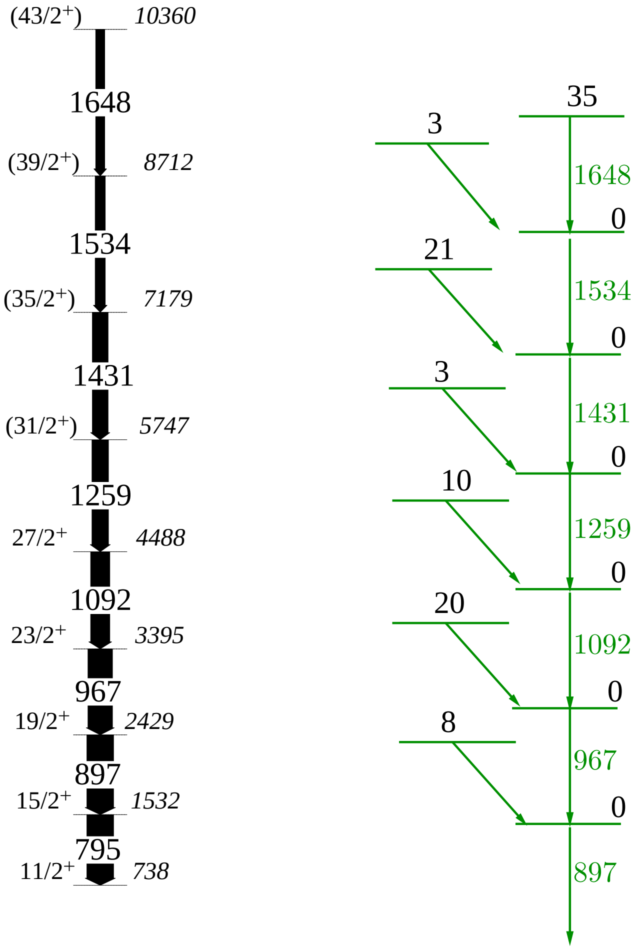

Figure 5-25.: Relative intensities of the transitions of the (+, −) band and the correspondig deduced level scheme (spin and parities were taken from Ref. [6]). The width of the black arrows is proportional to the intensity of the transition. The level scheme at right shows the initial relative population deduced from the measured intensities.

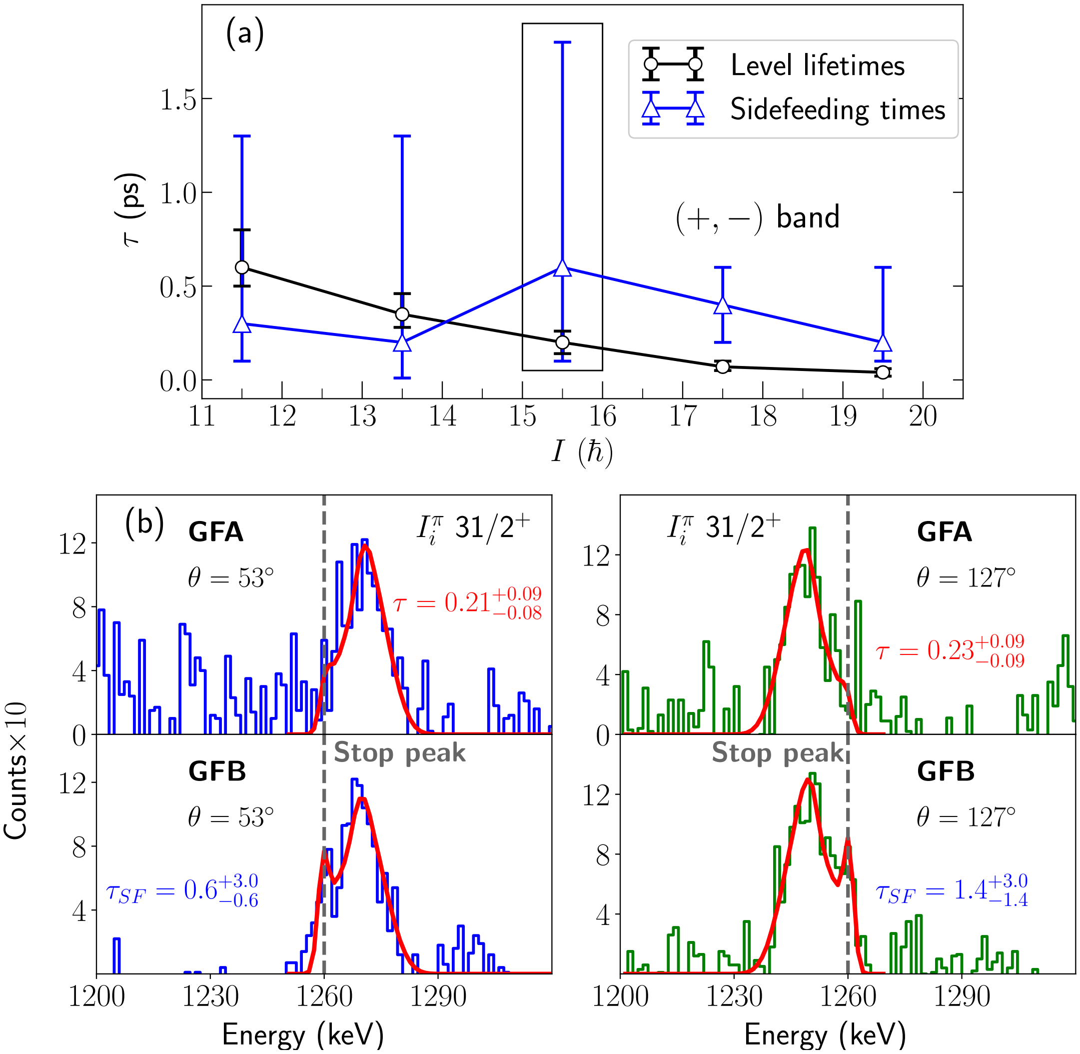

Figure 5-26.: (a) level lifetime and sidefeeding times for the $(+,-)$ band. It can be seen that in general $\tau_{SF} \gtrsim \tau$. The rectangle encloses the state at $(31/2^+)$ emitting the γ-ray of 1260 keV. (b) Lineshape of 1260 keV compared when making GFA at 1534 keV and GFB at 897 keV.

5.4. $(-,+)$ band

5.4.1. Doppler correction

The transitions of the $(-,+)$ band when a projection on the y-axis of the matrices is applied are shown in Figure **5-27**, where the Doppler correction using different β values was performed. It can be seen how the peaks corresponding to low energy transitions are destroyed by applying the Doppler correction even for small β values. On the other hand larger β values are needed to reconstruct the peaks of the highest energy transtions.

5.4.2. Relative intensity of the transitions of the $(-,+)$ band

To obtain the intensities of the $(-,+)$ band transitions, several gates were used due to the two γ-rays at 1162 and 1174 keV are very close in energy and the corresponding Doppler shifted spectra overlap each other as it is shown in Figure **5-28** which was produced by gating at 1026 keV.

Gate at 840 keV was used to obtain the intensities of the γ-rays of 752, 909, 1026, 1413, 1595, 1799, and 2041 keV. The value of the intensity of the transition of 752 keV when gated at 840 keV corresponds also to the intensity of the 840 keV transition due to the fact that, gating at 840 keV, there are no sidefeeding states contributing to the state emitting the 752 keV γ-ray.

By gating at 1174 keV the intensity of the transitions of 1162, 1245 and 1799 keV were determined. In this case the 1799 keV intensity was used to normalize the intensities determined with other gates. The value of the intensity of the transition of 1162 keV when gated at 1174 keV corresponds also to the intensity of the 1174 keV transition due to the fact that, for this gate, there are no sidefeeding states contributing to the state emitting the 1162 keV γ-ray.

The intensty of 1162 keV was calculated by substracting the intensity of the 1174 γ-ray from the sum of intensities of 1162 and 1174 keV determined from spectra gated from below at 1026 keV shown in Figure **5-28**. With the gate a 1026 keV the intensity of 1799 was determined and used to normalize the intensities determined using other gates.

Finally all γ-ray intensities were normalized to the intensity of the 840 keV transition. The resulting intensities for the $(-,+)$ band are shown in the Table **5-5**.

5.4.3. Discussion on the determination of the lineshapes of transitions of 1162 and 1174 keV

The overlap presented by the transitions of 1162 and 1174 keV shown in Figure **5-28** that had to be examined in detail for the determination of the intensities should be tretaed carefully in the study of the 1162 and 1174 keV lineshapes as well. By applying the proper gates the

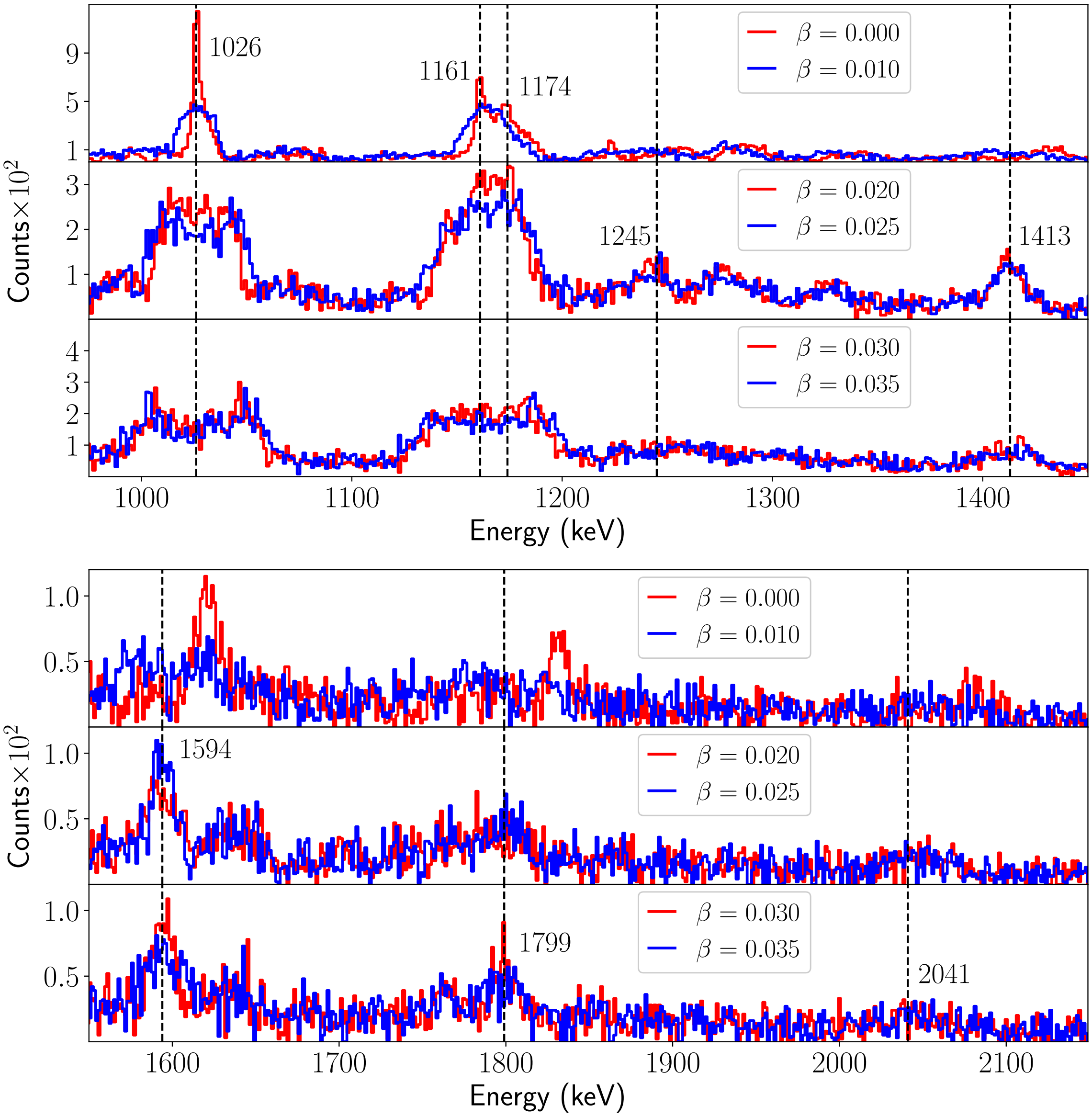

Figure 5-27.: Projection on the y-axis of the matrices showing the effect of the Doppler correction for the transitions of the $(-,+)$ band. The energy labels of the transitions are located in the figure whose β value is the one which best reconstructs the peak.

overlapping can be removed. The determination of all of the lineshapes analized for these two transitions in order to determine the level lifetimes and the side feeding times of the states of $I_i^\pi = (33/2^-), (29/2^-)$ was as follows:

- **Level lifetime and side feeding time of the state of** $I_i^\pi = (33/2^-)$. By applying whichever gate from above this state, the two transitions will appear overlapped in the resulting spectrum. However by applying the gate from below at the transition of 1162

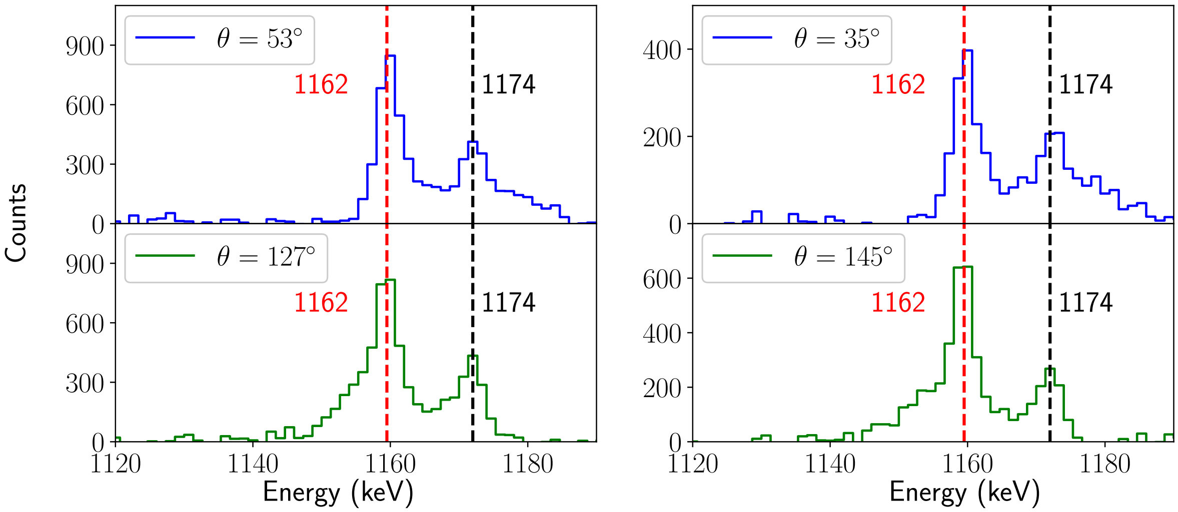

Figure 5-28.: γ-rays at 1162 and 1174 keV at different angles gated at 1026 keV.

keV, this lineshape will disappear from the resulting spectrum producing a clean 1174 keV lineshape. Therefore the gate from below at 1162 keV and the correlation method on the resulting lineshape were used to determine the level lifetime and sidefeeding time of the state of $I_i^\pi = (33/2^-)$.

- **Level lifetime of the state of** $I_i^\pi = (29/2^-)$. By applying the gate from above at the transition of 1174 keV, a clean 1162 keV lineshape was produced and used to determine the level lifetime of the state of $I_i^\pi = (29/2^-)$.
- **Sidefeeding time of the state of** $I_i^\pi = (29/2^-)$. Interference with the 1174 keV transition in this case is unavoidable because any gate from below the transtion of 1162 keV will produce an spectrum in coincidence with both 1162 and 1174 keV transitions. However this interference is not affecting significantly the lineshapes of 127° and 145° as it can be seen in the Figure **5-30**. Therefore for this sidefeeding time only the two lineshapes of 127° and 145° were used.

5.4.4. Lifetimes and sidefeeding times

The level lifetimes and sidefeeding times obtained for the $(-,+)$ band are shown in the Figure **5-31**. It can be seen that the inequality $\tau_{SF} \gtrsim \tau$ holds as well it did for the cases of the $(+,+)$ and $(+,-)$ bands. However the tendency of the level lifetimes to increase monotically when decreasing the spin is not maintained for the $(-,+)$ for which at $I_i = 33/2$ such tendency is broken. A detailed study of the effect of the evolution of the level lifetimes on the physics behavior of ^{83}Y will be presented in Chapter 7.

Relative intensities to I(840 keV)					
Gate at 840 keV					
E_γ (keV)	53°	127°	35°	145°	Average
840	100(2)	100(2)	100(2)	100(2)	100(3)
909	95(1)	95(1)	91(2)	95(2)	94(3)
1026	88(1)	90(1)	96(2)	91(2)	91(4)
Gate at 1026 and 1174 keV					
1162	91(4)	83(4)	87(6)	71(5)	83(20)
Gate at 1174 keV					
1174	54(3)	70(3)	46(4)	64(4)	58(11)
1245	43(3)	-	39(5)	-	40(8)
Gate at 840 keV					
1413	30(3)	33(3)	37(5)	39(5)	32(6)
1595	24(4)	28(4)	29(5)	29(5)	27(6)
1799	23(4)	20(4)	24(5)	26(5)	24(7)
2041	19(5)	13(5)	17(6)	17(6)	16(8)

Table 5-5.: Relative intensities of the transitions of the $(-,+)$ band obtained applying different gates.

(−, +) band	
Relative intensities to I(840 keV)	
E_γ (keV)	Average of the four angles
840	100.0(3)
909	94(3)
1026	91(4)
1162	83(20)
1174	58(11)
1245	40(8)
1413	32(6)
1595	27(6)
1799	24(7)
2041	16(8)

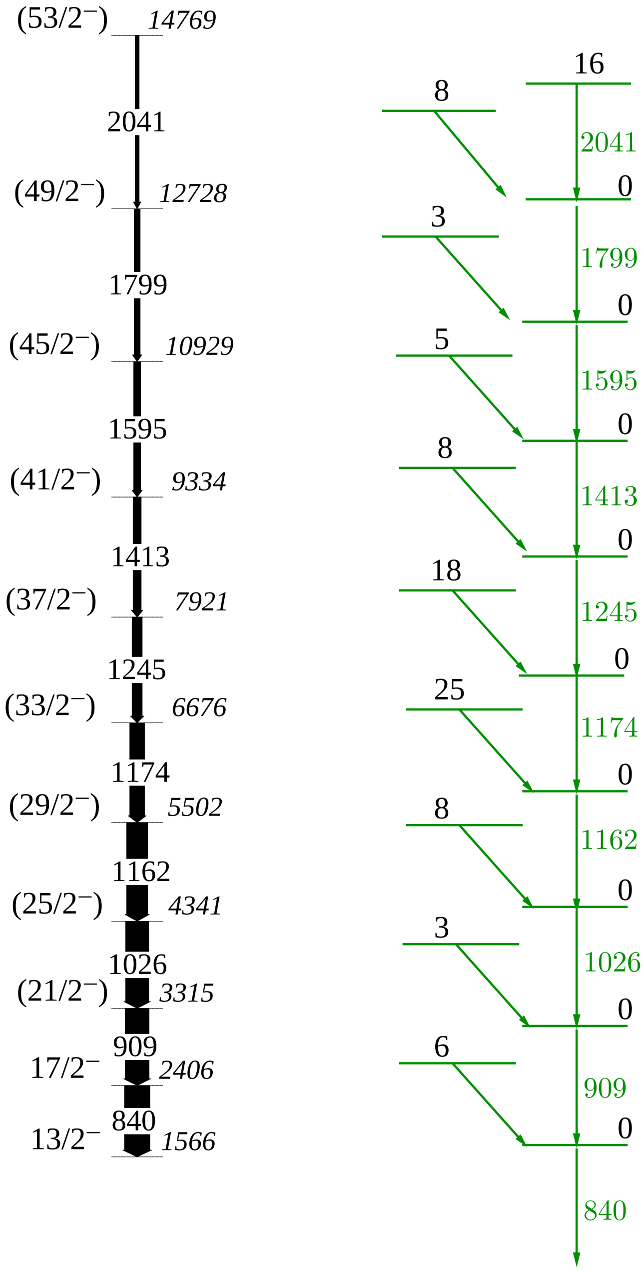

Figure 5-29.: Relative intensities of the transitions of the $(-, +)$ band and the correspondig deduced level scheme (spin and parities were taken from Ref. [6]). The width of the black arrows is proportional to the intensity of the transition. The level scheme at right shows the initial relative population deduced from the measured intensities.

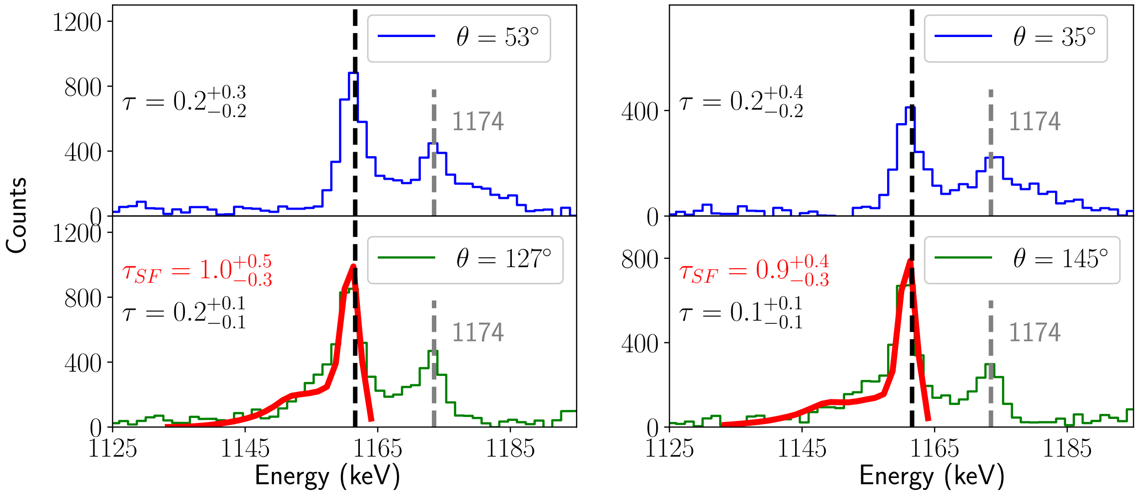

Figure 5-30.: Fits performed by the program AhKin to study the sidefeeding life time of the state at 5502 keV by using the γ-ray of 1162 keV detected at different angles.

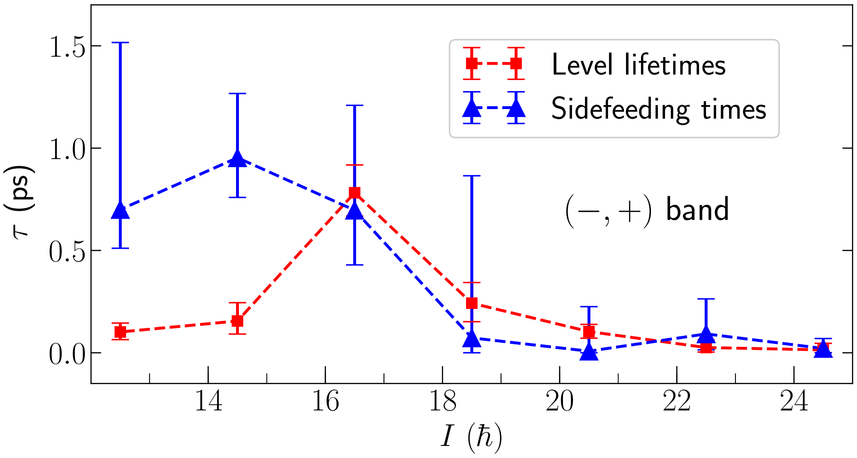

Figure 5-31.: level lifetime and sidefeeding times for the $(-,+)$ band. It can be seen that in general $\tau_{SF} \gtrsim \tau$.

5.5. Summary of lifetimes obtained

The same dataset analyzed in this work was evaluated by using gates from below only except for one of the transitions [64]. In this work lineshapes obtained by gating from above were possible for most of the states studied here, including high spin states. In Appendices B to D the measured and calculated lineshapes corresponding to different transitions can be found. The analysis of the lineshapes at different angles provided us a methodology that increases the precision of the lifetime measurements.

In some cases lineshapes with GFA could not be obtained because of interference with other transitions. That was the case in the $(-,+)$ band of the 1174 and 1162 keV transitions exposed in Section 5.4.3. For these special cases the determination of τ and τ_{SF} was done by applying a correlation method discussed in Section 5.1.6.

As it was shown in Appendix A the stopping time of the ^{83}Y nucleus inside the ^{181}Ta is around 1 ps which sets an upper limit for the lifetimes that can be obtained with the data acquired in this experiment. For states having lifetimes around 1 ps or larger the lineshape obatained for its depopulating transition does not show a Doppler broadening which does not allow the lifetime determination by DSAM. Thus lifetimes were determined starting from the highest spin state populated down to the states at $(21/2^{+})$, $(19/2^{+})$, $(25/2^{-})$ for the $(+,+)$, $(+,-)$ and $(-,+)$ bands respectively.

Regarding the $(-,-)$ band, some of the transitions shown in Fig. **5-1** were observed although with low intensity. Lifetime measurements were not possible for any of these states. For the 909 keV γ-ray, emitted by the $(23/2^{-})$ state no Doppler broadening was observed showing that its lifetime is around 1 ps or above. For the 1065, 1154 and 1286 keV γ-rays there was always interference from transitions of other bands in ^{83}Y. Such interferences combined with the low intensity observed for these transitions did not allow the lineshape analysis.

Table **5-6** shows the measured τ and τ_{SF} in this work alongside the previously reported values.

In Chapter 7 the reduced transition probabilities, $B(E2)$, transition quadrupole moments, Q_t, and quadrupole deformation parameters, β_2, determined from the measured lifetimes will be presented together with the analysis and discussion of the results obtained.

Table 5-6.: Level energies E_x, spin and parities I^π, transition γ-ray energies E_γ, τ and τ_{SF} for the $(+,+)$, $(+,-)$ and $(-,+)$ bands of the ^{83}Y.

E_x (keV)	I^π ($\hbar$)	E_γ (keV)	τ (ps)[a]	τ (ps)[b]	τ (ps)	τ_{SF} (ps)
			$(+,+)$ band			
12792	$(49/2^+)$	1966		$0.01^{+0.05}_{-0.01}$	$0.10^{+0.03}_{-0.02}$ [c]	-
10826	$45/2^+$	1754		$0.02^{+0.08}_{-0.01}$	$0.05^{+0.03}_{-0.02}$	$0.03^{+0.05}_{-0.03}$
9072	$41/2^+$	1604		$0.02^{+0.08}_{-0.01}$	$0.05^{+0.02}_{-0.02}$	$0.20^{+0.08}_{-0.07}$
7468	$37/2^+$	1485		$0.07^{+0.04}_{-0.03}$	$0.04^{+0.02}_{-0.02}$	$0.25^{+0.05}_{-0.05}$
5984	$33/2^+$	1340	≤ 0.39	$0.32^{+0.13}_{-0.10}$	$0.15^{+0.02}_{-0.02}$	$0.4^{+0.1}_{-0.1}$
4644	$29/2^+$	1193	0.29(7)	$0.28^{+0.05}_{-0.04}$	$0.13^{+0.02}_{-0.02}$	$1.0^{+0.5}_{-0.5}$
3451	$25/2^+$	1080	0.38(8)		$0.35^{+0.03}_{-0.03}$	$1.1^{+0.3}_{-0.3}$
2371	$21/2^+$	965	0.6(1)		$0.9^{+0.2}_{-0.2}$	$1.0^{+0.3}_{-0.2}$
1406	$17/2^+$	812	1.39(15)			
595	$13/2^+$	595	7.8(7)			
			$(+,-)$ band			
10360	$(43/2^+)$	1648			$0.16^{+0.11}_{-0.07}$ [c]	-
8712	$(39/2^+)$	1534			$0.04^{+0.02}_{-0.02}$	$0.2^{+0.4}_{-0.1}$
7179	$(35/2^+)$	1431		< 0.34	$0.07^{+0.03}_{-0.02}$	$0.4^{+0.2}_{-0.2}$
5747	$(31/2^+)$	1259		$0.29^{+0.11}_{-0.10}$	$0.20^{+0.06}_{-0.06}$	$0.6^{+1.2}_{-0.5}$
4488	$27/2^+$	1092		$0.29^{+0.09}_{-0.11}$	$0.35^{+0.11}_{-0.07}$ [d]	$0.2^{+1.1}_{-0.2}$ [d]
3395	$23/2^+$	967		$0.62^{+0.16}_{-0.13}$	$0.6^{+0.2}_{-0.1}$ [d]	$0.3^{+1.0}_{-0.2}$ [d]
			$(-,+)$ band			
14796	$(53/2^+)$	2041			$0.08^{+0.04}_{-0.03}$ [c]	-
12728	$(49/2^+)$	1799			$0.01^{+0.03}_{-0.01}$	$0.02^{+0.05}_{-0.02}$
10929	$(45/2^+)$	1595			$0.03^{+0.04}_{-0.02}$	$0.09^{+0.17}_{-0.07}$
9334	$(41/2^+)$	1413			$0.10^{+0.10}_{-0.03}$ [d]	$0.01^{+0.22}_{-0.01}$ [d]
7921	$(37/2^+)$	1245			$0.24^{+0.09}_{-0.03}$ [d]	$0.07^{+0.79}_{-0.07}$ [d]
6676	$(33/2^+)$	1174			$0.78^{+0.14}_{-0.11}$ [d]	$0.7^{+0.5}_{-0.3}$ [d]
5502	$(29/2^+)$	1162			$0.16^{+0.09}_{-0.06}$	$0.9^{+0.3}_{-0.2}$
4341	$(25/2^+)$	1026			$0.22^{+0.13}_{-0.11}$	$0.7^{+0.8}_{-0.2}$

---

[a] Values adopted in Ref. [4].

[b] Values reported in Ref. [6].

[c] Effective lifetime, not corrected by feeding.

[d] Lifetime determined by gating from below only.

6. Methodology to study the nuclear continuum

The numerical simulations of the nuclear decay from the continuum states are tools which allow to study the physics of the continuum nuclear states. In this thesis we investigate two methods for the study of the nuclear continuum and quasicontinuum. Both methods make use of simulations carried out with the codes Gammapace [65] and Gamble [66] which will be described in the upcoming subsections. Comparison of simulations with experimental data of the side feeding times allows to investigate the nuclear properties in the quasicontinuum region (see Section 2.2) and Gamble simulations are used to explore the capabilities of the Hk-EOS technique (Section 6.3).

6.1. Entry states distribution

The entry states can be calculated by using the simulation code Gammapace that calculates the excitation energy and angular momentum distribution of the compound nucleus. By using the Fermi's golden rule, Equation (6-1)

$$P_{i \to f} \propto \rho(E_f, I_f) \langle \varphi_i | H | \varphi_f \rangle, \tag{6-1}$$

the program calculates the cross section of the formation of each nucleus produced by emission of nucleons from the compound nucleus. The code Gammapace [67] provides the entry states distribution for each selected channel (in nuclear physics, “a channel” is referred to one of the products of the reaction). Gamble takes as input the entry states distribution and simulates the γ decay of the nucleus by including most of the decay physics known to date. As an example of the results of Gammapace, the **6-1**a shows in an spin-energy plane, the entry states distribution for the ^{154}Dy produced in the reaction ^{36}S + $^{122}_{50}$Sn at 154 MeV. The reasons to use this nucleus as test in the numerical simulations were given in Section 3.2.1.

6.1.1. Spin entry distribution

The initial spin distribution in Gamble can be produced with three options:

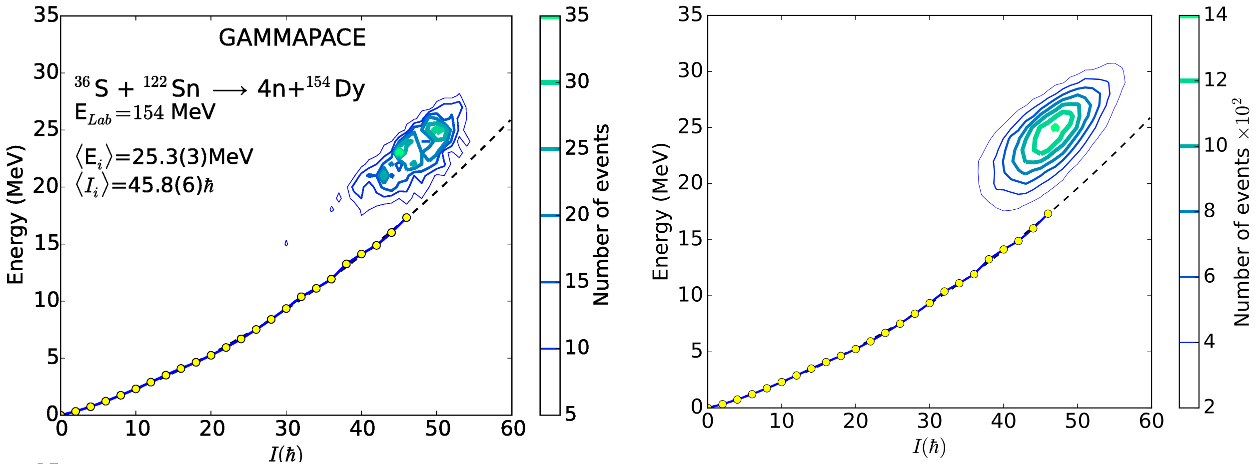

(a) Entry states of ^{154}Dy obtained using GAMMAPACE. **(b)** Entry states of ^{154}Dy obtained using GAMBLE.

Figure 6-1.: Entry states distribution of ^{154}Dy generated using the reaction ^{36}S + $^{122}_{50}$Sn at 154 MeV.

1. Triangular, with the vertices as input parameters.
2. Gaussian:

$$f(I) = \frac{1}{\sqrt{2\pi}\sigma_I} \exp^{(I-\langle I\rangle)^2/2\sigma_I^2} \tag{6-2}$$

   The parameters of the Gaussian, σ_I and $\langle I\rangle$ can be given as input parameters.

3. Customized entry distribution can be utilized. In this case the weight for each value of spin can be entered as input parameter.

The spin distribution produced by GAMMAPACE and by the different options of GAMBLE are shown in Figure **6-2**a, where it can be seen that the Gaussian distribution, of GAMBLE, is the one that best approximate the GAMMAPACE distribution.

6.1.2. Energy entry distribution

The energy distribution is calculated in a similar way for GAMBLE and GAMMAPACE. Both programs start from the Lang's formula [68] for the level density. Thus the probability energy distribution of the nucleus after the emission of the fourth neutron (in the reaction simulated here) is considered as the distribution of the density of states, $\rho(U, I)$

$$f_p(U, I) = \rho(U, I) \exp^{-\beta_p U^{\alpha_p}} . \tag{6-3}$$

In previous equation, α_p is a parameter which can be fixed to 1 to produce a thermal (Boltzman) distribution. The sub-index p in Equation (6-3) makes reference to a pre-distribution

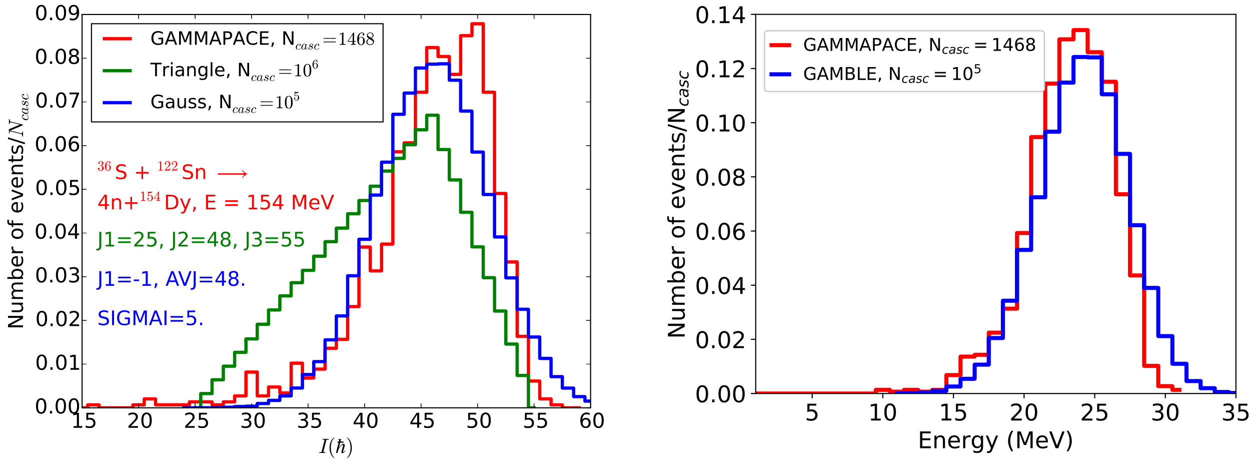

(a) Projection in spin of the entry population generated by GAMMAPACE and GAMBLE.

(b) Projection in energy of the entry population generated by GAMMAPACE and GAMBLE.

Figure 6-2.: Projection in energy and spin of the entry population.

which has to be modified because when a particle is emitted another nucleus is generated and some of the states at high excitation energy should not be considered. This effect is taken into account with a Boltzman distribution $f_e(U, I)$ over the initial pre-distribution $f_p(U, I)$.

$$f_e(U, I) = f_p(U, I) \exp^{-\beta_e U^{\alpha_e}} \tag{6-4}$$

The sub-index e in Equation (6-3) makes reference to the energy-distribution. Once the entry states distribution is defined, the next step is to simulate the γ-decay of the nucleus.

6.2. Gamma decay of the nucleus

There are three types of decay simulated by GAMBLE which are briefly described in this document

- Discrete decay, intended to describe the decay of the discrete states of the nucleus. GAMBLE allows to enter the experimental values if they are known.
- In GAMBLE every point of the spin-energy plane has the possibility to be a member of a collective band in the continuum region. In the decay of these collective states the spread of the transition energies due to the rotational damping [69] is also considered.
- Statistical $M1$ and $E2$ transitions are considered in the continuum region. $E1$ statistical transitions are considered as Giant Dipole Resonance (GDR) [70].

Gamble takes the physical properties of the nucleus as input parameters. A detailed description of these input parameters can be found in Ref. [66]. It is important to emphasize here that the level density parameter (discussed in Section 2.15.1) was fixed to a value of $a = 21.0$ MeV^{-1}.

6.3. Energy Ordered Spectra (EOS)

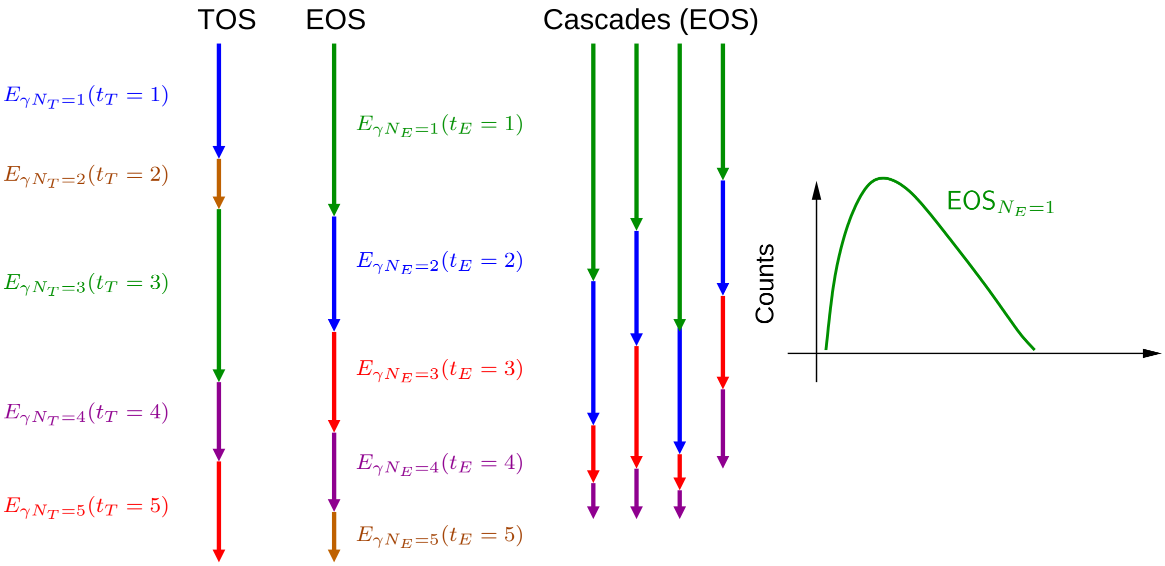

Figure 6-3.: Schematic representation of the construction of the EOS spectra.

Figure **6-3** shows a representation of a γ-ray cascade in which the construction of EOS is illustrated by comparing with a cascade used to generate the Time Ordered Spectra (TOS). The EOS are produced by sorting the radiation emitted by a nucleus in decreasing order according to its energy. If a cascade of n γ-rays is emitted by a nucleus, the time ordering is

$$\begin{gathered} E_{\gamma N_T=1}(t_{T1}), E_{\gamma N_T=2}(t_{T2}), E_{\gamma N_T=3}(t_{T3}), \ldots, E_{\gamma N_T=4}(t_{TM}) \\ t_{T1} < t_{T2} < t_{T3} < \ldots < t_{TM}, \end{gathered} \tag{6-5}$$

where t_{Ti} is the time of emission of transition T_i. The associated energy-ordering of the cascade is

$$E_{\gamma N_E=1}(t_{E1}) \geq E_{\gamma N_E=2}(t_{E2}) \geq \ldots \geq E_{\gamma N_E=M}(t_{EM}) \quad \text{in general} \quad t_{Ti} \neq t_{Ei} \tag{6-6}$$

where t_{Ei} is the time of the emission of a γ-ray with the energy E. The EOS constructed from the most energetic γ-rays of a cascade are called the EOS of order $N = 1$. The goal is to extract physical information from the EOS spectra which can be experimentally obtained.

The first approximation proposed to study the EOS spectra is to assume that $E_{\gamma N_E=1}(t_{E1}) = E_{\gamma N_T=1}(t_{T1})$, that means to consider that the most energetic γ-ray emitted in a cascade is also the first one emitted. Based on the fact that most of this spectrum is produced by GDR transitions as can be seen from Figure **6-4** a fitting function to the EOS spectra of order $N = 1$, to extract the level density parameter of Equation (2-44) can be proposed. The shape of the spectra can be modeled, in first approximation, as it was proposed in [2]

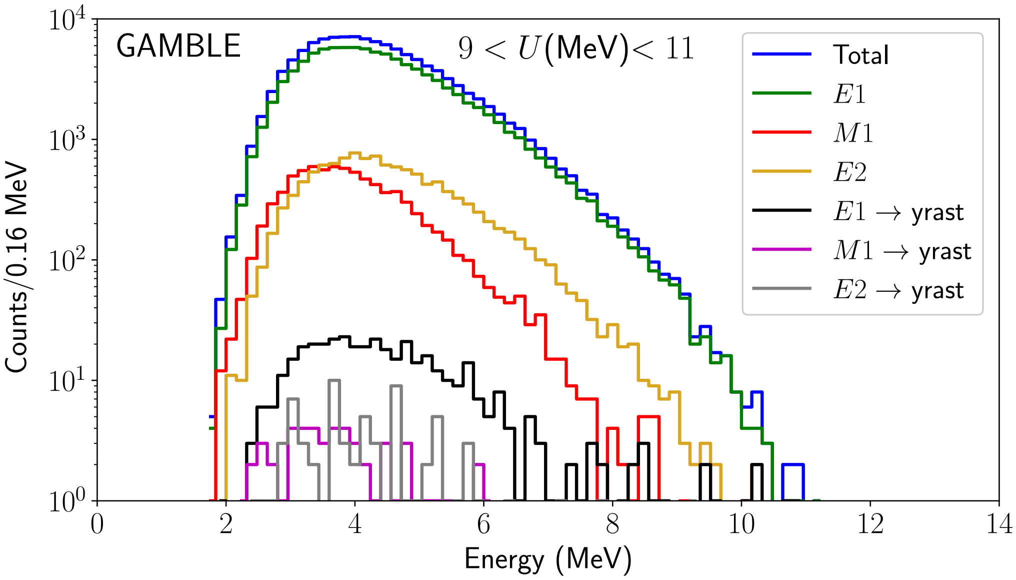

Figure 6-4.: Decomposition of the EOS in the different types of radiation showing that the $E1$ statistical transitions have the larger contribution. It is the GDR transitions.

$$I_\gamma(E_\gamma) = C \cdot \Gamma_{GDR}(E1, E_\gamma) \frac{e^{2\sqrt{a(U_s - E_\gamma)}}}{\left(U_s - E_\gamma + \frac{3}{2}T_f\right)^2}. \tag{6-7}$$

In Equation (6-7), U_s, represent an effective initial excitation energy. Equation (6-7) can be used as a fitting function of the EOS spectrum. By setting $U_s = U_h = 11$ MeV the fitting function depends only on the level density parameter a and the constant C which just plays a role of a scaling factor. As example of the application of this fitting function see the Figure **6-5** where the level density parameter was given as a fixed input parameter of $a = 21.0$ MeV^{-1}.

In Figure **6-5** the subindex E_ℓ indicates the starting energy value from which the EOS spectrum was considered to perform the fit. Mathematical tools have been used to study the shape of the EOS spetrum. It was demonstrated that order statistics can be applied to approximate the shape of the EOS. Afterwards and with this background a satisfactory approximation to the EOS with $N = 1$ was developed [53]. This fitting function not only produces a fit to the EOS but also provides the level density parameter a as a result. This

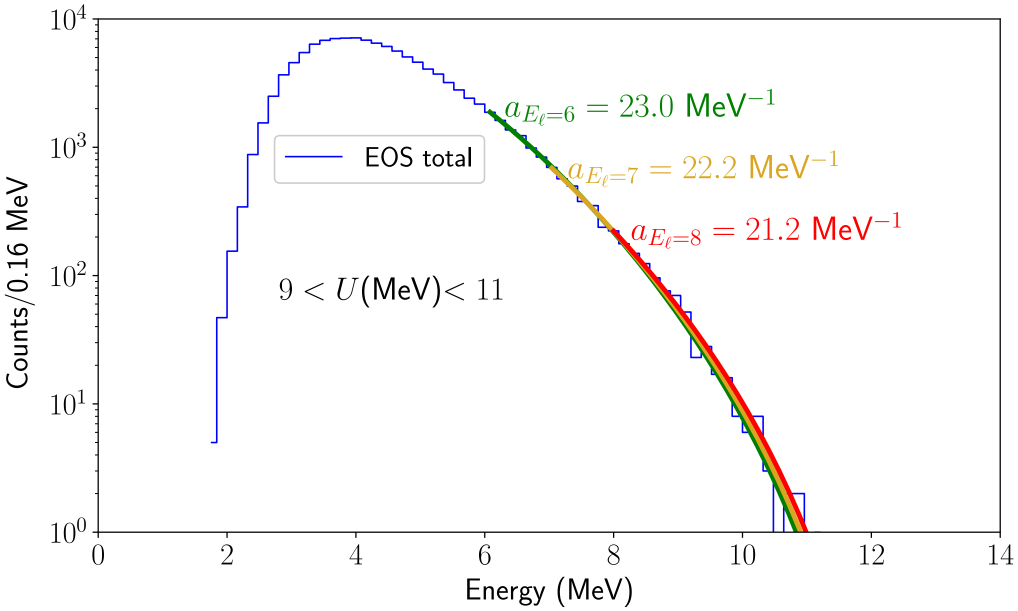

Figure 6-5.: Application of the fitting function of Equation (6-7) to the EOS of order $N = 1$.

function was developed by considering the possibility that the highest energy γ-ray was emitted at a random position in every casacade. A series of terms is generated where the first one correspond to Equation (6-7). The second one correspond to the consideration that the highest energy γ-ray was emitted at the second position in the cascade and so on. This fitting function applied to a simulation of the γ-decay coming from a specific point in the spin-energy plane at $(I, E) = (47\hbar, 29.0 \text{ MeV})$ with excitation energy above the yrast line, $U = 11.0$ MeV is shown in Figure **6-6**. $p^S_{NE=1}$ in Figure **6-6** means that the spectrum corresponds to the first order EOS. The level density parameter a was fixed in the simulation to $a = 18.4$ MeV^{-1}. From the fitting function the value obtained was $a = 18.5(3)$ MeV^{-1}. The fit shows the capabilities of the full method to extract physical information from the EOS spectra that can be obtained experimentally.

At this point the effect of the experimental array on the shape of the EOS spectra have to be studied. Moreover the study of the feasibility of obtaining the initial (E, I) point from which a determined EOS is produced have to be investigated as well. The Hk technique that will be discussed in the next section aims provide a methodology to solve these issues.

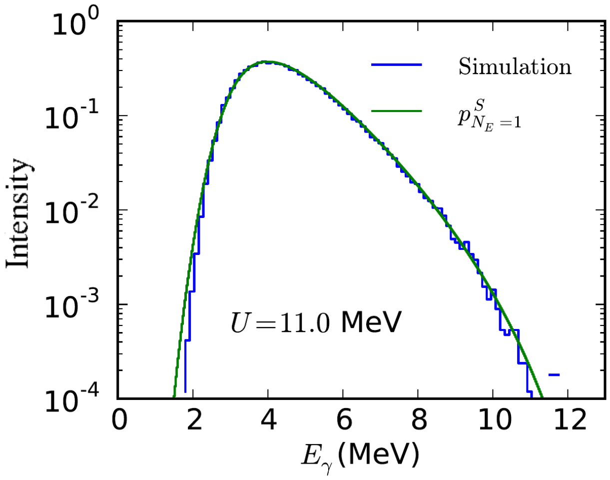

Figure 6-6.: Simulation of ^{154}Dy EOS spectrum. The transitions come from a point in the spin-energy plane at $(I, E) = (47\hbar, 29.0\text{MeV})$ with $U = 11.0$ MeV. The fititng function in Ref. [53] is also shown.

6.4. The Hk technique

The Hk technique is proposed in order to provide an experimental methodology from which measurements in different zones in the continuum region can be obtained. Such measurements can contribute to the explanation of the phenomena exposed in Section 3.2.1 producing phase transitions between determined regions of the spin-energy plane.

The Hk technique aims to reconstruct the (E, I) point from which a cascade was emitted as it is shown in Figure **6-7**. The number of γ-rays emitted by a nucleus when it decays from the continuum region until it reaches its ground state is called the multiplicity of the cascade M. This value can be related with the initial spin of the nucleus I, taking into account the multipolarity character of the radiation emitted. The sum of the energy of the M γ-rays emitted in a cascade is the excitation energy of the nucleus at the begining of the cascade.

$$E = \sum_{i=1}^{M} E_{\gamma i}. \tag{6-8}$$

Experimentally not all of the γ-rays are detected and there is also a probability of not to record the full energy of every γ-ray, which makes that the values (I, E) cannot be experimentally obtained. Nevertheless an aproximation $P(E, I)$ can be produced. If we call h_i the energy registered by a detector and k the number of γ-rays detected of a cascade by the experimental set-up, the value associated with the excitation energy will be in this case

$$H = \sum_{i=1}^{k} h_i. \tag{6-9}$$

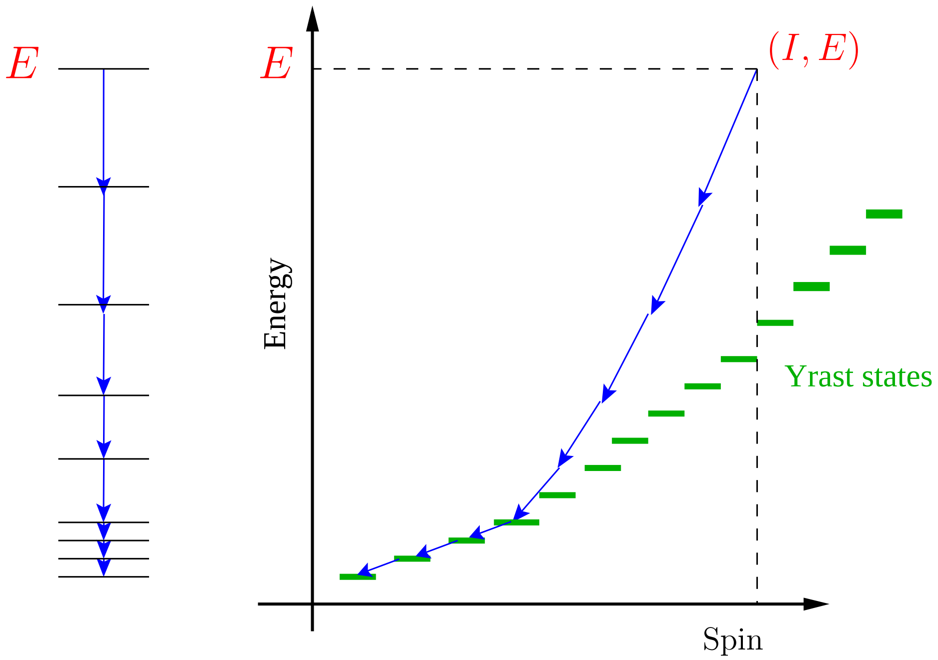

Figure 6-7.: Scheme of a nuclear decay cascade. The blue arrows indicate the transitions and the γ-rays emitted.

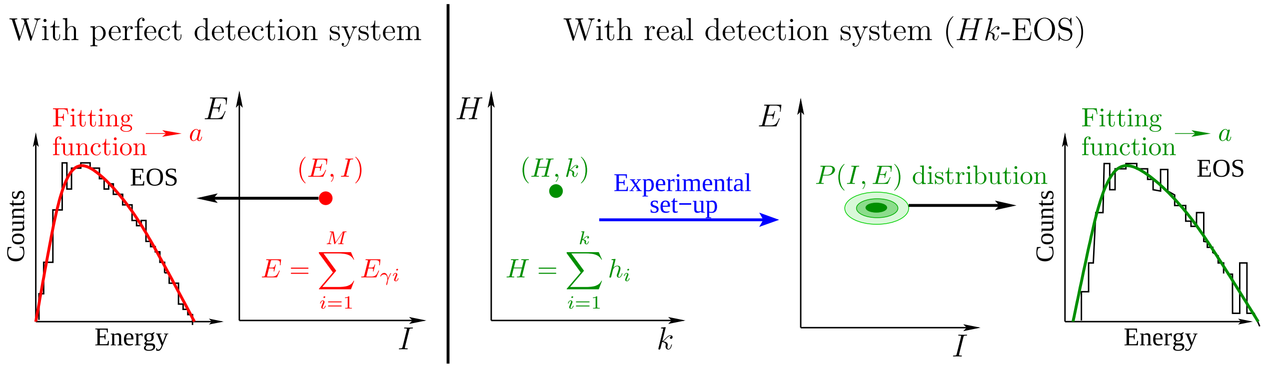

Figure 6-8.: Schematic explanation of the conversion of a Hk point into a EI distribution.

Instead of the (M, E) values what can be obtained in an experiment is a (k, H) point that can be related to a distribution of energy and spin as it is illustrated in Figure **6-8**. The relation between a (k, H) point and the corresponding $P(I, E)$ distribution depends on the experimental array used [38]. With the Hk technique we can achieve a probabilistic reconstruction of the region in the spin energy plane from wich a cascade was emitted. The construction of the EOS spectra by using the γ-rays emited from a specific region allow us to study physical properties of the nucleus (like the level density parameter a) in different regions of the spin energy plane. Figure **6-8** shows schematically the general procedure to obtain the level density parameter, a by using the Hk-EOS technique. If it would be possible to isolate the radiation coming from an specific point (E_b, I_b) as shown in Figure **6-9**, the excitation energy could also be extracted from the EOS spectrum.

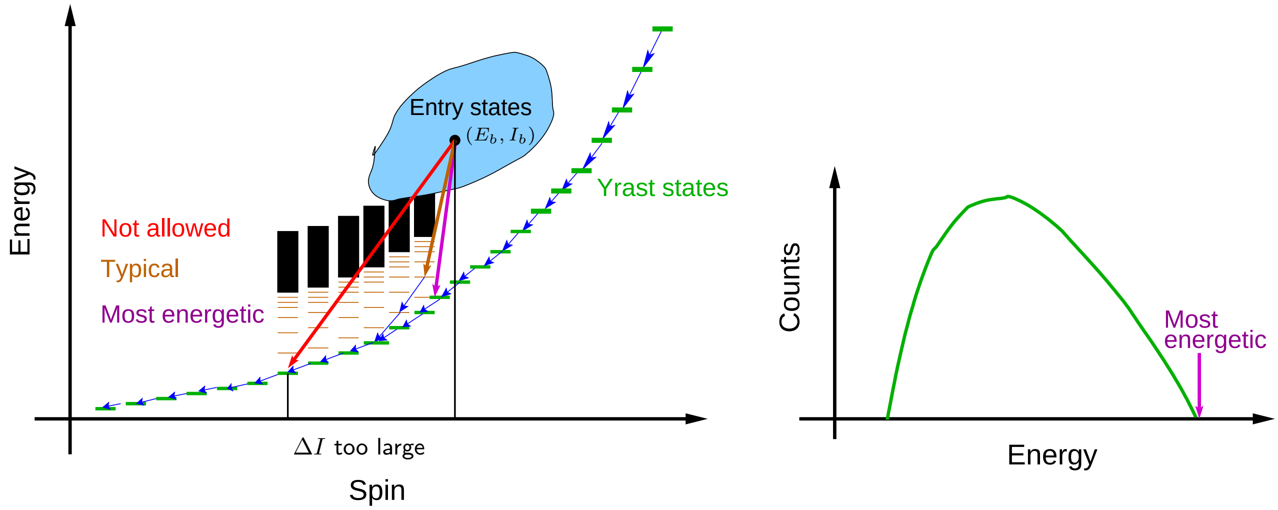

Figure 6-9.: Decay scheme from the entry states in a I-E (spin-energy) plane, showing the most energetic transition possible for a given state (E_b, I_b).

At this point we have shown that the level density parameter can be obtained from a fit of the simulated γ decay of the nucleus (Section 6.3). However the experimental details involved in obtaining the EOS spectrum need to be simulated in order to propose an experiment. The experimental set-up used to apply the Hk technique should satisfy the following properties:

- To cover a solid angle as close as possible to 4π in order to try to detect most of the γ-rays emitted in a cascade.
- To have a good detection efficiency at energies higher than 2 MeV. As it is shown in Figure **6-6** the EOS spectra constructed from cascade starting in the continuum region are composed for γ-rays of energies $\gtrsim 2$ MeV.
- To have good granularity or segmentation of the γ-rays in order to increase the probability to detect each γ-ray in a cascade with a different detector.

6.5. The simulated geometry for the PARIS array

The features of the proposed experimental array PARIS look promising for the requirements of the Hk technique stated above. As it was stated in Section 4.3 the complete array will be composed of 18 clusters of 9 phoswhich detectors as the ones shown in Figure **6-10**. The geometry of PARIS as it was built in the GEANT4 simulations in this thesis starting from the initial tool [57] is shown in Figure **6-10**.

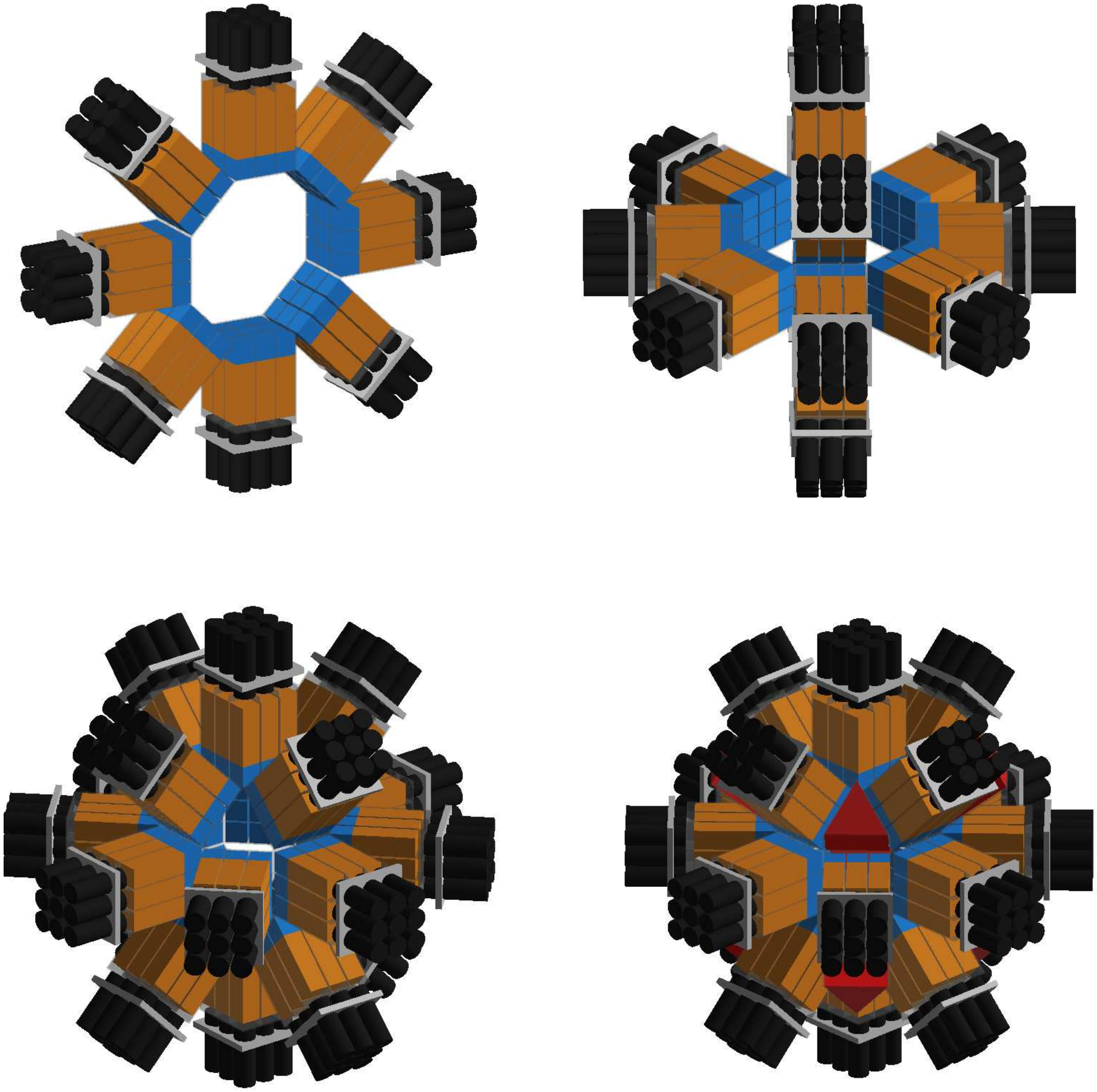

Figure 6-10.: Decomposition of the geometry of the PARIS array composed by 3 rings orthogonally placed, each one composed by 8 clusters. The remaining holes in the geometry with 3 rings were filled with the red triangle shape NaI detectors for simulation purposes. However this last detectors have not been planed to be build under the PARIS proposals. Instead one single phoswhich is planed to be located.

6.6. Combined triggering efficiency

The efficiency of the array is defined as

$$\text{Efficiency}(\,\%) = \frac{\#\text{ of }\gamma\text{-rays emitted}}{\#\text{ of }\gamma\text{-rays detected in the photopeak}} \times 100\,\% \qquad (6\text{-}10)$$

The typical efficiency determined and reported to characterize an experimental array is what it will be called here as the "singles efficiency". It is the efficiency produced by counting the detection of the energy deposited in each of the detectors recording data independently in every event. On the other hand all of the energy detected within the time window of an event by the entire array can be added up and with this energy a new efficiency can be determined. This efficiency will be called here the "combined triggering efficiency". The aim to determine such an efficiency is to determine the capabilities of the array to reconstruct the initial energy as it was depicted in the Figure **6-7**. To understand the need of the later efficiency consider the case when a γ-ray scatters by Compton interaction in one of the detectors and afterwards it is absorbed by photoelectric effect in another detector. If these two energies are added up, the energy will be registered as one count in the photopeak. On the other hand if those two energies are treated independently, ("singles efficiency") the energy detected will be lower than the initial energy of the γ-ray.

In the time window defining one event a cascade of γ-rays are emitted as it was illustrated in Figure **6-7**. In order to reconstruct the initial energy value the combined triggering efficiency needs to be evaluated.

In Section 7.8 the results of the numerical simulations aimed to test the PARIS array for the implementation of the Hk technique will be discussed.

7. Results and analysis

7.1. Reduced transition probabilities ($B(E2)$ W.u.)

Figure **7-1** shows the level lifetimes determined in this work together with the $B(E2)$ values calculated within the Weisskopf model using the Equation (2-27). From Figure **7-1** it can be seen that the level lifetimes for the $(-,+)$ band do not follow the general tendency of positive parity bands which show a clear tendency to decrease when increasing the rotational frequency $\hbar\omega$. Level lifetimes are not in itself a quantity describing the collectivity of the transitions or the shape of the nucleus. To extract better physical information from the lifetimes measurements, models should be applied as the Weisskopf model used here. From Figure **7-1** it can be seen that the $B(E2)$ values for the $(+,+),(+,-)$ and $(-,+)$ bands are around 80 W.u. indicating transitions of high collectivity. This result matches with the interpretation of rotational behaviour for the excited states analized here. At $\hbar\omega \sim 0.6$ there is a sudden change in the level lifetime of the $(-,+)$ band and this change is reflected also in $B(E2)$ indicating a reduction in the collectivity of the transitions. A more detailed study on the physics of this phenomenon will be presented in the next sections.

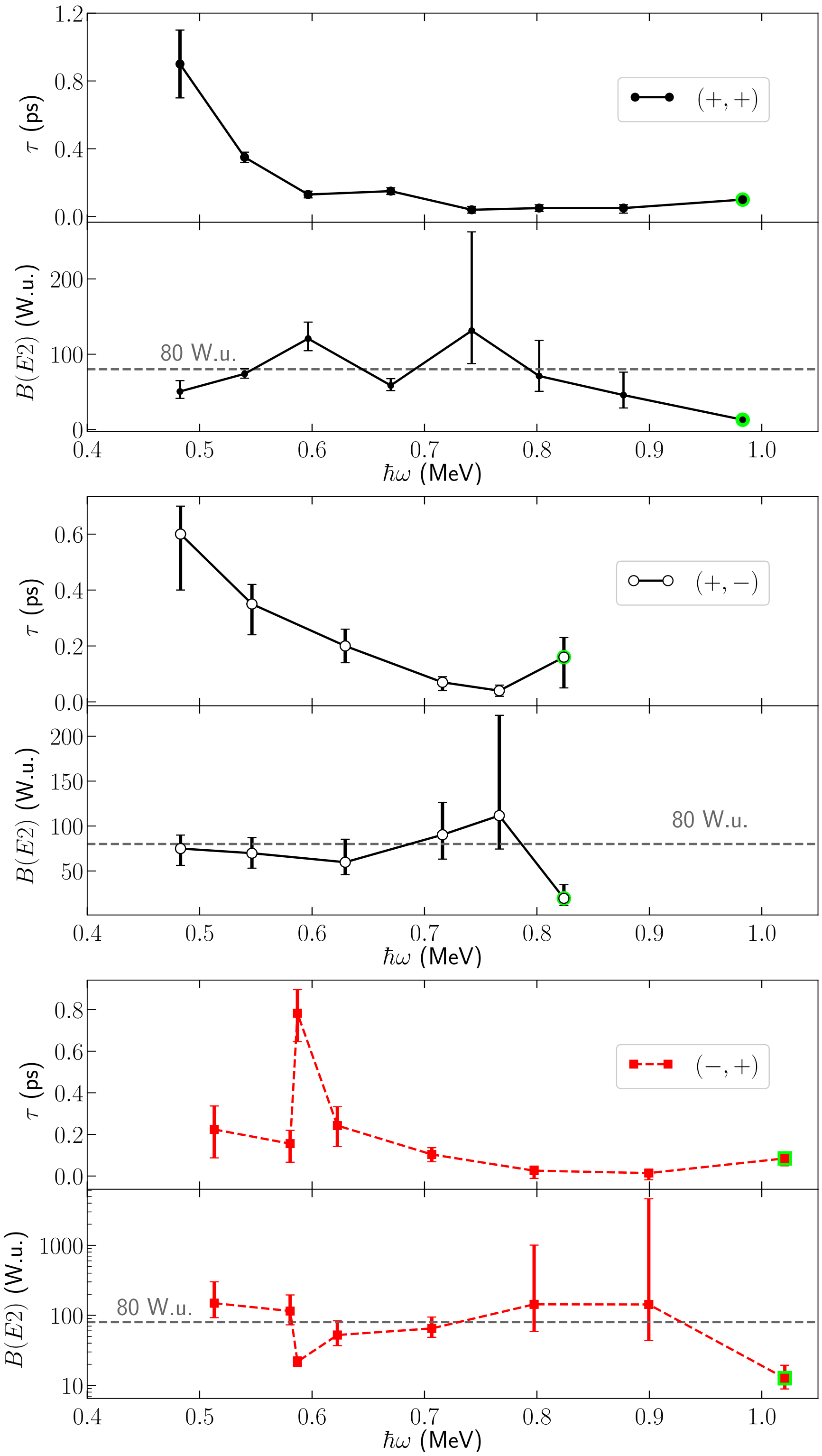

Figure 7-1.: Level lifetimes τ and reduced transition probabilities $B(E2)$ for the $(+,+), (+,-)$ and $(-,+)$ bands, calculated using the lifetimes measured in this work through the Equation (2-27). The light green circle in the lifetimes measurements corresponds to effective lifetime and thus a higher limit for the value of τ. For the $B(E2)$ figures, the light green circle represents the lower limit.

7.2. Quadrupole moments

Q_t can be calculated by means of the Equation (2-25) of Section 2.10

$$|Q_t| = \sqrt{\frac{16\pi}{5}} \frac{\sqrt{B(E2)}}{|\langle I, K; 20|I-2, K\rangle|}, \tag{7-1}$$

where K is the component of the nuclear spin along the rotation axis and I is the spin of the initial state of the transition. Following Eqs. (2-24), (2-25) the $|Q_t|$ values were calculated and the results are shown in Table **7-1**. The $|Q_t|$ values determined in this work are shown in Fig. **7-2** together with the previously reported values. For the $(+,+)$ band the values for the $I \geq 37/2$ states are in agreement with the values reported in Ref. [6]. The previously reported values for transitions of lower spin states of this band differs from our measurements possibly due to the fact that the methodology applied in Refs. [4,6] to determine the lifetimes did not make use of the GFA technique producing the possibility of getting imprecise values of lifetimes determined using the correlation method only. For the $(+,-)$ band the values reported in [6] are all in agreement with values reported here. All of the $|Q_t|$ values reported here for the $(-,+)$ band, and shown in Fig. **7-2**(c), were measured for the first time with the data analyzed in this work. Notice that the smallest value of $|Q_t|$ is found for the state at $(33/2)^-$ of the $(-,+)$ band. In Section 7.5 a discussion on this $|Q_t|$ value will be made and in Section 7.6 comparison with theoretical calculations will be made for all of the measured $|Q_t|$ values.

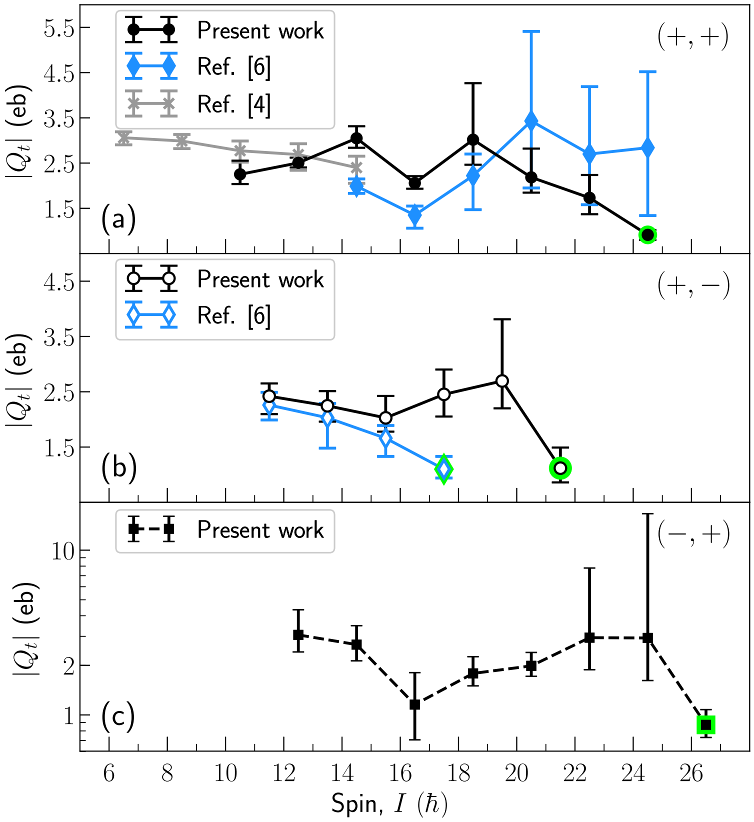

Figure 7-2.: Transition quadrupole moments determined from the lifetime measurements performed in this work together with previously reported values. The light green circle indicates a lower limit for the quadrupole moment that was calculated using the effective lifetime.

Table 7-1.: Level energies E_x, spin and parities I^π, transition energies E_γ, reduced transition probabilities $B(E2)$, trasition electric quadrupole moments $|Q_t|$, and quadrupole deformation β_2 (assuming $\gamma = 0°$ or $\gamma = -60°$) for three normally deformed bands of ^{83}Y.

E_x (keV)	I^π ($\hbar$)	E_γ (keV)	$B(E2)$ (W.u.)	$\lvert Q_t\rvert$ (eb)	β_2
$(+,+)$ band					
12792	$(49/2^+)$	1966	13^{+3}_{-3} [a]	$0.9^{+0.1}_{-0.1}$ [b]	$0.08^{+0.01}_{-0.01}$ [b]
10826	$45/2^+$	1754	46^{+30}_{-17}	$1.7^{+0.5}_{-0.4}$	$0.15^{+0.05}_{-0.04}$
9072	$41/2^+$	1604	71^{+47}_{-20}	$2.2^{+0.6}_{-0.3}$	$0.19^{+0.07}_{-0.03}$
7468	$37/2^+$	1485	131^{+126}_{-44}	$3.0^{+0.1}_{-0.6}$	$0.27^{+0.13}_{-0.06}$
5984	$33/2^+$	1340	59^{+9}_{-7}	$2.1^{+0.2}_{-0.1}$	$0.21^{+0.02}_{-0.01}$
4644	$29/2^+$	1193	121^{+22}_{-16}	$3.1^{+0.3}_{-0.2}$	$0.31^{+0.03}_{-0.02}$
3451	$25/2^+$	1080	74^{+7}_{-6}	$2.5^{+0.1}_{-0.1}$	$0.26^{+0.01}_{-0.01}$
2371	$21/2^+$	965	50^{+14}_{-9}	$2.3^{+0.3}_{-0.2}$	$0.23^{+0.02}_{-0.03}$
$(+,-)$ band					
10360	$(43/2^+)$	1648	20^{+15}_{-8} [b]	$1.1^{+0.4}_{-0.3}$ [b]	$0.11^{+0.04}_{-0.03}$ [b]
8712	$(39/2^+)$	1534	112^{+105}_{-37}	$2.7^{+1.1}_{-0.5}$	$0.28^{+0.11}_{-0.05}$
7179	$(35/2^+)$	1431	90^{+36}_{-27}	$2.5^{+0.5}_{-0.4}$	$0.25^{+0.05}_{-0.04}$
5747	$(31/2^+)$	1259	60^{+26}_{-14}	$2.0^{+0.4}_{-0.3}$	$0.21^{+0.04}_{-0.03}$
4488	$27/2^+$	1092	70^{+17}_{-17} [b]	$2.2^{-0.3}_{+0.3}$ [c]	$0.23^{+0.03}_{-0.03}$ [c]
3395	$23/2^+$	967	75^{+15}_{-19} [c]	$2.4^{+0.2}_{-0.3}$ [c]	$0.25^{+0.02}_{-0.03}$ [c]
$(-,+)$ band					
14796	$(53/2^+)$	2041	13^{+7}_{-4} [b]	$0.9^{+0.2}_{-0.1}$ [b]	$0.09^{+0.02}_{-0.01}$ [b]
12728	$(49/2^+)$	1799	143^{+4473}_{-99}	$2.9^{+14.0}_{-1.3}$	$0.30^{+1.41}_{-0.13}$
10929	$(45/2^+)$	1595	144^{+862}_{-85}	$2.9^{+4.9}_{-1.1}$	$0.30^{+0.49}_{-0.13}$
9334	$(41/2^+)$	1413	65^{+30}_{-16} [c]	$2.0^{+0.4}_{-0.3}$ [c]	$0.20^{+0.04}_{-0.03}$ [c]
7921	$(37/2^+)$	1245	52^{+31}_{-15} [c]	$1.8^{+0.5}_{-0.3}$ [c]	$0.18^{+0.05}_{-0.03}$ [c]
6676	$(33/2^+)$	1174	22^{+4}_{-3} [c]	$1.2^{+0.7}_{-0.5}$ [c]	$0.12^{+0.01}_{-0.01}$ [c]
5502	$(29/2^+)$	1162	115^{+80}_{-42}	$2.7^{+0.8}_{-0.5}$	$0.28^{+0.08}_{-0.06}$
4341	$(25/2^+)$	1026	149^{+152}_{-56}	$3.1^{+1.3}_{-0.6}$	$0.31^{+0.13}_{-0.07}$

---

[a] Values calculated using the effective lifetime and thus only providing a lower limit of the value.

[b] Lifetime was determined by gating from below only.

7.3. Quadrupole deformation β_2

As it was stated at the end of Section 2.5 the quadrupole deformation β_2, and the transition quadrupole moment Q_t are related and the mathematical [71] expression is

$$Q_t = \frac{6ZeA^{2/3}}{(15\pi)^{1/2}} r_0^2 \beta_2 (1 + 0.16\beta_2)\cos(30^\circ + \gamma). \tag{7-2}$$

For $\beta_2 \sim 0.3$, the term $0.16\beta_2$ takes values ~ 0.05 which implies a contribution to Q_t smaller than the values of the experimental uncertainties. Therefore Eq. (7-2) can be simplified for this case as

$$|Q_t| = \frac{6ZeA^{2/3}}{(15\pi)^{1/2}} r_0^2 |\beta_2| \cos(30^\circ + \gamma), \tag{7-3}$$

where it was also taken into account that only the absolute value of β_2 can be calculated since from the experimental values we can only determine the absolute value of the quadrupole moments. Note that since $-120^\circ \leq \gamma \leq 60^\circ$ the cosine in Equation (7-3) will be always positive. In Eqs. (7-2), (7-3) $\gamma = 0^\circ$ and $\gamma = -60^\circ$ represent the maximum collectivity for a prolate shape ($\gamma = 0^\circ$) and an oblate shape ($\gamma = -60^\circ$). As reference values to calculate $|\beta_2|$ we take $\gamma = 0^\circ$ or $\gamma = -60^\circ$, both producing the same results in Eq. (7-3). The values of $|\beta_2|$ found are reported in Table **7-1** where it can be seen that $0.18 \lesssim |\beta_2| \lesssim 0.31$ which corresponds to normally deformed band values.

The functional behavior with $\hbar\omega$ of the $|\beta_2|$ parameter are the same as the ones for $|Q|$ and $B(E2)$ as these quantities are proportional. Therefore we are interested now in the values themselves more than in the functional dependence. From Figure **7-3** it can be seen that for all of the bands $|\beta_2| \sim 0.25$.

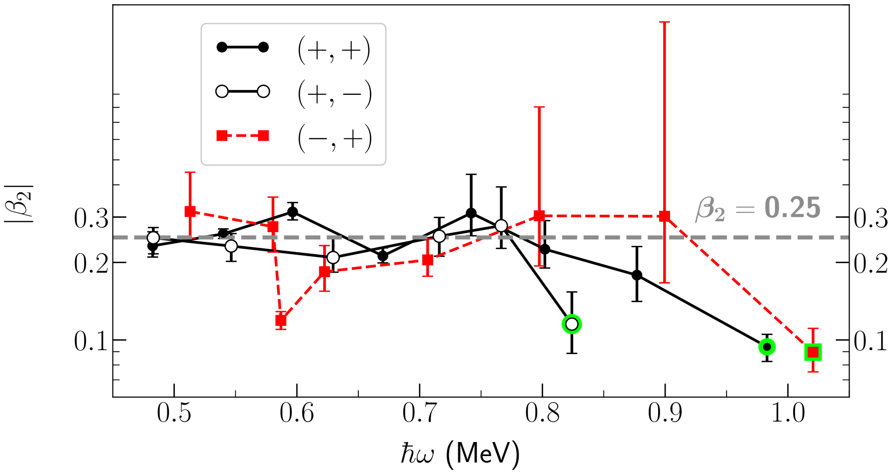

Figure 7-3.: Absolute value of the deformation parameter, $|\beta_2|$, deduced for the rotational bands $(+,+)$, $(+,-)$ and $(-,+)$.

7.4. Rotating liquid drop reference

The rotating liquid drop reference energy E_{rld}(def) can be calculated as it was exposed in Section 2.13. E_{rld}(def) can be subtracted from the energy of the excited states to examine the relative variations of the energy levels of different bands of ^{83}Y. Equation (2-37) is useful because allows us to calculate the deviations of the rigid rotor behavior that are exhibited by each band. Figure **7-4**(a) shows the excitation energy as a function of the spin for the bands studied in this work. However no significant differences can be inferred from such plot. By substracting the energy of the rotating liquid drop reference, the differences between the configurations of different bands can be visualized as it is shown in the Figure **7-4**(b).

In Figure **7-4** positive and negative parity states are drawn by full and dashed lines, respectively. Closed (open) symbols are used for signature $\alpha = 1/2$ ($\alpha = -1/2$). This notation is adopted for all of the figures.

Figures **7-4**(a,b) show that at low spins the energy relationship $E_{(+,+)} < E_{(+,-)} < E_{(-,+)} < E_{(-,-)}$ stands, which means that the positive signature and positive parity are both favoured in energy. The subsequent swaps from the initial energy relationship when increasing the spin will be examined. Swaps on this relationship occur for the negative parity bands which can be barely noticed in Fig. **7-4**(a). Fig. **7-4**(b) shows these swaps more clearly.

The term "signature inversion" will be used to indicate the case when the corresponding energy value of the curve of the signature which is generally not favoured in energy decreases its energy to a value lower than the one for the curve of the unfavoured signature. Signature inversion occurs for the negative parity bands at spins $I \approx 9$ and the initial relation is recovered at $I \approx 18$. The negative parity $(-,+)$ band swaps in energy with the positive parity band $(+,+)$ at $I \approx 24$. This swap is manifested also in the energy levels as a function

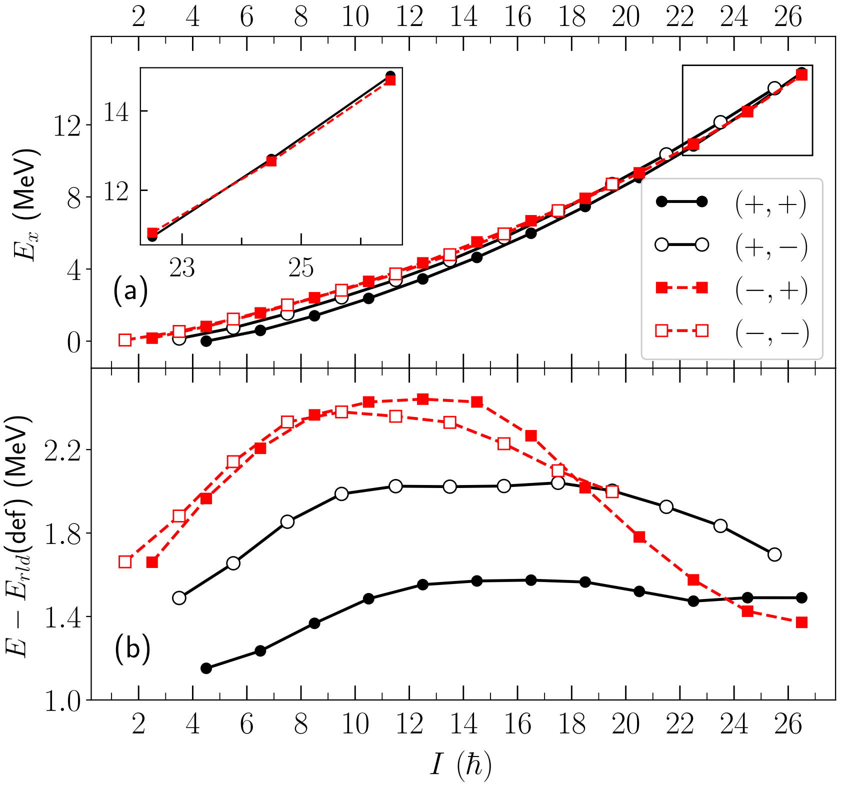

Figure 7-4.: (a) Energy as function of the spin I of the rotational bands $(+,+)$, $(+,-)$, $(-,+)$ and $(-,-)$. The rectangle in the top panel emphasizes the region in which the yrast band swaps from $(+,+)$ to $(-,+)$ band. (b) Energy after subtracting the rotating liquid drop reference energy. In all figures, positive and negative parity states are drawn by full and dashed lines, respectively. Closed (open) symbols are used for signature $\alpha = 1/2$ ($\alpha = -1/2$).

of the spin (Fig. **7-4**(a)), showing that at high spin states the yrast states belong to the $(-,+)$ band. The later meaning, that none of the single bands drawn in Fig. **5-1** can be referred individually as the yrast band. The relatively large energy reduction that undergoes the $(-,+)$ band from $I = 14.5$ to cross and become more favoured in energy than the $(+,+)$ band (Fig. **7-5**(a)) and its relationship with the $|Q_t|$ values, moment of inertia and quasiparticle alignments will be analyzed in Section 7.5.3. Similar but less dramatic behavior is exhibited for the $(-,-)$ band whose energy starts to decrease from $\hbar\omega \approx 0.54$ MeV to take a value which is lower than the one for the $(+,-)$ band at $\hbar\omega \approx 0.7$ MeV.

7.5. Cranked shell model analysis

7.5.1. Comparisons with neighboring nuclei

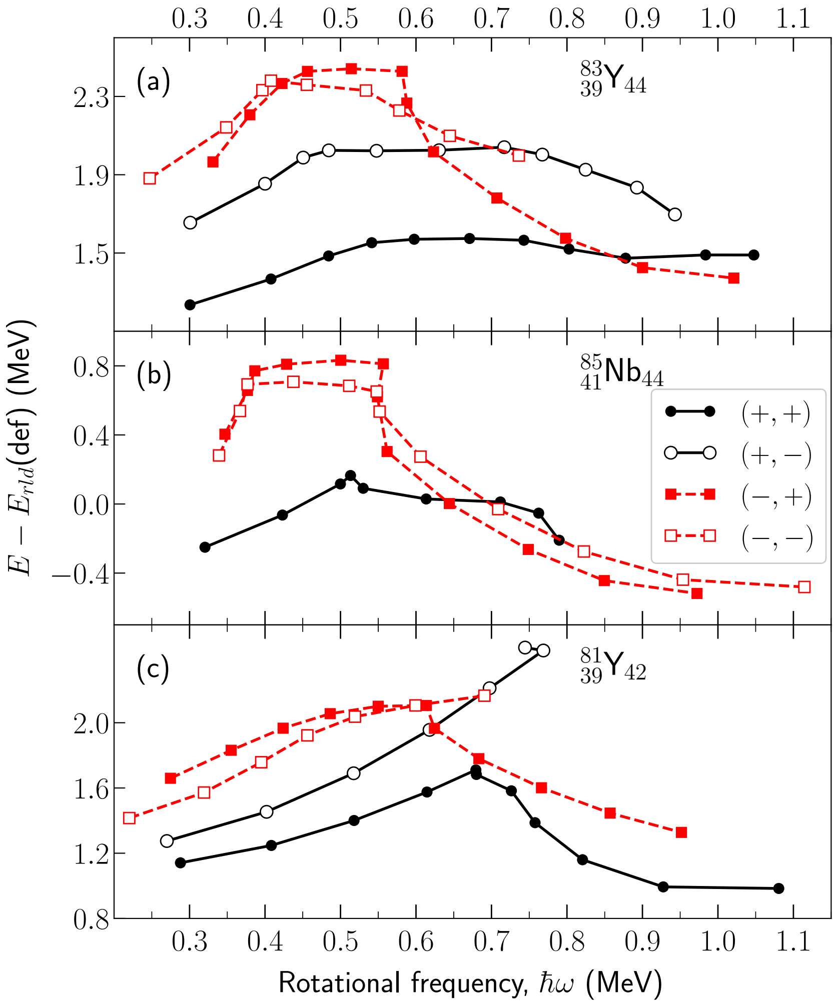

Figure 7-5.: Energy after subtracting the rotating liquid drop reference energy as a function of rotational frequency. (a) normally deformed bands of ^{83}Y. (b) Similar to (a) but for ^{85}Nb. (c) ^{81}Y. (b) and (c) were produced with data from Refs. [72] and [73].

A comparison of the $E - E_{rld}$(def) quantity with the odd-Z even-N neighboring nuclei was performed. Among these nuclei $^{81}_{37}$Rb$_{44}$ presents two backbendings in the negative parity bands both at $\hbar\omega \approx 0.42$ MeV (see Refs. [74, 75]) which makes this nucleus not suitable for the comparison with $^{83}_{39}$Y$_{44}$ in the $E - E_{rld}$(def) quantity. Data for other bands than $(+,+)$ in $^{85}_{39}$Y$_{46}$ is not available. For $^{85}_{41}$Nb$_{44}$ and $^{81}_{39}$Y$_{42}$ the $E - E_{rld}$(def) quantity is shown in Figures **7-5**(b,c) where the data to produce the plots were taken from Refs. [72] and [73] respectively. The curves of ^{85}Nb present similar behavior to the curves of ^{83}Y in Fig. **7-5**. Signature inversion in the negative parity bands is present for both ^{85}Nb and ^{83}Y as it can be seen from Figures **7-5**(a,b). Likewise both nuclei present a remarkable change in the curve of the $(-,+)$ band after the second band crossings at $\hbar\omega \approx 0.58$ and 0.56 MeV for ^{83}Y and ^{85}Nb respectively. Since the curves of $^{85}_{41}\text{Nb}_{44}$ resemble the ones of $^{83}_{39}\text{Y}_{44}$ it would be interesting to compare also with the $^{87}_{43}\text{Tc}_{44}$ isotone. However only three transitions of the $(+,+)$ band have been reported for ^{87}Tc. Different from ^{85}Nb and ^{83}Y the curves for ^{81}Y do not present signature inversion. Nonetheless the remarkable change in the $(-,+)$ band curve after the second band crossing at $\hbar\omega \approx 0.62$ MeV appears in ^{81}Y as well. Thus it is interesting to compare the quadrupole moments of the $(-,+)$ band for ^{81}Y and ^{83}Y which are shown in Fig. **7-6**. No comparison with ^{85}Nb $(-,+)$ band was possible since no quadrupole moments have been reported. At spin $I = 33/2$ a decrease in $|Q_t|$ was found for the $(-,+)$ band of ^{83}Y. This spin coincides with the second band crossing. For ^{81}Y this lowering in $|Q_t|$ seems to appear as well. However the $|Q_t|$ uncertainty does not allow to confirm this tendency that however cannot be ruled out. In Section 7.6 theoretical calculations of several quantities including $E - E_{rld}(\text{def})$ will be compared with the experimental values.

The evolution of measured $|Q_t|$ with the rotational frequency will be compared with the evolution of other physical quantities in Secs. 7.5.3 and 7.5.4.

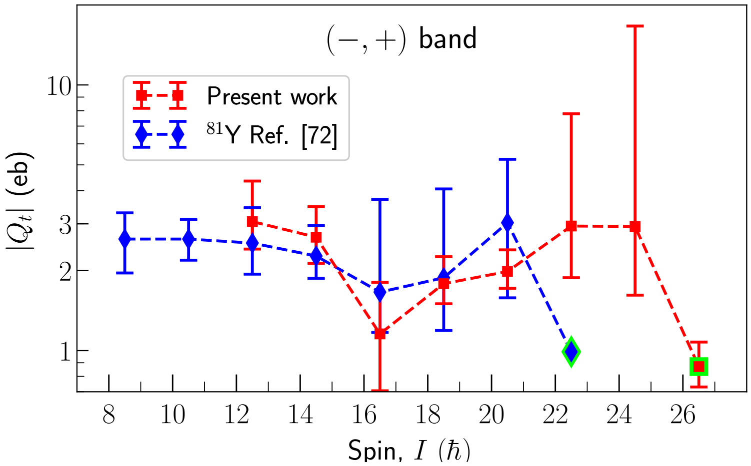

Figure 7-6.: Transition quadrupole moments determined for $(-,+)$ bands of ^{81}Y [73] and ^{83}Y determined in this work.

7.5.2. Quasiparticle routhians $e(\omega)$

As it was stated in Section 2.12.1 the parametrization of the moment of inertia of the ^{82}Sr nucleus will provide the reference from which the quasiparticle routhians $e(\omega)$ and alignments $i(\omega)$ of the ^{83}Y nucleus can be obtained. By using Equation (2-33) to fit the functional behavior of $\mathcal{J}^{(1)}$ before the first band crossing at $\hbar\omega \approx 0.53$ MeV. The parameters obtained are

$$(\mathcal{J}_0, \mathcal{J}_1, \mathrm{i}) = (23\ \hbar^2/\mathrm{MeV}, 0, -5\ \hbar). \tag{7-4}$$

The parameters in Equation (7-4) were used in Equations (2-32) and (2-34) to obtain the energy and angular momentum of the ground configuration of ^{82}Sr allowing to obtain $e(\omega)$ and $i(\omega)$ from Equations (2-30) and (2-31). Fig. **7-7** shows $e(\omega)$ as a function of $\hbar\omega$ for the bands analyzed here. At low spins the relationship $e_{(+,+)} < e_{(+,-)} < e_{(-,+)} < e_{(-,-)}$ stands. Such relationship is the same as the one found for $E - E_{rld}(\mathrm{def})$ in Fig **7-5**(a). Now the swaps in this inequality when increasing rotational frequency $\hbar\omega$ will be examined. For convinience the word "inversion" will be used when a swap from the initial relationship occurs and the word "recovery" will be used when the initial relationship is recovered. Fig. **7-7** emphasizes the swaps exhibited from the initial relationship present at low spins.

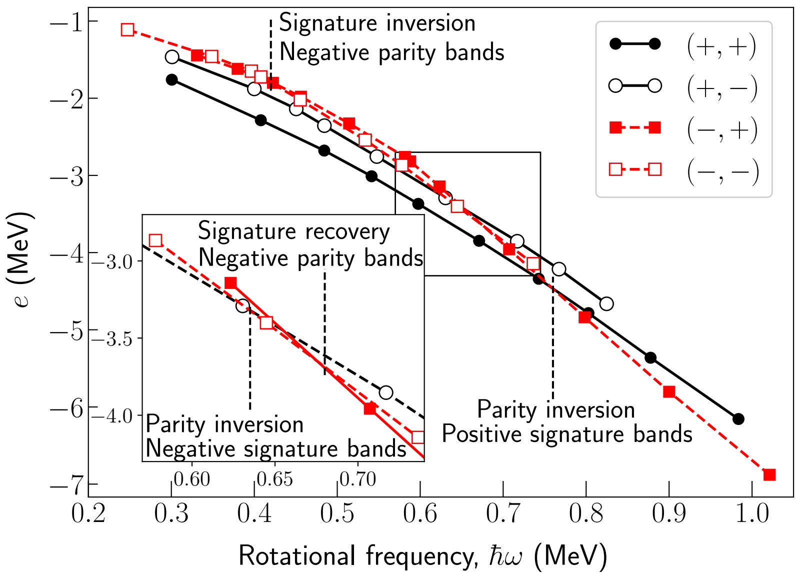

Figure 7-7.: Experimental routhinas in normally deformed bands of ^{83}Y. The deviations of the initial relationship $e_{(+,+)} < e_{(+,-)} < e_{(-,+)} < e_{(-,-)}$ are pointed out. The square box indicates the zoomed area.

For the negative parity bands at $0.42 \leq \hbar\omega \leq 0.67$ MeV signature inversion occurs. This signature inversion was already discussed in Ref. [58]. The same swaps or inversions of the initial relationship that were found for $E - E_{rld}(\mathrm{def})$ are found now for $e(\omega)$ as well. The later could mean that the origin of the swaps in $E - E_{rld}(\mathrm{def})$ lie in the quasiparticle routhians.

Notice that there is a relatively strong downward bend of the $(-,+)$ curve at $\hbar\omega \approx 0.58$ MeV which corresponds to the second band crossing. Similar behavior is present in the $(-,-)$ curve of Fig.**7-7** showing a downward bend at $\hbar\omega \approx 0.40$ MeV which corresponds to the second band crossing. This particular behavior after the second crossing of the negative parity bands appears at the same frequency $\hbar\omega \approx 0.58$ MeV for which the $|Q_t|$ takes its lowest value among all of the states studied in this work. However, as it was stated in Section 5.5 for the $(-,-)$, it was not possible to measure any lifetime and therefore no $|Q_t|$ values are available.

7.5.3. Negative parity bands

Fig. **7-8** shows $|Q_t|$, the kinetic and dynamic moments of inertia $\mathcal{J}^{(1)}$ and $\mathcal{J}^{(2)}$, the quasiparticle alignment $i(\omega)$ and the relative energy to the rotating liquid drop reference $E - E_{rld}(\mathrm{def})$ as a function of the rotational frequency $\hbar\omega$.

Fig. **7-8**(a) shows that the quadrupole moments for the $(-,+)$ band remain approximately constant for the entire range of rotational frequencies measured, except at $\hbar\omega \sim 0.58$ where the second band crossing appears. This band crossing is causing the sharpest and the largest effect on the quasiparticle alignment (increment of $\sim 3\ \hbar$) and the kinetic moment of inertia. The most notable change after this band crossing at $\hbar\omega > 0.58$ MeV is revealed by the $E - E_{rld}(\mathrm{def})$ quantity which starts to decrease significantly up to values even lower than those of the $(+,+)$ band (see Fig. **7-5**(a) and the discussion of Section 7.4) at frequencies of ~ 0.95 MeV.

Fig. **7-8**(b) shows two peaks in $\mathcal{J}^{(2)}$ for each band demonstrating the presence of the band crossings. For the $(-,+)$ band, calculations in Ref. [58] associate the first crossing at $\hbar\omega \approx 0.45$ MeV with protonic character. In Ref. [6] the proton alignment for the first crossing was also adopted. Since two consecutive decouplings of protons pairs is unlikely, the second crossing at $\hbar\omega \approx 0.58$ MeV was associated with the $\nu(g_{9/2})^2$ alignment scenario in Refs. [6, 58]. In Section 7.6.2 new calculations resulting in opposite conclusions to the ones in Refs. [6, 58] will be discussed.

The kinetic moments of inertia, $\mathcal{J}^{(1)}$, in the region $A \sim 80$ converge to values between 20 and 25 $\hbar^2$/MeV [18], regardless of whether they are even-even, odd-even or odd-odd nuclei. The moment of inertia of the even-even nuclei increases with rotational frequency whereas that of odd-odd nuclei decreases. On the other hand odd-even nuclei show an intermediate behavior. Values shown in Figures **7-8**(c) and **7-9**(c) are in agreement with this systematics.

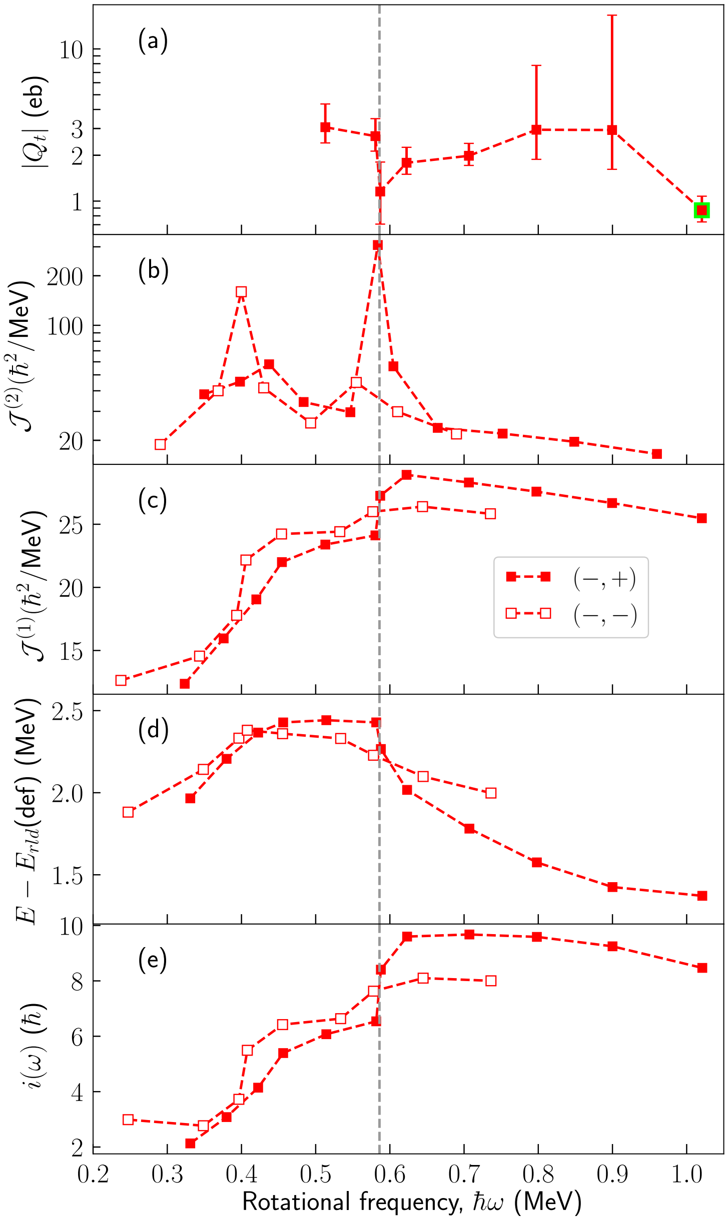

Figure 7-8.: Physical quantities describing the behaviour of the ^{83}Y nucleus in its discrete states for the negative parity bands.

Band termination for the $(-,+)$ band has been suggested in Ref. [6] based in the single particle alignment $i(\omega)$ of this band which starts to decrease at $\hbar\omega \gtrsim 0.8$ MeV. However no level lifetimes were measured before the present work for this band and no quadrupole moment values have been used to support the band termination interpretation. In Section 7.6.4 terminating configurations in the bands analyzed here will be discussed.

7.5.4. Positive parity bands

Fig. **7-9** shows the same physical quantities as in Fig. **7-8** but for the positive parity bands. Fig. **7-9**(b) shows the dynamic moment of inertia where band crossings can be observed. For these band crossings several suggestions have been made. For the $(+,+)$ band the first crossing at $\hbar\omega \approx 0.55$ MeV was associated with the decoupling of a $g_{9/2}$ proton pair in Ref. [3]. Based on calculations and on the systematics, the scenario in which the $\nu(g_{9/2})^2$ alignment occurs first followed by $\pi(g_{9/2})^2$ alignment was the one adopted in Ref. [58] for both $(+,+)$ and $(+,-)$ bands.

Besides presenting the band crossings, Fig. **7-9** also shows that the $(+,+)$ band is the only one for which the quadrupole moments were measured before the first band crossing $\hbar\omega \approx 0.55$ MeV. Notice that this frequency value is the largest among the bands studied here which made possible to obtain measurements of quadrupole moments before the crossing. $|Q_t|$, $\mathcal{J}^{(1)}$, $i(\omega)$ and the $E - E_{rld}(\text{def})$ quantities increase in this region. This makes sense under the interpretation that the configuration before the crossing is just one valence proton. This valence proton being aligned along the rotation axis could be the responsible for increasing both the moment of intertia and the quadrupole moment.

The following are common features found in Figures **7-8** and **7-9**

- In general band crossings which are manifested as peaks in $\mathcal{J}^{(2)}$ (Figures (b)) come with relatively sharp increments of $\mathcal{J}^{(1)}$ and $i(\omega)$ in Figs (c,e) respectively. Being this a general behavior illustrated in this case with the analysis of the ^{83}Y bands. It is thus exemplified that quasiparticle alignment produced in the band crossings is responsible for increments in the moment of inertia.

- The quantities $E - E_{rld}(\text{def})$ of Figures (d) and the kinetic moment of inertia $\mathcal{J}^{(1)}$ in Figures (c) start to saturate right after the first band crossings.

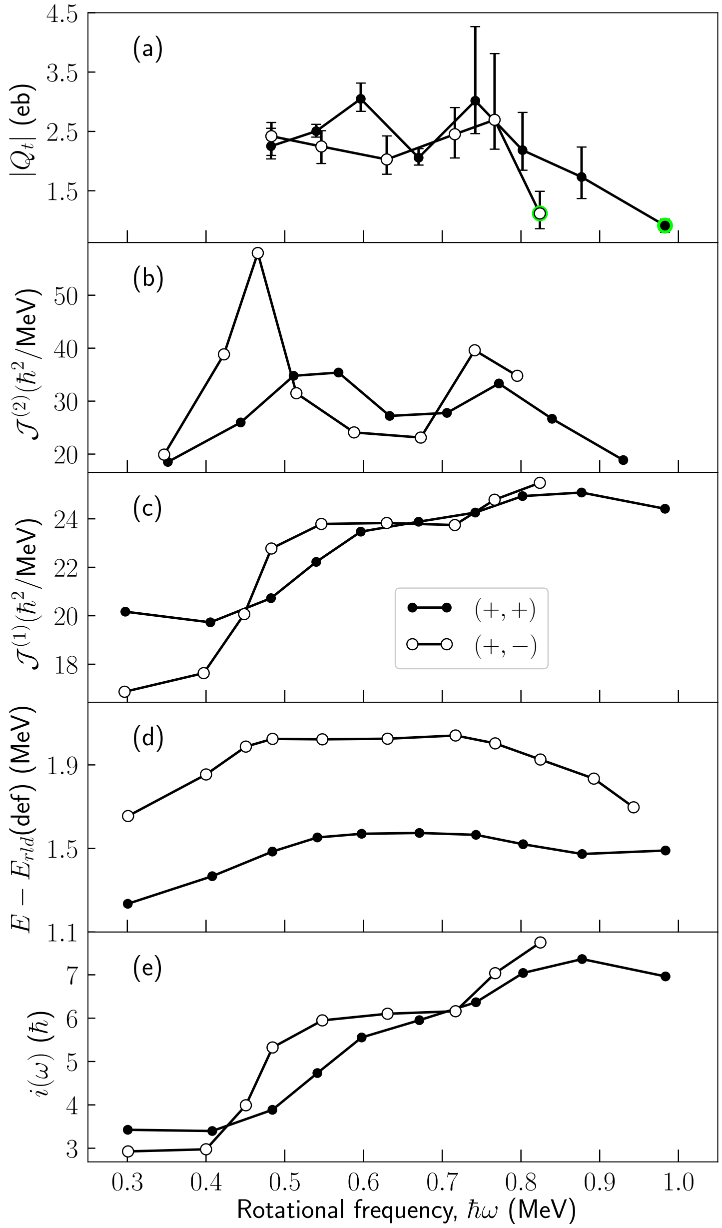

Figure 7-9.: Physical quantities describing the behavior of the ^{83}Y nucleus in its discrete states for the positive parity bands.

7.6. CNS and CNSB calculations

CNS and CNSB calculations described in Section 2.14 were carried out for the ^{83}Y normally deformed bands in the main paper of this thesis [76]. The CNS model used is defined in Refs. [16, 27, 28]. The CNSB model is based on the Ultimate Cranker which was developed by Tord Bengtsson [77]. The formalism in the calculations are defined in Refs. [26, 78]. The

$A = 80$ parameters in Ref. [16] were used. In the CNS formalism the configurations are labelled as $[p_1p_2, n_1n_2]$ or shorter as $[p_2, n_2]$. The number of holes in the $Z = (N =)40$ core are noted as p_1 (n_1) while p_2 (n_2) denotes the number of $g_{9/2}$ protons (neutrons). The signature is specified by subscripts when not equal to zero, which are '+' for $\alpha = 1/2$ and '−' for $\alpha = -1/2$. Since the only quantum numbers preserved in the CNSB formalism are parity and signature for protons and neutrons configurations, thus the configurations are specified as $(\pi_p, \alpha_p)(\pi_n, \alpha_n)$. The Q_t values are calculated from the deformation parameters as defined in Ref. [79] and references therein.

7.6.1. CNS assignments

The experimental energies are drawn relative to the rotating liquid drop reference in Figure **7-10**(a). The resulting energies produced by CNS calculations relative to the same reference are drawn in Figure **7-10**(b). Only the low lying energy configurations within a range of 1 MeV above the yrast band were considered in Figure **7-10**(b). The $[p_2, n_2] = [1, 6]$ band was omitted since for spin values $I \gtrsim 15$ it is outside the 1 MeV energy range. Therefore it is foreseeable that the configurations in Figure **7-10**(b) produce the major contribution to the observed bands.

The reported γ-deformations in Ref. [76] for all the configurations in Figure **7-10**(b) are in the range $[-40°, -60°]$, i.e. close to collective rotation at oblate shape. The ε_2 deformation is in the range $\varepsilon_2 = [0.25, 0.30]$ for low spin values, reaching $\varepsilon_2 \approx 0.15$ at high spin but with no termination in a non-collective state. The single-particle orbitals for protons are drawn for a typical deformation in Figure **7-11**. The proton and neutron orbitals are similar, so, in order to get a general understanding, this diagram can be used also for neutrons. For the case of the 44 neutrons of the ^{83}Y nucleus it can be clearly seen that the configuration with six neutrons in the $g_{9/2}$ shell (noted as $\nu[g_{9/2}]^6$) is the most favoured in terms of energy for the entire rotational frequency range. On the other hand there is a much higher level density around the number 39 corresponding to the proton number of ^{83}Y. Figure **7-11** suggest that the configurations with two or three $g_{9/2}$ protons are favoured at low or intermediate spin and maybe with four $g_{9/2}$ protons at the highest spin values. Thus these configurations are the ones assigned to the observed bands, i.e. $[p_2, n_2] = [3, 6]$ to the positive parity bands and $[p_2, n_2] = [2, 6]$ and $[p_2, n_2] = [4, 6]$ at low and high spin, respectively, for the negative parity bands. With these assignments, experiment and calculations are compared in Figure **7-10**(c). The differences bewteen experimental values and the calculated ones are collected within a range of ±0.5 MeV for which the average difference increases with decreasing spin as expected because of an increasing pairing energy. The fluctuations around the average value should then be understood as coming from different pairing energy in different configurations but certainly also from the general uncertainty in the calculations.

Figure **7-10**(b) shows the calculated energies for the bands having energies lower than

1 MeV above the yrast line. From Figure **7-10**(b) the theoretical band crossings can be identified. Note for example the crossing between the B5,$(-,+)$ bands, labeled as $[3_+2,26]$ and $[5_+4,26]$ at $I \approx 17$. The spin value of this crossing coincides with the second band

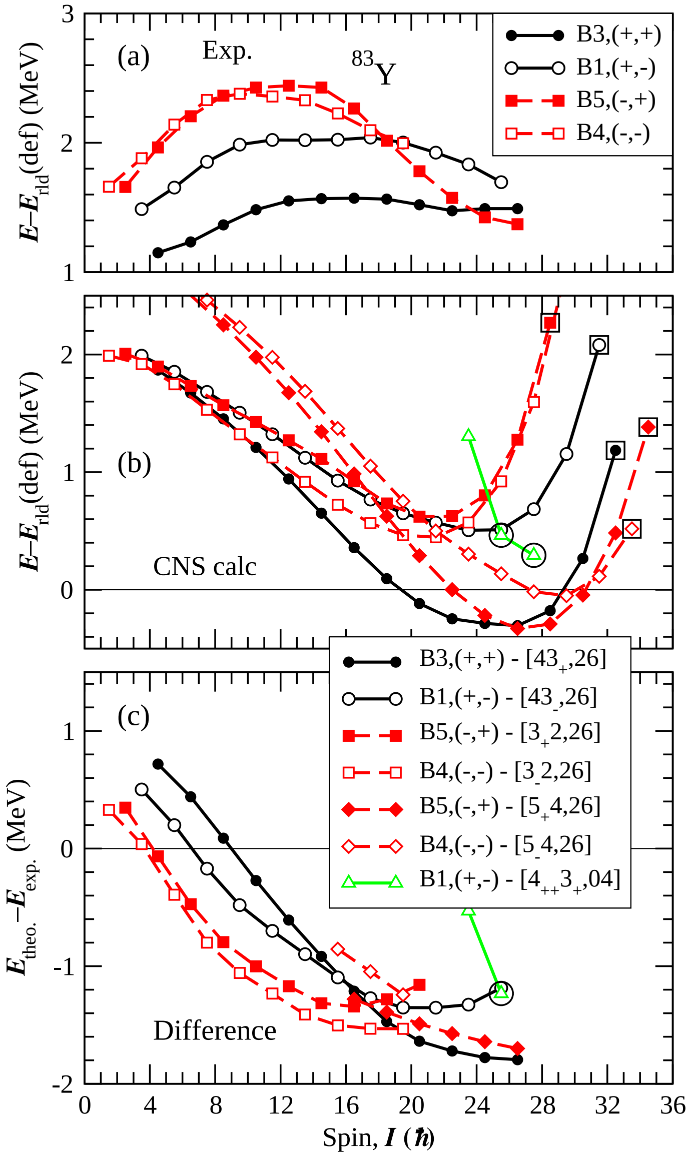

Figure 7-10.: Comparison between experiment and CNS calculations. (a) Observed bands drawn relative to the rotating liquid drop reference. (b) Calculated configurations assigned to the experimental bands. (c) Difference between calculations and experiment. States which are calculated to be fully aligned are encircled while large squares are used for states which have reach the I_{max} value of their configuration, but which are still collective. Figure taken from the main paper of this thesis [76] submitted to Phys. Rev. C.

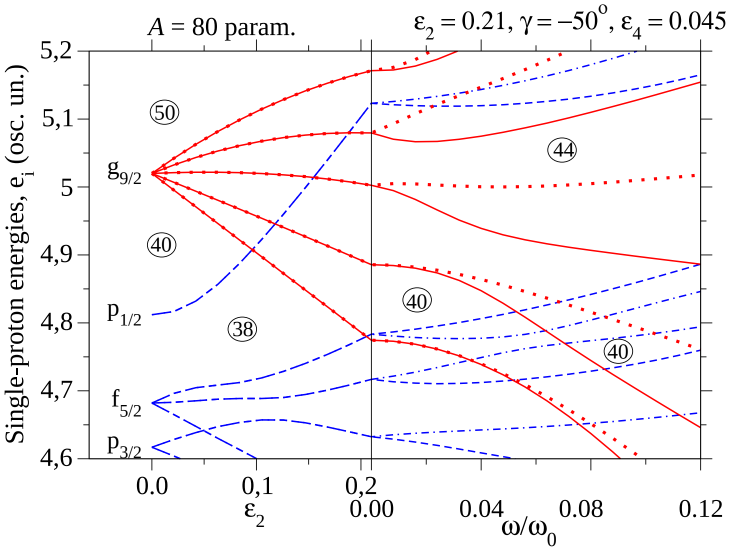

Figure 7-11.: Proton single-particle orbitals for a typical deformation for the configurations assigned to the observed bands in ^{83}Y, $\varepsilon_2 = 0.21$, $\gamma = -50°$, $\varepsilon_4 = 0.045$. In the left part of the diagram, the ε_2 and ε_4 deformations increase linearly up to 0.21 and 0.045, respectively, at a constant value of $\gamma = -50°$, while the single-particle routhians are shown as a function of the rotational frequency at constant deformation in the right part. Figure taken from the main paper of this thesis [76] submitted to Phys. Rev. C.

crossing of the $(-,+)$ band indicated in Figure **7-8** by the vertical dashed line. Figure **7-8**(d) shows a notable energy reduction after this band crossing. Such energy reduction is in agreement with the strong separation that the curves under discussion in Figure **7-10**(b) undergo.

7.6.2. CNSB calculations

The experimental energy values are compared now with CNSB calculations in Figure **7-12**. It can be seen that the agreement between calculations and theory is better than in the CNS case, Figure **7-10**. Figure **7-12**(c) shows that the experiment and theory differences are now approximately constant and not decreasing with spin as it was stated in Section 2.14. The spread of the differences in Figures **7-10** and **7-12** is similar and within a range of ~ 0.5 MeV. This indicates that the particle configurations used in the CNS formalism are approximately valid also for the CNSB formalism. Therefore the positive parity bands can be labelled as $\pi(g_{9/2})^3\nu(g_{9/2})^6$ in their full spin range or possibly as $\pi(g_{9/2})^1\nu(g_{9/2})^6$ at low spin. However, they go through a band-crossing around $I = 11$ ($\hbar\omega = 0.45$ MeV), which shows up in a similar way also in the negative parity bands (see Figures **7-8**(b) and **7-9**(b)). This suggests that the crossing is caused by a similar mechanism for both parities since

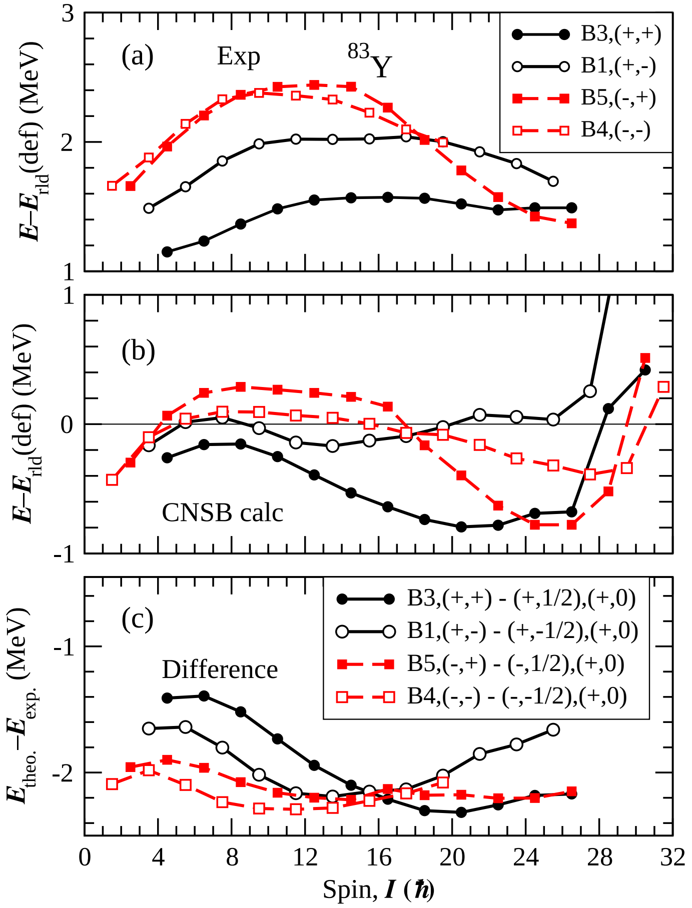

Figure 7-12.: Comparison between experiment and CNSB calculations. Note that only signature and parity for protons and neutrons is specified for the calculated bands contrary to the CNS calculations in Figure **7-10**(b) where the configurations are specified in more detail. Figure taken from the main paper of this thesis [76] submitted to Phys. Rev. C.

the neutron configuration $\nu(g_{9/2})^6$ is common for both parities which is in contrast to the conclusions in Refs. [6, 58].

For the negative parity bands, the second band crossing appears to be produced by the change between the $\pi(g_{9/2})^2$ and $\pi(g_{9/2})^4$ configurations as it is illustrated in the Figure **7-10**(b) and described in the previous section.

The second band crossing of the $(-,+)$ band deserves a more detailed description as it is causing the most notable changes in the nuclear structure of ^{83}Y as discussed in Section 7.5.3. The calculated total energy surfaces (explained in Figure **2-7**) are shown in Figure **7-13** for the states before and after this band crossing. The minima of these figures indicate the predicted ε_2 and γ parameters. It can be seen how the energy surfaces start at low spin with a unique and very well defined minimum at $I = 12.5^-$ that undergo into two minima when

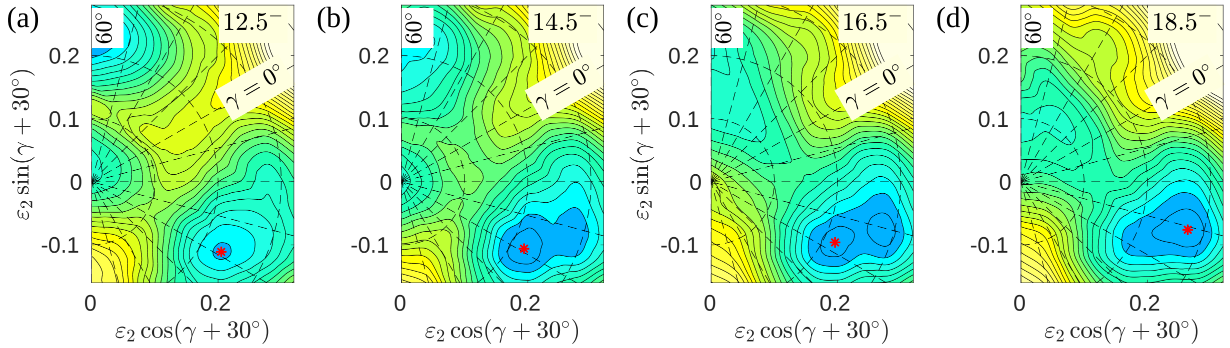

Figure 7-13.: Calculated total energy surfaces for $(-, 1/2)(+, 0)$ configuration in the CNSB formalism illustrating the states before and after the second band crossing. The contour line separation is 0.2 MeV. The general minima are indicated by a red asterisk in each of the figures. Figures taken from the main paper of this thesis [76] submitted to Phys. Rev. C

increasing the spin and to finalize again with a unique minimum but corresponding to a larger ε_2 value and therefore larger deformation.

7.6.3. The transitional quadrupole moment

Figure **7-14** shows the CNSB and CNS calculated energy surfaces for some of the states of the $(+, +)$ band. The figures for both formalisms are very similar resulting in another indication that the configuration labeling produced in the CNS calculations is approximately valid for the CNSB results as well. From the localization of the minimum energy in the energy surfaces the deformation parameters can be obtained for each state and with Equation (7-2) the quadrupole moment can be computed. The minima are located at similar deformation parameters in Figures **7-14**(a) and (b) and thus the resulting $|Q_t|$ values are expected to be likewise similar.

Figure **7-15** shows the comparison of the calculated and measured quadrupole moments. There is in general a good agreement bewteen theory and experiment. Calculated and measured values for the $(+, -)$ band are all of them in agreement within uncertainties. For the $(-, +)$ band it can be seen that the configuration change from $\pi(g_{9/2})^2$ to $\pi(g_{9/2})^4$ produced in the second band crossing is manifested also with an increase of $|Q_t|$. In general, it is expected that at band-crossings and configuration changes, the $B(E2)$ values and thus Q_t should be smaller. It is therefore gratifying that at the configuration change of the $(-, +)$ band at $I \approx 16$, the experimental $|Q_t|$ appears to be particularly small. For $I \lesssim 16$ the calculated values in Figure **7-15**(c) are outside the uncertainties. A possible explanation arises from an eventual shifting of the experimental value for $I = 16.5$ produced by the value of the lifetime obtained by gating from below only. Since the value of the lifetime of every state depends on

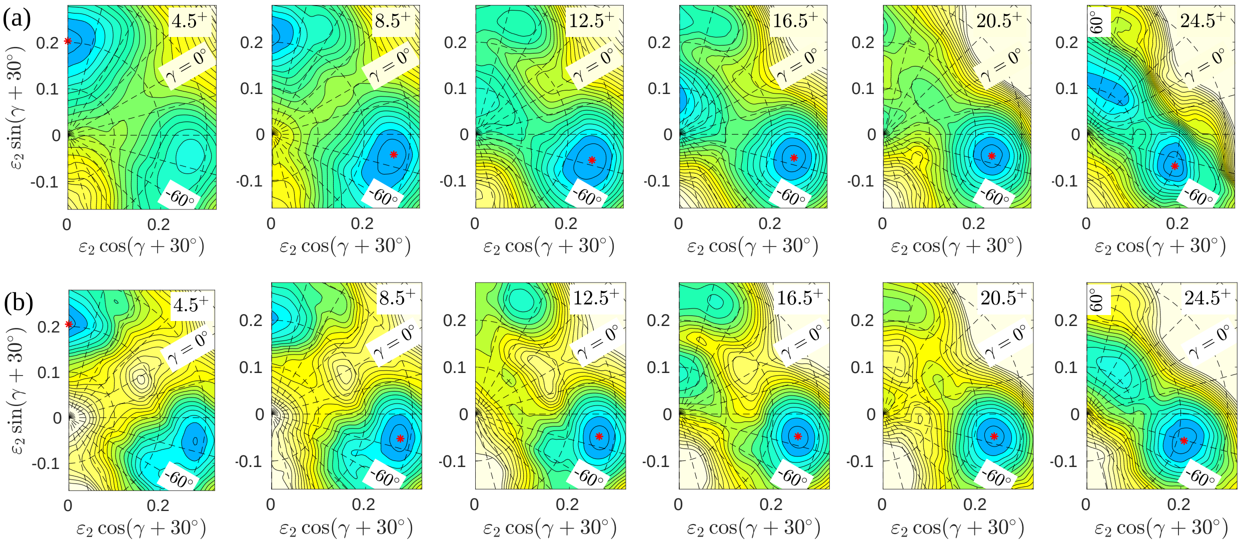

Figure 7-14.: Calculated total energy surfaces for $(+, 1/2)(+, 0)$ configurations. The contour line separation is 0.2 MeV. (a) energy surfaces calculated in the CNSB formalism, i.e. with pairing included. (b) energy surfaces calculated in the CNS formalism, i.e. with no pairing energy. The general minima are indicated by a red asterisk in each of the figures. Figure taken from the main paper of this thesis [76] submitted to Phys. Rev. C.

the lifetimes measured for higher spin states, thus the values for the states 12.5^-, 14.5^- could be impacted as a result of a possible non-valid correlation induced in the determination of a lifetime at higher spin. Another posibility is a mixing of non-collective states with the collective states considered with the CNS and CNSB models. Non collective excitations could produce states at energy values that result competitive when compared with the energy of the collective states. If that is the case, a mixing with non-collective states that was not considered in the calculations could explain the discrepancy for the values at $I < 16.5$ in the $(-, +)$ band. The latter can also be the case of the 14.5^+ $|Q_t|$ value in Figure **7-15**(a).

The fact that the calculated values with and without pairing come close together is another indication that the wave-functions are rather similar and thus that the more detailed configuration labelling used in the CNS calculations is approximately valid also in the CNSB calculations.

7.6.4. Band termination discussion

Band termination phenomena was briefly described in Section 2.6. Here the discussion on the normally deformed bands of ^{83}Y will be made. It was concluded in Ref. [6] that the observed $(+, +)$ band is not terminating in a non-collective state. Indeed all of the bands which are drawn in Figure **7-10**(a) are not terminating in a non-collective state. The spin in these

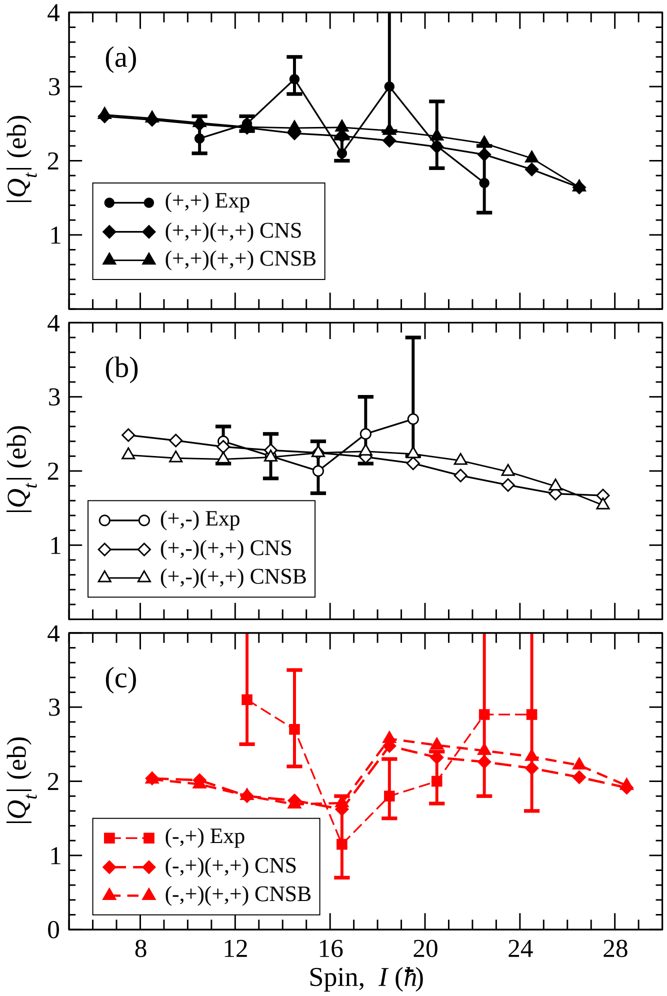

Figure 7-15.: Comparison between observed $|Q_t|$ values and values obtained from calculated deformations along the collective trajectories in calculations including (CNSB) and neglecting (CNS) pairing correlations. Figure taken from the main paper of this thesis [76] submitted to Phys. Rev. C

configurations is limited with a value of I_{max} which is not much larger than presently observed highest spin values. This appears consistent also with the present measurements of Q_t. In fact, the collective configurations show some very interesting features when they approach their I_{max} values. Thus, as seen in Figure **7-10**(b), the energies of these configurations are calculated to increase strongly when they approach I_{max}, where the $E - E_{rld}$ curves resemble e.g, the curves of the smooth terminating bands in the $A = 110$ region [16]. Furthermore, such an energy increase has been observed experimentally in the neighbour nucleus ^{84}Zr where the ground band has been identified [80] to the maximum spin, $I = 34$, of the configuration which is assigned [80] to this band, [4, 6]. Note especially that the strong increase of the $E - E_{rld}$ was predicted, before it was observed, see e.g. Figure 12 of Ref. [80]. A closer study of these configurations show that they remain collective when they reach their I_{max} values, i.e. they can be described as nonterminating bands [25]. The configurations of the different configurations are drawn to their I_{max} values in Figure **7-10**(b). At present the band B3 has been observed three transitions short of its maximum spin and the other bands are even further away from termination. B3 is built in the configuration

$$\pi[(pf)^{-5}_{6.5}(g_{9/2})^{4}_{12}]_{18.5}\nu[(pf)^{-2}_{4}(g_{9/2})^{6}_{12}]_{16} \qquad (7\text{-}5)$$

which is defined relative to a ^{80}Zr core and where the subscripts represent the maximum spin within the configurations, i.e. $I_{max} = 18.5 + 16 = 34.5$. As discussed in Ref. [25] it should in principle be possible to observe even the $I_{max} + 2$ state but it will lie very high above yrast. Thus, in Figure **7-10**(b), these bands have not been followed beyond their I_{max} values.

7.7. Sidefeeding times

^{32}S + ^{58}Ni at 135 MeV → ^{90}Ru → ^{83}Y + α +3p			
Statistical decay	GDR parameters		Quantities describing collective transitions in the continuum
$B(M1)_{Stat.} = 0.01$ W.u.	$E_{G1} = 20.8$	$E_{G2} = 16.4$	$\beta_2 = 0.25$
$B(E2)_{Stat.} = 1$ W.u.	$\Gamma_{G1} = 2.8$	$\Gamma_{G2} = 4.7$	$\mathcal{J}^{(1)} = 24.4\ \hbar^2/\text{MeV}$
	$\omega_1 = 0.3$	$\omega_2 = 0.7$	$B(E2) = 10, 40, 80$ W.u.
			$i(\omega) = 7.5, 2.5, 0.5\ \hbar$
Energy lost inside target = 8 MeV		Pairing energy $\Delta = 1.5$ MeV	

Table 7-2.: GAMMAPACE input parameters used to simulate the side feeding times.

The values obtained for the sidefeeding times, τ_{SF}, shown in Table **5-6** vary from around 0.01 ps at high spins up to values close to 1 ps at low spins, are similar to values found for ^{84}Zr using the same reaction as in the experiment analyzed in this work [80]. These values are also similar to the values found for ^{82}Sr measured in the reaction ^{56}Fe(^{29}Si,2pn)^{82}Sr at 95 MeV [81].

To try to get an insight of the physics in the continuum the sidefeeding times were simulated by using the GAMMAPACE code [65]. The γ-ray transition probabilities are calculated from the product of the level density formula given in Ref. [68] with the γ-ray strengths. The input parameters given in Table **7-2** were used in GAMMAPACE for the simulation of the side-feeding times. Statistical $M1$ and $E2$ transitions are considered with reduced transition probabilities $B(M1)_{stat.}$ and $B(E2)_{stat.}$. $E1$ statistical transitions are considered as Giant Dipole Resonance transitions GDR with parameters calculated using the parameterization given in Ref. [70] which depends on the mass number A and the quadrupole deformation parameter β_2. In Gammapace every point of the spin-energy plane has the possibility to be a member of a collective band in the continuum region. In the decay of these collective states the spread of the transition energies due to the rotational damping [69] was also considered. The sidefeeding times are generated as the effective lifetime resulting from the decay chain feeding the state under study. The energy lost in the target was calculated using the SRIM code [60] and the pairing energy was computed from the difference between the binding energy of ^{83}Y and the average binding energy of the $A-1$ and $A+1$ neighboring nuclei.

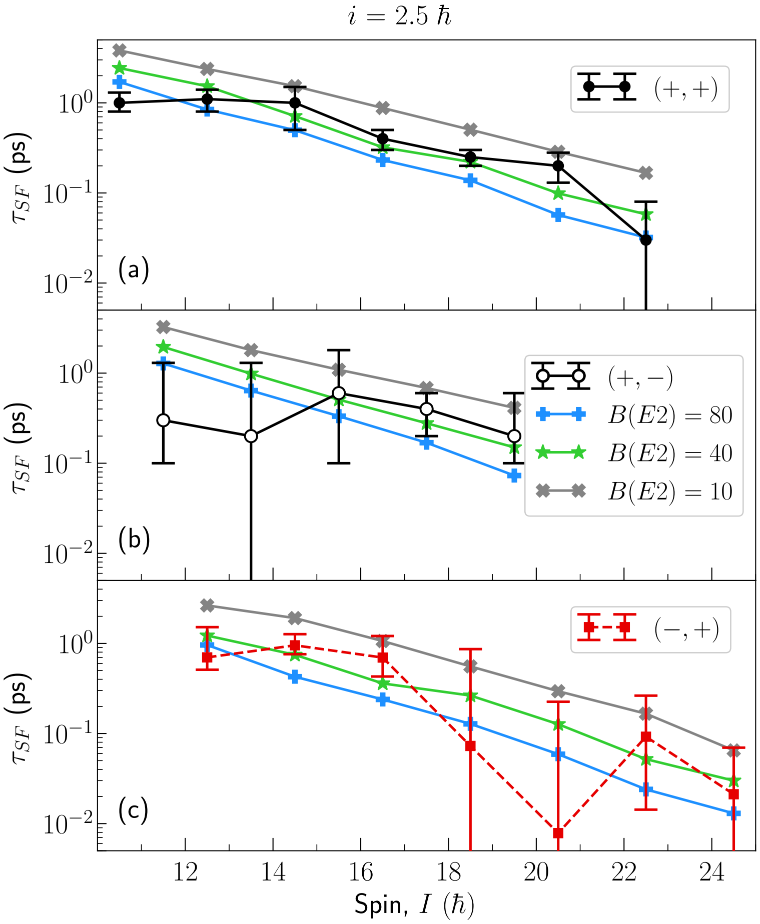

Figure 7-16.: Measured sidefeeding times together with the values produced by simulations carried out using the Gammapace code and asuming different vaues of the collective decay $B(E2)$ (in W. u.) while fixing $i = 2.5\ \hbar$. It can be seen that the $B(E2) = 80$ W.u. curves are the ones best following the experimental data for the three bands plotted.

The properties of the collective transitions coming from the continuum depend on several parameters. The $\mathcal{J}^{(1)}$ value used in the Gammapace simulation corresponds to the rigid rotor value to which all the discrete bands tend to converge. This value is related wtih the quadrupole deformation of the nucleus β_2 and these two variables were fixed to the values given in Table **7-2** that were extracted from the experimental data obtained for

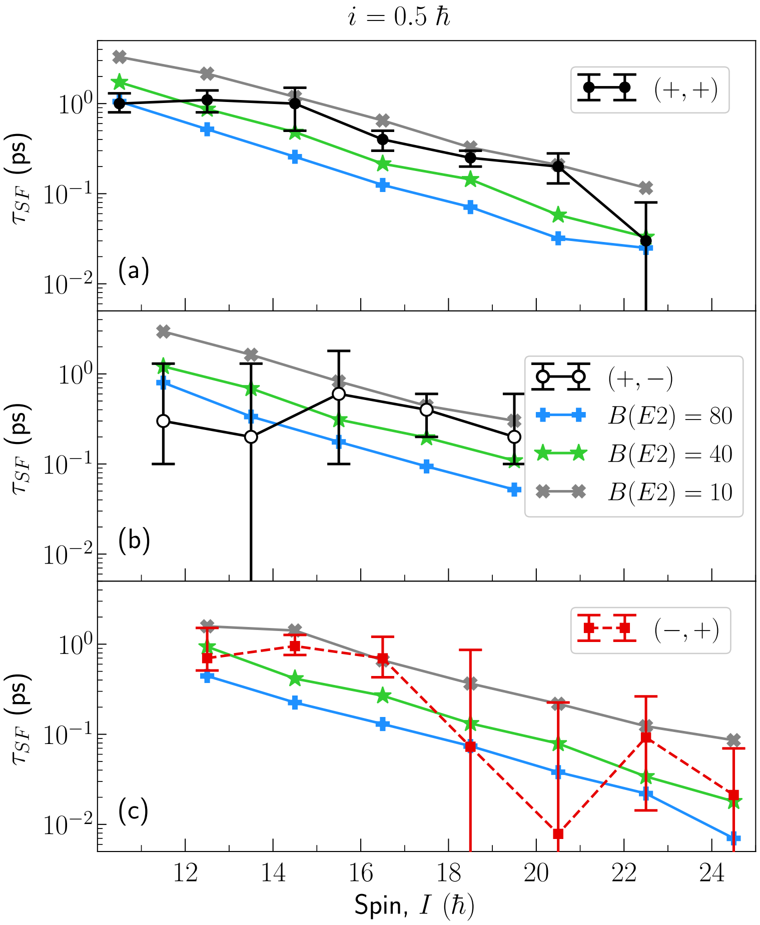

Figure 7-17.: Measured sidefeeding times together with the values produced by simulations carried out using the GAMMAPACE code and asuming different vaues of the collective decay $B(E2)$ (in W. u.) while fixing $i = 0.5\ \hbar$. It can be seen that the $B(E2) = 40$ W.u. curves are the ones best following the experimental data for the three bands plotted.

the discrete states. On the other hand there is no argument for fixing the single particle alignment i and the degree of collectivity of the transitions in the continuum. Therefore the different values of $B(E2)$ and i given in Table **7-2** were used for the simulations of the side feeding times. The simulated curves that best follow the experimental values are shown in Figs. **7-16** and **7-17** from which it can be seen that the higher the collectivity the lower the sidefeeding times, in agreement wtih the Equation (2-24) which is used in GAMMAPACE code. Note also that the larger the single particle the larger the sidefeeding times. Note also that the general tendency of the τ_{SF} values to increase when decreasing the spin is followed by both the simulated values and the experimental ones, considering the uncertainties. This tendency can be explained since the quasicontinuum states have similar properties to discrete states of similar spin. Among them the lifetimes of quasicontinuum states increase with decreasing the spin. Therefore lower the spin of a discrete state the more

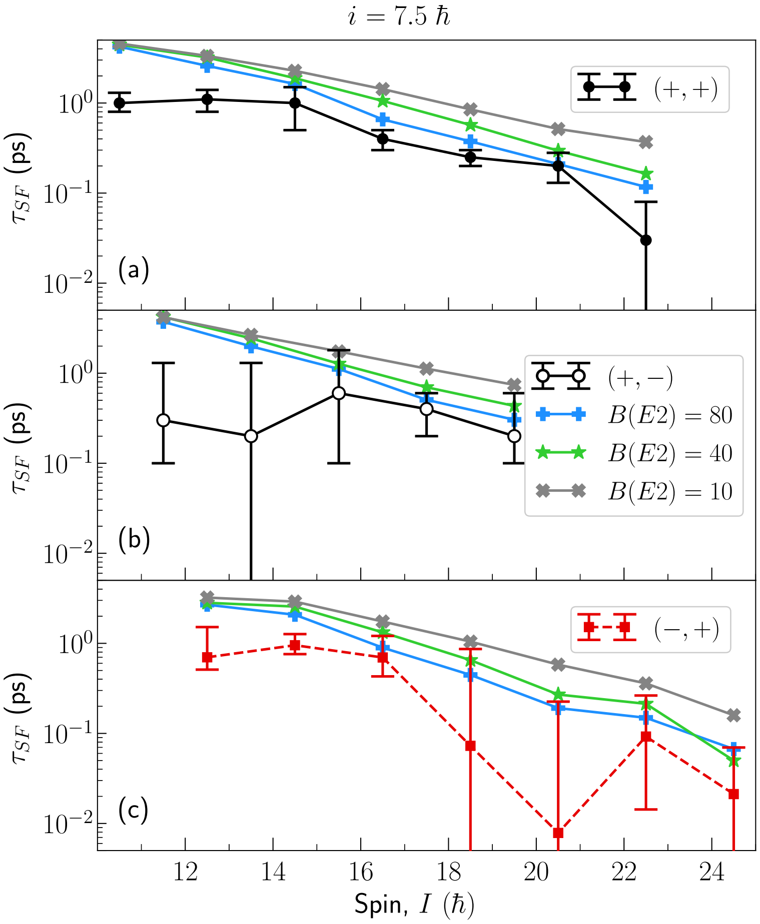

Figure 7-18.: Measured sidefeeding times together with the values produced by simulations carried out using the Gammapace code and asuming different vaues of the collective decay $B(E2)$ (in W. u.) while fixing $i = 7.5\ \hbar$. It can be seen that the $B(E2) = 40$ W.u. curves are the ones best following the experimental data for the three bands plotted. It can be seen that none of the simulated values reproduce the experimental ones.

low spin values in the quasicontinuum contribute to their sidefeeding times increasing the resulting sidefeeding time value.

From the simulated values, two sets were found to follow the experimental data similarly well for all of the three bands analized here. These values are shown in Table **7-3**. Two

Set	$B(E2)$ (W.u.)	i ($\hbar$)	Fig.
1	80 - 40	2.5	**7-16**
2	40	0.5	**7-17**

Table 7-3.: Gammapace input parameters that best reproduce the experimental sidefeeding times.

conditions were examined for assigning the values of Table **7-3**. 1) The curves for a given $B(E2)$ value follow the experimental data for all of the three bands analized. See for instance the curves in Fig. **7-17** with $B(E2) = 80$ W.u. which show larger distance than in Fig. **7-16** from the experimental data for the $(+,+)$ and $(+,-)$ bands, although for the $(+,-)$ band seems to be a good approximation to the experimental data. 2) The simulated curves follow the experimental tendency all along the spin range. The later was not the case for the $B(E2) = 10$ W.u. curves which include the simulated points with the largest disagreement with the experiment. Such points appear at low spin values for which the simulation resulted in values up to 4 times larger than the experimental ones for the $(+,+)$ and the $(+,-)$ bands. From Table **7-3** it can be said that either medium to high collective states with a medium single particle alignment or medium collective states with no single particle alignment are the physical scenarios for which the collective transitions from the c ontinuum best reproduces the experimental data. It is important to notice that values different to the ones reported in Table **7-3** can be ruled out since they do not reproduce the experimental values. The satisfactory results of the simulation using the values given in Table **7-3** confirm that the values that were fixed in Table **7-2** were adequate. The agreement of experimental data with simulations shows that the theory used in the Ref. [65] is consistent with the experimental results.

It is important to point out that this study does not represent a definitive description of the states coming from the continuum region, it provides an insight of the physics of the nucleus in the continuum. Nevertheless further experimental and theoretical studies are required to understand the behavior of the nuclei in the continuum region.

7.8. Testing the PARIS array for the implementation of the Hk technique

The capability for the reconstruction of the total energy H in Equation (6-9) was tested by GEANT4 numerical simulations for the PARIS array with the geometry described in Section 6.5. The singles and combined triggering efficiencies defined in Section 6.6 were determined by simulating γ-rays of different energies emitted at the center of the array. The singles efficiency was determined by considering every phoswhich as one single detetector adding the energies detected by the $LaBr_3$ stage and the NaI stage of each phoswhich. The results obtained are shown in Figure **7-19**. The higher the energy the larger the relative increase of the efficiency produced with the combined triggering compared with the singles case. The result is coherent with the fact that low energy γ-rays have a larger photoelectric cross section than larger energy γ-rays. This produces that the ratio between photoelectric and Compton counts is larger at low energies.

Figure **7-20** shows the simulated singles and combined triggering spectra. It can be seen

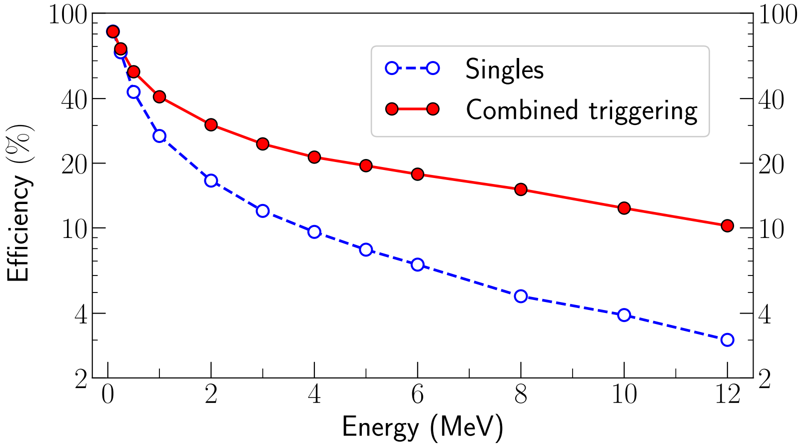

Figure 7-19.: Efficiencies for the PARIS array determined by means of Monte Carlo simulations.

that some of the counts in the Compton region become counts in the photopeak when going from the singles to the combined triggering spetrum. The higher the energy the larger this effect as it can be noted from the comparisons of the two Figures **7-20**.

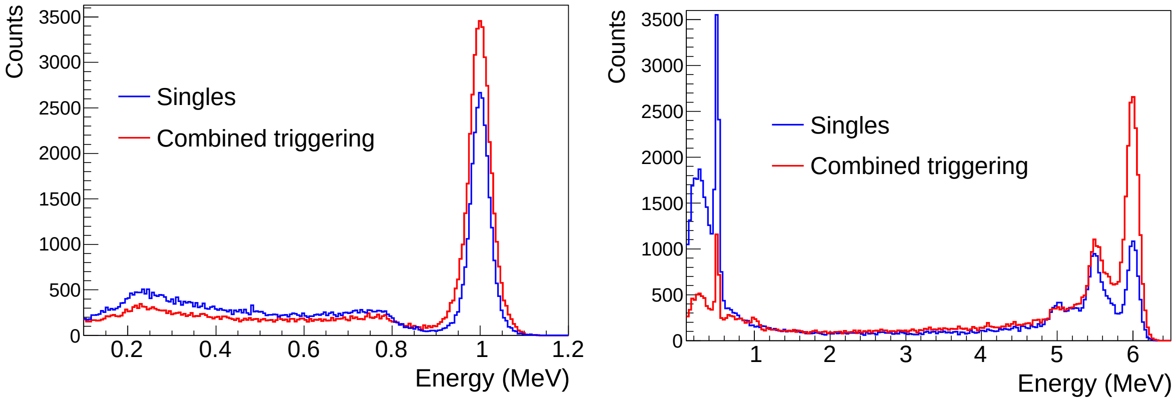

Figure 7-20.: Simulated singles and combined triggering spectra for the detection of 1 and 6 MeV γ-rays.

The combined triggering efficiency of Figure **7-19** is too low for the reconstruction of the total energy. It was previously shown [38] that the resulting (M, E) distribution after applying the Hk technique to the GASP array in the so-called configuration I [55] has a standard deviation in the energy distribution of 3 MeV. Figure **7-21** shows the comparison of the efficiencies of the GASP and PARIS arrays. It is shown that the GASP array is up to ~ 8 times more efficient than PARIS. With such a big difference the reconstructed energy distribution will not allow to distinguish different regions in the spin energy plane making the simulated geometry for PARIS not suitable for the implementation of the Hk

technique. There are two main reasons that explain this difference. 1) The geometry of the GASP array have a spherical shape in which for every radial trajectory starting from the center of the array there is a detector material of approximately the same thickness. On the other hand it is not possible to build a similar geometry by using only cubic clusters and phoswich detectors as in the case of the PARIS array. 2) GASP is composed mainly of BGO detectors which are ~ 5 times more efficient than NaI and $LaBr_3$ detectors that were used in PARIS. Therefore the GASP detectors do not need to have a large thickness to produce a high detection efficiency for high energy γ-rays. The GASP array was disassembled some years ago whereas PARIS seemed promising for the application of the Hk technique because of the length of the detectors and because its design is specifically intended for having a high detection efficiency for high energy γ-rays. It was only after completing and running the simulation of PARIS that the result could be produced.

It is concluded that spherical shell geometries covering a large percentage of 4π with a high granularity distribution are the only ones suitable for the application of the Hk technique. The use of BGO detectors is also adviced otherwise the thickness of the detectors should be ~ 5 times larger.

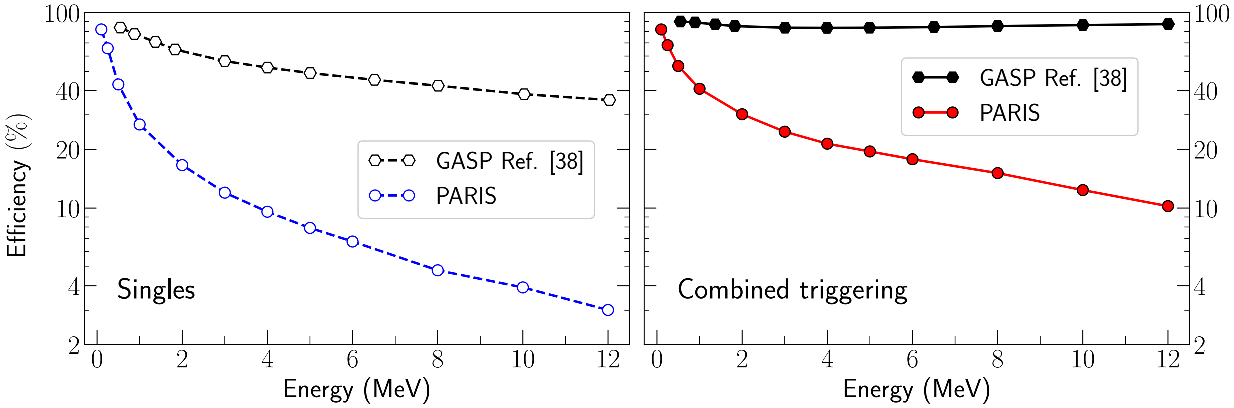

Figure 7-21.: Comparison of the efficiencies of the GASP and PARIS arrays.

8. Summary and conclusions

The transitional quadrupole moments of high spin states in three normally deformed bands of ^{83}Y were measured and their evolution with rotational frequency was compared with other physical quantities. As a result it was found that the smallest measured $|Q_t|$ value appears at the sharpest band crossing among the bands studied, namely the second crossing in the $(-,+)$ band. Contrary to what was previously assigned in Refs. [6,58], this band crossing is associated with a change between $\pi(g_{9/2})^2$ and $\pi(g_{9/2})^4$ configurations which is manifested as an increase of the deformation. Figure **7-6** shows that the $|Q_t|$ values for the $(-,+)$ band in ^{81}Y and ^{83}Y are equal within uncertainties, both exhibit a minimum value at the second band crossing. It was also shown that the measured $|Q_t|$ values for the $(+,+)$ and the $(-,+)$ bands are similar to those previously measured. Cranked Nilsson Strutinsky calculations with (CNSB) and without (CNS) inclusion of pairing correlations are in general agreement with the measured values, of which, the few ones that fall outside the uncertainties could be explained by two possible scenarios. 1) A possible mixing with non-collective states and 2) the introduction of non valid correlations induced by the experimental method of gating from below only and thus possibly impacting also the values for lower spins.

CNS calculations were carried out and used to specify the configurations in the CNSB formalism which was used to study the normally deformed bands of ^{83}Y. Three facts supported that the CNS assigments are approximately valid also for the CNSB formalism: 1) The spread of the difference between the experimental $E - E_{rld}$ energies and those calculated for both the CNS and the CNSB formalism is within a range of 0.5 MeV (see Figs. **7-10**(c) and **7-12**(c)). 2) The calculated Q_t are very similar in the two formalisms, Figure **7-15**. 3) The energy surfaces are very similar, Figure **7-14**.

The calculations indicate that the observed bands will not terminate if their I_{max} values are reached (non-termination). The absence of termination is in agreement with the conclusions of Ref. [6] for the $(+,+)$ band but in contrast to what was said for the $(-,+)$ band.

The measured level lifetimes and sidefeeding times follow the inequality $\tau_{SF} \gtrsim \tau$ and comparisons of the sidefeeding times with GAMMAPACE simulations showed an agreement with the experiment by asuming $B(E2)$ values in the range 40 - 80 W. u. for the collective transitions in the continuum region. This indicates that the theory used in GAMMAPACE for the simulation of the transitions in the continuum region may be a good approach to the description of the decay in that region.

The Hk-EOS technique was studied with the purpose of providing a new experimental methodology to be used in future research of the nuclear continuum region. With the use of the Hk technique the EOS of different regions in the continuum can be obtained and with a fit to the EOS, the level density parameter can be extracted. The experimental detector array PARIS was tested by Monte Carlo simulation for the application of the Hk technique. The results show that the PARIS array has a combined triggering efficiency at high energies which is very low for the implementation of the Hk technique, in spite that the design of the PARIS detectors was intended for the detection of high energy γ-rays. Geometries with an spherical shell shape in which the thickness of the detector material should be sufficient for the detection of high energy γ-rays are found to be the only ones adequate for the application of the Hk technique. The use of BGO is suggested although other scintillation materials could be used, provided that the thickness is large enough.

A. Calculation of some quantities inferred in the DSA experiment

The nuclear reaction used in the DSA experiment is depicted in the Figure **A-1**.

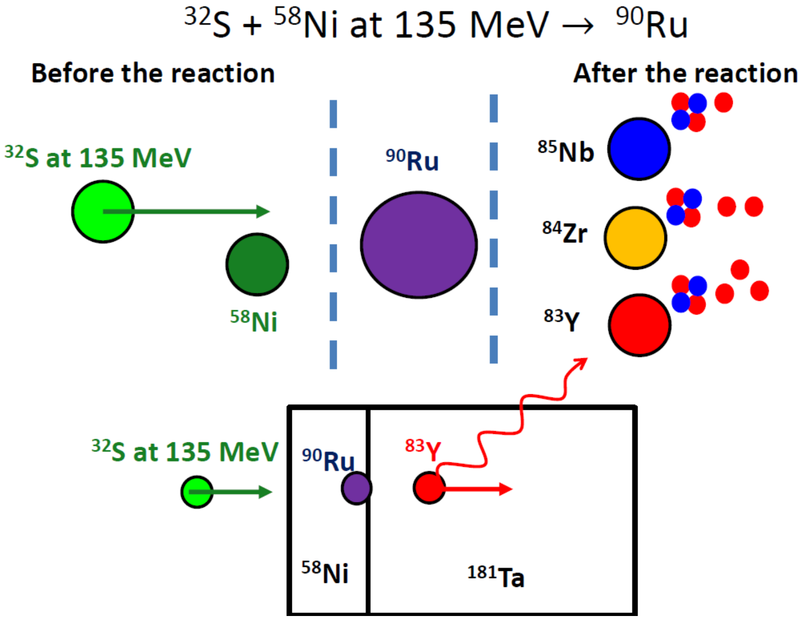

Figure A-1.: Schematic representation of the nuclear reaction used in the experiment performed with the objective to measure lifetimes of excited states of the nuclei.

Since the experiment is intended to measure the level lifetime and sidefeeding times therefore an estimation of the velocities and stopping times of the nuclei implied in the reaction are useful for the data analysis.

A.1. Initial velocities

Depending on the nucleus implied (beam ^{32}S, compound nucleus ^{90}Ru and the product of the reaction ^{83}Y) the initital velocity has to be calculated with a different procedure for each case.

A.1.1. Projectile (^{32}S)

The beam or projectile velocity, v_P is related with the kinetic energy by

$$T_P = \frac{1}{2} m_c v_P^2 \;\text{ and this equation can be solved for } v_P \tag{A-1}$$

$$v_P = \sqrt{\frac{2T_P}{mc^2}} \cdot c \;\text{ with }\; T_P = 135(1)\text{ MeV} \tag{A-2}$$

$$v_P = 0.095 \cdot c \Longrightarrow 9.5\,\%\text{ of the light velocity} \tag{A-3}$$

This velocity can be writen in several units from which the one is most adequate in this case is μm/ps because the distances traveled by the nuclei studied are some μm and the lifetimes are in the order of ps.

$$v_P = 0.095 \cdot c = 0.095 \cdot 3 \times 10^8 (\text{m/s}) = 28.6 \times 10^6 (\text{m/s}) \tag{A-4}$$

$$= 0.095 \cdot 1080 \times 10^6 (\text{km/h}) = 102.8 \times 10^6 (\text{km/h}) \tag{A-5}$$

$$= 28.6 \times 10^6 \left(\frac{\text{m}}{\text{s}}\right) \frac{1\text{s}}{10^{12}\text{ps}} \frac{10^6 \mu\text{m}}{1\text{m}} = 28.6(3) \left(\frac{\mu\text{m}}{\text{ps}}\right) \tag{A-6}$$

A.1.2. Compound nucleus (^{90}Ru)

$E_{Lab} = (135 \pm 1)$ MeV	
Nucleus	mc^2 ($\times 10^3$ MeV)
Projectile (^{32}S)	29.782
Target (^{58}Ni)	53.966
Compound (^{90}Ru)	83.769

Table A-1.: Masses of the nuclei of interest.

From energy conservation

$$E_i = E_{Lab} + m_p c^2 + m_t c^2 = E_f = m_c c^2 + T_c + E^*. \tag{A-7}$$

where m_p, m_t, m_c are the masses of the projectile, target and compound respectively. T_c and E^* are the kinetic energy and the excitation energy of the compound nucleus.

Equation (A-7) can be solved for the excitation energy of the compound nucleus as

$$
\begin{aligned}
E^* &= E_{Lab} - T_c + (m_p + m_t - m_c)\, c^2 && \text{(A-8)}\\
&= E_{Lab} - \frac{m_p}{m_c} E_{Lab} + Q && \text{(A-9)}\\
&= \left(1 - \frac{m_p c^2}{m_c c^2}\right) E_{Lab} + Q. && \text{(A-10)}
\end{aligned}
$$

With $Q = (m_p + m_t - m_c)\, c^2 = (29782 + 53966 - 83769)$ MeV $= -21$ MeV, the kinetic energy of the compound nucleus is given by

$$T_c = \frac{m_p}{m_c} E_{Lab} = \frac{m_p c^2}{m_c c^2} E_{Lab} = 48.0 \text{ MeV}. \tag{A-11}$$

On the other hand the kinetic energy can be related with the velocity of the nucleus for the non-relativistic case as

$$
\begin{aligned}
T_c &= \frac{1}{2} m_c v_c^2 = \frac{1}{2c^2} m_c c^2 v_c^2. \text{ this expression can be solved for the velocity} && \text{(A-12)}\\
v_c &= \sqrt{\frac{2T_c}{mc^2}} \cdot c \;\; \text{con} \;\; T_c = 48.0 \text{ MeV} && \text{(A-13)}\\
v_c &= 0.0338 \cdot c \Longrightarrow 3.4\,\% \text{ of the light velocity} && \text{(A-14)}
\end{aligned}
$$

Thus the velocity of the compound nucleus in c (light velocity) units is

$$\beta = \frac{v}{c} = 0.034 \tag{A-15}$$

With the reaction of Table **A-1** the excitation energy of the compound nucleus will be

$$E^* = E_{Lab} - T_c + Q = (135 - 48 - 21) \text{ MeV} = 66(1) \text{ MeV}. \tag{A-16}$$

A.1.3. ^{83}Y

From PACE2 calculations (see Ref. [82]) the mean proton and α energies ($\langle E_p\rangle, \langle E_\alpha\rangle$) emmited by the ^{83}Y nucleus are

$$\langle E_p\rangle = 8.8 \text{ MeV}, \quad \langle E_\alpha\rangle = 15.7 \text{ MeV} \tag{A-17}$$

The velocities can be calculated as

$$v = \sqrt{2m(\mathrm{MeV}/c^2)E(\mathrm{MeV})} \cdot c \tag{A-18}$$

$$v_p = 0.14 \cdot c = 41.2\ \mu\mathrm{m/ps}, \tag{A-19}$$

$$v_\alpha = 0.092 \cdot c = 27.5\ \mu\mathrm{m/ps} \tag{A-20}$$

From momentum conservation of the process ^{90}Ru ⟶ 3p + α + ^{83}Y the initial velocity of the ^{83}Y can be calculated as

$$m(^{90}\mathrm{Ru})v(^{90}\mathrm{Ru}) = m(^{83}\mathrm{Y})v(^{83}\mathrm{Y}) \pm 3m(p)v(p) \pm m(\alpha)v(\alpha) \tag{A-21}$$

$$v(^{83}\mathrm{Y}) = \frac{m(^{90}\mathrm{Ru})v(^{90}\mathrm{Ru}) \pm 3m(p)v(p) \pm m(\alpha)v(\alpha)}{m(^{83}\mathrm{Y})} \tag{A-22}$$

From Equation (A-22) it can be seen that the velocity of the the ^{83}Y nucleus will depend on the direction of emission of the the protons and the α particles. However the range covered for the two extreme cases when all the particles are emitted in the forward and backward directions will be reported at the end of this appendix.

A.2. Thickness of the target (^{58}Ni) and the stopper (^{181}Ta)

A.2.1. Target (^{58}Ni)

The thickness of the target (^{58}Ni) is usually expressed in an indirect way to take into account the density. The quantity reported in this case is

$$\rho T_t = 415 \frac{\mu\mathrm{g}}{\mathrm{cm}^2} \tag{A-23}$$

Thus by using the known density of the target ^{56}Ni, the thickness of the target T_t is

$$T_t = \frac{415\mu\mathrm{g/cm}^2}{\rho} \left(\frac{1\ \mathrm{g}}{10^6 \mu\mathrm{g}} \right) \tag{A-24}$$

$$= \frac{415 \cdot 10^{-6}\ \mathrm{g/cm}^2}{8.908\ \mathrm{g/cm}^3} = 46.59 \cdot 10^{-6}\ \mathrm{cm} \tag{A-25}$$

$$= 0.47 \cdot 10^{-6}\ \mathrm{m} = 0.47\ \mu\mathrm{m} \tag{A-26}$$

A.2.2. Stopper (^{181}Ta)

The reported thickness of the stopper, T_s, is

$$\rho T_s = 10.3\frac{mg}{\text{cm}^2} \tag{A-27}$$

Thus by using the known density of the target ^{181}Ta, the thickness of the target is

$$T = \frac{10.3\text{mg/cm}^2}{\rho}\left(\frac{1\text{ g}}{10^3\text{mg}}\right) \tag{A-28}$$

$$= \frac{10.3 \cdot 10^{-3}\text{ g/cm}^2}{16.650\text{ g/cm}^3} \tag{A-29}$$

$$= 0.62 \cdot 10^{-3}\text{ cm} = 620 \cdot 10^{-6}\text{ m} = 620\mu\text{m} \tag{A-30}$$

A.3. Summary of the calculations

The Lindhard-Scharff-Schiøtt (LSS) theory is an analytical theory developed in 1963 to calculate the range and the stopping power of the ions traveling across materials [83]. Table **A-2** shows some equations of the LSS theory as well as the definition of the quantities to be calculated.

Table **A-3** shows the results of the calculations where all the quantities impliying the velocity of the ^{83}Y nucleus are shown in a range as it was explained in Appendix A.1.3.

A.3.1. Approximations made in the calculations

- From the second column of Table **A-3** it can be seen that the velocity attenuation in percentage of the ^{32}S traveling inside the target of ^{58}Ni is only of 2.92 %. Besides this value was calculated in the extreme case when the ^{32}S travels along the complete thickness of the target without producing the nuclear fusion reaction. Thus this attenuation can be neglected and the reaction can be considered to occur always at 135 MeV for most of the analysis.

- The velocity attenuation of the ^{90}Ru inside the target (^{58}Ni) was of only 4.87 % and this value was calculated in the extreme case when the ^{90}Ru travels along the complete thickness of the target (^{58}Ni). Thus this attenuation can be neglected.

- In the extreme case when the ^{83}Y crosses the complete thickness of the target (^{58}Ni) the velocity attenuation of the ^{83}Y was of (6.2 - 3.7) %, thus this attenuation was neglected and the initial velocity of the ^{83}Y inside the stopper was assumed to be the same calculated in the previous column.

τ_{stopping} (ps)	$\frac{A_{\text{P}}A_{\text{T}}}{50.8\rho f(Z_{\text{T}},Z_{\text{P}})}$ with $f(Z_{\text{T}},Z_{\text{P}}) \approx \frac{Z_{\text{T}}Z_{\text{P}}}{\left(Z_{\text{T}}^{2/3}+Z_{\text{P}}^{2/3}\right)^{3/2}}$. Stopping time in equation $v(t) = v_0 \exp\left[-\frac{t}{\tau_{\text{stopping}}}\right]$
v_0 (μm/ps)*	Initial velocity of the traveling nucleus*.
$\beta_i = v/c$	Velocity in c units of the traveling nucleus.
E_i (MeV)	Initial energy of the traveling nucleus.
x_{stopping} (μm)	Since $x(t) = v_0\tau_{\text{stopping}}\left[1-\mathrm{e}^{-t/\tau_{\text{stopping}}}\right]$ thus x_{stopping} is defined as $v_0\tau_{\text{stopping}}$ and it is the maximum distance that the nucleus can reach with a initial velocity v_0 and a stopping time τ_{stopping}
Thickness (μm)	It is the thickness of the target or stopper, calculated by using the density and the reported value of density×thickness
Traveling time (ps)	$x(t) = v_0\tau_{\text{stopping}}\left[1-\mathrm{e}^{-t/\tau_{\text{stopping}}}\right]$ $t = -\tau_{\text{stopping}} \ln\left(1-\frac{x}{v_0\tau_{\text{stopping}}}\right)$ It is the time spent by the traveling nucleus to cross the complete thickness of the target.
v_f(T) (μm/ps)	It is the final velocity of the traveling nulceus after crossing the thickness of the target or the stopper
$\beta_f = v/c$	Final velocity of the traveling nucleus, in c units. after crossing the thickness of the target or the stopper
E_f (MeV)	Final energy of the traveling nucleus. after crossing the thickness of the target or the stopper
Velocity attenuation (%)	$\frac{v_0 - v_f}{v_0} \cdot 100\,\% = \left(1-\exp\left[-\frac{t}{\tau_{\text{stopping}}}\right]\right) \cdot 100\,\%$

Table A-2.: Calculations made using the Lindhard-Scharff-Schiøtt (LSS) theory [83].
*Values are calculated in a different way for each case

A.3.2. Conclusions

- The velocity attenuation of the projectile (^{32}S), the compund nucleus (^{90}Ru), and the ^{83}Y nucleus inside the target (^{58}Ni) are negligible even in the extreme cases when the traveling nucleus crosses the complete thickness of the target (0.47 μm).
- The thickness of the stopper (620μm) is much greater than the stopping distance of ^{83}Y (13.5μm) inside the stopper which was calculated with maximum kinetic energy

$^{32}\mathrm{S} + {}^{58}\mathrm{Ni}$ at 135 MeV $\longrightarrow {}^{90}\mathrm{Ru} \longrightarrow 3\mathrm{p} + \alpha + {}^{83}\mathrm{Y}$

	Inside the target (^{58}Ni)			Inside the stopper (^{181}Ta)
	Before the reaction	After the reaction		
Traveling nucleus	^{32}S	^{90}Ru	^{83}Y	^{83}Y
τ_{stopping} (ps)	0.56	0.94	0.92	0.97
v_0 (μm/ps)	28.6	10.2	8.2 - 13.9	8.2 - 13.9
$\beta_i = v/c$	0.095	0.034	0.027 - 0.046	0.027 - 0.046
E_i (MeV)	135	48	29 - 83	29 - 83
x_{stopping} (μm)	16.0	9.6	7.6 - 12.8	8.0 - 13.5
Thickness (μm)	0.47	0.47	0.47	620
Traveling time (ps)	0.02	0.05	0.06 - 0.03	—
v_f(T) (μm/ps)	27.8	9.7	7.7 - 7.9	0.0
$\beta_f = v/c$	0.093	0.032	0.026 - 0.026	0.0
E_f (MeV)	127	43.8	25.6 - 27.0	0.0
Velocity attenuation (%)	2.92	4.87	6.2 - 3.7	100

Table A-3.: Calculations made using the Lindhard-Scharff-Schiøtt (LSS) theory [83].

possible for ^{83}Y. Therefore it is clear that the ^{83}Y is completely stopped inside the stopper.

- The initial velocity of the ^{83}Y inside the stopper is in the range of (0.027 - 0.046)$\cdot c$ which are values to take into account to perform the doppler correction of the matrices. Matrices with $\beta > 0.046$ do not make physical sense.

- The lifetimes that can be measured with the data of the experiment are $\tau \leq \tau_{\mathrm{stopping}} = 0.97$ ps. For lifetimes geater than the $\tau_{\mathrm{stopping}} = 0.95$ ps, the Doppler correction won't be observed because the nuclei of ^{83}Y will emmit mostly at rest.

B. Lineshapes determined ($(+,+)$ band)

B.1. Effective lifetime of the state at $I = (49/2)$ using the γ-ray of 1966 keV

E_γ (keV)	Gates used (keV)	Position of the gates
1966	1754 - 1604 - 1485 - 1340	Gates from below

Table B-1.: Gates used to obtain the spectrum of Figure **B-1**.

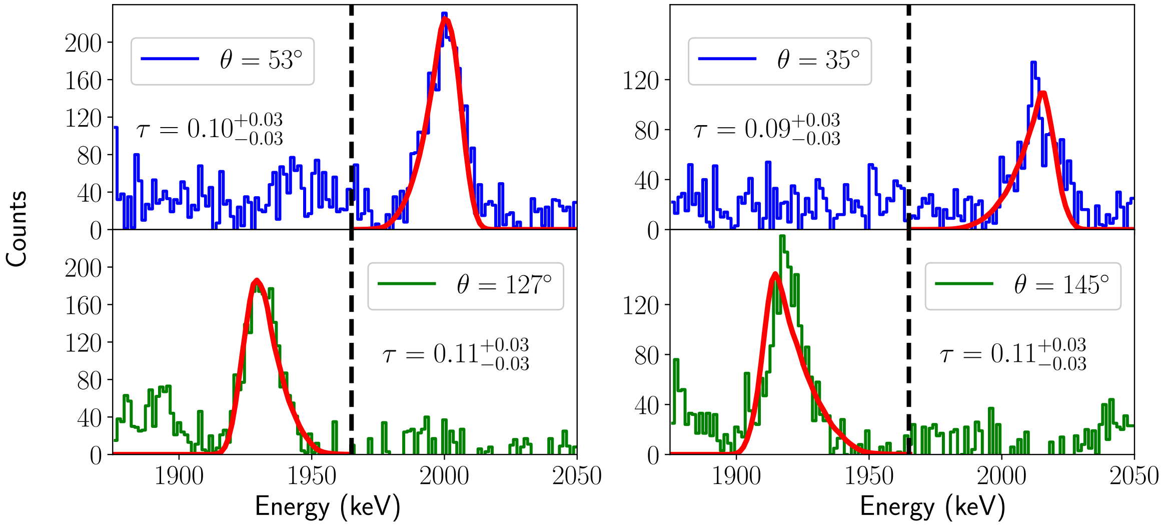

Figure B-1.: Fits performed by the program AhKin to study the excited state at 12792 keV by using the γ-ray of 1966 keV detected at different angles.

B.2. Lifetime of the state at the state at $I = 45/2$ using the γ-ray of 1754 keV

E_γ (keV)	Gate used (keV)	Position of the gate
1754	1966	Gate from above

Table B-2.: Gate used to obtain the spectrum of Figure **B-2**.

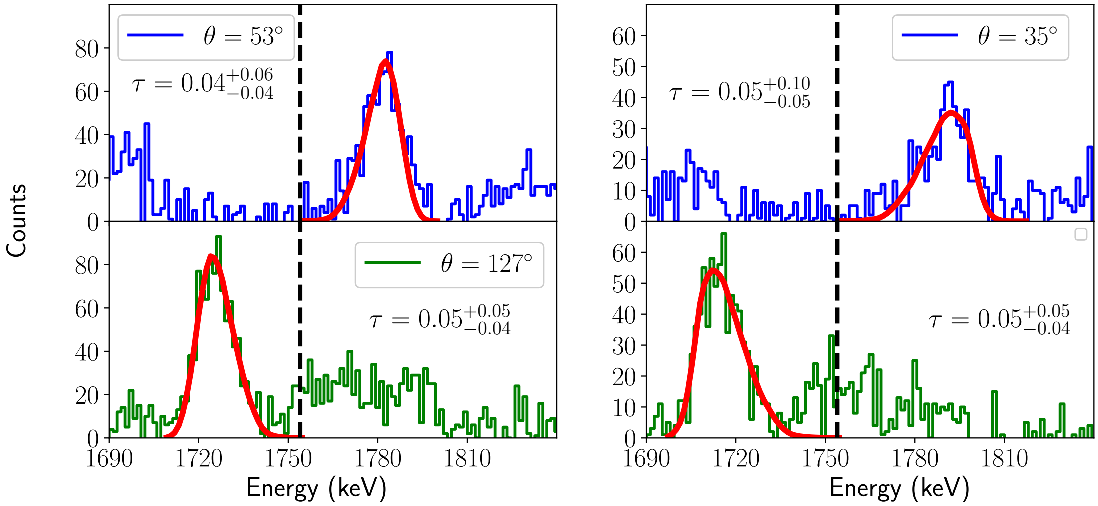

Figure B-2.: Fits performed by the program AHKIN to study the excited state at 10826 keV by using the γ-ray of 1754 keV detected at different angles.

B.3. Sidefeeding time of the state at $I = 45/2$ using the γ-ray of 1754 keV

E_γ (keV)	Gate used (keV)	Position of the gate
1754	1604 - 1485 - 1340	Gates from below

Table B-3.: Gates used to obtain the spectrum of Figure **B-3**.

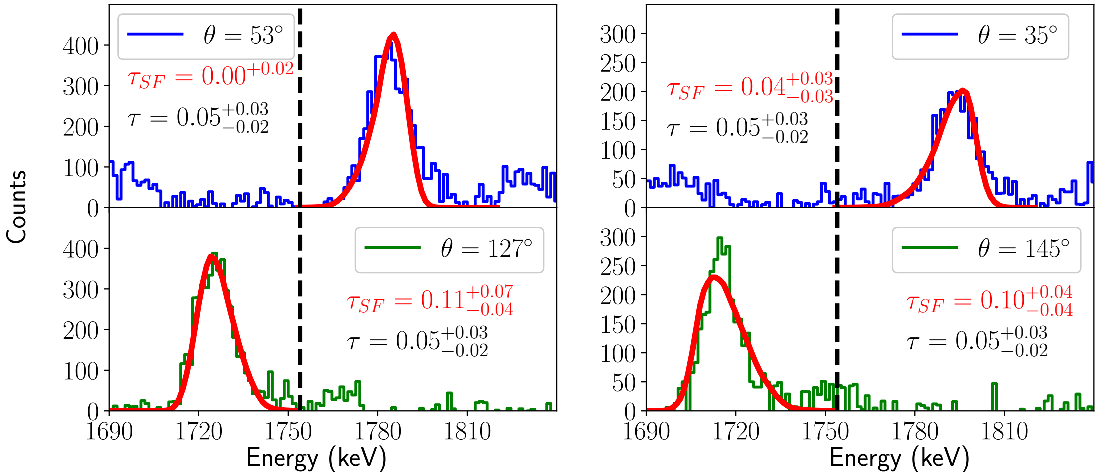

Figure B-3.: Fits performed by the program AhKin to study the excited state at $I = 45/2$ by using the γ-ray of 1754 keV detected at different angles.

B.4. Lifetime time of the state at $I = 41/2$ using the γ-ray of 1604 keV

E_γ (keV)	Gates used (keV)	Position of the gates
1604	1754	Gate from above

Table B-4.: Gate used to obtain the spectrum of Figure **B-6**.

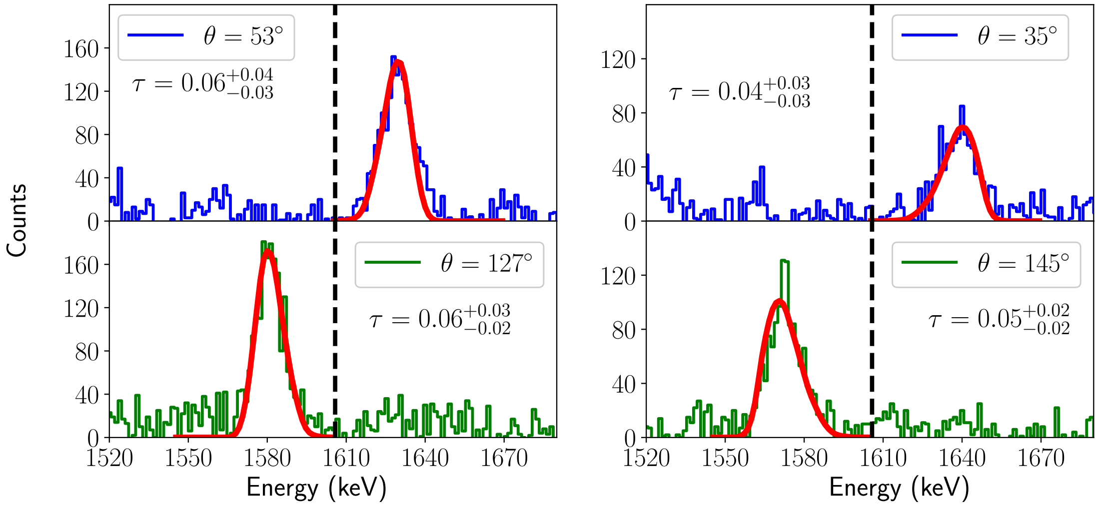

Figure B-4.: Fits performed by the program AhKin to study the excited state at 9072 keV by using the γ-ray of 1604 keV detected at different angles.

B.5. Side feeding time of the state at $I = 41/2$ using the γ-ray of 1604 keV

E_γ (keV)	Gates used (keV)	Position of the gates
1604	1485 - 1340	Gate from below

Table B-5.: Gate used to obtain the spectrum of Figure **B-5**.

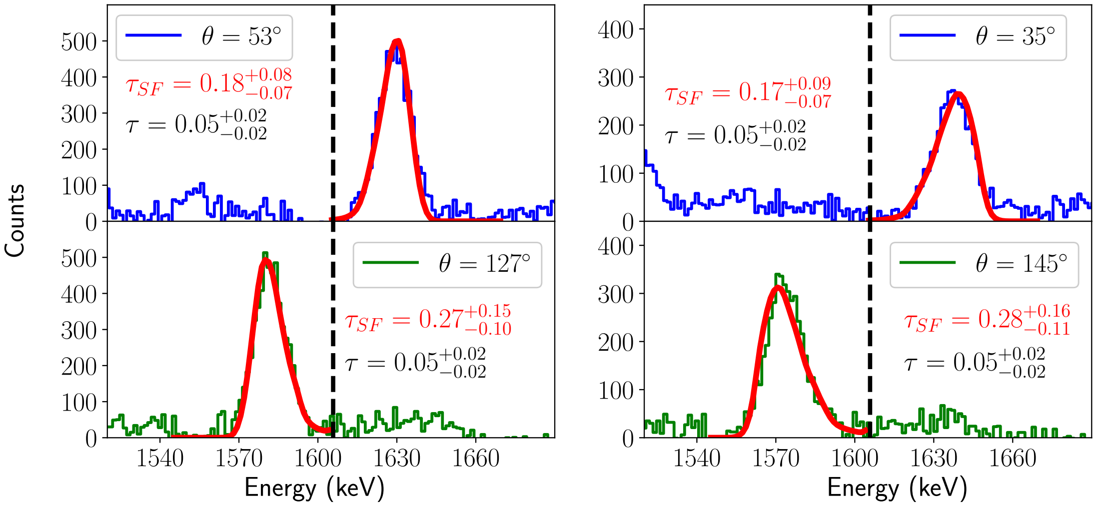

Figure B-5.: Fits performed by the program AhKin to study the excited state at 9072 keV by using the γ-ray of 1604 keV detected at different angles.

B.6. Lifetime of the state at $I = 37/2$ using the γ-ray of 1485 keV

E_γ (keV)	Gates used (keV)	Position of the gates
1486	1604	Gate from above

Table B-6.: Gate used to obtain the spectrum of Figure **B-6**.

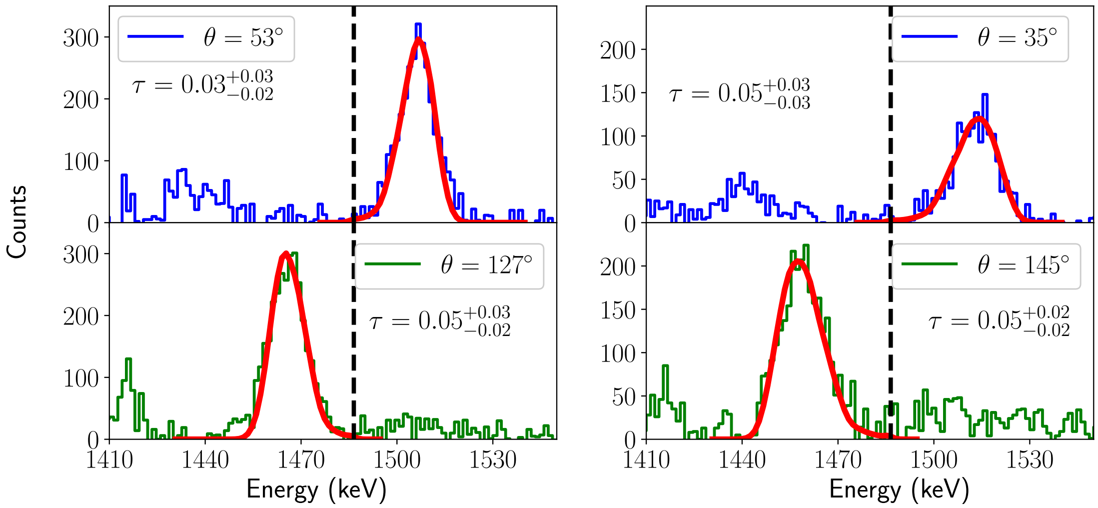

Figure B-6.: Fits performed by the program AHKIN to study the excited state at 7468 keV by using the γ-ray of 1486 keV detected at different angles.

B.7. Side feeding time of the state at $I = 37/2$ using the γ-ray of 1486 keV

E_γ (keV)	Gates used (keV)	Position of the gates
1486	1340	Gate from below

Table B-7.: Gate used to obtain the spectrum of Figure **B-7**.

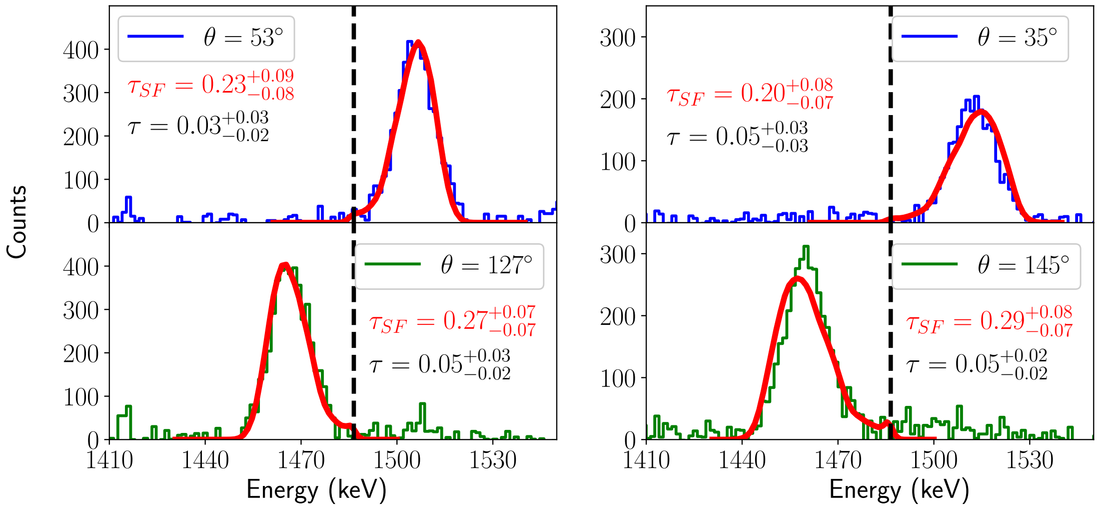

Figure B-7.: Fits performed by the program AHKIN to study the excited state at 7468 keV by using the γ-ray of 1486 keV detected at different angles.

B.8. Lifetime of the state at $I = 33/2$ using the γ-ray of 1340 keV

E_γ (keV)	Gates used (keV)	Position of the gates
1340	1485	Gate from above

Table B-8.: Gate used to obtain the spectrum of Figure **B-8**.

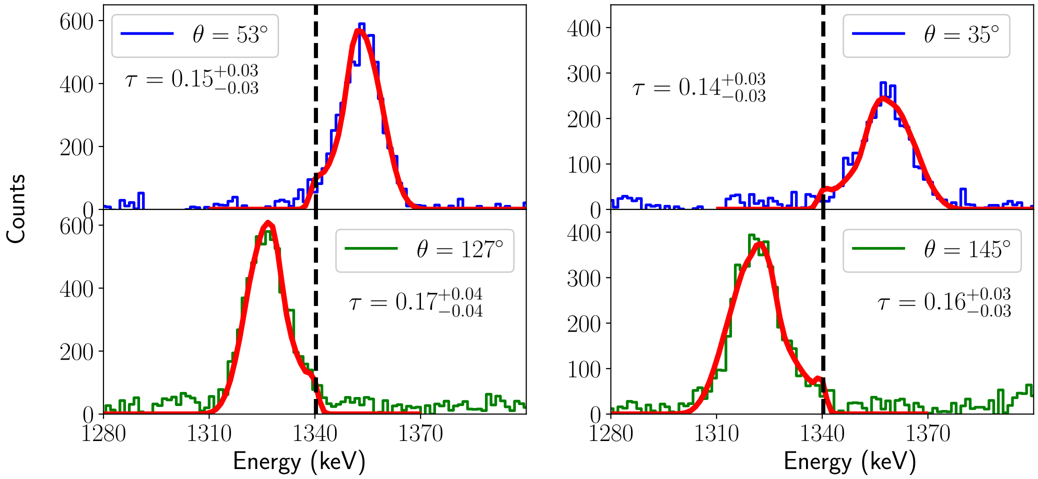

Figure B-8.: Fits performed by the program AhKin to study the excited state at 5984 keV by using the γ-ray of 1340 keV detected at different angles.

B.9. Sidefeeding time of the state at $I = 33/2$ using the γ-ray of 1340 keV

E_γ (keV)	Gates used (keV)	Position of the gates
1340	1193	Gate from below

Table B-9.: Gate used to obtain the spectrum of Figure **B-9**.

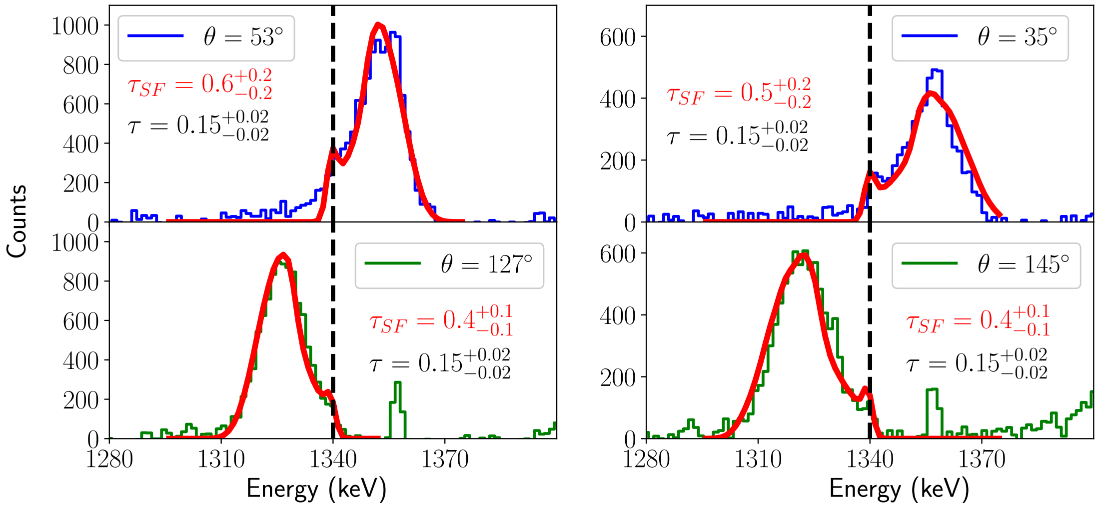

Figure B-9.: Fits performed by the program AhKin to study the excited state at 5984 keV by using the γ-ray of 1340 keV detected at different angles.

B.10. Lifetime of the state at $I = 29/2$ using the γ-ray of 1193 keV

E_γ (keV)	Gate used (keV)	Position of the gate
1193	1340	Gate from above

Table B-10.: Gate used to obtain the spectrum of Figure **B-10**.

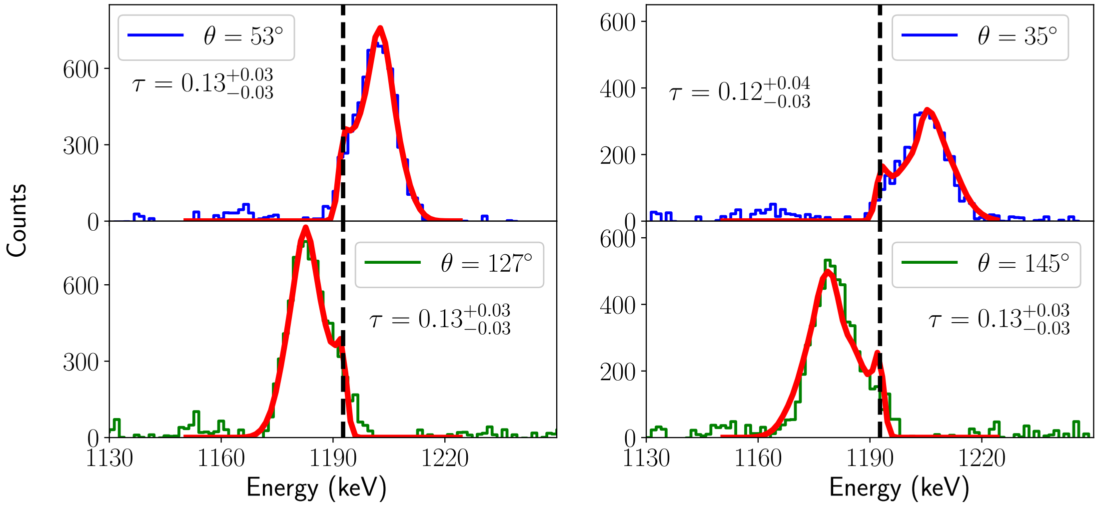

Figure B-10.: Fits performed by the program AhKin to study the excited state at 4644 keV by using the γ-ray of 1193 keV detected at different angles.

B.11. Side feeding time of the state at $I = 29/2$ using the γ-ray of 1193 keV

E_γ (keV)	Gates used (keV)	Position of the gates
1193	595 - 811	Gate from below

Table B-11.: Gate used to obtain the spectrum of Figure **B-11**.

Interference with transitions of the yrast band of ^{84}Zr. Transition energies (540 - 723 - 873 - **952** - 979 - **1067** - **1195** - 1196) keV.

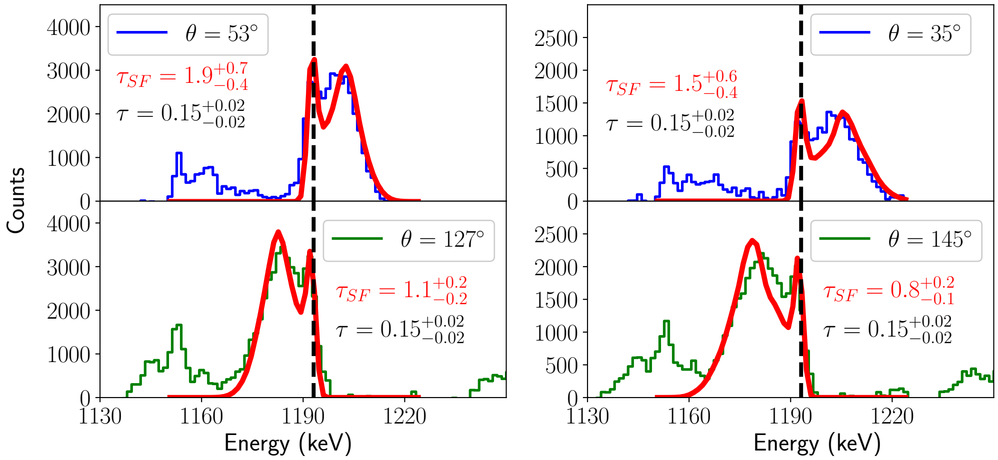

Figure B-11.: Fits performed by the program AhKin to study the excited state at 4644 keV by using the γ-ray of 1193 keV detected at different angles.

B.12. Lifetime of the state at $I = 25/2$ using the γ-ray of 1080 keV

E_γ (keV)	Gates used (keV)	Position of the gates
1080	1340	Gate from above

Table B-12.: Gate used to obtain the spectrum of Figure **B-12**.

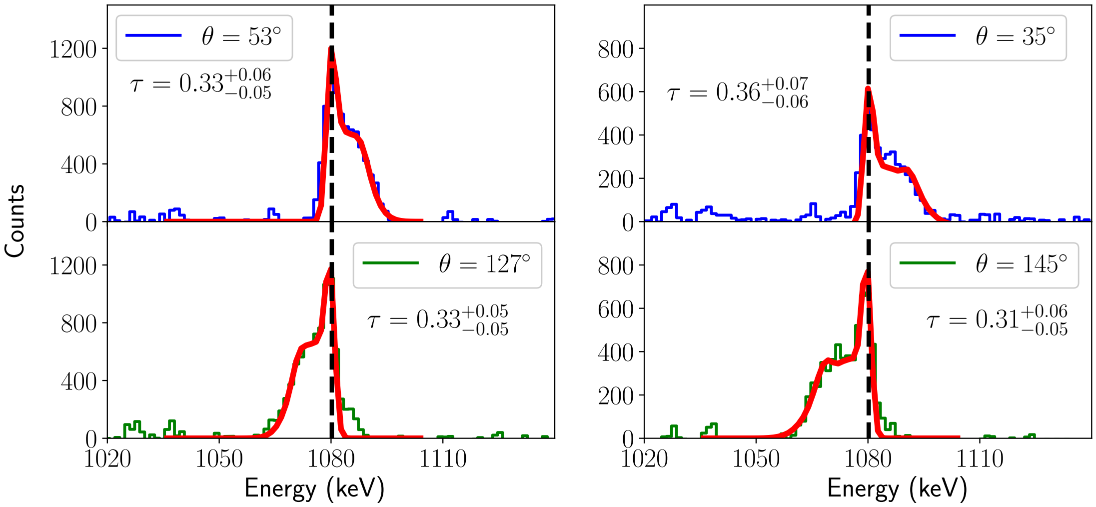

Figure B-12.: Fits performed by the program AhKin to study the excited state at 3451 keV by using the γ-ray of 1080 keV detected at different angles.

B.13. Side feeding time of the state at $I = 25/2$ using the γ-ray of 1080 keV

E_γ (keV)	Gates used (keV)	Position of the gates
1080	595	Gate from below

Table B-13.: Gate used to obtain the spectrum of Figure **B-13**.

Interference with transitions of the ^{80}Sr.
Gate at 965. ^{84}Zr Transition energies band 1 (540 - 723 - 873 - 952 - **979** - **1067** - 1195 - 1196) keV.
Gate at 811. ^{83}Y Transition energies band (-,-) (475 - 687 - **812** - 908 - **1065**) keV.
Gate at 595. ^{80}Sr Yrast band transition energies (386 - **595** - 783 - 937 - **1065**) keV.
The lower iterference was for the the gate at 595 keV.

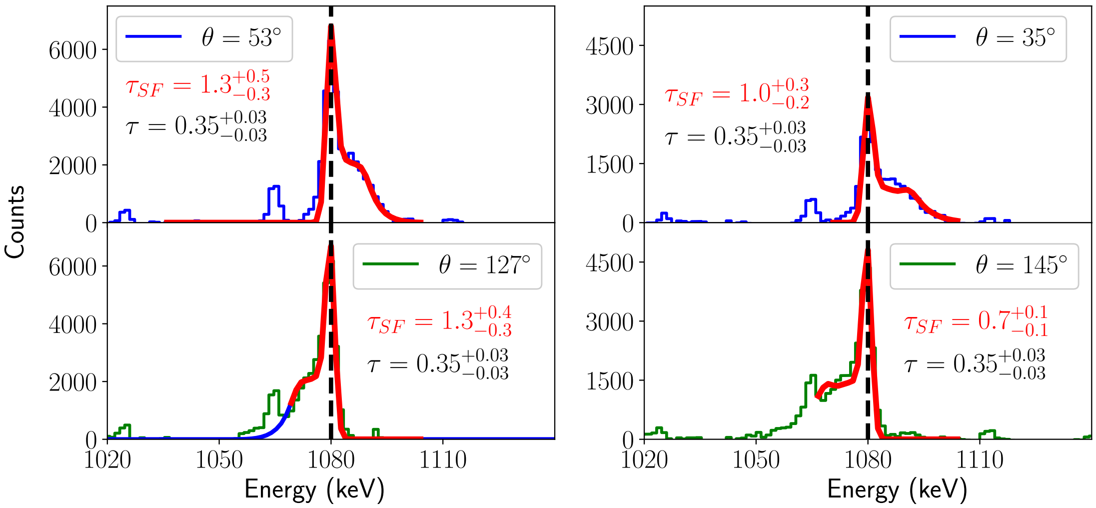

Figure B-13.: Fits performed by the program AhKin to study the excited state at 3451 keV by using the γ-ray of 1080 keV detected at different angles.

B.14. Lifetime of the state at $I = 21/2$ using the γ-ray of 965 keV

E_γ (keV)	Gates used (keV)	Position of the gates
965	1080	Gate from above

Table B-14.: Gate used to obtain the spectrum of Figure **B-14**.

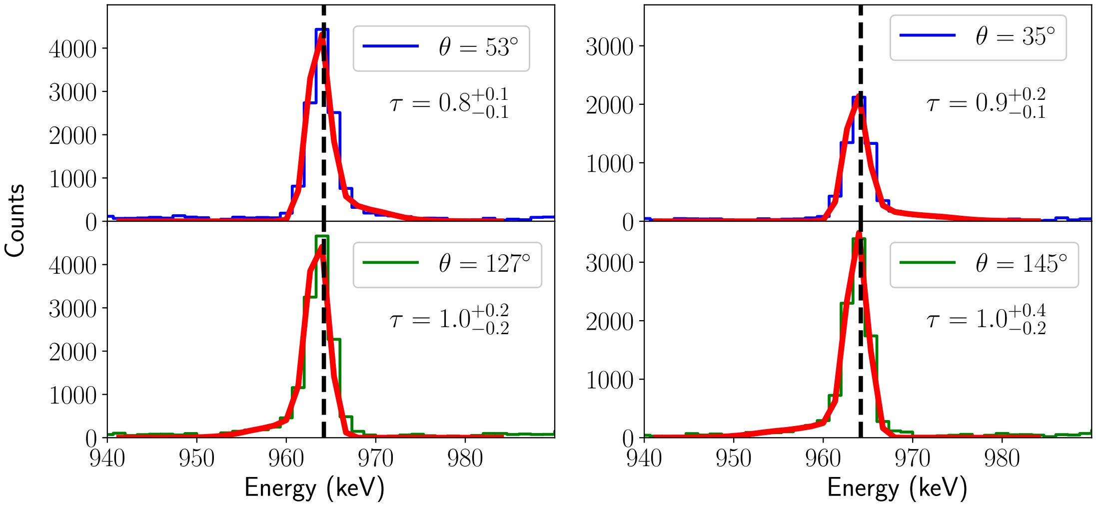

Figure B-14.: Fits performed by the program AhKin to study the excited state at 2371 keV by using the γ-ray of 965 keV detected at different angles.

B.15. Side feeding time of the state at $I = 21/2$ using the γ-ray of 965 keV

E_γ (keV)	Gates used (keV)	Position of the gates
965	811	Gate from below

Table B-15.: Gate used to obtain the spectrum of Figure **B-14**.

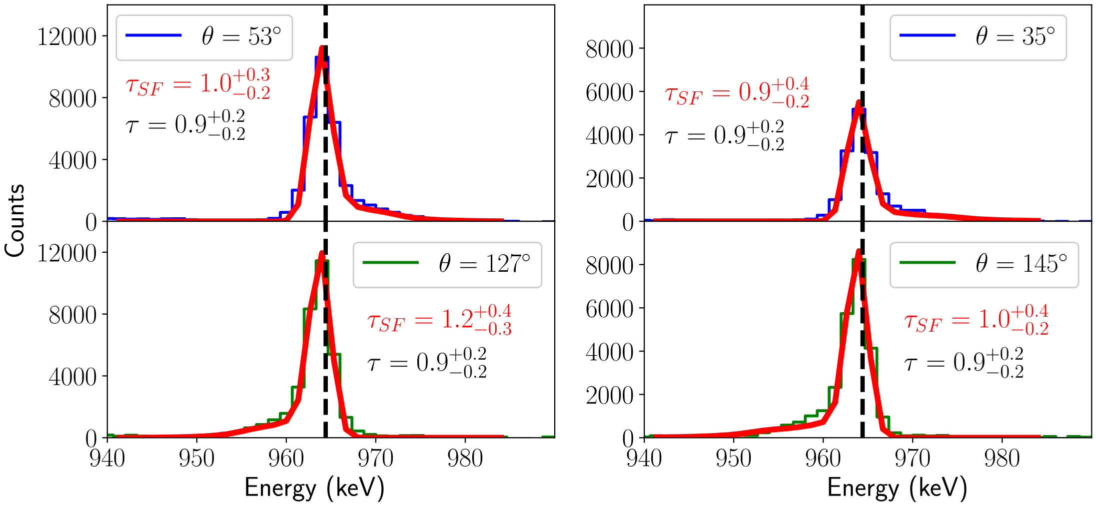

Figure B-15.: Fits performed by the program AhKin to study the excited state at 2371 keV by using the γ-ray of 965 keV detected at different angles.

C. Lineshapes determined ($(+,-)$ band)

C.1. Lifetime of the state at $I = (43/2)$ using the γ-ray of 1648 keV gate at 1534 keV

E_γ (keV)	Gates used (keV)	Position of the gates
1648	1534	Gate from below

Table C-1.: Gate used to obtain the spectrum of Figure **C-1**.

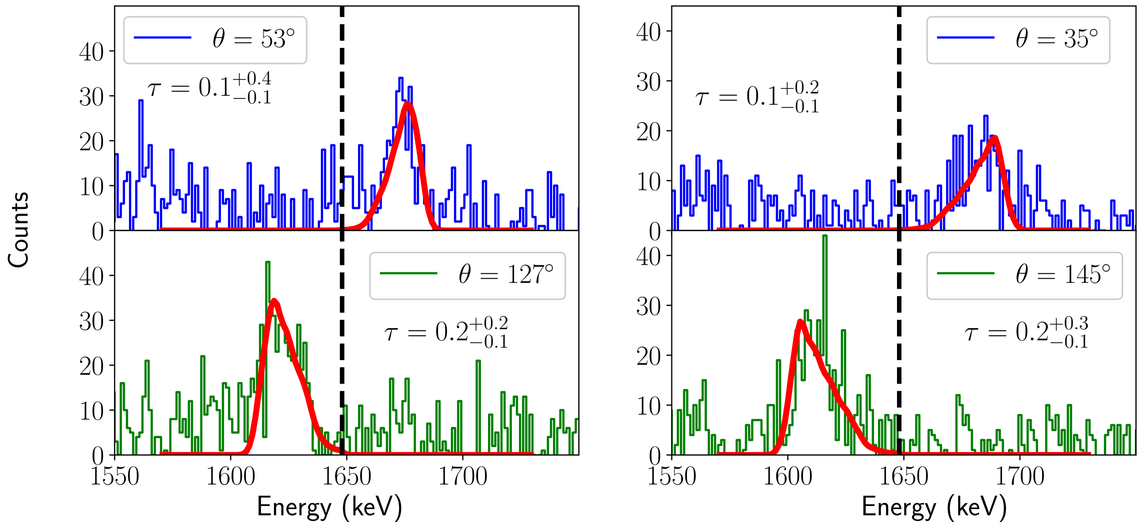

Figure C-1.: Fits performed by the program AhKin to study the excited state at 10360 keV by using the γ-ray of 1648 keV detected at different angles.

C.2. Lifetime of the state at $I = (39/2)$ using the γ-ray of 1534 keV gated at 1648 keV

E_γ (keV)	Gates used (keV)	Position of the gates
1534	1648	Gate from above

Table C-2.: Gate used to obtain the spectrum of Figure **C-2**.

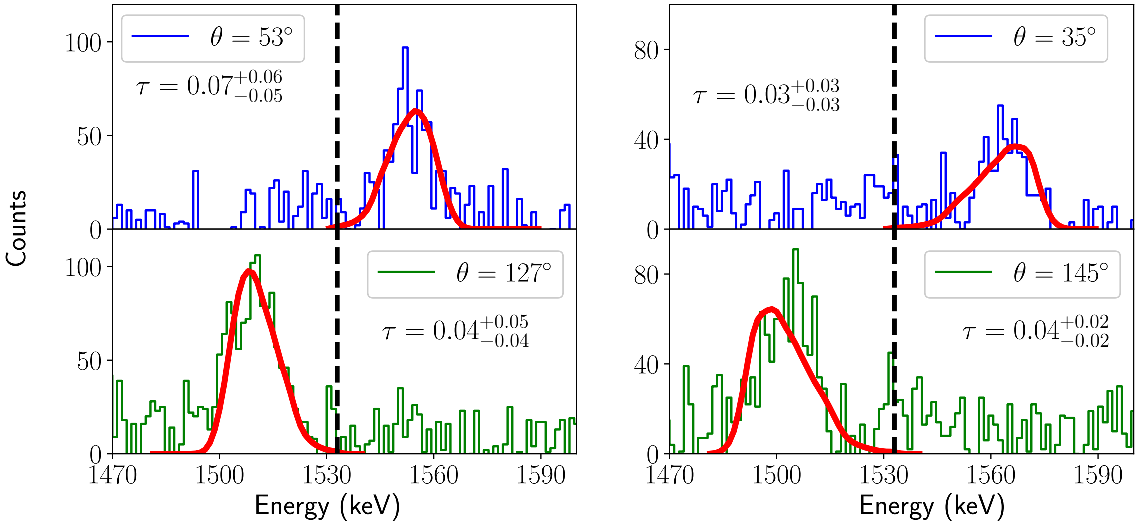

Figure C-2.: Fits performed by the program AhKin to study the excited state at 8712 keV by using the γ-ray of 1534 keV detected at different angles.

C.3. Sidefeeding time of the state at $I = (39/2)$ using the γ-ray of 1534 keV gated at 1431 keV

E_γ (keV)	Gates used (keV)	Position of the gates
1534	1431	Gate from below

Table C-3.: Gate used to obtain the spectrum of Figure **C-3**.

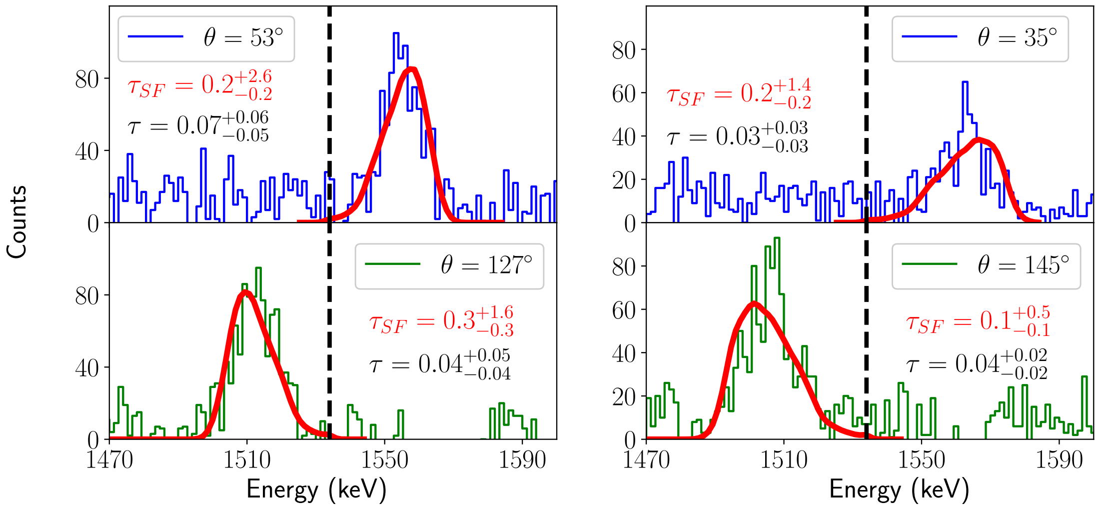

Figure C-3.: Fits performed by the program AhKin to study the feeding time of the state at 8712 keV by using the γ-ray of 1534 keV detected at different angles.

C.4. Lifetime of the state at $I = (35/2)$ using the γ-ray of 1431 keV gated at 1648 keV

E_γ (keV)	Gates used (keV)	Position of the gates
1431	1648	Gate from above

Table C-4.: Gate used to obtain the spectrum of Figure **C-4**.

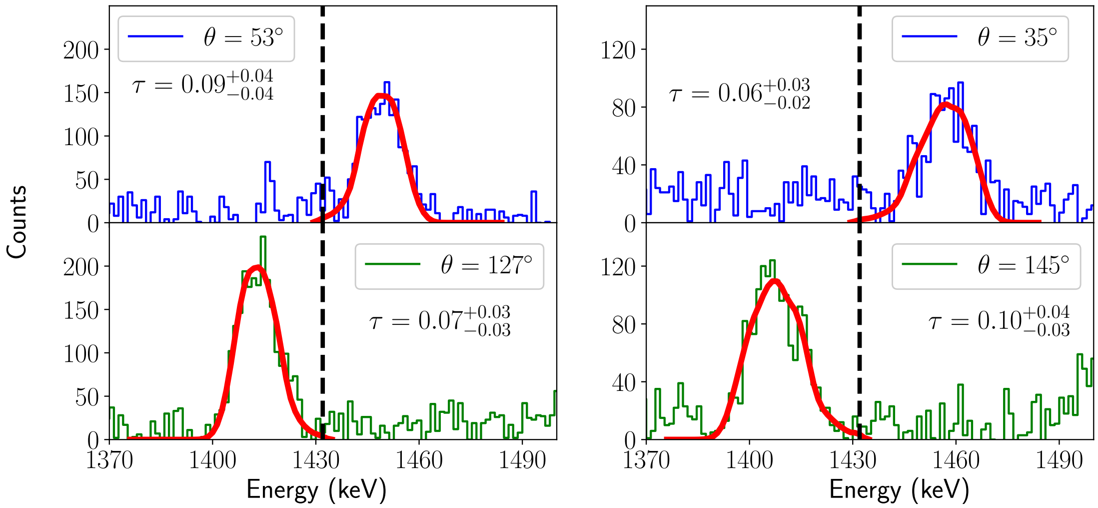

Figure C-4.: Fits performed by the program AhKin to study the excited state at 7179 keV by using the γ-ray of 1431 keV detected at different angles.

C.5. Sidefeeding time of the state at $I = (35/2)$ using the γ-ray of 1431 keV gated at 897 keV

E_γ (keV)	Gates used (keV)	Position of the gates
1431	897	Gate from below

Table C-5.: Gate used to obtain the spectrum of Figure **C-5**.

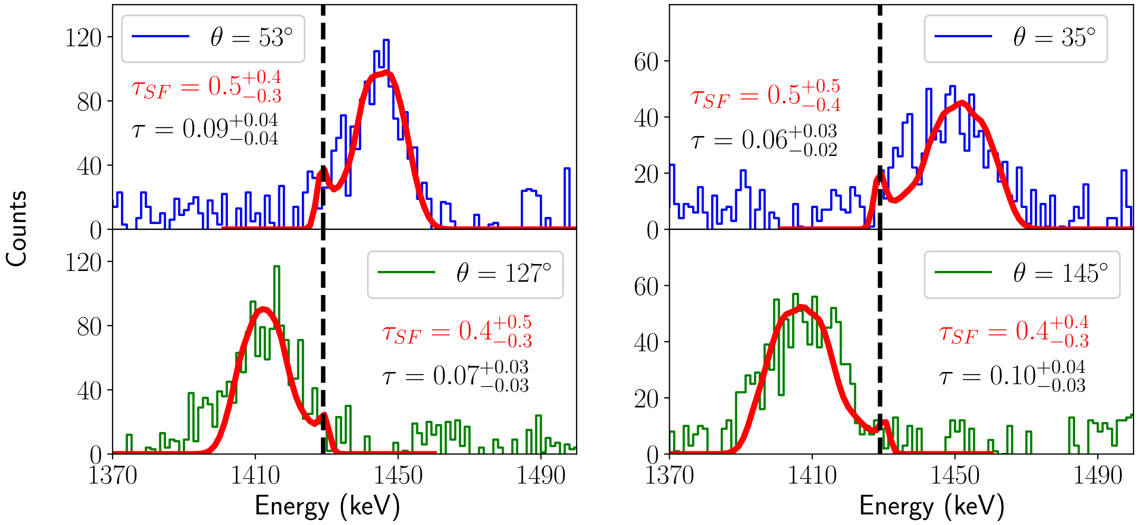

Figure C-5.: Fits performed by the program AhKin to study the feeding time of the state at 7179 keV by using the γ-ray of 1431 keV detected at different angles.

C.6. Sidefeeding time of the state at $I = (35/2)$ using the γ-ray of 1431 keV gated at 897 and 1092 keV

E_γ (keV)	Gates used (keV)	Position of the gates
1431	897 - 1092	Gate from below

Table C-6.: Gate used to obtain the spectrum of Figure **C-6**.

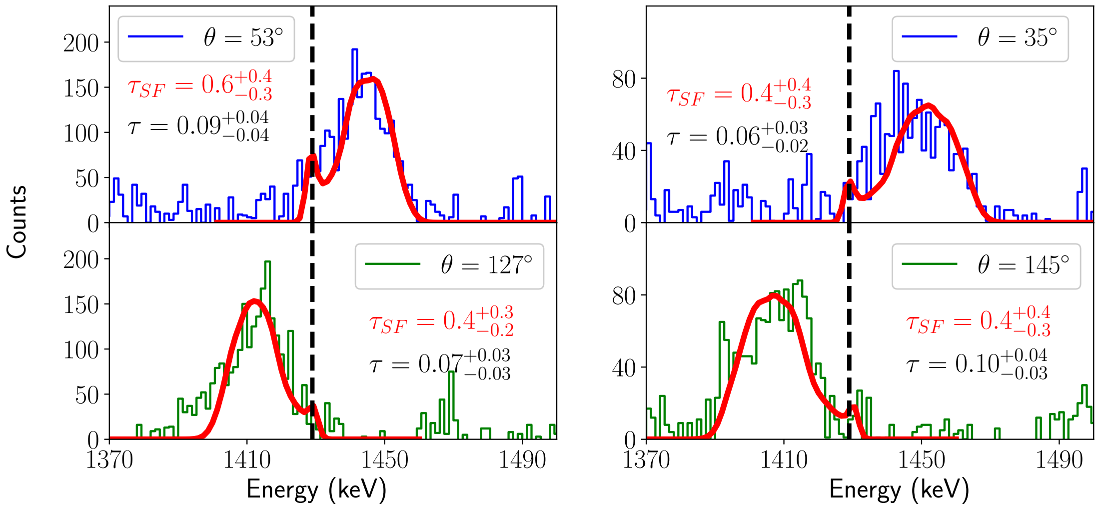

Figure C-6.: Fits performed by the program AhKin to study the feeding time of the state at 7179 keV by using the γ-ray of 1431 keV detected at different angles.

C.7. Lifetime of the state at $I = (31/2)$ using the γ-ray of 1259 keV gated at 1534 keV

E_γ (keV)	Gates used (keV)	Position of the gates
1259	1534	Gate from above

Table C-7.: Gate used to obtain the spectrum of Figure **C-7**.

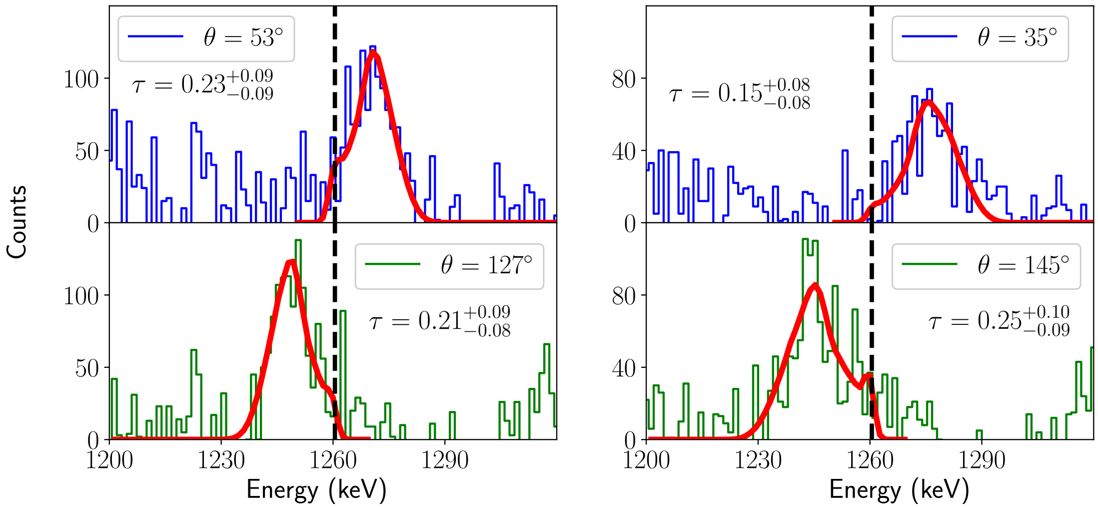

Figure C-7.: Fits performed by the program AhKin to study the excited state at 5747 keV by using the γ-ray of 1259 keV detected at different angles.

C.8. Sidefeeding time of the state at $I = (31/2)$ using the γ-ray of 1260 keV gated at 897 keV

E_γ (keV)	Gates used (keV)	Position of the gates
1259	897	Gate from below

Table C-8.: Gate used to obtain the spectrum of Figure **C-8**.

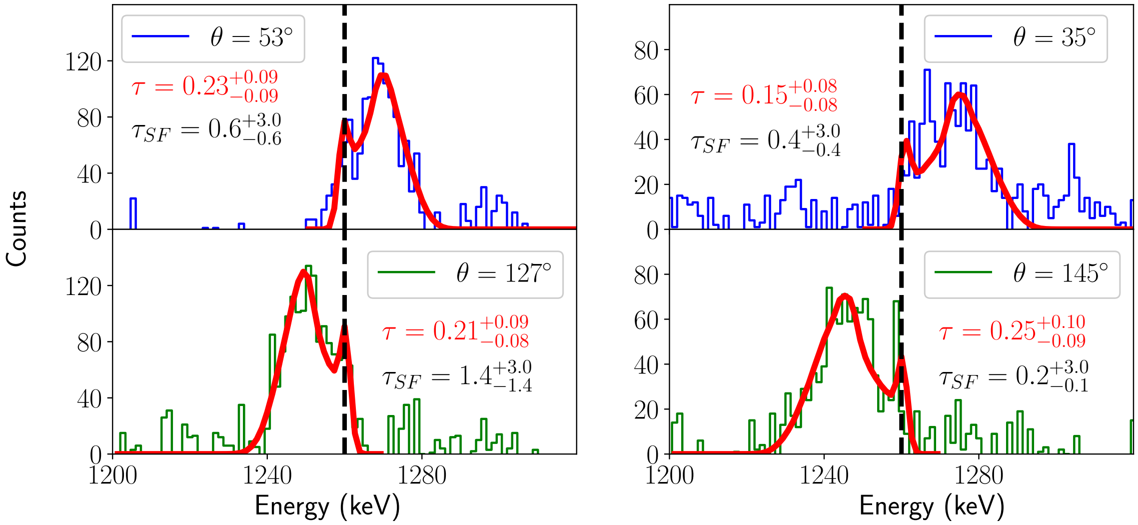

Figure C-8.: Fits performed by the program AhKin to study the feeding time of the state at 5747 keV by using the γ-ray of 1259 keV detected at different angles.

C.9. Level lifetime and sidefeeding time of the state at $I = 27/2$ using the γ-ray of 1092 keV gated at 897 keV

E_γ (keV)	Gates used (keV)	Position of the gates
1092	897	Gate from below

Table C-9.: Gate used to obtain the spectrum of Figure **C-9**.

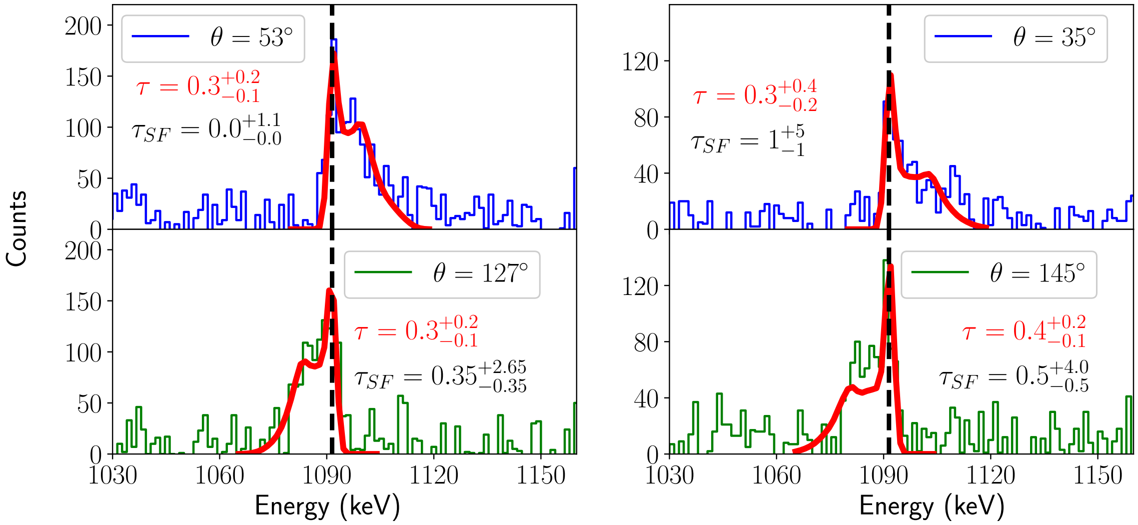

Figure C-9.: Fits performed by the program AhKin to study the level life time of the state at 4488 keV by using the γ-ray of 1092 keV detected at different angles.

D. Lineshapes determined ($(-,+)$ band)

D.1. Effective lifetime of the state at $I = (53/2)$ using the γ-rays of 2041 keV gated at 840 and 909 keV

E_γ (keV)	Gates used (keV)	Position of the gates
2041	840 - 909	Gates from below

Table D-1.: Gate used to obtain the spectrum of Figure **D-1**.

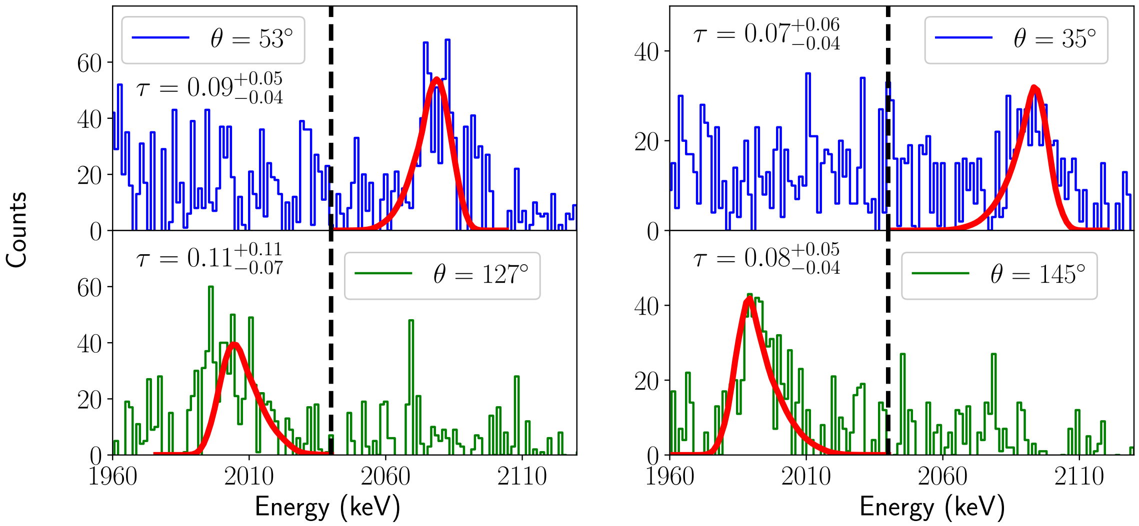

Figure D-1.: Fits performed by the program AhKin to study the excited state at 14769 keV by using the γ-ray of 2041 keV detected at different angles.

D.2. Lifetime of the state at $I=(49/2)$ using the γ-ray of 1799 keV gated at 2041 keV

E_γ (keV)	Gates used (keV)	Position of the gates
1799	2041	Gate from above

Table D-2.: Gate used to obtain the spectrum of Figure **D-2**.

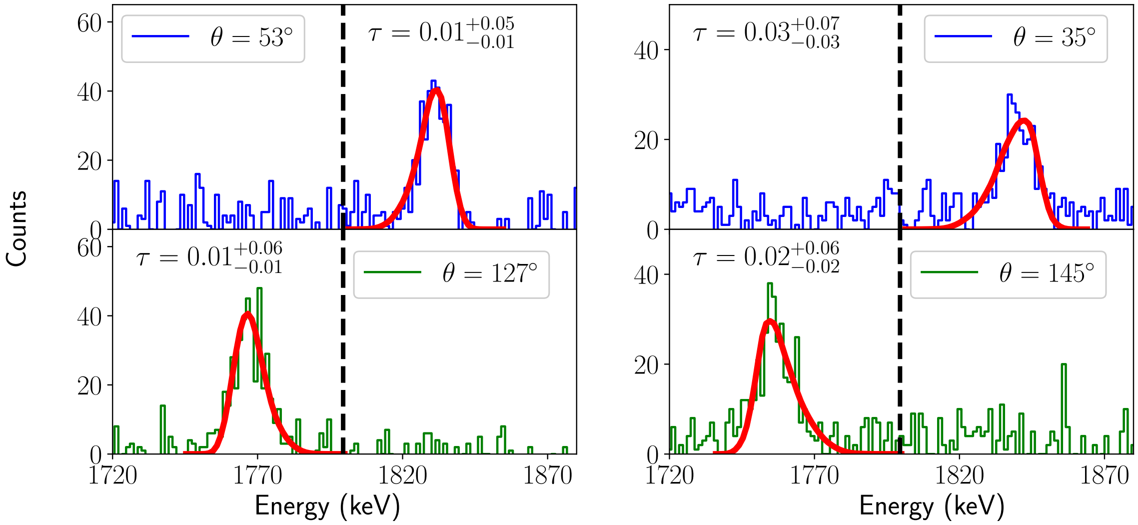

Figure D-2.: Fits performed by the program AhKin to study the excited state at 12728 keV by using the γ-ray of 1799 keV detected at different angles.

D.3. Sidefeeding time of the state at $I=(49/2)$ using the γ-ray of 1799 keV gated at 909 and 840 keV

E_γ (keV)	Gates used (keV)	Position of the gates
1799	840 - 909	Gate from below

Table D-3.: Gate used to obtain the spectrum of Figure **D-3**.

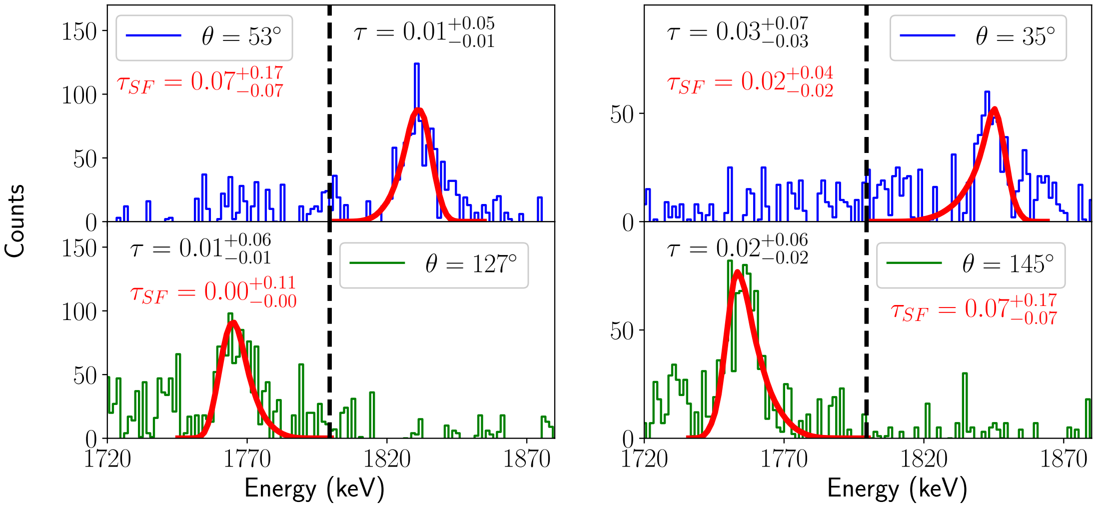

Figure D-3.: Fits performed by the program AhKin to study the sidefeeding time of the state at 12728 keV by using the γ-ray of 1799 keV detected at different angles.

D.4. Lifetime of the state at $I = (45/2)$ using the γ-ray of 1595 keV gated at 2041 keV

E_γ (keV)	Gates used (keV)	Position of the gates
1595	2041	Gate from above

Table D-4.: Gate used to obtain the spectrum of Figure **D-4**.

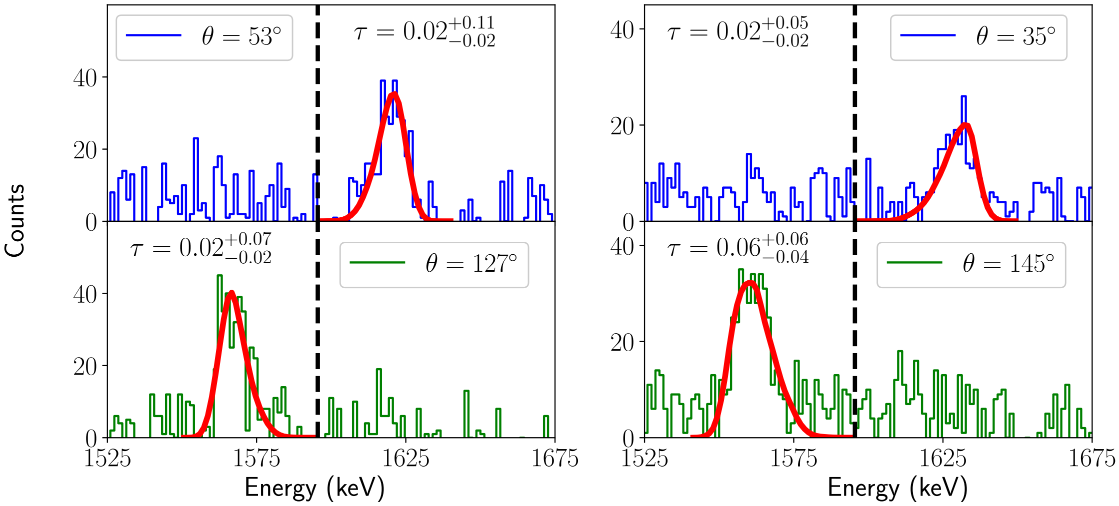

Figure D-4.: Fits performed by the program AhKin to study the excited state at 10929 keV by using the γ-ray of 1595 keV detected at different angles.

D.5. Sidefeeding time of the state at $I = (45/2)$ using the γ-ray of 1595 keV

E_γ (keV)	Gates used (keV)	Position of the gates
1595	1413	Gate from below

Table D-5.: Gate used to obtain the spectrum of Figure **D-5**.

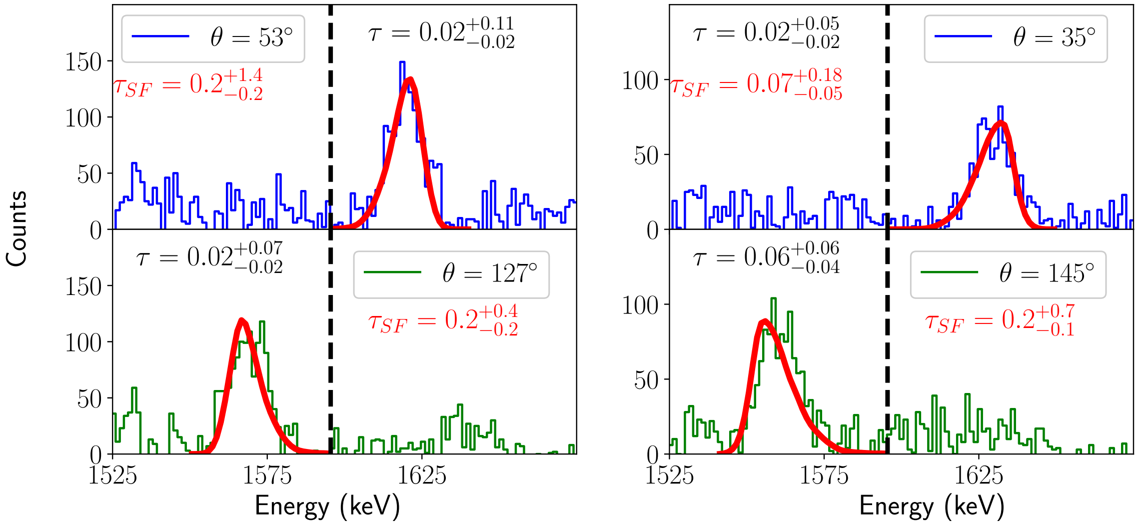

Figure D-5.: Fits performed by the program AhKin to study the excited state at 10929 keV by using the γ-ray of 1595 keV detected at different angles.

D.6. Level lifetime and sidefeeding time of the state at $I = (41/2)$ using the γ-ray of 1413 keV gated at 840 keV

E_γ (keV)	Gates used (keV)	Position of the gates
1413	840	Gate from below

Table D-6.: Gate used to obtain the spectrum of Figure **D-6**.

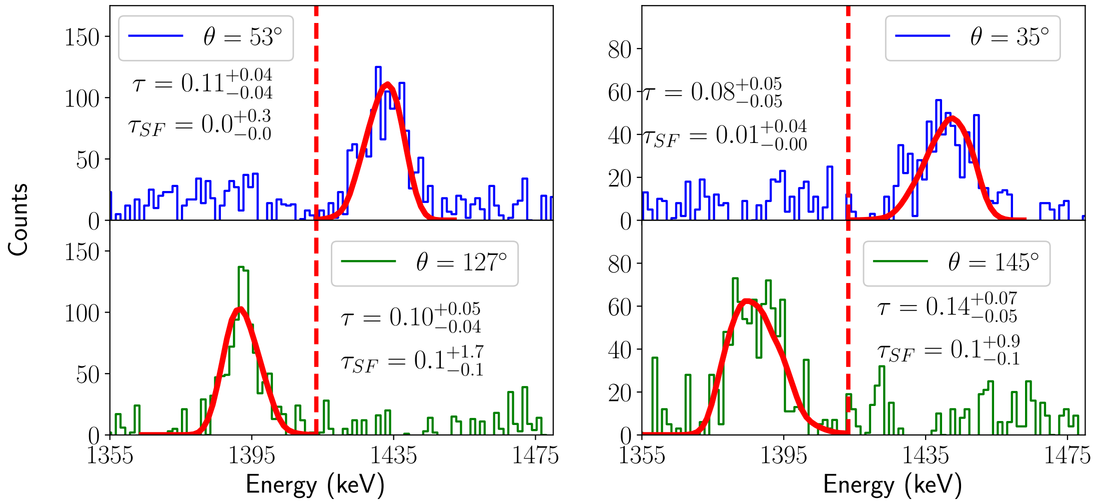

Figure D-6.: Fits performed by the program AhKin to study the sidefeeding time of the state at 9334 keV by using the γ-ray of 1413 keV detected at different angles.

D.7. Level lifetime and sidefeeding time of the state at $I = (37/2)$ using the γ-ray of 1245 keV gated at 1174 keV

E_γ (keV)	Gates used (keV)	Position of the gates
1245	1174	Gate from below

Table D-7.: Gate used to obtain the spectrum of Figure **D-7**.

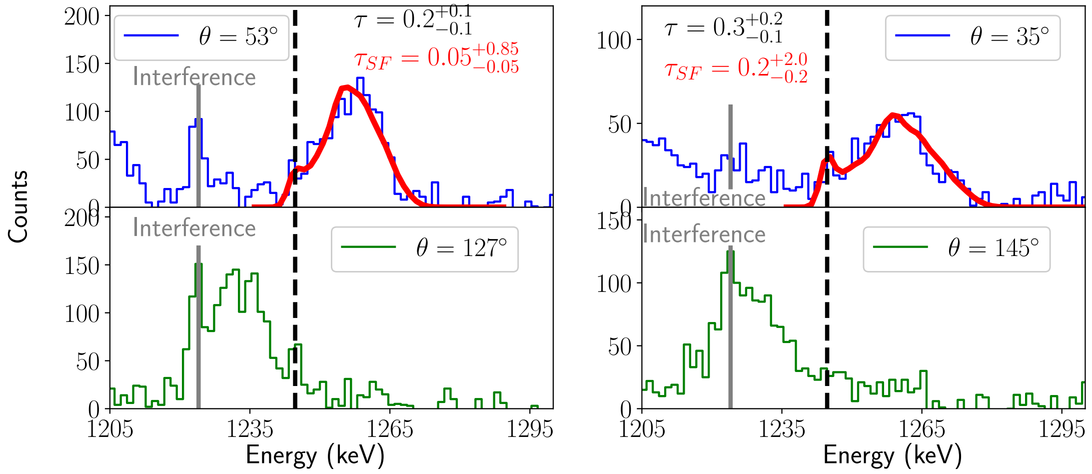

Figure D-7.: Fits performed by the program AhKin to study the sidefeeding time of the state at 7921 keV by using the γ-ray of 1245 keV detected at different angles.

D.8. Level lifetime and sidefeeding time of the state at $I = (33/2)$ using the γ-ray of 1174 keV gated at 1162 keV

E_γ (keV)	Gates used (keV)	Position of the gates
1174	1162	Gate from below

Table D-8.: Gate used to obtain the spectrum of Figure **D-8**.

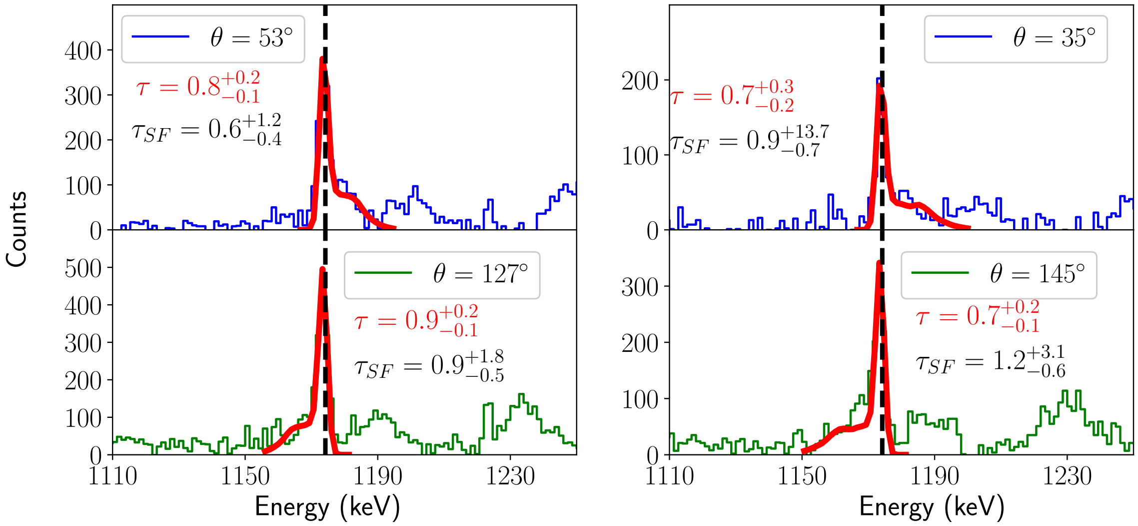

Figure D-8.: Fits performed by the program AhKin to study the level life time of the state at 6676 keV by using the γ-ray of 1174 keV detected at different angles.

D.9. Level lifetime and sidefeeding time of the state at $I = (33/2)$ using the γ-ray of 1174 keV gated at 1026 keV

E_γ (keV)	Gates used (keV)	Position of the gates
1174	1026	Gate from below

Table D-9.: Gate used to obtain the spectrum of Figure **D-9**.

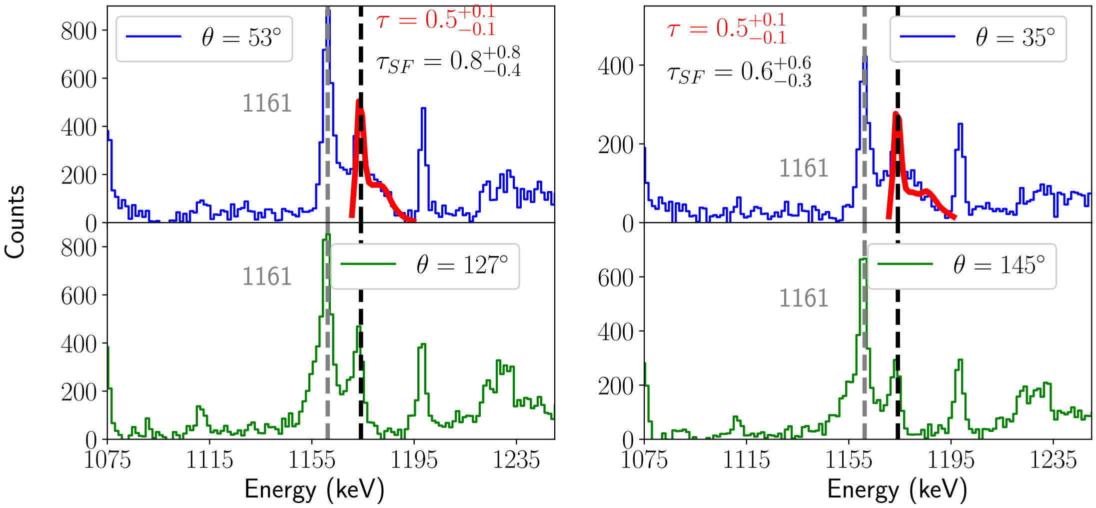

Figure D-9.: Fits performed by the program AhKin to study the level life time of the state at 6676 keV by using the γ-ray of 1174 keV detected at different angles.

D.10. Lifetime of the state at $I = (29/2)$ using the γ-ray of 1162 keV gated at 1174 keV

E_γ (keV)	Gates used (keV)	Position of the gates
1162	1174	Gate from above

Table D-10.: Gate used to obtain the spectrum of Figure **D-10**.

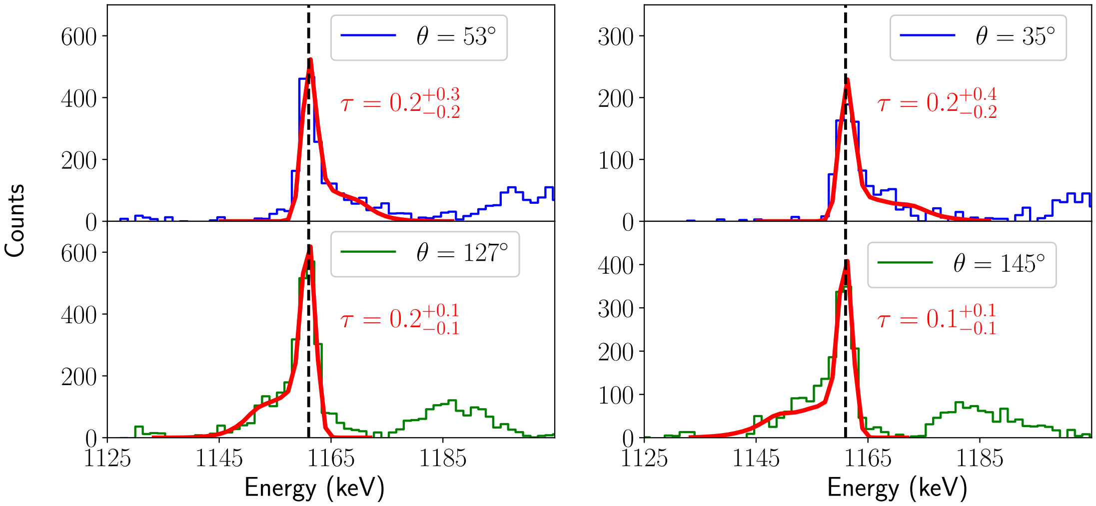

Figure D-10.: Fits performed by the program AhKin to study the excited state at 5502 keV by using the γ-ray of 1162 keV detected at different angles.

D.11. Sidefeeding time of the state at $I = (29/2)$ using the γ-ray of 1161 keV gated at 1026 keV

E_γ (keV)	Gates used (keV)	Position of the gates
1161	1026	Gate from below

Table D-11.: Gate used to obtain the spectrum of Figure **D-11**.

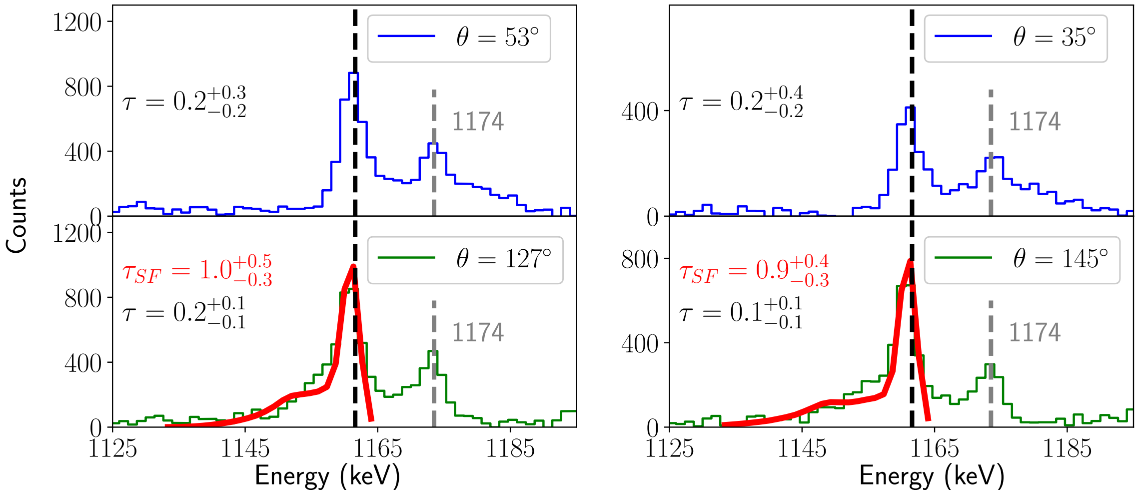

Figure D-11.: Fits performed by the program AhKin to study the level life time of the state at 5502 keV by using the γ-ray of 1161 keV detected at different angles.

D.12. Level lifetime and sidefeeding time of the state at $I = (25/2)$ using the γ-ray of 1026 keV gated at 840 keV

E_γ (keV)	Gates used (keV)	Position of the gates
1174	1026	Gate from below

Table D-12.: Gate used to obtain the spectrum of Figure **D-12**.

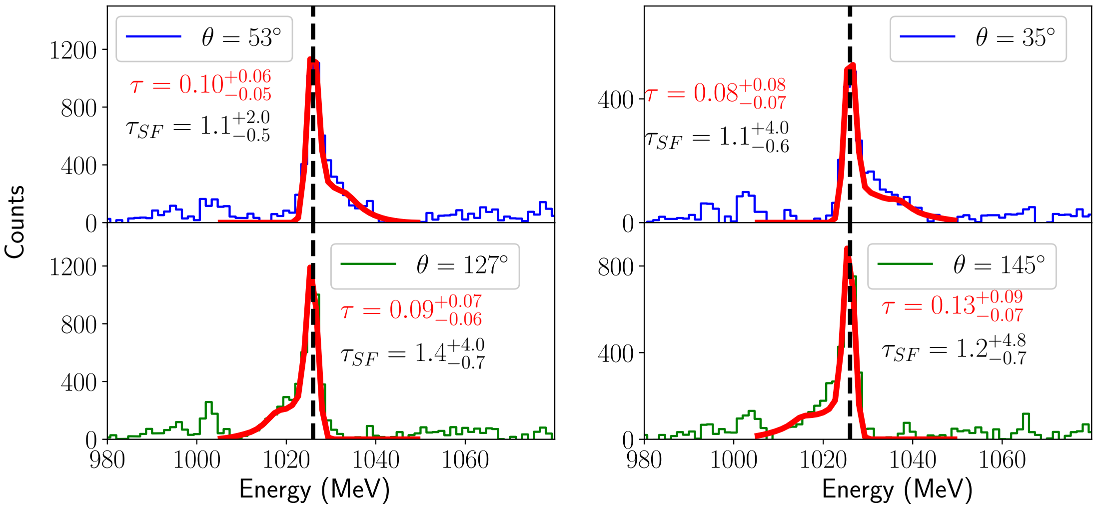

Figure D-12.: Fits performed by the program AHKIN to study the level life time of the state at 4341 keV by using the γ-ray of 1026 keV detected at different angles.

D.13. Level lifetime and sidefeeding time of the state at $I = (25/2)$ using the γ-ray of 1026 keV gated at 1161 and 840 keV

E_γ (keV)	Gates used (keV)	Position of the gates
1026	1162 - 840	Gate from below

Table D-13.: Gate used to obtain the spectrum of Figure **D-13**.

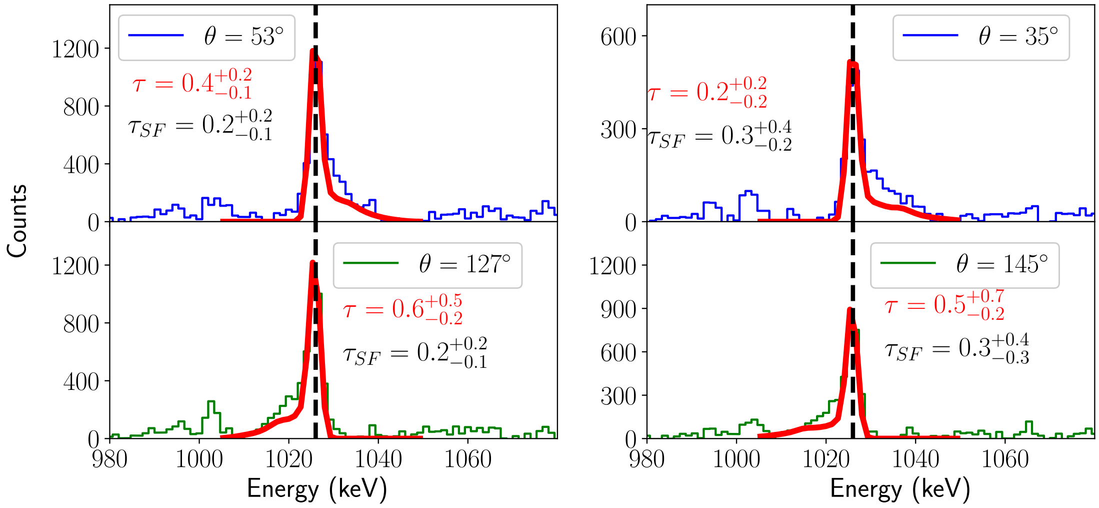

Figure D-13.: Fits performed by the program AhKin to study the level life time and sidefeeding time of the state at 4341 keV by using the γ-ray of 1026 keV detected at different angles.

D.14. Discussion τ and τ_{SF} of the state at $I = (25/2)$

When gating from above we got a good fit but when gating from below and using the time found with the GFA, thus the fit does not look as good as the fit perfomed by gating from below and adjusting simultaneosly τ and τ_{SF}. When comparing the values of τ and τ_{SF} by using the two methods it is found that the values of τ barely overlap at the extreme of the uncertainty limits whereas the values of τ_{SF} do not overlap. It is important to clarify that for all the mesurements of level lifetimes and sidefeeding times carried out in this work, this one is the only one whose results do not match between the uncertainty ranges, but they are not so far away. From the pure experimental point of view there are no arguments to invalidate any of the lifetimes or sidefeeding times found by using both methods. So we decide to take an average of both τ and τ_{SF} and use them for the analysis and calculations perfomed in this document.

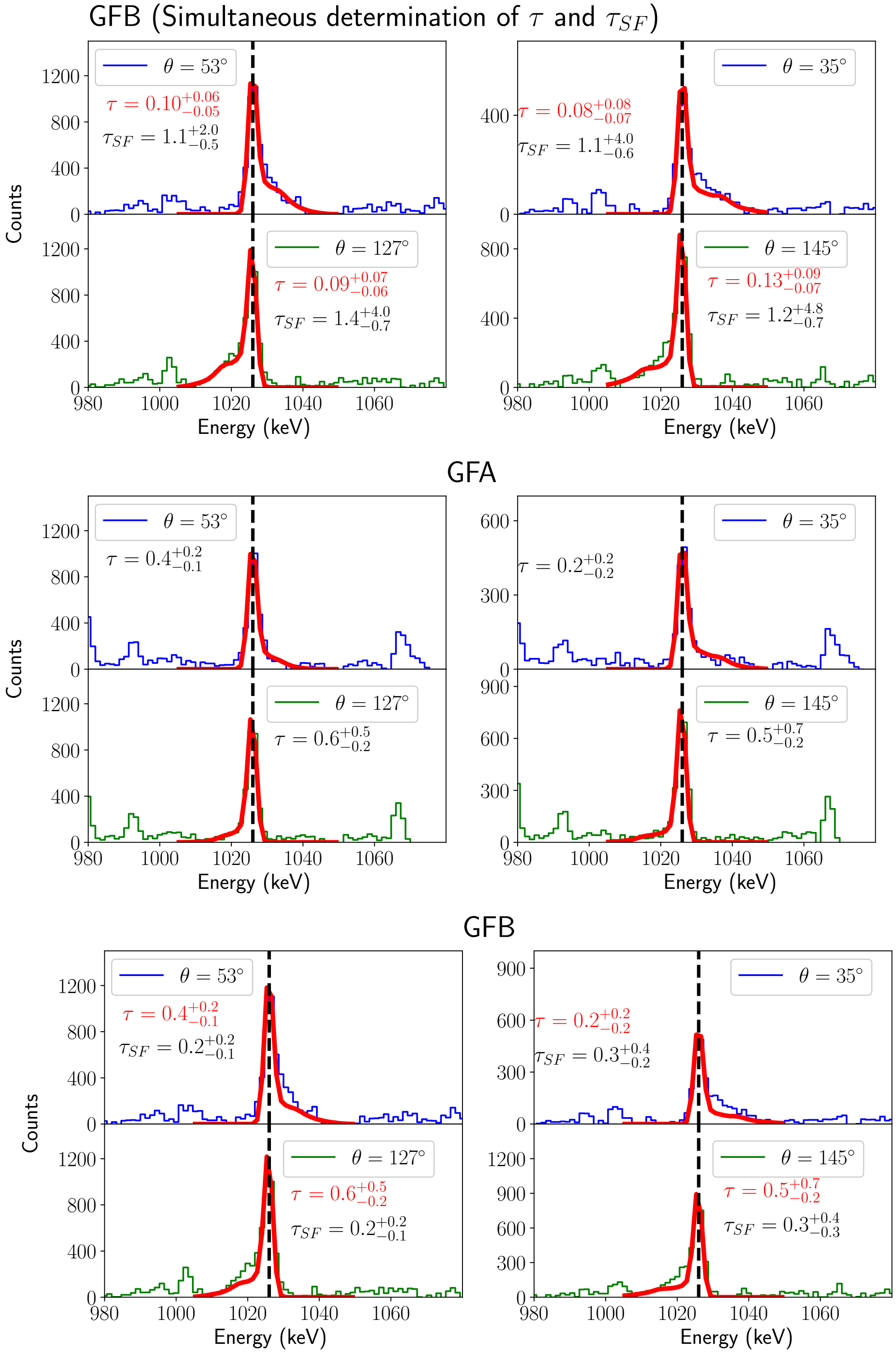

Figure D-14.: Resulting fits by doing gates from abovce and below . In the spectra gated from below the lifetime is fixed we vary only the sidefeeding time.

References

[1] L. Henden, L. Bergholt, M. Guttormsen, J. Rekstad, and T.S. Tveter, *On the relation between the statistical γ-decay and the level density in* ^{162}Dy, Nuclear Physics A **589** (1995), no. 2, 249 –266.

[2] F. Cristancho, *Energy-Ordered Spectra in Continuum Gamma Decay*, Heavy Ion Physics **2** (1995), 299–313.

[3] C. J. Lister, B. J. Varley, W. Fieber, J. Heese, K. P. Lieb, E. K. Warburton, and J. W. Olness, *Structure of high spin states in* ^{83}Y, Zeitschrift für Physik A Atomic Nuclei **329** (1988 Dec.), no. 4, 413–427.

[4] F. Cristancho, K.P. Lieb, J. Heese, C.J. Gross, W. Fieber, Th. Osipowcz, and S. Ulbig, *Side-feeding times and level lifetimes measured in the reaction* $^{54}\mathrm{Fe}(^{32}\mathrm{S}, 3\mathrm{p})^{83}\mathrm{Y}$, Nuclear Physics **A501** (1989), 118–136.

[5] T.D. Johnson, F. Cristancho, C.J. Gross, M. Kabadiyski, K.P. Lieb, D. Rudolph, M. Weiszflog, T. Burkardt, J. Eberth, and S. Skoda, *Transitional quadrupole moments in* ^{83}Y, Zeitschrift für Physik A Hadrons and Nuclei **347** (1994), 285–286.

[6] T. D. Johnson, A. Aprahamian, C. J. Lister, D. J. Blumenthal, B. Crowell, P. Chowdhury, P. Fallon, and A. O. Machiavelli, *New high spin states and band termination in* ^{83}Y *and* ^{84}Zr, Phys. Rev. C **55** (1997 Mar.), 1108–1118.

[7] National Nuclear Data Center, *Chart of nuclides*, Brookhaven National Laboratory, 2019. www.nndc.bnl.gov.

[8] I. Ragnarsson and S.G. Nilsson, *Shapes and shells in nuclear structure*, Cambridge University Press, 2005.

[9] Bohr A. and Mottelson B.R., *Nuclear structure*, Nuclear Structure, World Scientific, 1998.

[10] J.M. Blatt and V.F. Weisskopf, *Theoretical nuclear physics*, Dover Books on Physics Series, Dover Publications, 1991.

[11] Alan L. Goodman, *Finite-temperature HFB theory*, Nuclear Physics **A352** (1981), 30–44.

[12] Alan L. Goodman, *Temperature-induced deformation in* ^{148}Sm, Phys. Rev. C **33** (1986 Jun.), 2212–2214.

[13] Alan L. Goodman, *Shape transitions in* ^{148}S*m*, Physical Review C **48** (1993), 2679.

[14] Sven Gosta Nilsson and Ingemar Ragnarson, *Shapes and shells in nuclear structure*, Cambridge University Press, 1995.

[15] Giulio Racah, *Nuclear coupling and shell model*, Phys. Rev. **78** (1950 June), 622–623.

[16] A.V. Afanasjev, D.B. Fossan, G.J. Lane, and I. Ragnarsson, *Termination of rotational bands: disappearance of quantum many-body collectivity*, Physics Reports **322** (1999), no. 1, 1 –124.

[17] W. Nazarewicz, J. Dudek, R. Bengtsson, T. Bengtsson, and I. Ragnarsson, *Microscopic study of the high-spin behaviour in selected a 80 nuclei*, Nuclear Physics A **435** (1985), no. 2, 397 –447.

[18] S. L. Tabor, *Convergence of the moments of inertia in f-p-g shell nuclei*, Phys. Rev. C **45** (1992 Jan.), 242–248.

[19] J.D. Jackson, *Classical electrodynamics*, Wiley, 1998.

[20] J.M. Blatt and V.F. Weisskopf, *Theoretical nuclear physics*, Dover Books on Physics Series, Dover Publications, 1991.

[21] R. Bengtsson and S. Frauendorf, *Quasiparticle spectra near the yrast line*, Nuclear Physics A **327** (1979), no. 1, 139 –171.

[22] S. Cohen, F. Plasil, and W.J. Swiatecki, *Equilibrium configurations of rotating charged or gravitating liquid masses with surface tension. ii*, Annals of Physics **82** (1974), no. 2, 557 –596.

[23] Ingemar Ragnarsson, Zheng Xing, Tord Bengtsson, and Mark A Riley, *Properties of terminating bands in nuclei*, Physica Scripta **34** (1986), no. 6A, 651.

[24] R. Cardona, F. Cristancho, S. L. Tabor, R. A. Kaye, G. Z. Solomon, J. Döring, G. D. Johns, M. Devlin, F. Lerma, D. G. Sarantites, I.-Y. Lee, A. O. Macchiavelli, and I. Ragnarsson, *High-spin structure of normal-deformed bands in* ^{84}Zr, Phys. Rev. C **68** (2003 Aug.), 024303.

[25] J. J. Valiente-Dobón, T. Steinhardt, C. E. Svensson, A. V. Afanasjev, I. Ragnarsson, C. Andreoiu, R. A. E. Austin, M. P. Carpenter, D. Dashdorj, G. de Angelis, F. Dönau, J. Eberth, E. Farnea, S. J. Freeman, A. Gadea, P. E. Garrett, A. Görgen, G. F. Grinyer, B. Hyland, D. Jenkins, F. Johnston-Theasby, P. Joshi, A. Jungclaus, K. P. Lieb, A. O. Macchiavelli, E. F. Moore, G. Mukherjee, D. R. Napoli, A. A. Phillips, C. Plettner, W. Reviol, D. Sarantites, H. Schnare, M. A. Schumaker, R. Schwengner, D. Seweryniak, M. B. Smith, I. Stefanescu, O. Thelen, and R. Wadsworth, *Evidence for nontermination of rotational bands in* ^{74}Kr, Phys. Rev. Lett. **95** (2005 Nov.), 232501.

[26] Hai-Liang Ma, B. Gillis Carlsson, Ingemar Ragnarsson, and Hans Ryde, *Interpretation of the high spin states in* ^{161}Lu*: A paired and unpaired study*, Phys. Rev. C **90** (2014 July), 014316.

[27] Tord Bengtsson and Ingemar Ragnarsson, *Rotational bands and particle-hole excitations at very high spin*, Nuclear Physics A **436** (1985), no. 1, 14 –82.

[28] B. G. Carlsson and I. Ragnarsson, *Calculating the nuclear mass in the very high angular momentum regime*, Phys. Rev. C **74** (2006 July), 011302.

[29] P. Ring and P. Schuck, *The nuclear many-body problem*, Physics and astronomy online library, Springer, 2004.

[30] A. Gilbert and A. G. W. Cameron, *A composite nuclear level density formula with shell corrections*, Canadian Journal of Physics **43** (1965), 1446–1496.

[31] Mamta Aggarwal, *Hot rotating fp shell nuclei near proton drip*, Physical Review C **69** (2004), no. 034602.

[32] Peter Axel, *Electric dipole ground-state transition width strength function and* $7-$Mev *photon interactions*, Phys. Rev. **126** (1962 Apr.), 671–683.

[33] G. A. Leander, *Statistical E1 and M1 gamma strength functions from heavy-ion, xn-gamma data*, Phys. Rev C (1988).

[34] R. Holzmann, T. L. Khoo, W. C. Ma, I. Ahmad, and B. K Dichter, *Structure in the E2 quasicontinuum spectrum of* ^{154}Dy, Physical Review Letters (1989).

[35] R. Holzmann, I. Ahmad, B.K. Dichter, H. Emling, R.V.F. Janssens, T.L. Khoo, W.C. Ma, M.W. Drigert, U. Garg, D.C. Radford, P.J. Daly, Z. Grabowski, H. Helppi, M. Quader, and W. Trzaska, *Evolution of nuclear structure with increasing spin and internal excitation energy in* ^{152}Dy, Physics Letters B **195** (1987), no. 3, 321 –325.

[36] J. C Bacelar, G. B. Hagemann, B. Herskind, B. Lauritzen, A. Holm, J. C. Lisle, and P. O. Tjom, *Determination of the spreading width for the collective transition strength at finite temperature*, Physical Review Letters (1985).

al

[37] W. C. Ma and et al, *Phase transitions above the yrast line in* ^{154}Dy, Physical Review Letters **84** (2000), no. 5967.

[38] Edana Merchán, *New Hk-*EOS *method for the investigation of the nuclear continuum: Performance evaluation with simulated and experimental data*, Ph.D. Thesis, Universidad Nacional de Colombia 2006.

[39] D. G. Sarantites, P.F. Huaa, M. Devlina, L.G. Sobotkaa, J. Elsona, J.T. Hooda, D.R. LaFossea, J.E. Sarantitesa, and M.R. Maierb, *The microball design, instrumentation and response characteristics of a 4π-multidetector exit channel-selection device for spectroscopic and reaction mechanism studies with gammasphere*, Nuclear Instruments and Methods in Physics Research Section A **381** (1996), 418–432.

[40] I-Yang Lee, *The gammasphere*, Nuclear Physics A **520** (1990), c641–c655.

[41] A Schiller, L Bergholt, M Guttormsen, E Melby, S Messelt, J Rekstad, and S Siem, *Level densities and γ-strength functions in rare earth nuclei*, Physica Scripta **2000** (2000), no. T88, 144.

[42] M Guttormsen, E Melby, J Rekstad, S Siem, A Schiller, T Lönnroth, and A Voinov, *Level density and γ-ray strength in* ^{27,28}Si, Journal of Physics G: Nuclear and Particle Physics **29** (2003), no. 2, 263.

[43] M. Guttormsen, A. Bagheri, R. Chankova, J. Rekstad, S. Siem, A. Schiller, and A. Voinov, *Thermal properties and radiative strengths in* ^{160,161,162}Dy, Physical Review C **68** (2003), 064306.

[44] U. Agvaanluvsan, A. Schiller, J. A. Becker, L. A. Bernstein, P. E. Garrett, M. Guttormsen, G. E. Mitchell, J. Rekstad, S. Siem, A. Voinov, and W. Younes, *Level densities and γ-ray strength functions in* ^{170,171,172}Yb, Physical Review C **70** (2004), 054611.

[45] H. K. Toft, A. C. Larsen, U. Agvaanluvsan, A. Bürger, M. Guttormsen, G. E. Mitchell, H. T. Nyhus, A. Schiller, S. Siem, N. U. H. Syed, and A. Voinov, *Level densities and γ-ray strength functions in Sn isotopes*, Physical Review C **81** (2010), 064311.

[46] M. Guttormsen, B. Jurado, J. N. Wilson, M. Aiche, L. A. Bernstein, Q. Ducasse, F. Giacoppo, A. Görgen, F. Gunsing, T. W. Hagen, A. C. Larsen, M. Lebois, B. Leniau, T. Renstrøm, S. J. Rose, S. Siem, T. Tornyi, G. M. Tveten, and M. Wiedeking, *Constant-temperature level densities in the quasicontinuum of Th and U isotopes*, Physical Review C **88** (2013), 024307.

[47] T. G. Tornyi, M. Guttormsen, T. K. Eriksen, A. Görgen, F. Giacoppo, T. W. Hagen, A. Krasznahorkay, A. C. Larsen, T. Renstrøm, S. J. Rose, S. Siem, and G. M. Tveten, *Level density and γ-ray strength function in the odd-odd* ^{238}Np *nucleus*, Physical Review C **89** (2014), 044323.

[48] T. Renstrøm, H.-T. Nyhus, H. Utsunomiya, R. Schwengner, S. Goriely, A. C. Larsen, D. M. Filipescu, I. Gheorghe, L. A. Bernstein, D. L. Bleuel, T. Glodariu, A. Görgen, M. Guttormsen, T. W. Hagen, B. V. Kheswa, Y.-W. Lui, D. Negi, I. E. Ruud, T. Shima, S. Siem, K. Takahisa, O. Tesileanu, T. G. Tornyi, G. M. Tveten, and M. Wiedeking, *Low-energy enhancement in the γ-ray strength functions of* ^{73,74}Ge, Physical Review C **93** (2016), 064302.

[49] C. Baktash, M.L. Halbert, D.C. Hensley, N.R. Johnson, I.Y. Lee, J.W. McConnell, and F.K. McGowan, *Study of spin-temperature effects using energy-ordered continuum gamma-ray spectroscopy technique*, Nuclear Physics A **520** (1990), c555 –c565.

[50] John Jairo Sandoval, *Resonancia Dipolar Gigante y Gas de Fermi en el decaimiento del continuo nuclear*, Master's Thesis, Universidad Nacional de Colombia 2008.

[51] J. Cardona and F. Cristancho, *Order Statistics Applied to Energy Ordered Spectra*, Heavy Ion Physics **16** (1995), 75–83.

[52] R. F. García Ruiz and F. Cristancho, *On the use of the Extreme Value Theory in analyses of continuum gamma decay*, AIP Conference proceedings, 2010, pp. 106.

[53] Javier Pinzón, *Fitting function for experimental energy ordered spectra in nuclear continuum studies*, Master's Thesis, Universidad Nacional de Colombia 2012.

[54] Martha Ferrer Pacheco, *Simulación de un sistema de detección combinado de detectores de rayos gamma de BGO y germanio*, Master's Thesis, Universidad Nacional de Colombia 2007.

[55] D. Bazzacco and The GASP Collaboration, *The gamma ray spectrometer GASP*, Proc. int. conf. nuclear structure at high angular momentum, 1992, pp.–382@.

[56] PARIS collaboration, *Photon Array for Studies with Radioactive Ions and Stable beams*, 2015. http://paris.ifj.edu.pl/index.php?lng=en.

[57] Marc Labiche, *NPTool, an analysis and simulation framework for nuclear physics experiment based on root and geant4.*, 2017. http://nptool.org/manual/paris/.

[58] F. Cristancho, C.J. Gross, K.P. Lieb, D. Rudolph, O. Skeppstedt, M.A. Bentley, W. Gelletly, H.G. Price, J. Simpson, J.L. Durell, B.J. Varley, and S. Rastikerdar, *Band crossing in* ^{83}Y *revisited*, Nuclear Physics A **540** (1992), no. 1, 307 –327.

[59] A. Garzón, W. Rodriguez, F. Cristancho, and M. Tao, *A modular and efficient code for the doppler shift attenuation method*, 2019. Submitted to Computer Physics Communications.

[60] J.F. Ziegler, J.P. Biersack, and M.D. Ziegler, *Srim, the stopping and range of ions in matter*, SRIM Company, Unknown Month SRIM.

[61] E. F. Moore, P. D. Cottle, C. J. Gross, D. M. Headly, U. J. Hüttmeier, S. L. Tabor, and W. Nazarewicz, *Shape coexistence effects and quasiparticle alignment in* ^{81}Sr, Physical Review C **38** (1988), 696–711.

[62] D.W.O. Rogers, *Analytic and graphical methods for assigning errors to parameters in non-linear least squares fitting*, Nuclear Instruments and Methods **127** (1975), no. 2, 253 –260.

[63] Ramiro Cardona, *Estructura a alto espín de las bandas normalmente deformadas de 84zr*, Ph.D. Thesis, 2003.

[64] D. A. Torres, N. De La Rosa, F. Cristancho, S. L. Tabor, R. A. Kaye, G. Z. Solomon, J. Döring, G. D. Johns, M. Devlin, F. Lerma, D. G. Sarantites, I.-Y. Lee, A. O. Macchiavelli, and A. Garzón, *Band termination in normally deformed bands in* ^{83}Y, AIP Conference Proceedings **1529** (2013), no. 1, 170–173.

[65] F. Cristancho and K.P. Lieb, *Side-feeding times in even dysprosium isotopes*, Nuclear Physics A **524** (1991), no. 3, 518 –536.

[66] G. A. Leander, *Nuclear quasicontinuum gamma-ray spectra*, Computer Physics Communications **47** (1987), 311–340.

[67] A. Gavron, *Computational nuclear physics 2, nuclear reactions*, Springer-Verlag, Unknown Month 1993 p. 108.

[68] Donald W. Lang, *The angular momentum-dependence of the nuclear level density*, Nuclear Physics **77** (1966), 545–558.

[69] B. Lauritzen, T. Dossing, and R.A. Broglia, *Damping of rotational motion*, Nuclear Physics A **457** (1986), no. 1, 61 –83.

[70] G. A. Leander, *Statistical* E1 *and* M1 *gamma strength functions from heavy-ion, xnγ data*, Phys. Rev. C **38** (1988 Aug.), 728–736.

[71] R. Casten, *Nuclear structure from a simple perspective*, Oxford science publications, Oxford University Press, 2000.

[72] K. Jonsson, B. Cederwall, A. Johnson, R. Wyss, T. Back, J. Cederkall, M. Devlin, J. Elson, D.R. LaFosse, F. Lerma, D.G. Sarantites, R.M. Clark, I.Y. Lee, A.O. Macchiavelli, and R.W. Macleod, *Collective excitations and band termination in* ^{85}Nb, Nuclear Physics A **645** (1999), no. 1, 47 –60.

[73] R. A. Kaye, C. T. Rastovski, S. L. Tabor, J. Döring, F. Cristancho, M. Devlin, G. D. Johns, I. Y. Lee, F. Lerma, A. O. Macchiavelli, D. G. Sarantites, and G. Z. Solomon, *Evolution of collectivity with spin in* ^{81}Y, Phys. Rev. C **66** (2002 Nov.), 054305.

[74] S. L. Tabor, P. D. Cottle, C. J. Gross, U. J. Hüttmeier, E. F. Moore, and W. Nazarewicz, *Proton and neutron alignments and transition strengths in the transitional nucleus* ^{81}Rb, Phys. Rev. C **39** (1989 Apr.), 1359–1370.

[75] J. Döring, R. Schwengner, L. Funke, H. Rotter, G. Winter, B. Cederwall, F. Lidén, A. Johnson, A. Atac, J. Nyberg, and G. Sletten, *High-lying three-quasiparticle bands and signature splitting in* ^{81}Rb, Phys. Rev. C **50** (1994 Oct.), 1845–1850.

[76] W. Rodriguez, F. Cristancho, S. Tabor, A. Kardan, I. Ragnarsson, G. Z. Solomon, R. A. Kaye, J. Döring, G. D. Johns, M. Devlin, F. Lerma, D. G. Sarantites, I.Y. Lee, A. O. Macchiavelliand, and A. Garzón, *Study of high spin states of the normally deformed bands of* ^{83}Y, 2019. Submitted to Phys. Rev. C.

[77] Tord Bengtsson, *The high-spin structure of* ^{158}Er*: A theoretical study*, Nuclear Physics A **512** (1990), no. 1, 124 –148.

[78] B. G. Carlsson, I. Ragnarsson, R. Bengtsson, E. O. Lieder, R. M. Lieder, and A. A. Pasternak, *Triaxial shape with rotation around the longest principal axis in* ^{142}Gd, Phys. Rev. C **78** (2008 Sep.), 034316.

[79] X. Wang, M.A. Riley, J. Simpson, E.S. Paul, J. Ollier, R.V.F. Janssens, A.D. Ayangeakaa, H.C. Boston, M.P. Carpenter, C.J. Chiara, U. Garg, D.J. Hartley, D.S. Judson, F.G. Kondev, T. Lauritsen, N.M. Lumley, J. Matta, P.J. Nolan, M. Petri, J.P. Revill, L.L. Riedinger, S.V. Rigby, C. Unsworth, S. Zhu, and I. Ragnarsson, *Quadrupole moments of collective structures up to spin* $\sim 65\hbar$ *in* ^{157}Er *and* ^{158}Er*: A challenge for understanding triaxiality in nuclei*, Physics Letters B **702** (2011), no. 2, 127 –130.

[80] C. J. Chiara, D. G. Sarantites, M. Montero, J. O'Brien, W. Reviol, O. L. Pechenaya, R. M. Clark, P. Fallon, A. Görgen, A. O. Macchiavelli, D. Ward, Y. R. Shimizu, and W. Satuła, *Decay-out properties of a linked superdeformed band in* ^{84}Zr, Phys. Rev. C **73** (2006 Feb.), 021301(R).

[81] S. L. Tabor, J. Döring, J. W. Holcomb, G. D. Johns, T. D. Johnson, T. J. Petters, M. A. Riley, and P. C. Womble, *Transition strengths and multiple band structure in* ^{82}Sr, Phys. Rev. C **49** (1994 Feb.), 730–742.

[82] K. Langanke, J. Maruhn, and S.E. Koonin, *Computational nuclear physics 1: Nuclear structure*, Springer series in computational physics, Springer Berlin Heidelberg, 2013.

[83] M. Scharff J. Lindhard and H. E. Schiott, *Range and concepts and heavy ions ranges*, Mat. Fys. Medd. Dan. Vid. Selsk. **33** (1963), no. 14, 4–10.